Understanding the Connection Between Active Galactic Nuclei and Host Star Formation Through Multi-Wavelength Population Synthesis Modeling

A Thesis
Presented to
The Academic Faculty

by

Aden R. Draper

In Partial Fulfillment
of the Requirements for the Degree
Doctor of Philosophy

School of Physics
Georgia Institute of Technology
December 2012

Understanding the Connection Between Active Galactic Nuclei and Host Star Formation Through Multi-Wavelength Population Synthesis Modeling

Approved by:

Professor David Ballantyne, Advisor
School of Physics
Georgia Institute of Technology

Professor Ignacio Taboada
School of Physics
Georgia Institute of Technology

Professor Pablo Laguna
School of Physics
Georgia Institute of Technology

Professor John Wise
School of Physics
Georgia Institute of Technology

Professor D. Michael Crenshaw
Department of Physics & Astronomy
Georgia State University

Date Approved: July 25, 2012

To the family, friends, and community who kept my head above the water.

(And yes, that is a Dolly Parton reference.)

ACKNOWLEDGEMENTS

I would like to thank the Draper family for their love, support and encouragement for the last 28 years and for teaching me to be curious and follow my dreams. I'd also like to thank the Meng and the Spratt/Richards families for welcoming me into their families and making Atlanta feel like my home. I especially want to thank my best friend Sarah for her many many pep talks and my partner G for her counsel, level-headedness, etc. I also appreciate the support and baked goods of all of my friends and the Keene area and Atlanta queer communities.

I am indebted to the many teachers and professors who have encouraged me as a student and a person. I especially want to thank my middle school math teacher Nancy Belsky and undergraduate advisor Prof. Art Bowling. I would also like to thank Georgia Tech and the School of Physics for a great environment in which to pursue my Ph.D. I particularly appreciate the faculty, post-docs, and students of the Center for Relativistic Astrophysics for an academically interesting and fun environment. I would especially like to thank my advisor, David Ballantyne, for introducing me to the world of AGN and for giving me the opportunity to do exciting research. I'd also like to thank the astrophysics community, and particularly the folks of WGLE, for their camaraderie.

TABLE OF CONTENTS

LIST OF TABLES

LIST OF FIGURES

SUMMARY

Supermassive black holes, black holes with masses $\gtrsim 10^6$ $M_\odot$, are found at the centers of all massive galaxies. These massive black holes grew from smaller seed black holes through accretion events. Accreting black holes are very bright in the radio through very hard X-ray spectral regimes. Due to the location of these accreting black holes at the centers of galaxies, they are referred to as active galactic nuclei (AGN). It is understood that AGN are an important phase of galaxy evolution; however, the role of AGN in massive galaxy formation is very poorly constrained.

Here, the unique tool of multi-wavelength population synthesis modeling is used to study the average properties of AGN and their host galaxies with a focus on host galaxy star formation and the role of black hole growth in galaxy evolution. Knowledge of the AGN population from deep X-ray surveys is combined with theoretical AGN spectral energy distributions to predict various observables of the AGN population in wavelength regions from the far infrared to very hard X-rays. Comparison of the model predictions to observations constrains the model input parameters and allows for the determination of average properties of the AGN population.

Particular attention is paid to a special class of AGN known as Compton thick AGN. These AGN are deeply embedded in gas and dust such that the column density obscuring the line of sight to the central engine of the AGN exceeds $1/\sigma_T \sim 10^{24}$ cm^{-2}, where σ_T is the Thomson cross-section of the electron—a column density comparable to that of the human chest. Theoretical and simulational evidence suggest that these Compton thick AGN may be recently triggered, rapidly accreting AGN, making them of special interest to researchers. I found that Compton thick AGN are likely to contribute $\sim$20% of the peak of the cosmic X-ray background (XRB) at $\sim$30 keV and demonstrated that a significant portion of Compton thick AGN may be accreting very rapidly. Moreover, Compton thick

AGN do not appear to follow the orientation based unified model of AGN. According to the unified model, AGN exhibit a range of obscuration levels due to a dusty "torus" which, depending on the orientation of the torus to the observer's line of sight, may obscure the central engine of the AGN. Upon further investigation into the stellar populations of AGN host galaxies, it appears that the unified model holds in general at $z \lesssim 1$, but not at $z \gtrsim 1$. I found that this is likely due to the dominant triggering mechanism of AGN switching from major mergers at $z \gtrsim 1.5$ to secular processes by $z \sim 1$.

CHAPTER I

INTRODUCTION

By the mid 1990's it was widely understood that all massive galaxies contain a supermassive black hole at their center (Kormendy & Richstone, 1995), even the Milky Way (e.g., Backer & Sramek, 1999; Reid et al., 1999). Supermassive black holes are compact objects with masses 10^6–10^{10} $M_\odot$. The vast majority of these supermassive black holes are quiescent and accreting at $\lambda \lesssim 10^{-6}$, where $\lambda = L_{bol}/L_{Edd}$ is the Eddington ratio, L_{bol} is the bolometric luminosity, and L_{Edd} is the Eddington luminosity, the theoretical maximum luminosity for spherical accretion. However, a small fraction of supermassive black holes are accreting at $\lambda \sim 1$. These accreting black holes are bright sources across the entire electromagnetic spectrum, from the radio to the γ-ray spectral regions. As supermassive black holes tend to be located at the center of massive galaxies, these bright sources are referred to as active galactic nuclei (AGN). As all massive galaxies host a supermassive black hole which grew from a smaller seed black hole through accretion events, it is expected that there must be a connection between the growth of supermassive black holes and the formation of massive galaxies. However, at this point researchers do not understand what the connection between black hole and galaxy evolution is. Furthermore, various relations between the mass of the black hole and the host galaxy bulge have been observed and appear to have very little intrinsic scatter (e.g., Magorrian et al., 1998; Tremaine et al., 2002). This suggests that supermassive black holes and their host bulges co-evolve; it is likely that epochs of black hole growth tend to be epochs of host bulge stellar mass growth. This thesis investigates the connection between supermassive black hole growth and host galaxy evolution, particularly AGN host galaxy star formation.

Long before it was known that AGN are powered by accretion onto supermassive black holes, astronomers found AGN to be interesting sources. At the turn of the twentieth century, before it was understood that other galaxies existed outside of and independent

from the Milky Way, observations of the optical spectra of "spiral nebulae" showed that some sources exhibit nuclear emission lines on top of a spectrum indicative of a collection of unresolved stars (e.g., Fath, 1909; Slipher, 1917). Seyfert (1943) began a systematic study of galaxies with nuclear emission lines. However, it was the expanding capabilities of radio astronomy in the 1950's which jump-started studies of AGN.

Approximately 10–20% of AGN are considered radio loud (Donoso et al., 2009), characterized by $f_{5GHz}/f_B \gtrsim 10$, where f_{5GHz} is the 5 GHz radio flux and f_B is the B band optical flux. These radio loud AGN dominate the radio number counts at fluxes $\gtrsim$ 1 mJy (e.g., Windhorst et al., 1993). Thus, early radio surveys found large numbers of AGN. The third Cambridge catalogue (Edge et al., 1959) included a couple hundred radio loud AGN and their locations, which allowed for optical identification of these sources. These sources were termed "Quasi-stellar radio sources" which was then shortened to quasars (Chiu, 1964). Around the same time, optical surveys found a population of bright quasi-stellar objects (QSOs). Sandage (1965) realized the optical spectra of QSOs were very similar to the optical spectra of quasars, suggesting that these two classes of sources were related. However, QSOs did not exhibit the same strength of radio emission as quasars. Thus, the classification of AGN into radio quiet and radio loud sources was begun.

The optical spectra of QSOs and quasars exhibit several prominent emission lines; however, these lines are not at wavelengths corresponding to observed emission lines in galactic nebulae. Schmidt (1963) realized that some of the observed lines in the AGN spectra are in fact redshifted Balmer series lines and was thus able to determine the redshift of these objects, proving that indeed, AGN are not of galactic origin. The realization that QSOs and quasars are located at cosmological distances raised a new issue. Given the observed fluxes and the measured redshifts, these sources touted bolometric luminosities $\gtrsim 10^{45}$ erg s^{-1}. Based on the time scales of observed variations in the optical spectra of these sources, the size scale of QSOs and quasars was limited to the sub-parsec scale (e.g., Mathews & Sandage, 1963). Given the large amount of energy emitted from such a small volume, it was concluded that stellar processes could not be responsible for observed emission of QSOs and quasars (e.g., Smith, 1967). Due to the expected efficiency of the release of gravitational

potential energy into electro-magnetic radiation through accretion onto a gravitationally collapsed body, accretion was understood to be the most likely method for fueling AGN (e.g., Hoyle et al., 1964; Salpeter, 1964; Odgers & Stewart, 1966; Lynden-Bell, 1969).

Our current picture of the anatomy of an AGN was primarily developed during the 1970's and 1980's. Both Shakura & Sunyaev (1973) and Novikov & Thorne (1973) developed models of a thin accretion disk which would circle the central supermassive black hole. The viscosity within the accretion disk allows for the dissipation of angular momentum and gravitational potential energy, allowing particles to fall in toward the innermost circular orbit about the black hole and finally plummet into the black hole. A large fraction ($\sim$10%) of the gravitational potential energy of the in-falling material is converted into electromagnetic radiation, explaining the intrinsic brightness of AGN (e.g., Novikov & Thorne, 1973; Sołtan, 1982; Shankar et al., 2009).

The idea of gas orbiting the supermassive black hole is a natural explanation for the width of the broad emission lines observed in the optical spectra of a significant fraction of AGN (e.g., Osterbrock & Ferland, 2006). These broad lines exhibit full width-half maximum (FWHM) widths of thousands of km s^{-1}. Sources with broad lines are termed type 1 AGN. The spectra of type 1 AGN also include narrow emission lines with FWHM widths of hundreds of km s^{-1}. However, a large fraction of the AGN population exhibits only narrow lines in their optical spectra (e.g., Osterbrock & Ferland, 2006). AGN which lack broad optical emission lines are termed type 2 AGN. Figure 1.1 illustrates the difference between the optical spectra of type 1 and type 2 AGN.

The difference between the optical spectra of type 1 and type 2 AGN raises the question of whether these two source classes are caused by the same phenomenon. By observing polarized optical spectra of type 2 AGN, Antonucci (1983) found that at least some type 2 AGN do have broad lines, however, a source of obscuration along the line of sight washes out the broad lines from the non-polarized optical spectra. This observation led to the unified model, in which an AGN comprises a central supermassive black hole orbited by an accretion disk with a dusty torus enveloping the central engine. Figure 1.2 shows a schematic diagram of the proposed AGN anatomy. Thus, a type 1 AGN is seen when the

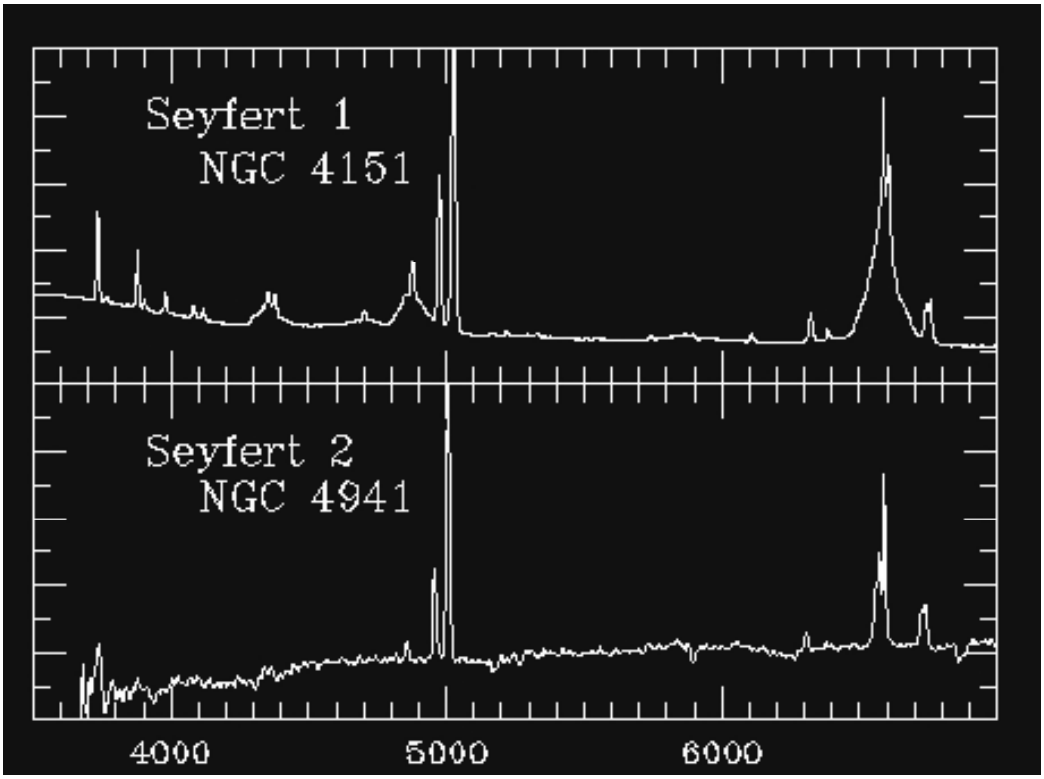

Figure 1.1: The optical spectra of a Type 1 AGN (top) and Type 2 AGN (bottom). The top panel shows the broad lines of the Balmer series and the narrow lines present in the optical spectra of a type 1 AGN NGC 4151. The bottom panel shows the absence of broad emission lines and the presence of narrow emission lines in the optical spectra of type 2 AGN NGC 4941. Seyferts are a class of AGN characterized by $L_X < 10^{44}$ erg s^{-1}. Image credit W.C. Keel.

line of sight to the central engine happens to look down the throat of the torus, and a type 2 AGN is seen when the line of sight to the central engine looks through the dusty torus (e.g., Antonucci, 1993).

A similar dichotomy of AGN spectra is observed in the X-rays. Figure 1.3 shows the effects of obscuration on the X-ray AGN spectra. The larger the column density along the line of sight, the harder the AGN spectrum is between the soft (0.5–2 keV) and hard (2–10 keV) X-ray bands. The majority of sources which show obscuration in their X-ray spectrum also show signs of obscuration in their optical spectrum (e.g., Winter et al., 2009), suggesting that the X-ray and optical obscuration are due to a common absorber.

As mentioned above, 10–20% of AGN have relativistic radio jets and are termed radio loud. An orientation based unified model similar to that described above for radio quiet AGN has been developed to describe the connection between different types of radio loud AGN (see Urry & Padovani, 1995). For most radio loud AGN, our line of sight allows us to view the jet in profile (e.g., M87). These sources are referred to as radio galaxies. Sometimes the radio jet is oriented such that our line of sight to the central engine of the AGN is looking down the jet. These sources are referred to as blazars and are very powerful and variable sources due the effects of relativistic beaming (e.g., Urry et al., 1991; Padovani & Urry, 1992; Padovani et al., 2007).

The simple unified model, which describes type 1 and type 2 AGN as having the same central engine viewed along different lines of sight, is not without its critics. For example, not all type 2 AGN have broad lines in their polarized optical spectra (e.g., Trump et al., 2011). An alternative model has been suggested where type 1 and type 2 AGN are related by an evolutionary sequence. In this model, a major merger triggers a highly obscured AGN and a large starburst (e.g., Hopkins et al., 2006). As the black hole grows, radiation pressure on the surrounding dusty gas pushes the gas out of the central region of the host galaxy, reducing the obscuration to the central engine of the AGN. Eventually, all the gas and dust is blown out and the AGN is observed as a type 1 AGN (e.g., Hickox et al., 2009). This model suggests that type 2 AGN tend to be younger than type 1 AGN. However, due to the difference in time scales for AGN activity and the relaxation of a merger remnant

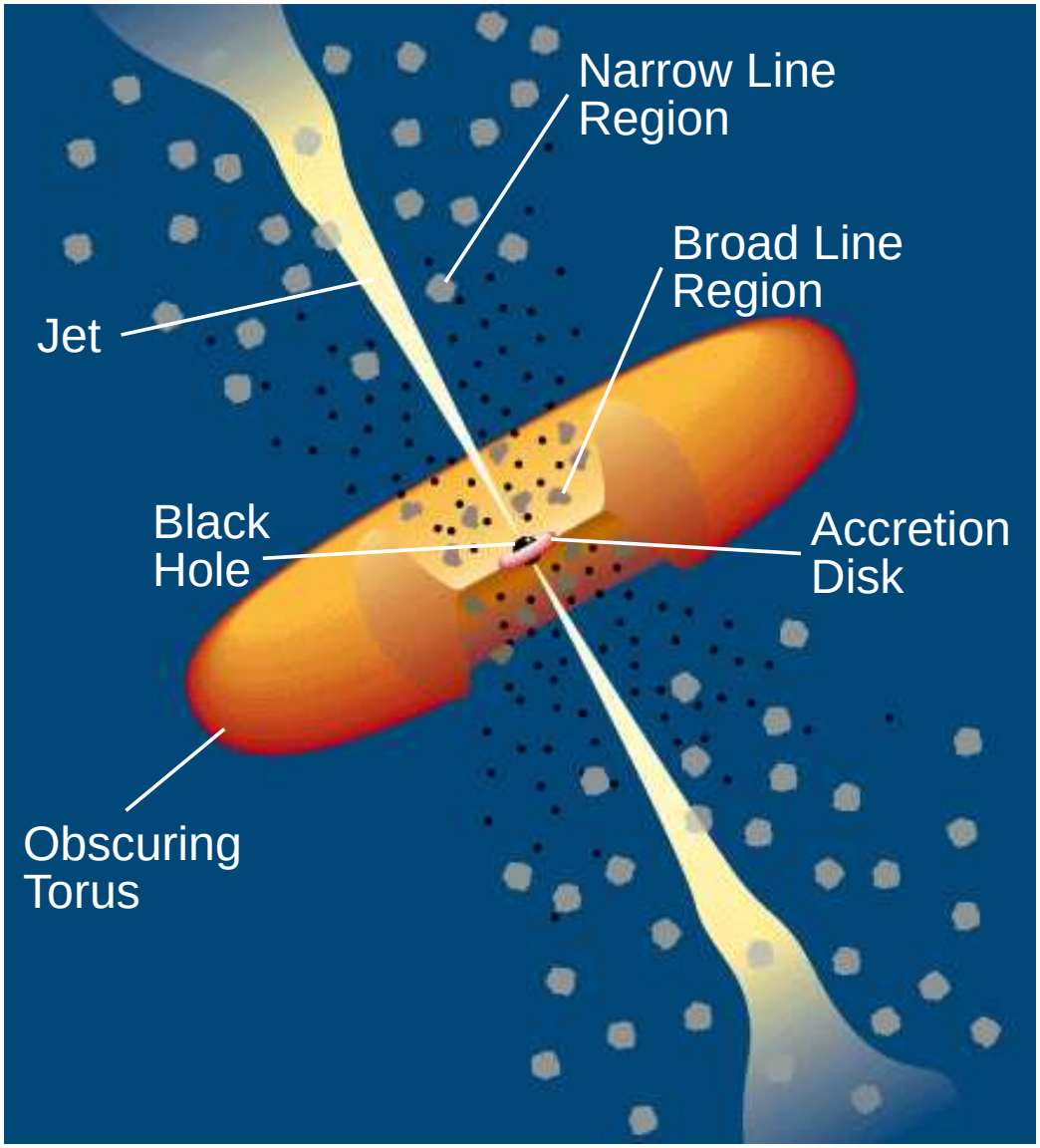

Figure 1.2: A schematic diagram showing the orientation based unified model of AGN. The diagram shows the central black hole surrounded by an accretion disk and enveloped by a dusty torus. When the central engine of an AGN is viewed through the dusty torus, the emission from the broad line region clouds is absorbed by the dusty torus and broad lines are not seen in the optical spectrum of the AGN; however, emission from the clouds of the narrow line region is still visible. Thus, the source is a type 2 AGN. If the line of sight to the central engine of the AGN is instead down the throat of the dusty torus, emission from both the clouds of the broad line region and narrow line region are visible giving rise to both broad and narrow lines in the AGN optical spectrum and the source is considered a type 1 AGN. Image credit C.M. Urry and P. Padovani.

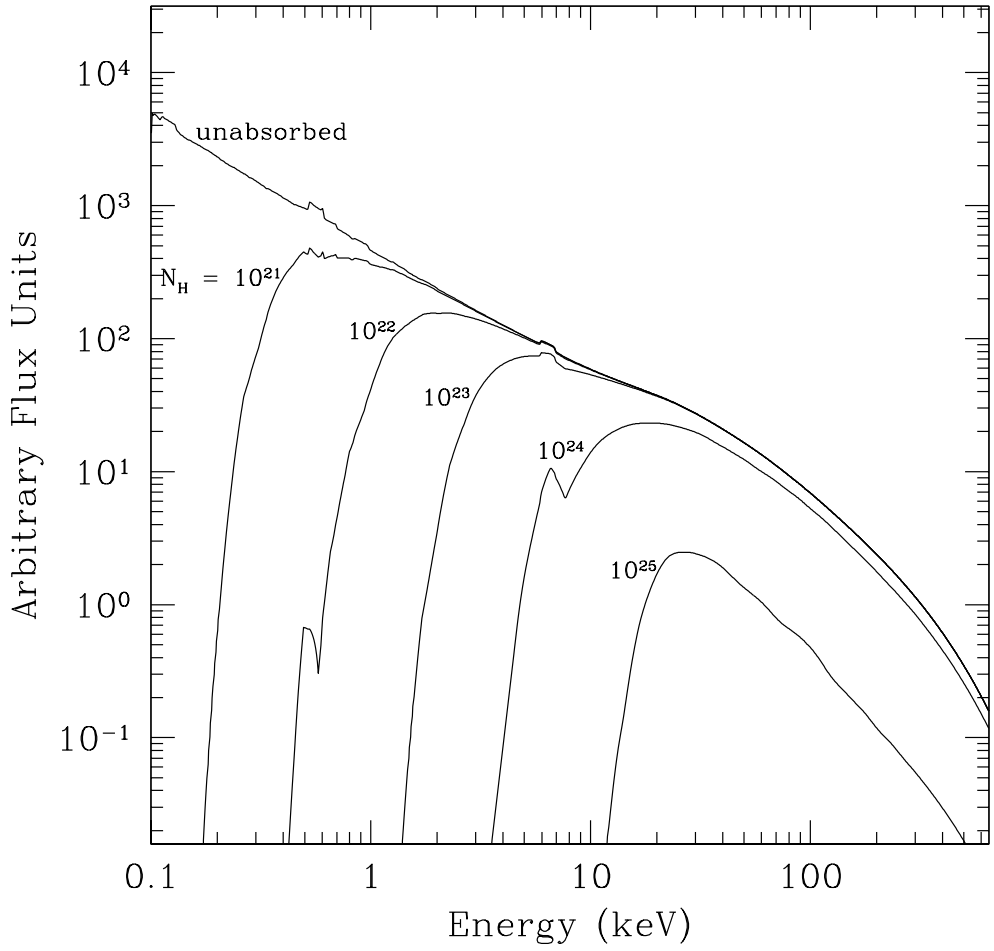

Figure 1.3: A plot showing the effects of obscuration by neutral hydrogen column densities $N_H = 10^{21}$, 10^{22}, 10^{23}, 10^{24}, and 10^{25} cm^{-2} on the AGN X-ray spectrum. The line labeled "unabsorbed" shows the intrinsic, unabsorbed AGN spectra.

galaxy, it is observationally difficult to determine whether a given AGN was triggered by a major merger. Thus, determining what mechanism is responsible for triggering AGN is important in understanding both the role of AGN in galaxy evolution and the relation between the different spectral types of AGN.

In order to study the AGN population, a large, unbiased sample of AGN is necessary. X-ray observations have proven to be an efficient method to identify large numbers of AGN which, due to obscuration, would not have been identified as AGN by their optical spectra. Observations in the hard X-ray band have shown that more than half of AGN are obscured by cold gas along our line of sight to the central engine (e.g., Brandt & Hasinger, 2005). This gas tends to absorb the optical-UV-soft X-ray light emitted by the AGN. Therefore, deep hard X-ray surveys are the least biased method of discovering large samples of AGN which are unbiased against all but the most highly obscured AGN, which have obscuring column densities $N_H \gtrsim 10^{23}$ cm^{-2}. Thus, deep X-ray surveys have allowed researchers to determine the hard X-ray luminosity function (HXLF) of bright AGN and the evolution of the AGN HXLF up to redshift $z \sim 3$ (e.g., Ueda et al., 2003; La Franca et al., 2005; Silverman et al., 2008; Aird et al., 2010). Extremely deep hard X-ray surveys, such as the *Chandra* 4 Ms observations of the Chandra Deep Field-South (CDF-S; e.g., Lehmer et al., 2012), will allow researchers to determine the low luminosity slope of the HXLF and the evolution of the AGN population to even higher redshifts. These deep X-ray surveys by observatories such as *Einstein*, *Ginga*, ROSAT, *Chandra X-ray Observatory* and *XMM-Newton* have resolved the majority of the extragalactic X-ray background (XRB) at energies < 10 keV into individual AGN (Hasinger et al., 1998; Mushotzky et al., 2000; Giacconi et al., 2001, 2002; Hasinger et al., 2001; Alexander et al., 2003; Worsley et al., 2004, 2005; Brandt & Hasinger, 2005). The growing understanding of the AGN HXLF has allowed researchers to develop AGN population synthesis models, which show that AGN are likely to be the dominant contributors of the XRB (e.g., Setti & Woltjer, 1989; Comastri et al., 1995; Reid et al., 1999). The understanding of the AGN population gained through hard X-ray surveys has been instrumental in the development of the work presented here.

Studying AGN host galaxies also offers insight into the role of AGN in galaxy evolution. Investigating local AGN host galaxies using the Sloan Digital Sky Survey (SDSS), Kauffmann et al. (2003) showed that bright AGN tend to have young stellar populations. In general, AGN hosts have on-going star formation (e.g., Ballantyne, 2009; Lutz et al., 2010; Santini et al., 2012). This star formation may be related to AGN fueling and/or obscuration (e.g., Davies et al., 2007; Ballantyne, 2008) or AGN host star formation may simply be due to the fact that star formation and AGN fueling both require a reservoir of cool gas. In order to understand the role of AGN in the evolution and formation of massive galaxies, it is necessary to understand the star formation history of AGN host galaxies and the connection between black hole accretion and on-going star formation.

In order to reveal the role of AGN in galaxy evolution, researchers must first understand the properties of AGN and their host galaxies. However, AGN tend to be highly variable sources, exhibiting short and long term variability as well as object-to-object variability between different AGN and their host galaxies. Thus, the overall trends within the AGN and host population which we seek to study are difficult to determine by fitting individual sources. Here, a method is used to determine the average properties of AGN and their hosts by considering integrated characteristics of the AGN population, such as luminosity functions, number counts, and extragalactic background light. This method is typically termed population synthesis modeling. Furthermore, since deep X-ray surveys are the most unbiased method for identifying AGN, the HXLF and the XRB are important tools in determining the average characteristics of the AGN population. By employing model AGN spectral energy distributions (SEDs), knowledge of the AGN population from these deep X-ray surveys can be applied at different wavelengths to study star formation and the stellar populations of AGN host galaxies.

Using the method of population synthesis modeling, the spectral intensity of the XRB at energy E, $I(E)$ (in units of keV cm^{-2} keV^{-1} sr^{-1}), is simply calculated as a double integral over the luminosity and redshift distribution of the AGN population (Comastri et

al., 1995; Pompilio et al., 2000; Ballantyne et al., 2006a):

$$I(E) = \frac{c}{H_0} \int_{z_{min}}^{z_{max}} \int_{\log L_X^{min}}^{\log L_X^{max}} \frac{d\Phi_X(L_X, z)}{d(\log L_X)} \times \frac{S_E(L_X, z) d_l^2}{(1+z)^2 [\Omega_M (1+z)^3 + \Omega_\Lambda]^{1/2}} d(\log L_X) dz, \tag{1.1}$$

where L_X is the rest-frame 2–10 keV X-ray luminosity, $L_X^{min} = 10^{41.5}$ erg s^{-1}, $L_X^{max} = 10^{48}$ erg s^{-1}, $d\Phi_X(L_X, z)/d(\log L_X)$ is the AGN HXLF (in Mpc^{-3} dex^{-1}), $S_E(L_X, z)$ is the absorbed observed-frame AGN model SED (in keV cm^{-2} s^{-1} keV^{-1}) for a source with intrinsic luminosity L_X at redshift z, and d_l is the luminosity distance to redshift z which is calculated as

$$d_l = (1+z) \frac{c}{H_0} \int_0^z \frac{dz'}{[\Omega_M (1+z')^3 + \Omega_\Lambda]^{1/2}}. \tag{1.2}$$

A similar method is used to calculate the number of sources per square degree with flux greater than F in a given wave band, $N(> F)$:

$$\begin{aligned} N(> F) &= \frac{K_{sr}^{deg} c}{H_0} \\ &\times \int_{z_{min}}^{z_{max}} \int_{max(\log L_X^{min}, \log L_X^F)}^{\log L_X^{max}} \frac{d\Phi_X(L_X,z)}{d \log L_X} \frac{d_l^2}{(1+z)^2 [\Omega_M (1+z)^3 + \Omega_\Lambda]^{1/2}} d \log L_X dz, \end{aligned} \tag{1.3}$$

where the factor $K_{sr}^{deg} = 3.05 \times 10^{-4}$ converts from sr^{-1} to deg^{-2} and L_X^F is the rest-frame 2–10 keV X-ray luminosity corresponding to the observed-frame flux F at redshift z for the wave band of interest, as determined by the absorbed observed-frame AGN model SED.

One advantage of multi-wavelength population synthesis modeling is that knowledge of the AGN population acquired from deep hard X-ray surveys can be applied to study the AGN and AGN host galaxy population at different wavelengths. This is done by calculating a model SED which includes the emission from the AGN and the host galaxy stellar population and ongoing star formation. The AGN and host model SED can then be used to translate the AGN HXLF into an AGN and host galaxy luminosity function at any frequency ν, $d\Phi_\nu/d(\log \nu L_\nu)$, where the model SED is valid. The AGN and host galaxy luminosity function is found using the relation

$$\frac{d\Phi_\nu(\nu L_\nu, z)}{d(\log \nu L_\nu)} = \frac{d\Phi_X(L_x, z)}{d(\log L_X)} \frac{d(\log L_X)}{d(\log \nu L_\nu)}, \tag{1.4}$$

where the fraction $d(\log L_X)/d(\log \nu L_\nu)$ is determined by the AGN and host model SED. This method is used extensively throughout this work to constrain the average properties of AGN and their host galaxies.

1.1 Outline

Here, the exploration of the role of AGN in galaxy evolution and massive galaxy formation starts by investigating the space density and evolution of a special class of AGN known as Compton thick AGN. Compton thick AGN are characterized by an obscuring column density $N_H > 1/\sigma_T \gtrsim 10^{24}$ cm^{-2}, where σ_T is the Thomson scattering cross-section of electrons, and are thought to be AGN which were recently triggered and in a stage of rapid black hole accretion and host bulge growth (e.g., Sansers et al., 1988; Fabian, 1999; Hopkins et al., 2006; Fabian et al., 2009; Treister et al., 2010). Compton thick AGN are difficult to study due to the extreme levels of obscuration which define this class of AGN. Even deep X-ray surveys often miss Compton thick AGN (e.g., Brandt & Hasinger, 2005). However, the existence of a large population of Compton thick AGN is inferred from the spectrum of the XRB. It is understood that the XRB encodes the cosmic history of accretion onto supermassive black holes (e.g., Fabian & Barcons, 1992). However, when the emission from known AGN is integrated, the resulting spectrum does not match the shape of the XRB, specifically around the peak of the XRB at ∼30 keV (e.g., Treister & Urry, 2005; Ballantyne et al., 2006a). The SED of a Compton thick AGN is the appropriate shape to account for the missing XRB emission (see Figure 1.3).

XRB population synthesis models (e.g., Risaliti et al., 1999; Treister & Urry, 2005; Ballantyne et al., 2006a; Gilli et al., 2007), which are used to constrain the space density of Compton thick AGN, already account for emission from most classes of AGN, however, they do not consider the contribution from blazars. Blazars are a rare and powerful class of AGN where a relativistic jet associated with the AGN is observed nearly on axis. Due to relativistic beaming and Compton up-scattering of synchrotron radiation, blazars are bright sources in the radio through gamma-ray spectral regions.

In Chapter 2, the contribution of blazars to the XRB is calculated and the implications for the predicted population of Compton thick AGN is considered. In Chapter 3, the hypothesis that Compton thick AGN are rapidly accreting sources is tested by calculating the first XRB population synthesis model where sources are classified based on their physical characteristics such as accretion rate and black hole mass. The accretion rate is considered

in terms of the Eddington ratio, L_{Edd}/L_{bol}, where L_{bol} is the bolometric luminosity and $L_{Edd} = 4\pi G M_{\bullet} m_p c/\sigma_T$ is the Eddington luminosity, where G is the gravitational constant, $M_{\bullet}$ is the black hole mass, m_p is the proton mass, c is the speed of light, and σ_T is the Thomson cross-section for electron scattering. Most population synthesis models assume Compton thick AGN evolve in the same manner as less highly obscured AGN, which is unlikely if Compton thick AGN are in a special evolutionary stage. Thus, by computing an XRB population synthesis model based on AGN Eddington ratios, Compton thick AGN can be added as sources with specific, physically motivated Eddington ratios rather than assuming that Compton thick AGN evolve like less highly obscured AGN.

Next, we turn our attention to the host galaxies of AGN. AGN tend to be bright infrared sources (e.g., Soifer et al., 1987; Treister et al., 2006; Hatziminaoglou et al., 2010) due to star formation in the host galaxy and the re-emission by dust of absorbed X-ray and UV emission. Near and mid infrared emission from AGN and their host galaxies can be dominated by the hot dust surrounding the AGN, and thus far infrared emission tends to be a better indicator of star formation in AGN hosts. In Chapter 4, predictions for far-infrared number counts of AGN are presented based on various AGN host star formation scenarios. The average properties of AGN host stellar populations are constrained in Chapter 5 by combining stellar population synthesis models (Bruzual & Charlot, 2003) with the framework of XRB population modeling and model AGN SEDs.

It is possible that AGN are triggered by a variety of different mechanisms which have different effects on the AGN host galaxy. For example, AGN may be triggered by major mergers or by stellar bars (e.g., Crenshaw et al., 2003; Hopkins et al., 2006). However, the effects of a stellar bar on the AGN host galaxy are very different from the effects of a violent major merger. Therefore, the triggering mechanism of AGN must be investigated in order to understand the role of AGN in galaxy evolution. In Chapter 6, the contribution of major merger triggered AGN to the HXLF is investigated at different luminosity and redshift ranges by combining an observationally motivated major merger rate and a theoretical AGN light curve. In Chapter 7, this model is extended to consider the contribution of major merger triggered AGN-starburst galaxies to the ultra-luminous infrared galaxy population.

Chapter 8 summarizes the conclusions of this work and presents future work. Throughout this thesis a ΛCDM cosmology is assumed with $h = 0.7$ and $\Omega_\Lambda = 1$ - $\Omega_M = 0.7$ as necessary (Hinshaw et al., 2009).

1.2 References

Aird, J., Nandra, K., Laird, E.S., et al. 2010, MNRAS, 401, 2531

Alexander, D.M., Bauer, F.E., Brandt, W.N., et al. 2003, AJ, 126, 539

Antonucci, R.R.J. 1983, Nature, 303, 158

Antonucci, R. 1993, ARA&A, 31, 473

Backer, D.C. & Sramek, R.A. 1999, ApJ, 524, 805

Ballantyne, D.R. 2008, ApJ, 685, 787

Ballantyne, D.R. 2009, ApJ, 698, 1033

Ballantyne, D.R., Everett, J.E., & Murray, N. 2006, ApJ, 639, 740

Ballantyne, D.R., Shi, Y., Rieke, G.H., et al. 2006, ApJ, 653, 1070

Brandt, W.N. & Hasinger G. 2005, ARA&A, 43, 827

Bruzual, G. & Charlot, S. 2003, MNRAS, 344, 1000

Chiu, H.-Y. 1964, Physics Today, 17, 21

Comastri, A., Setti, G., Zamorani, G., & Hasinger, G. 1995, A&A, 296, 1

Crenshaw, D.M., Kraemer, S.B., & Gabel, J.R. 2003, AJ, 126, 1690

Davies, R.I., Müller Sánchez, F., Genzel, R., et al. 2007, ApJ, 671, 1388

Donoso, E., Best, P.N., & Kauffmann, G. 2009, MNRAS, 392, 617

Edge, D.O., Shakeshaft, J.R., McAdam, W.B., Baldwin, J.E., & Archer, S. 1959, MNRAS, 67, 37

Fabian, A.C. 1999, MNRAS, 308, L39

Fabian, A.C., Vasudevan, R.V., Mushotzky, R.F., Winter, L.M., Reynolds, C.S. 2009, MNRAS, 394, L89

Fabian, A.C. & Barcons, X. 1992, ARA&A, 30, 429

Fath, E.A. 1909, Lick Obs. Bull., 5, 71

Giacconi, R., Rosati, P., Tozzi, P., et al. 2001, ApJ, 551, 624

Giacconi, R., Zirm, A., Wang, J.X., et al. 2002, ApJS, 139, 369

Gilli, R., Comastri, A., & Hasinger, G. 2007, A&A, 463, 79

Hasinger, G., Burg, R., Giacconi, R., et al. 1998, A&A, 329, 482

Hasinger, G., Altieri, B., Arnaud, M., et al. 2001, A&A, 365, L45

Hatziminaoglou, E., Omont, A., Stevens, J.A., et al. 2010, A&A, 518, L33

Hickox, R., Jones, C., Forman, W.R., et al. 2009, ApJ, 696, 891

Hinshaw, G., Weiland, J.L., Hill, R.S., et al. 2009, ApJS, 180, 225

Hopkins, P.F., Hernquist, L., Cox, T.J., et al. 2006, ApJS, 163, 1

Hoyle, F., Fowler, W.A., Burbidge, G.R., Burbidge, E.M. 1964, ApJ, 139, 909

Kauffmann, G., Heckman, T.M., Tremonti, C., et al. 2003, MNRAS, 346, 1055

Kormendy, J. & Richstone, D. 1995, ARA&A, 33, 581

La Franca, F., Fiore, F., Comastri, A., et al. 2005, ApJ, 635, 864

Lehmer, B.D., Xue, Y.Q., Brandt, W.N., et al. 2012, ApJ, 752, 46

Lutz, D., Mainieri, V., Rafferty, D., et al. 2010, ApJ, 712, 1287

Lynden-Bell, D. 1969, Nature, 223, 690

Magorrian, J., Tremaine, S., Richstone, D., et al. 1998, AJ, 115, 2285

Mathews, T.A. & Sandage, A.R. 1963, ApJ, 138, 30

Mushotzky, R.F., Cowie, L.L., Barger, A.J., & Arnaud, K.A. 2000, Nature, 404, 459

Novikov, I.D. & Thorne, K.S., "Astrophysics of Black Holes", 1973, in Dewitt C., Dewitt B. S., eds, *Black Holes*. Gordon & Breach, New York, p. 343

Odgers, G.J. & Stewart, R.W. 1966, Nature, 211, 1284

Osterbrock, D.E. & Ferland, G.J. 2006, *Astrophysics of Gaseous Nebulae and Active Galactic Nuclei* (2nd ed.;Sausalito, CA: University Science Books)

Padovani, P., Giommi, P., Landt, H., Perlman, E.S. 2007, ApJ, 662, 182

Padovani, P. & Urry, C.M. 1992, ApJ, 387, 449

Pompilio, F., La Franca, F., & Matt, G. 2000, A&A, 353, 440

Reid, M.J., Readhead, A.C.S., Vermeulen, R.C., & Treuhaft, R.N. 1999, ApJ, 524, 816

Risaliti, G., Maiolino, R., & Salvati, M. 1999, ApJ, 522, 157

Salpeter, E.E. 1964, ApJ, 140, 796

Sandage, A.R. 1965, ApJ, 141, 1560

Sanders, D.B., Soifer, B.T., Elias, J.H., et al. 1988, ApJ, 325, 74

Santini, P., Rosario, D.J., Shao, L., et al. 2012, A&A, 540, 109

Schmidt, M. 1963, Nature, 197, 1040

Setti, G. & Woltjer, L. 1989, A&A, 224, L21.

Seyfert, C.K. 1943, ApJ, 97, 28

Shakura, N.I. & Sunyaev, R.A. A&A, 24, 337

Shankar, F., Weinberg, D.H., & Miralda-Escudé, J. 2009, ApJ, 690, 20

Silverman, J.D., Green, P.J., Barkhouse, W.A., et al. 2008, ApJ, 679, 118

Slipher, V.M. 1917, Lowell Obs. Bull. 3, 59

Smith, F.G. 1967, Nature, 213, 967

Soifer, B.T., Sanders, D.B., Madore, B.F., et al. 1987, ApJ, 320, 238

Sołtan, A. 1982, MNRAS, 200, 115

Treister, E., Natarajan, P., Sanders, D.B., et al. 2010, Science, 328, 600

Treister, E. & Urry, C.M. 2005, ApJ, 630, 115

Treister, E., Urry, C.M., Van Duyne, J., et al. 2006, ApJ, 640, 603

Tremaine, S., Gebhardt, K., Bender, R., et al. 2002, ApJ, 574, 740

Trump, J.R., Nagao, T., Ikeda, H., et al. 2011, ApJ, 732, 23

Ueda, Y., Akiyama, M., Ohta, K., & Miyaji, T. 2003, ApJ, 598, 886

Urry, C.M. & Padovani, P. 1995, PASP, 107, 803

Urry, C.M., Padovani, P., & Stickel, M. 1991, ApJ, 382, 501

Windhorst, R., Fomalont, E., Partridge, R., & Lowenthal, J. 1993, ApJ, 405, 498

Winter, L.M., Mushotzky, R.F., Reynolds, C.S., & Tueller, J. 2009, ApJ, 690, 1322

Worsley, M., Fabian, A.C., Barcons, X., et al. 2004, MNRAS, 352, L28

Worsley, M., Fabian, A.C., Bauer, F.E., et al. 2005, MNRAS, 357, 1281

CHAPTER II

BALANCING THE COSMIC ENERGY BUDGET: THE COSMIC X-RAY BACKGROUND, BLAZARS, AND THE COMPTON THICK AGN FRACTION

2.1 Introduction

Nearly half a century after the cosmic X-ray background (XRB) was discovered (Giacconi et al., 1962), the majority of the XRB up to 10 keV has been resolved into distinct point sources by deep observations conducted by *ROSAT*, *Chandra*, and *XMM-Newton* (Hasinger et al., 1998; Mushotzky et al., 2000; Giacconi et al., 2001, 2002; Hasinger et al., 2001; Alexander et al., 2003; Worsley et al., 2004; Brandt & Hasinger, 2005; Worsley et al., 2005). These discrete sources are active galactic nuclei (AGN), compact extra-galactic sources powered by accretion onto black holes (Lyndon-Bell, 1969; Rees, 1984). As such, the XRB encapsulates the history of accretion onto super massive black holes and provides a powerful tool to aid scientific understanding of accretion processes (Fabian & Barcons, 1992). It has been shown that a large portion of this accretion is shrouded from our view by intervening matter along the line of sight (Setti & Woltjer, 1989; Celotti et al., 1992; Madau et al., 1994; Comastri et al., 1995; Fiore et al., 1999; Treister et al., 2009). For AGN spectral and spatial density models to match the peak of the XRB at ∼30 keV, the models must predict a large number of highly obscured sources known as Compton thick (CT) AGN (Risaliti et al., 1999; Ueda et al., 2003; Treister & Urry, 2005; Ballantyne et al., 2006; Gilli et al., 2007), which have a neutral hydrogen column density $N_{\rm H} > 1/\sigma_T \gtrsim 10^{24}$ cm^{-2} where σ_T is the Thomson scattering cross-section of the electron (Treister et al., 2009), making them practically invisible in the 2-10 keV band (Ghisellini et al., 1994). XRB synthesis models predict CT sources make up roughly half of the obscured AGN population (Risaliti et al., 1999; Ueda et al., 2003; Treister & Urry, 2005; Ballantyne et al., 2006; Gilli et al., 2007).

In recent years, observational studies have led to discrepancies in the fraction of AGN which are CT, which may be a function of redshift. At first, small local studies seemed to agree with the model predictions that half of all obscured AGN are CT (Risaliti et al., 1999; Guainazzi et al., 2005). Malizia et al. (2009) studied 88 AGN observed by INTEGRAL/IBIS in the 20-40 keV band and found that at least 16% of obscured AGN are CT and $\gtrsim$24% of the AGN in their local sample ($z \leq 0.015$) are CT. If $\sim$75% of local AGN are obscured (Risaliti et al., 1999; Treister et al., 2009), the local AGN sample of Malizia et al. (2009) suggests that $\gtrsim$32% of obscured AGN are CT, considerably lower than model predictions. These studies have also had implications on the maximum contribution of CT AGN to the XRB. Population synthesis studies previously suggested that CT AGN account for nearly a third of the XRB around its peak at $\sim$30 keV (Gilli et al., 2007). However, a recent study by Treister et al. (2009), using samples from *INTEGRAL* and *Swift* observations and high redshift, IR-selected CT AGN candidates, suggests that CT AGN contribute only about 9% of the X-ray background at $\sim$30 keV. Given the uncertainty of the CT AGN fraction and the contribution of CT AGN to the XRB, smaller classes of XRB contributors must be considered. The XRB contribution from the small class of AGN known as blazars has previously been ignored by XRB synthesis models and CT AGN fraction predictions, even though blazars are known to emit in a broad range from radio to TeV energies. To further constrain model predictions of the CT AGN fraction, the blazar class of AGN must be considered.

Blazars are a unique and extreme class of AGN. Unified models of AGN, as summarized by Anotonucci (1993) and Urry & Padovani (1995), explain blazars as radio galaxies with relativistic jets viewed close to the line of sight. Flat spectrum radio quasars (FSRQs) are relativistically beamed FRIIs (luminous radio galaxies) and BL Lac objects (BL Lacs) are relativistically beamed FRIs (less luminous radio galaxies). The features which define blazars (extreme variability, high luminosity, high polarization, and radio core-dominance) are due to the relativistic beaming caused by looking down the relativistic jet of the blazar (Padovani et al., 2007). The details of the spectral energy distribution (SED) of blazars is still a topic riddled with uncertainties (Kneiske & Mannheim, 2008). The extreme variability

that distinguishes the blazar class necessitates simultaneous multi-wavelength observations to understand the spectral properties (Ghisellini & Tavecchio, 2008). However, the two-hump form of the blazar SED, spanning from radio to γ-ray energies, is well known (Urry, 1999). Figure 2.1 shows the SED for FSRQs and low-frequency peaked BL Lacs (LBLs) as the dashed line and the SED for high-frequency peaked BL Lacs (HBLs) as the dotted line (Urry, 1998). The lower energy hump is due to synchrotron radiation while the higher energy hump is due to inverse Compton scattering (Urry & Padovani, 1995). It has been shown that blazars are significant progenitors of the γ-ray background (Giommi et al., 2006; Narumoto & Totani, 2006; Kneiske & Mannheim, 2008); therefore it is expected that blazars should have a non-negligible contribution to the XRB.

Giommi et al. (2006) predict that blazars should account for 11-12% of the soft XRB around 1 keV; however, no estimation is made for the blazar contribution to the peak region of the XRB around 30 keV. A recent study by Ajello et al. (2009), based on the three year *Swift*/BAT blazar sample, claims that blazars contribute about 10% of the X-ray background in the 2-10 keV band. In the 15-55 keV band Ajello et al. (2009) predict blazars contribute $\sim$20% if blazars are modeled as a single population or $\sim$9% if FSRQs and BL Lacs are modeled as two distinct populations. Both Giommi et al. (2006) and Ajello et al. (2009) found that blazars could contribute 100% of the XRB in the MeV band.

Due to uncertainties in the low luminosity end of the AGN hard X-ray luminosity function (HXLF), multiple HXLFs must be considered (e.g., Ueda et al., 2003; La Franca et al., 2005; Silverman et al., 2008; Ebrero et al., 2009; Yencho et al., 2009; Aird et al., 2010) to understand the range of predicted CT AGN. Recent AGN HXLFs find that luminosity-dependent density evolution (LDDE) provides the best fit to the observational data (Ueda et al., 2003; Hasinger et al., 2005; La Franca et al., 2005; Silverman et al., 2008; Ebrero et al., 2009; Yencho et al., 2009). Aird et al. (2010) find a new evolutionary model, luminosity and density evolution (LADE), also fits the observational data well. Both the LDDE and LADE models are in keeping with the findings that the scarce, high-luminosity sources, quasars, show sharp positive evolution from $z \approx$0–2, while less luminous sources, Seyferts, evolve more temperately (Barger et al., 2005; Brandt & Hasinger, 2005; Hasinger

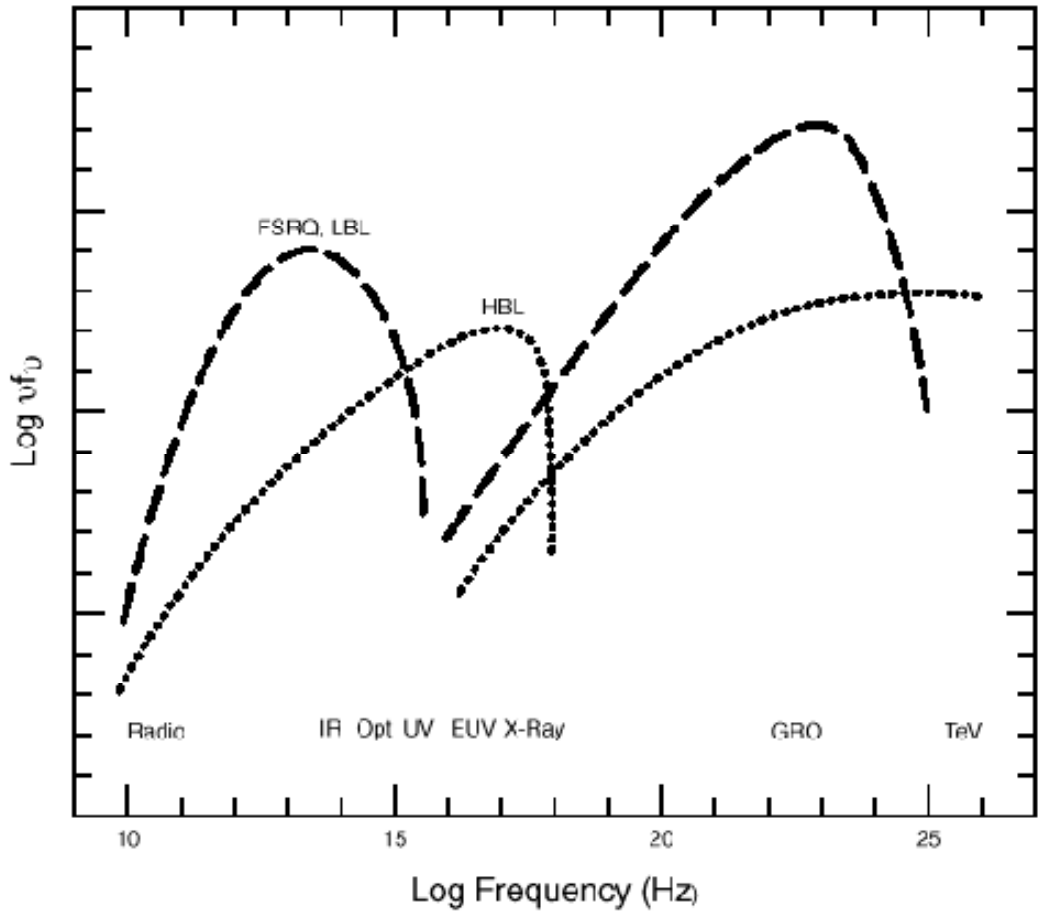

Figure 2.1: Spectral energy distributions for blazars broken into three sub-populations. The longer wavelength hump is due to synchrotron emission and peaks in the submillimeter to infrared wavelengths for FSRQs and low-frequency peaked BL Lacs (LBLs). The synchrotron peak of high-frequency peaked BL Lacs (HBLs) peaks in the UV to X-ray spectral range. Inverse Compton scattering powers the high frequency peak which is at GeV energies for FSRQs and LBLs and TeV energies for HBLs. Image credit Urry (1998).

et al., 2005). Given the connection between AGN and galaxy evolution (e.g., Ferrarese & Merritt, 2000; Smolčić, 2009), it is not surprising that AGN evolution matches the trend of galaxy formation, where massive galaxies formed earlier in cosmological time while smaller structures have waited until more recent times to form (e.g., Cowie et al., 1999).

In this chapter the blazar contribution to the XRB is predicted and the implications for the CT AGN fraction are discussed in the context of multiple HXLFs. In §2.2 the model used for the blazar and non-blazar AGN contributions to the XRB is presented. In §2.3 the results of this study are presented while discussions and conclusions are given in §2.4. A ΛCDM cosmology with $H_0 = 70$ km s^{-1} Mpc^{-1}, $\Omega_\Lambda = 0.7$, and $\Omega_m = 0.3$ is assumed as necessary (Spergel et al., 2007).

2.2 Calculations

2.2.1 Blazar Contribution to X-ray Background

2.2.1.1 Luminosity Function

The widely accepted unified scheme of radio loud AGN provides that FSRQs are FRIIs, luminous radio galaxies, with jets pointed along the line of sight causing the observed radiation to be relativistically beamed, and that BL Lacs have an analogous relationship with FRIs, less luminous radio galaxies (Urry & Padovani, 1995). Thus, the blazar luminosity function, which describes blazar space density and evolution, should be well represented by the relativistically beamed radio galaxy luminosity function (Urry et al., 1991; Padovani & Urry, 1992; Padovani et al., 2007).

Willott et al. (2001) represent the radio galaxy luminosity function as the sum of the low and high luminosity radio galaxies. The luminosity function is of the form

$$\frac{d\Phi(L_{151MHz},z)}{d\log L_{151MHz}} = \frac{d\Phi_l(L_{151MHz},z)}{d\log L_{151MHz}} + \frac{d\Phi_h(L_{151MHz},z)}{d\log L_{151MHz}} \tag{2.1}$$

where

$$\frac{d\Phi_l(L_{151MHz},z)}{d\log L_{151MHz}} = \rho_{l0}\left(\frac{L}{L_{l*}}\right)^{-\alpha_l} exp\left(-\frac{L}{L_{l*}}\right) f_l(z) \tag{2.2}$$

and

$$\frac{d\Phi_h(L_{151MHz},z)}{d\log L_{151MHz}} = \rho_{h0}\left(\frac{L}{L_{h*}}\right)^{-\alpha_h} exp\left(-\frac{L_{h*}}{L}\right) f_h(z), \tag{2.3}$$

where L_{151MHz} is the monochromatic luminosity at 151 MHz.

Willott et al. (2001) use three different evolutionary models for $f_h(z)$, which differ by the evolutionary scenario for high luminosity radio galaxies for $z \gtrsim 2$. Model A assumes a symmetric evolutionary scenario where the density of high luminosity radio galaxies positively evolves until $z \sim 2$ and then evolves negatively at the same rate for $z \gtrsim 2$. Model B assumes a positive evolution up to $z \sim 2$ and no evolution beyond $z \sim 2$. Model C assumes positive evolution of high luminosity radio galaxies up to $z \sim 2$ and for $z \gtrsim 2$ negative evolution is assumed, however the negative evolution is not assumed to be symmetric with respect to $z \sim 2$. Due to the lack of high redshift sources in the sample used by Willott et al. (2001), all three models fit the data well. Model C is used here as it is the most general scenario. The Willott luminosity function is converted from Einstein-de Sitter cosmology to ΛCDM cosmology.

To relate the parent luminosity function to the beamed luminosity function we use the procedure laid out by Urry & Shafer (1984) and Urry & Padovani (1991). The beamed luminosity L is assumed to be related to the rest frame luminosity $\mathcal{L}$ by

$$L = (1 + f\delta^p)\,\mathcal{L}, \tag{2.4}$$

where f is the fraction of the unbeamed luminosity that is relativistically beamed by the jet, and $\delta = [\gamma\,(1 - \beta\cos\theta)]^{-1}$ is the jet Doppler factor with β the apparent velocity in units of c, the speed of light. Finally, $\gamma = \left(1 - \beta^2\right)^{-\frac{1}{2}}$ is the Lorentz factor, and θ is the angle between the stream of the jet and the line of sight. The exponent p is defined as $p = 3 + \alpha$ for continuous jets and $p = 2 + \alpha$ for discrete jets, where α is the spectral index, and accounts for aberration, time contraction, and the blue-shifting of the photons (Urry & Shafer, 1984). The probability of observing luminosity L given unbeamed luminosity $\mathcal{L}$ is

$$P_\gamma(L|\mathcal{L}) = \frac{1}{\beta\gamma p} f^{1/p} \mathcal{L}^{-1} \left(\frac{L}{\mathcal{L}} - 1\right)^{-(p+1)/p}. \tag{2.5}$$

The luminosity function for a particular Lorentz factor $d\Phi_\gamma/d\log L$ is found by integrating the intrinsic differential luminosity function $d\Phi_e/d\log L$ such that

$$\frac{d\Phi_\gamma(L)}{d\log L} = \int d\mathcal{L} \frac{d\Phi_e(\mathcal{L})}{d\log\mathcal{L}} \frac{d\log\mathcal{L}}{d\log L} P_\gamma(L|\mathcal{L}). \tag{2.6}$$

To accommodate a range of Lorentz factors, we define the Lorentz factor distribution $n(\gamma)$ so $n(\gamma) \propto \gamma^G$ and is normalized to one over the full range of Lorentz factors. Thus the observed blazar luminosity function $d\Phi_o/d\log L$ is

$$\frac{d\Phi_o(L)}{d\log L} = \int d\gamma \frac{d\Phi_\gamma(L)}{d\log L} n(\gamma). \tag{2.7}$$

By performing this procedure for L and $\mathcal{L}$ pairings allowed by $0 \leq \theta \leq \theta_c$, where θ_c is defined by $f\delta(\theta_c)^p \equiv 1$ (Urry & Padovani, 1991) the angle at which the beamed jet luminosity is equal to the intrinsic luminosity, the luminosity function for the population of radio galaxies which have spectra dominated by relativistic beaming is constructed.

To construct the blazar luminosity function the low luminosity function $d\Phi_l/d\log L_{151MHz}$, defined by equation 2.2, is set as the parent luminosity function for BL Lac objects and the high luminosity function $d\Phi_h/d\log L_{151MHz}$, defined by equation 2.3, is set as the parent luminosity function for FSRQs. Above $L_{151MHz} \approx 10^{43.8}$ erg s^{-1} or $L_{151MHz} \approx 10^{27.1}$ W Hz^{-1}, at $z = 0$, the luminosity function is dominated by FSRQs and below this point the BL Lac luminosity function is dominant. For BL Lacs $p = 3+\alpha = 2.7$ (Urry et al., 1991), and for FSRQs $p = 3+\alpha = 2.9$ (Padovani & Urry, 1992). To determine f and G, an average viewing angle and average Lorentz factor is selected in agreement with those found by Hovatta et al. (2009). For BL Lacs the average viewing angle is 5.5° and average Lorentz factor is 10.3 and for FSRQs the average viewing angle is 4.4° and average Lorentz factor is 16.2. The range of Lorentz factors for both BL Lacs and FSRQs is $5 \leq \gamma \leq 40$ (Padovani & Urry, 1992) and the range of intrinsic luminosities (in erg s^{-1}) is $39.5 \leq \log L_{151MHz} \leq 47.5$ (Smolčić et al., 2009; Ajello et al., 2009). The results are not sensitive to the limits of integration as long as for the lower limit $\log L^{min}_{151MHz} \lesssim 40.0$ and for the upper limit $\log L^{max}_{151MHz} \gtrsim 45.5$. The FSRQ (solid line) and BL Lac (dashed line) luminosity functions at $z = 1$ are shown in Figure 2.2.

2.2.1.2 Formalism

Following the formalism laid out in previous works (e.g., Comastri et al. 2005; Pompilio et al. 2000; Ballantyne et al. 2006) to compute the extragalactic background spectrum due to AGN and blazars, the spectral intensity at X-ray or γ-ray energy E due to blazars is given

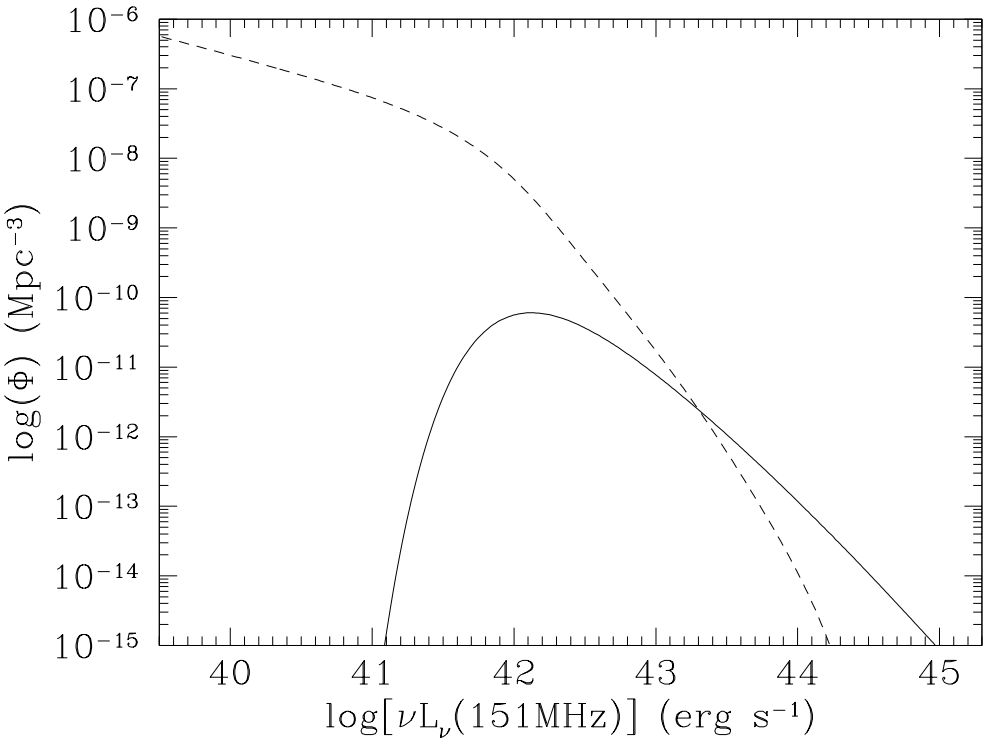

Figure 2.2: Rest frame radio AGN luminosity function by Willott et al. (2001) model C relativistically beamed using the method of Urry & Shafer (1984) and Urry & Padovani (1991) at $z = 1$ separated into FSRQs (solid line) and BL Lacs (dashed line).

by

$$\begin{aligned} I(E) &= \frac{c}{H_0}\int_{z_{\min}}^{z_{\max}}\int_{\log L_{151MHz}^{\min}}^{\log L_{151MHz}^{\max}} \frac{d\Phi(L_{151MHz},z)}{d\log L_{151MHz}} \frac{S_E(L_{151MHz},z)d_l^2}{(1+z)^2[\Omega_m(1+z)^3+\Omega_\Lambda]^{1/2}} \\ &\times d\log L_{151MHz}dz, \end{aligned} \tag{2.8}$$

where $d\Phi(L_{151MHz},z)/d\log L_{151MHz}$ is the blazar luminosity function at 151 MHz (in units of Mpc^{-3}), $S_E(L_{151MHz},z)$ is the observed spectrum at energy E (in units of keV cm^{-2} s^{-1} keV^{-1}) for a blazar with intrinsic 151 MHz luminosity L_{151MHz} at redshift z, and d_l is the luminosity distance of redshift z. A similar method is used to calculate the number counts within a specified energy band as shown by Ballantyne et al. (2006) Equation 3.

2.2.1.3 Spectrum

Blazars have a distinct spectral shape characterized by two bumps, a synchrotron peak and a higher frequency inverse Compton (IC) peak. The "Blazar Sequence", in which the spectrum of a blazar can be uniquely determined based solely on the bolometric luminosity of the blazar (Fossati et al., 1997, 1998; Ghisellini et al., 1998; Donato et al., 2001) was considered as a blazar SED model; however, the anti-correlation between the synchrotron peak frequency and the synchrotron peak luminosity has been proposed to be due to sample selection effects (Caccianiga & Marchã, 2004; Padovani, 2007; Ghisellini & Tavecchio, 2008) and possibly variable Doppler boosting (Nieppola et al., 2008). A "new Blazar Sequence" has been proposed which parametrizes the blazar SED by the black hole mass and the accretion rate (Ghisellini & Tavecchio, 2008); however, the new Blazar Sequence still predicts an anti-correlation between the synchrotron peak frequency and synchrotron peak luminosity (Nieppola et al., 2008).

As there is no widely accepted blazar SED model, the blazar population was split into three subclasses (FSRQs, Low-peaked BL Lacs (LBL), and High-peaked BL Lacs (HBL)) and SED models were created for each subclass based on well sampled spectra of subclass members. Details of the SED parametrization can be found in Appendix A. For each subclass we set the synchrotron peak frequency, ν_S, the IC peak frequency, ν_{IC}, and the relative luminosity of the synchrotron and IC peaks, L_{IC}/L_S.

For FSRQs the synchrotron peak frequency is set based on the average peak frequency depicted in Figure 5 of Antón & Browne (2005) for the 1 Jy sample. This gives an average

FSRQ peak frequency of $10^{14.0}$ Hz. The IC peak frequency of FSRQs is set at 1 MeV in accordance with Ajello et al. (2009). To determine the ratio L_{IC}/L_S the literature was searched yielding the spectra of forty FSRQs shown in Table 2.2.1.3. In cases where multiple spectra are given for the same object, the spectra corresponding to the most quiescent state is considered. Most sources show ratios of $\log(L_{IC}/L_S) \approx 1.0$ to 2.0 with a few sources showing ratios as low as $\log(L_{IC}/L_S) \approx 0.0$ or as high as $\log(L_{IC}/L_S) \approx 3.0$. The mode value for the ratio $\log(L_{IC}/L_S) = 1.0$ is used.

The BL Lac objects are divided into HBLs and LBLs assuming 10% of the BL Lac population are HBLs (Padovani et al., 2007)[1]. Similarly to the FSRQ subclass, the HBL and LBL synchrotron peak frequencies were assigned the average peak frequency from the Slew sample and 200mJy sample, respectively, as depicted in Figure 5 of Antón & Browne (2005). The average peak frequency is $10^{16.5}$ Hz for HBLs and $10^{14.5}$ Hz for LBLs. To set the IC peak frequency and IC peak luminosity for the HBL and LBL spectra,the ratios ν_{IC}/ν_S and L_{IC}/L_S from the SEDs modeled in the literature were consulted (see Table 2.2.1.3). All sources had $\log(\nu_{IC}/\nu_S) \approx 8.0$ to 9.0 and $\log(L_{IC}/L_S) \approx$ -1.5 to 1.5. The mode values for the ratios were used, giving $\log(\nu_{IC}/\nu_S)= 8.0$ and $\log(L_{IC}/L_S)$=0.0. Two LBLs were found to have complete spectrum models, BL Lacertae (Berger et al., 2008) and 3C 66A (Joshi & Böttcher, 2007). The spectra of BL Lacertae and 3C 66A both have $\log(\nu_{IC}/\nu_S) \approx 7.0$ and $\log(L_{IC}/L_S) \approx 0.0$.

Figure 2.3 depicts the spectra used for FSRQs (solid lines) for $L_{151MHz}= 10^{43.0}$ erg s^{-1}, LBLs (dashed lines) for $L_{151MHz}= 10^{41.5}$ erg s^{-1}, and HBLs (dot-dashed lines) for $L_{151MHz}= 10^{40.0}$ erg s^{-1}.

2.2.2 AGN Contribution to the XRB

The non-blazar AGN contribution to the hard XRB is computed using standard synthesis modeling techniques (e.g., Comastri et al., 1995; Treister & Urry, 2005; Ballantyne et al., 2006; Gilli et al., 2007). The fraction of Type 2 AGNs, f_2, is assumed to be a function of both redshift and 2–10 keV luminosity, L_X: $f_2 \propto (1+z)^a (\log L_X)^{-b}$, with $a = 0.4$

[1]Increasing the HBL fraction to 20% does not affect the results of this study.

Table 2.1: FSRQs used for determining L_{IC}/L_S.

Name	Source	$\approx \log(L_{IC}/L_S)$
RBS 315	Tavecchio et al. (2007)	2.0
S5 0836+71	Tavecchio et al. (2007)	2.0
J0746.3+2548	Watanabe et al. (2009)	1.5
PKS 2149-306	Bianchin et al. (2009)	1.0
3C 279	Giuliani et al. (2009)	1.0
3C 454.3	Vercellone et al. (2009)	1.0
2141.2+1730	Maraschi et al. (2008)	0.0
0521.7+7918	Maraschi et al. (2008)	0.0
1234.9+6651	Maraschi et al. (2008)	1.0
1050.9+5418	Maraschi et al. (2008)	0.5
0402.0-3613	Maraschi et al. (2008)	0.0
0828.7+6601	Maraschi et al. (2008)	1.0
1623.4+2712	Maraschi et al. (2008)	1.0
1340.7+2859	Maraschi et al. (2008)	1.0
0152.4+0424	Maraschi et al. (2008)	1.5
0232.5-0414	Maraschi et al. (2008)	0.0
SDSS J081009.94+384757	Maraschi et al. (2008)	1.5
MG3 J225155+2217	Maraschi et al. (2008)	3.0
0048-071	Ghisellini et al. (2009b)	1.5
0202-17	Ghisellini et al. (2009b)	1.5
0215-015	Ghisellini et al. (2009b)	0.0
0528+134	Ghisellini et al. (2009b)	2.0
2251-158	Ghisellini et al. (2009b)	1.0
0227-369	Ghisellini et al. (2009b)	2.0
0454-234	Ghisellini et al. (2009b)	1.0
0347-221	Ghisellini et al. (2009b)	2.0
0820+560	Ghisellini et al. (2009b)	1.5
0917+449	Ghisellini et al. (2009b)	1.0
1454-354	Ghisellini et al. (2009b)	1.0
1013-054	Ghisellini et al. (2009b)	1.5
1502+106	Ghisellini et al. (2009b)	1.0
1329-049	Ghisellini et al. (2009b)	1.5
1520-319	Ghisellini et al. (2009b)	2.0
1551+130	Ghisellini et al. (2009b)	1.0
2052-447	Ghisellini et al. (2009b)	2.0
1633+382	Ghisellini et al. (2009b)	1.5
2227-088	Ghisellini et al. (2009b)	1.5
2023-077	Ghisellini et al. (2009b)	2.0
2325+093	Ghisellini et al. (2009b)	2.0
PKS 1334-127	Foschini et al. (2006)	0.5

Table 2.2: HBLs used for determining L_{IC}/L_S and ν_{IC}/ν_S.

Name	Source	$\approx \log(L_{IC}/L_S)$	$\approx \log(\nu_{IC}/\nu_S)$
RGB J0152+017	Aharonian et al. (2008)	0.0	8.0
PKS 2155-304	Costamante et al. (2008)	0.0	9.0
J1456.0+5048	Maraschi et al. (2008)	0.0	9.0
1ES1959+650	Tagliaferri et al. (2008)	-1.5	8.0
0426-380	Ghisellini et al. (2009b)	1.5	8.0
0235+164	Foschini et al. (2006)	0.0	8.0
Mkn 501	Massaro et al. (2006)	0.0	8.0

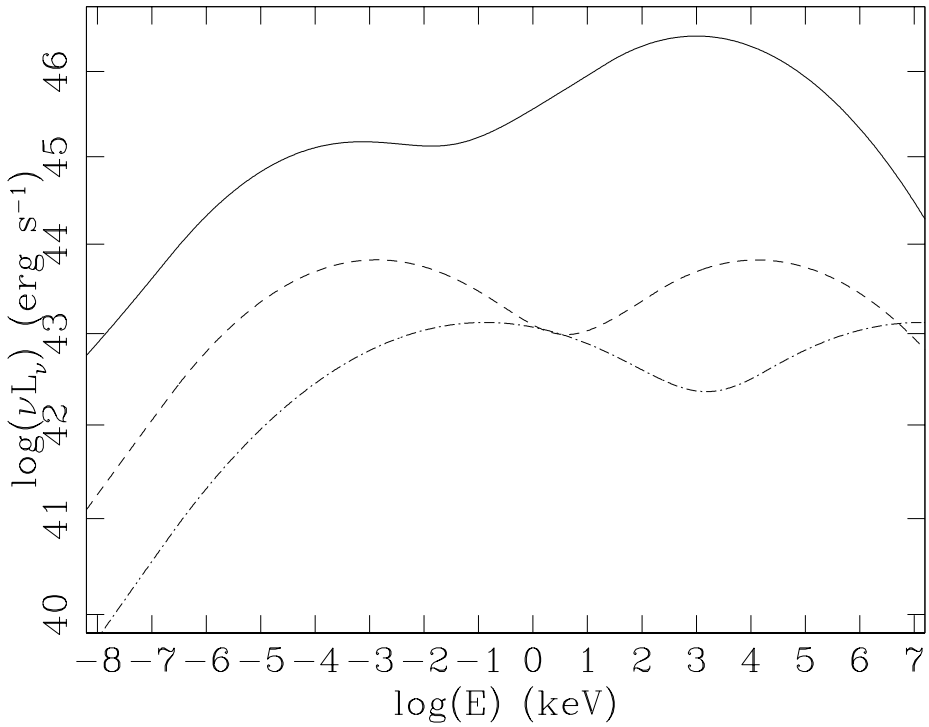

Figure 2.3: Rest frame spectral energy distributions used for FSRQ (solid line) with $\log \nu L_\nu$(151 MHz)=43.0, LBL (dashed line) with $\log \nu L_\nu$(151 MHz)=41.5, and HBL (dot-dashed line) with $\log \nu L_\nu$(151MHz)=40.0.

(Ballantyne et al., 2006; Treister & Urry, 2006) and $b = 4.7$. This evolution is normalized so that the non-blazar AGN type 2 to type 1 ratio is 4:1 at $z = 0$ and $\log L_X = 41.5$ (Risaliti et al., 1999; Ballantyne et al., 2006; Treister et al., 2009). The redshift evolution is halted at $z = 1$ in analogy with the evolution of the cosmic star-formation rate density (e.g., Ghandi & Fabian, 2003; Hopkins & Beacom, 2006).

AGNs with absorbing column densities less than $\log N_{\rm H} = 22$ are considered to be unabsorbed type 1 sources, and they are distributed evenly over the following columns: $\log N_{\rm H} = 20, 20.5, 21$ and 21.5. Compton-thin Type 2 AGNs are also distributed equally over $\log N_{\rm H} = 22, 22.5, 23$ and 23.5. As current hard X-ray luminosity functions are missing Compton-thick AGNs, a parameter controlling the Compton thick fraction is defined, and any CT AGNs are distributed equally over $\log N_{\rm H} = 24, 24.5$ and 25. It is assumed that CT AGNs evolve in the same manner as less absorbed AGNs. The CT fraction, f_{CT} is defined to be the fraction of obscured AGN which are CT.

The unabsorbed rest-frame AGN spectrum consists of a power-law with photon index Γ and an exponential cutoff at energy $E_{\rm cut}$, combined with a neutral reflection component calculated using the "reflion" model within XSPEC (Ross & Fabian 2005). The strength of the reflection features in the total spectrum is typically parametrized by a reflection fraction, R, that is related to the covering factor of the reflector. Observationally, it is found that the strength of the reflection features decreases with luminosity, a relationship that is sometimes called the X-ray Baldwin effect (e.g., Bianchi et al. 2007). Therefore, we do not assume a constant value of R, rather the reflection spectrum is added to the power-law component such that the equivalent width of the Fe Kα line agrees with the observed X-ray Baldwin effect found by Bianchi et al. (2007). In this way, the observed decrease in the strength of the reflection features with luminosity can be naturally included in the synthesis model. The relationship by Bianchi et al. (2007) gives an Fe Kα equivalent width of 143 eV at log $\rm L_X$ = 41.5, which is approximately equivalent to $R = 1.1$ for a $\Gamma = 1.9$ spectrum. The reflection fraction is proportional to the Fe Kα EW, so R reduces to approximately 0.4 at log $\rm L_X$ = 44 and 0.1 at log $\rm L_X$ = 47. All the models presented here assume $E_{\rm cut} = 250$ keV. Finally, following Gilli et al. (2007), spectra with $\Gamma = 1.5$ up to

2.3 are Gaussian averaged around $\Gamma = 1.9$ to account for the observed dispersion in AGN spectral slopes. This results in a final rest-frame spectrum with luminosity L_X with the correct reflection strength.

2.2.3 AGN HXLFs

The AGN HXLFs considered are listed with their parameters in Table 2.2.3. Five of the HXLFs considered are LDDE models as proposed by Ueda et al. (2003). The Aird et al. (2010) HXLF considered is a LADE model. For the LDDE models, the luminosity function is described by the local luminosity function, $d\Phi(L_X, z = 0)/d\log L_X$ and an evolution factor $e(z, L_X)$, such that

$$\frac{d\Phi(L_X, z)}{d\log L_X} = \frac{d\Phi(L_X, 0)}{d\log L_X} e(z, L_X). \tag{2.9}$$

The local luminosity function is of the form

$$\frac{d\Phi(L_X, 0)}{d\log L_X} = A\left[\left(\frac{L_X}{L_*}\right)^{\gamma_1} + \left(\frac{L_X}{L_*}\right)^{\gamma_2}\right]^{-1}. \tag{2.10}$$

And the evolution factor is given by

$$e(z, L_X) = \begin{cases} (1+z)^{p_1} & z < z_c(L_x) \\ e(z_c)\left[\frac{1+z}{1+z_c(L_x)}\right]^{p_2} & z \geq z_c(L_X) \end{cases} \tag{2.11}$$

where

$$z_c(L_X) = \begin{cases} z_c^* & L_X \geq L_a \\ z_c^*\left(\frac{L_X}{L_a}\right)^{\alpha} & L_X < L_a \end{cases}. \tag{2.12}$$

The LADE model takes the same form as the LDDE local luminosity function defined in equation 2.10 and L_* and A are allowed to evolve with redshift such that

$$\log L_*(z) = \log L_0 - \log\left[\left(\frac{1.0+z_c}{1.0+z}\right)^{p_1} + \left(\frac{1.0+z_c}{1.0+z}\right)^{p_2}\right] \tag{2.13}$$

and

$$\log A(z) = \log A_0 + \alpha(1+z). \tag{2.14}$$

Table 2.3: Parameters of AGN X-ray Luminosity Functions considered. [a] in units of h_{70}^3 Mpc^{-3}. [b] in units of h_{70}^{-2} erg s^{-1}. [c] an LADE model.

Luminosity Function	A/A_0^a	$\log L_*/\log L_0$ [b]	γ_1	γ_2	p_1	p_2	z_c^*/z_c	$\log L_a^b$	α
Ueda et al. (2003)	5.04e-6	43.94	0.86	2.23	4.23	-1.5	1.9	44.6	0.335
La Franca et al. (2005)	1.21e-6	44.25	1.01	2.38	4.62	-1.15	2.49	45.74	0.20
Silverman et al. (2008)	6.871e-7	44.33	1.10	2.15	4.22	-3.27	1.89	44.6	0.333
Ebrero et al. (2009)	4.78e-6	43.91	0.96	2.35	4.07	-1.5	1.9	44.6	0.245
Yencho et al. (2009)	7.24e-7	44.40	0.872	2.36	3.61	-2.83	2.18	45.09	0.208
Aird et al. (2010)[c]	2.95e-5	44.77	0.62	3.01	6.36	-0.24	0.75	-	-0.19

2.3 Results

2.3.1 Blazar contribution to the XRB

Figure 2.4 shows the calculated blazar and AGN contribution to the XRB and γ-ray background. The dotted line shows the AGN contribution to the XRB assuming the HXLF presented by Ueda et al. (2003) and $f_{CT} = 0.5$. The dashed line is the FSRQ contribution while the dot-dashed line shows the BL Lac contribution. The BL Lacs are found to contribute greater than 100% of the γ-ray background. The possibility that the overestimation was due to inappropriate beaming parameters was investigated. Hovatta et al. (2009) found that BL Lacs tend to have Lorentz factors of $1.0 \leq \gamma \leq 38$. When this range of Lorentz factors is used and the BL Lac beaming parameters are set so that the average Lorentz factor is 10.3 and the average viewing angle is 5.3°, in agreement with Hovatta et al. (2009), the model over-predicts the γ-ray background by a factor of $\sim$200.

Here it is assumed that all radio galaxies viewed in the appropriate orientation are blazars. However, evidence suggests that AGNs, specifically radio galaxies, are an intermittent phenomenon (Burns et al., 1983; Cavaliere & Padovani, 1989; Roettiger et al., 1993; Franceschini et al., 1998; Schoenmakers et al., 1999, 2000; Venturi et al., 2004; Jamrozy et al., 2007; Parma et al., 2007). BL Lac high energy radiation is primarily produced through synchrotron self-Compton (SSC) up-scattering, since BL Lac jets propagate through regions with very little external radiation (Ghisellini et al., 2009a). For BL Lacs to emit high energy radiation, processes within the jet must accelerate electrons to relativistic speeds such that the electrons have enough energy to create synchrotron photons and then up-scatter those photons. Therefore the high energy IC component of BL Lac jets would perhaps only be significant during infrequent events that cause rapid acceleration of electrons to high energies. Indeed, Giommi et al. (2006) found that unless BL Lacs have a small duty cycle, $\ll$100%, the predicted blazar γ-ray emission would over predict the γ-ray background. The blazar and AGN contribution to the XRB assuming an X-ray duty cycle of 13% for BL Lacs, as shown in Figure 2.5, fits the data well. If the fraction of BL Lacs which are HBLs is increased from 10% to 20%, an X-ray duty cycle of 13% still provides a good fit to the γ-ray background. The BL Lac number counts predicted by this model in the 15-55 keV

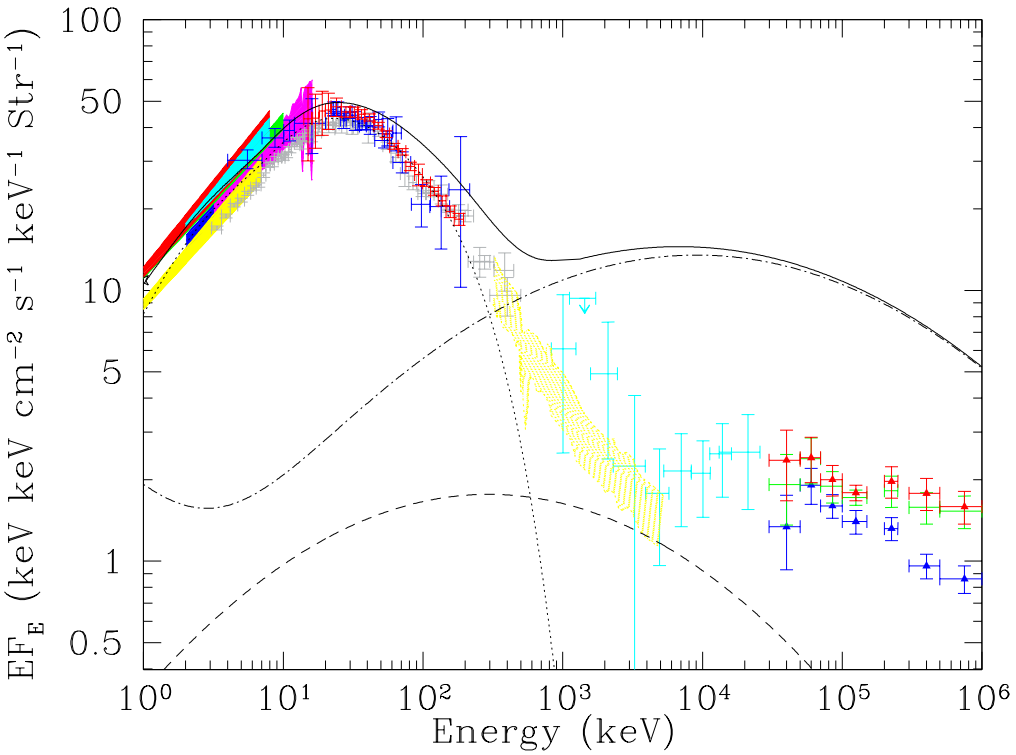

Figure 2.4: AGN and Blazar contribution (solid line) to the X-ray and γ-ray background if BL Lac duty cycle is 100%. AGN (dotted line- using Ueda et al. 2003 X-ray luminosity function and CT fraction $f_{ct} = 0.5$), FSRQs (dashed line), and BL Lacs (dot-dashed line). The colored data and areas denote measurements from various instruments: blue - ASCA GIS (Kushino et al., 2002); magenta - RXTE (Revnivtsev et al., 2003); green - XMM-Newton (Lumb et al., 2002); red - BeppoSAX (Vecchi et al., 1999); yellow - ASCA SIS (Gendreau et al., 1995); cyan - XMM-Newton (De Luca & Molendi, 2004); light yellow - SMM (Watanabe et al., 1999); grey data - HEAO-1 (Gruber et al., 1999); blue data - INTEGRAL (Churazov et al., 2007); red data - SWIFT BAT (Ajello et al., 2008); cyan data - COMPTEL (Weidenspointer et al., 2000); red triangles - EGRET (Sreekumar et al., 1998); blue triangles - reevaluation of EGRET (Strong et al., 2004); green data - renormalization of EGRET based Sreekumar et al. 1998 (Stecker et al., 2008).

band are shown in Figure 2.6 with the BL Lac number counts observed by Ajello et al. (2009). The number counts predicted by this work are slightly larger but within a factor of 2.5 of the observations by Ajello et al. (2009).

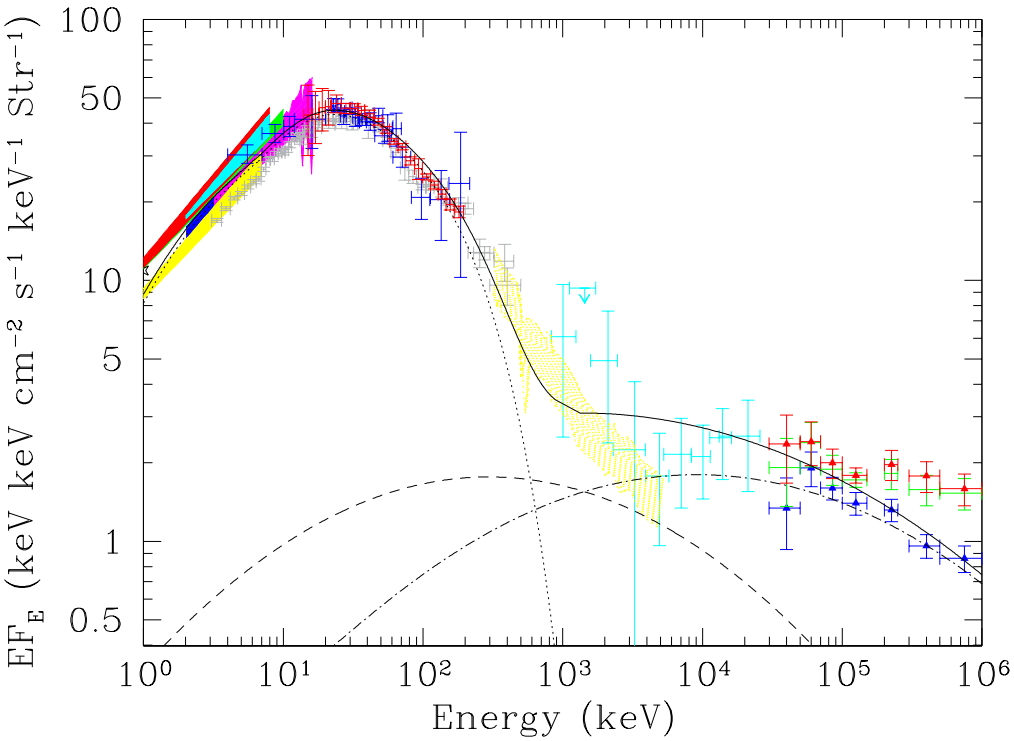

Figure 2.5: AGN and Blazar contribution (solid line) to the X-ray and γ-ray background. AGN (dotted line- using Ueda et al. 2003 X-ray luminosity function and CT fraction f_{ct} = 0.4), FSRQs (dashed line), and BL Lacs (dot-dashed line) with an X-ray duty cycle of 13%. Data the same as in Figure 2.4.

More powerful sources, like FSRQs, are expected to accrete more efficiently and at a higher rate than low luminosity sources (Ho, 2008). Ajello et al. (2009) studied variability in Palomar-QUEST survey blazars and found evidence that FSRQ duty cycles are greater than BL Lac duty cycles. No duty cycle for FSRQs is accounted for here, and indeed the background due to FSRQs is in reasonable agreement with that found by Ajello et al. (2009).

In the soft X-ray band (0.5-2 keV) the blazar contribution is found to be ∼12%, in agreement with the prediction of 11-12% by Giommi et al. (2006). The blazar contribution in the hard X-ray band (2-10 keV) is found to be ∼7.4%, in rough agreement with the

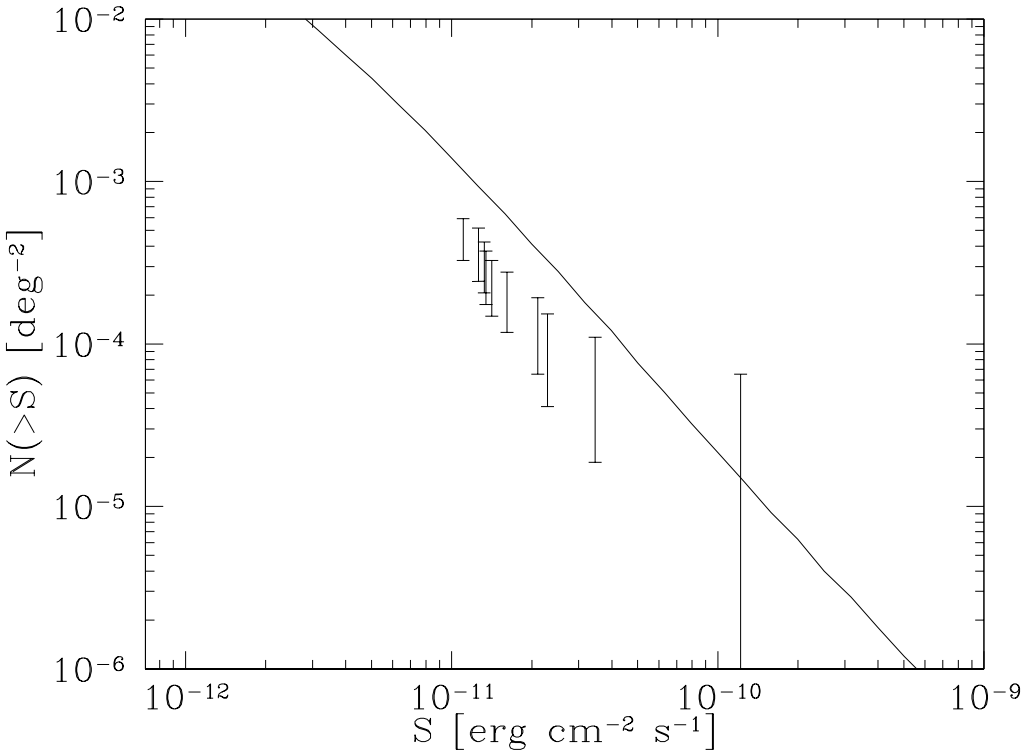

Figure 2.6: BL Lac number density counts for 15-55 keV band assuming an X-ray duty cycle of 13%. Data shown from Ajello et al. (2009) Figure 12b.

prediction of ∼10% by Ajello et al. (2009). In the 15.0-55.0 keV range blazars contribute ∼8.9% of the X-ray background, in good agreement with the prediction of two distinct blazar classes by Ajello et al. (2009) of ∼9%. Emissions from BL Lacs is found to account for the MeV background, in agreement with previous works (Giommi et al., 2006; Narumoto & Totani, 2006; Kneiske & Mannheim, 2008).

2.3.2 Implications for CT AGN

When the contribution of blazars to the XRB is properly considered, fewer CT AGN are required. In Figure 2.5 the AGN contribution to the XRB, as given by Ueda et al. (2003), is shown with $f_{CT} = 0.4$, in contrast to the canonical $f_{CT} = 0.5$. The CT fraction, f_{CT} required to appropriately model the peak of the XRB is shown for various HXLFs in Table 2.3.2 as well as the f_{CT} needed if the contribution of blazars is not considered. There is a ∼10% uncertainty in the peak intensity of the XRB (e.g. HEAO-1 vs *Swift*). For the purposes of this work we assume $EF_E \approx 44.2$ keV cm^{-2} s^{-1} str^{-1} at 30 keV. Note that the estimated CT AGN fraction strongly depends on the XRB peak intensity adopted in the model. The Yencho and Silverman HXLFs depend heavily on CT sources to match the peak of the XRB; therefore, when blazars are considered the CT AGN fraction is still quite high. The number density of CT AGN at $z = 0$ with $L_X > 10^{43}$ erg s^{-1} is also shown in Table 2.3.2 for the case of no blazar contribution to the XRB and for the case of blazar contribution to the XRB as described here. The number density as a function of redshift of CT AGN with $L_X > 10^{43}$ erg s^{-1} needed to model the peak of the XRB for the HXLF given by Ueda et al. (2003) (solid lines) and Ebrero et al. (2009) (dashed lines) are shown in Figure 2.7. The thin black lines are the case where the blazar contribution to the XRB is not taken into account. The thick blue lines show the case where blazars are considered. The CT AGN density is reduced by a factor of 1.7 for the Ueda HXLF and a factor of 3.0 for the Ebrero HXLF. The AGN luminosity functions proposed by Silverman et al. (2008) and Yencho et al. (2009) require CT fractions where the majority of obscured AGN are CT. The AGN luminosity functions proposed by Ueda et al. (2003), La Franca et al. (2005), and Ebrero et al. (2009) require that less than half the obscured AGN are CT, in agreement

with Malizia et al. (2009) and Treister et al. (2009).

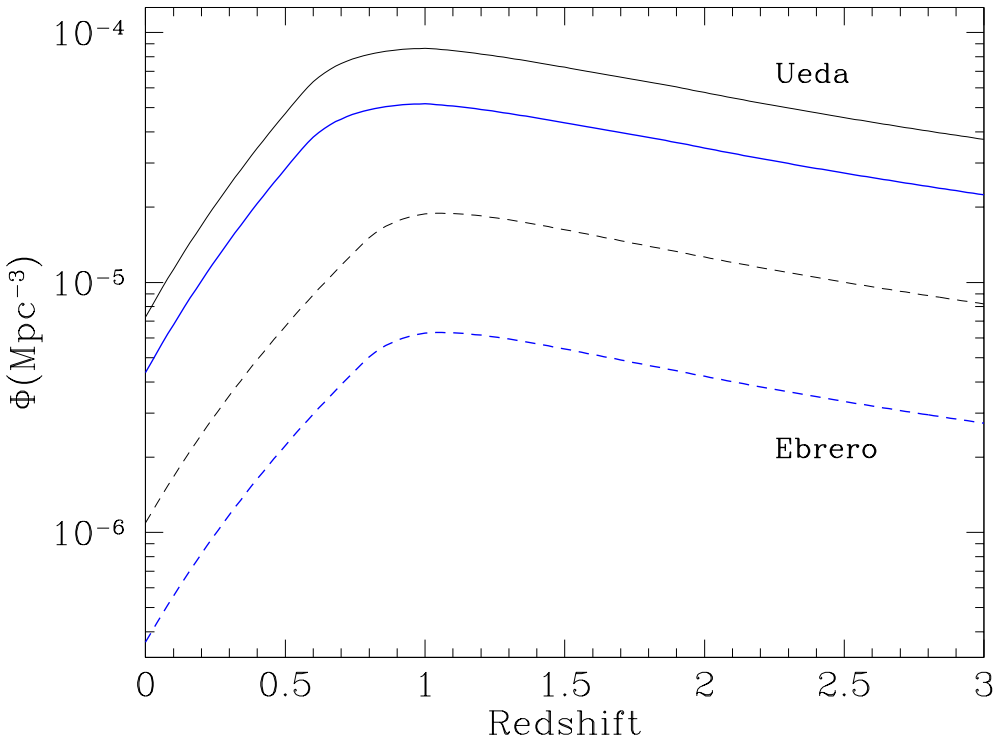

Figure 2.7: Number density of CT AGN with $L_X > 10^{43}$ erg s^{-1} as a function of redshift for the HXLFs given by Ueda et al. (2003) (solid lines) and Ebrero et al. (2009) (dashed lines). The black(thin) lines are the CT AGN needed if blazars are not considered. The blue(thick) lines are the CT AGN needed if the blazar contribution to the XRB is considered.

2.4 Discussion and Summary

It is clear that blazars make a non-negligible contribution to the XRB and significantly reduce the number of CT AGN predicted, and may be primarily responsible for the MeV background. This chapter presents an upper limit to blazar contribution to the XRB by utilizing the unified model of radio-loud AGN. The main conclusions found here do not change with a different choice of AGN radio luminosity function (e.g., Condon et al., 2002; Sadler et al., 2002; Best et al., 2005; Kaiser & Best, 2007; Mauch & Sadler, 2007); however, beaming parameters need to be modified as these luminosity functions do not distinguish between FRIs and FRIIs or high and low luminosity sources.

A recent study by Ajello et al. (2009), using the three year sample of *Swift*/BAT blazars,

Table 2.4: f_{CT} needed for luminosity function to match the peak of the X-ray background and corresponding CT number density at $z = 0$ in Mpc^{-3} for $L_X > 10^{43}$ erg s^{-1}

Luminosity Function	f_{CT}		CT number density at $z = 0$ (Mpc^{-3})	
	Without Blazars	With Blazars	Without Blazars	With Blazars
Ueda et al. (2003)	0.5	0.4	7.3×10^{-6}	4.4×10^{-6}
La Franca et al. (2005)	0.3	0.2	2.0×10^{-6}	1.6×10^{-6}
Silverman et al. (2008)	0.8	0.8	1.4×10^{-5}	1.2×10^{-5}
Ebrero et al. (2009)	0.1	0.02	1.1×10^{-6}	3.6×10^{-7}
Yencho et al. (2009)	0.8	0.8	1.7×10^{-5}	1.6×10^{-5}
Aird et al. (2010)	0.7	0.6	5.2×10^{-6}	4.7×10^{-6}

finds similar results for FSRQs as those found here; however, this work finds a greater contribution to the XRB and cosmic γ-ray background by BL Lacs. Due to the small number statistics and small redshift range of the *Swift*/BAT BL Lac sample, Ajello et al. (2009) are not able to uniquely determine the evolutionary parameters and thus assume no evolution for BL Lacs. This work assumes BL Lacs evolve in the same manner as low luminosity radio galaxies. Also, Ajello et al. (2009) assume a simple power law SED model for BL Lacs whereas this work utilizes an SED model based on average BL Lac properties taking into account the variety of BL Lac subclasses of LBLs and HBLs. Several studies have found that BL Lacs contribute substantially to the cosmic γ-ray background (Giommi et al., 2006; Narumoto & Totani, 2006; Kneiske & Mannheim, 2008), thus it is not expected that the BL Lac contribution to the XRB is negligible, as found by Ajello et al. (2009). As this work uses a more physical BL Lac SED model and a reasonable evolutionary model, we expect that this work may more accurately model the BL Lac contribution to the XRB, although the factor 2.5 discrepancy in the BL Lac source counts in the hard X-ray band must be solved in future works.

Treister et al. (2009) find the density of CT AGN at $z = 0$ with $L_X > 10^{43}$ erg s^{-1} is $\sim$2.2 $\times$ 10^{-6} Mpc^{-3}. The luminosity function of Ueda et al. (2003) predicts the density of CT AGN with $L_X > 10^{43}$ erg s^{-1} at $z = 0$ to be 7.3 $\times$ 10^{-6} Mpc^{-3} if blazars are not considered and 4.4 $\times$ 10^{-6} Mpc^{-3} if blazars are considered. With the blazar contribution to the XRB considered, the Ueda et al. (2003) over-predicts the CT AGN density found by Treister et al. (2009), by a factor of 2. Conversely, the luminosity function proposed by Ebrero et al. (2009) predicts the density of CT AGN with $L_X > 10^{43}$ erg s^{-1} at $z = 0$ to be 1.1 $\times$ 10^{-6} Mpc^{-3} if blazars are not considered and 3.6 $\times$ 10^{-7} Mpc^{-3} if blazars are considered, which is a factor of 6 smaller than the density reported by Treister et al. (2009). According to the INTEGRAL results of Malizia et al. (2009), the $f_{CT} \gtrsim 0.32$ with no upper limit given. Between different HXLFs there is a large scatter in the predicted f_{CT} and the predicted CT AGN density varies by a factor of 30. This clearly illustrates the limits imposed by the uncertainty of the low luminosity end of the AGN HXLF and how important it is for future missions to probe this portion of the HXLF.

It has been shown that blazars, specifically BL Lacs, contribute the majority of the γ-ray background (Giommi et al., 2006; Narumoto & Totani, 2006; Kneiske & Mannheim, 2008). Giommi et al. (2006) found that unless BL Lacs have a small high energy duty cycle the predicted blazar γ-ray emission would over predict the γ-ray background. Furthermore, Kneiske & Mannheim (2008) suggests that using radio blazar luminosity functions may cause an overestimation of the number of sources emitting robustly at higher energies, as it is not certain that all radio sources will have strong X-ray and γ-ray emission. Physical and evolutionary models of quasars indicate that AGN activity is short-lived and possibly recurrent (Sołtan, 1982; Cavaliere & Padovani, 1989; Chokshi & Turner, 1992). Franceschini et al. (1998) showed that long-lived, continuous AGN activity is not consistent with the black hole mass function they calculated from their sample of 13 local galaxies, but short-lived and recurrent AGN activity matches the data well. Several sources which appear to be restarted AGNs have been observed (Burns et al., 1983; Roettiger et al., 1993; Schoenmakers et al., 1999; Venturi et al., 2004; Jamrozy et al., 2007; Fabian et al., 2009). Sources have also been observed which have relic radio lobes but the AGN activity is not currently in an active phase (Parma et al., 2007; Dwarakanath & Kale, 2009; Fabian et al., 2009). Recent observations by *Hubble Space Telescope* and *Chandra* of the relativistic jet of nearby M87 provide evidence for the intermittent nature of jet X-ray emission (e.g., Perlman et al., 2003; Harris et al., 2006; Stawarz et al., 2006; Madrid, 2009). Large amplitude flaring has been observed from the previously quiescent knot HST-1 in the jet of M87 since 2000 (Madrid, 2009). This flaring activity is shown to be consistent with shocks occurring within the jet as faster moving particles collide with slower relativistic particles injected into the jet at an earlier time (Perlman et al., 2003; Stawarz et al., 2006; Madrid, 2009). Perlman et al. (2003) and Stawarz et al. (2006) suggest the recent X-ray flaring of HST-1 is directly related to material injected at the base of the jet 30-40 years ago. Therefore, a jet X-ray duty cycle is expected.

Finally, due to the spectral steepening that occurs after the flow of energetic particles into the jet has ceased, the best frequency range to search for relic radio lobes is the low radio regime, less than 1 GHz (Parma et al., 2007). Therefore, it is likely that the radio AGN

luminosity function given by Willott et al. (2001) at 151 MHz includes relic radio lobes. As this would affect the low luminosity end of the luminosity function more prevalently as relic sources tend to not be as luminous as active sources (Dwarakanath & Kale, 2009), the BL Lac luminosity function found here may over-predict the number of BL Lacs. Thus, the average BL Lac X-ray duty cycle is likely to be somewhat larger than the 13% found here.

2.5 References

Abdo, A.A., Ackermann, M., Ajello, M., et al. 2009, ApJS, 183, 46

Aharonian, F., Akhperjanian, A.G., Barres de Almeida, U., et al. 2008, A&A, 481, L103

Aird, J., Nandra, K., Laird, E.S., et al. 2009, MNRAS, 401, 2531

Ajello, M., Greiner, J., Sato, G., et al. 2008, ApJ, 689, 666

Ajello, M. Costamante, L., Sambruna, R.M., et al. 2009, ApJ, 699, 603

Alexander, D.M., Bauer, F.E., Brandt, W.N., et al. 2003, AJ, 126, 539

Antón, S. & Browne, I.W.A. 2005, MNRAS, 356, 225

Antonucci, R. 1993, ARA&A, 31, 473

Ballantyne, D.R., Everett, J.E., Murray, N. 2006, ApJ, 639, 740

Ballantyne, D.R. & Papovich, C. 2007, ApJ, 660, 988

Barger, A.J., Cowie, L.L., Mushotzky, et al. 2005, AJ, 129, 578

Bauer, A., Baltay, C., Coppi, P., et al. 2009, ApJ, 699, 1732

Berger, K., Wagner, R.M., Hayashida, M., et al. 2008, in AIP Conf. Proc. Vol. 1085, High Energy Gamma-Ray Astronomy, ed. F.A. Aharonian, W. Hofmann, & F. Reiger (Heidelberg: AIP), 467

Best, P.N., Kauffmann, G., Heckman, T.M., & Ivezić, Ž. 2005, MNRAS, 362, 9

Bianchi, S., Guainazzi, M., Matt, G. & Fonseca Bonilla, N. 2007, A&A, 467, L19

Bianchin, V. Foschini, L., Ghisellini, G., et al. 2009, A&A, 496, 423

Brandt, W.N. & Hasinger, G. 2005, ARA&A, 43, 827

Burns, J.O., Schwendeman, E., & White, R.A. 1983 ApJ, 271, 575

Caccianiga, A. & Marchã, M.J.M. 2004, MNRAS, 348, 937

Cavaliere, A. & Padovani, P. 1989, ApJ, 340, L5

Celotti, A., Fabian, A.C., & Rees, M.J. 1992, MNRAS, 255, 419

Chokshi, A. & Turner, E.L. 1992, MNRAS, 259, 421

Churazov, E., Sunyaev, R., Revnivtsev, M., et al. 2007, A&A, 467, 529

Comastri, A., Setti, G., Zamorani, G., & Hasinger G. 1995, A&A, 296, 1

Condon, J.J., Cotton, W.D., & Broderick, J.J. 2002, AJ, 124, 675

Costamante, L., Aharonian, F., Bühler, R., et al. 2008, in AIP Conf. Proc. Vol. 1085, High Energy Gamma-Ray Astronomy, ed. F.A. Aharonian, W. Hofmann, & F. Reiger (Heidelberg:AIP), 644

Cowie, L.L., Songaila, A., & Barger, A.J. 1999, ApJ, 118, 603

De Luca, A. & Molendi, S. 2004, A&A, 419, 837

Donato, D., Ghisellini, G., Tagliaferri, G., Fossati, G. 2001, A&A, 375, 739

Dwarakanath, K.S. & Kale, R. 2009, ApJ, 698, L163

Ebrero, J., Carrera, F.J., Page, M.J., et al. 2009, A&A, 493, 55

Fabian, A.C. & Barcons, X. 1992, ARA&A, 30, 429

Fabian, A.C., Chapman, S., Casey, C.M., Bauer, F. & Blundell, K.M. 2009, MNRAS, 395, L67

Ferrarese, L. & Merritt, D. 2000, ApJ, 539, L9

Fiore, F., La Franca, F., Giommi, P., et al. 1999, MNRAS, 306, L55

Foschini, L., Ghisellini, G., Raiteri, C. M., et al. 2006, A&A, 453, 829

Fossati, G., Celotti, A., Ghisellini, G., & Maraschi, L. 1997, MNRAS, 289, 136

Fossati, G., Maraschi, L., Celotti, A., Comastri, A., & Ghisellini, G. 1998, MNRAS, 299, 433

Franceschini, A., Vercellone, S, & Fabian, A.C. 1998, MNRAS, 297, 817

Gendreau, K.C., Mushotzky, R., Fabian, A.C., et al. 1995, PASJ, 47, L5

Gandhi, P. & Fabian, A.C., 2003, MNRAS, 339, 1095

Ghisellini, G., Haardt, R., & Matt, G. 1994, MNRAS, 267, 743

Ghisellini, G., Celotti, A., Fossati, G., Maraschi, L., & Comastri, A. 1998, MNRAS, 301, 451

Ghisellini, G. & Tavecchio, F. 2008, MNRAS, 387, 1669

Ghisellini, G., Maraschi, L., & Tavecchio, F. 2009a, MNRAS, 396, L105

Ghisellini, G., Tavecchio, F., & Ghirlanda, G. 2009b, MNRAS, 399, 2041

Giacconi, R., Gursky, H., Paolini, F.R., & Rossi, B.B. 1962, Phys. Rev. Lett., 9, 439

Giacconi, R., Rosati, P., Tozzi, P., et al. 2001, ApJ, 551, 624

Giacconi, R., Zirm, A., Wang, J.X., et al. 2002, ApJS, 139, 369

Gilli, R., Comastri, A. & Hasinger, G. 2007, A&A, 463, 79

Giommi, P., Colafrancesco, S., Cavazzuti, E., Perri, M., & Pittori, C. 2006, A&A, 445, 843

Giuliani, A., D'Ammando, F., Vercellone, S., et al. 2009, A&A, 494, 509

Gruber, D.E., Matteson, J.L., Peterson, L.E. & Jung, G.V. 1999, ApJ, 520, 124

Guainazzi, M., Matt, G., & Perola, G.C. 2005, A&A, 444, 119

Harris, D.E., Cheung, C.C., Biretta, J.A., et al. 2006, ApJ, 640, 211

Hasinger, G., Burg, R., Giacconi, R., et al. 1998, A&A, 329, 482

Hasinger, G., Altieri, B., Arnaud, M., et al. 2001, A&A, 365, L45

Hasinger, G., Miyaji, T., & Schmidt, M. 2005, A&A, 441, 417

Ho, L.C. 2008, ARA&A, 46, 475

Hopkins, A.M. & Beacom, J.F. 2006, ApJ, 651, 142

Hovatta, T., Valtaoja, E., Tornikoski, M., & Lähteenmäki, A. 2009, A&A, 494, 527

Jamrozy, M., Konar, C., Saikia, D.J., et al. 2007, MNRAS, 378, 581

Joshi, M. & Böttcher, M. 2007, ApJ, 662, 884

Kaiser, C.R. & Best, P.N. 2007, MNRAS, 381, 1548

Kneiske, T.M. & Mannheim, K. 2008, A&A, 479, 41

Kushino, A., Ishisaki, Y., Morita, U., et al. 2002, PASJ, 54, 327

La Franca, F. Fiore, F., Comastri, A., et al. 2005, ApJ, 635, 864

Lumb, D.H., Warwick, R.S., Page, M. & De Luca, A. 2002, A&A, 389, 93

Lynden-Bell, D. 1969, Nature, 223, 690

Madau, P., Ghisellini, G., & Fabian, A.C. 1994, MNRAS, 270, L17

Madrid, J.P. 2009, AJ, 137, 3864

Malizia, A., Stephen, J.B., Bassani, et al. 2009, MNRAS, 399, 944

Maraschi, L., Foschini, L., Ghisellini, G., Tavecchio, F., & Sambruna, R.M. 2008, MNRAS, 391, 1981

Massaro, E., Tramacere, A., Perri, M., Giommi, P., & Tosti, G. 2006, A&A, 448, 861

Mauch, T. & Sadler, E.M. 2007, MNRAS, 375, 931

Mushotzky, R.F., Cowie, L.L., Barger, A.J., & Arnaud, K.A. 2000, Nature, 404, 459

Narumoto, T. & Totani, T. 2006, ApJ, 643, 81

Nieppola, E., Valtaoja, E., Tornikoski, M., Hovatta, T., & Kotiranta, M. 2008, A&A, 488, 867

Padovani, P. 2007, Ap&SS, 309, 63

Padovani, P., Giommi, P., Landt, H., Perlman, E.S. 2007, ApJ, 662, 182

Padovani, P. & Urry, C.M. 1992, ApJ, 387, 449

Parma, P., Murgia, M., de Ruiter, H.R., et al. 2007, A&A, 470, 875

Perlman, E.S., Harris, D.E., Biretta, J.A., Sparks, W.B., & Macchetto, F.D. 2003, ApJ, 599, L65

Pompilio, F., La Franca, F., & Matt, G. 2000, A&A, 353, 440

Rees, M.J. 1984, ARA&A, 22, 471

Revnivtsev, M., Gilfanov, M., Sunyaev, R., Jahoda, K. & Markwardt, C. 2003, A&A, 411, 329

Risaliti, G., Maiolino, R., & Salvati, M. 1999, ApJ, 522, 157

Roettiger, K., Burns, J.O., Clarke, D.A., & Christiansen, W.A. 1993, BAAS, 25, 1444

Ross, R.R. & Fabian, A.C. 2005, MNRAS, 358, 211

Sadler, E.M., Jackson, C.A., Cannon, R.D., et al. 2002, MNRAS, 329, 227

Schoenmakers, A.P., de Bruyn, A.G., Rötgering, H.J.A., & van der Laan, H. 1999, A&A, 341, 44

Schoenmakers, A.P., de Bruyn, A.G., Rötgering, H.J.A., van der Lann, H., & Kaiser, C.R. 2000, MNRAS, 315, 371

Setti, G. & Woltjer, L. 1989, A&A, 224, L21

Silverman, J.D., Green, P.J., Barkhouse, W.A., et al. 2008, ApJ, 679, 118

Smolčić, V. 2009, ApJ, 699, L43

Smolčić, V., Zamorani, G., Schinnerer, E., et al. 2009, ApJ, 696, 24

Sołtan, A. 1982, MNRAS, 200, 115

Spergel, D.N., Bean, R., Doré, O., et al. 2007, ApJS, 170, 377

Sreekumar, P., Bertsch, D.L., Dingus, B.L., et al. 1998, ApJ, 494, 523

Stawarz, Ł., Aharonian, F., Kataoka, J., et al. 2006, MNRAS, 370, 981

Stecker, F.W., Hunter, S.D., & Kniffen, D.A. 2008, Astropart. Phys., 29, 25

Strong, A.W., Moskalenko, I.V., & Reimer, O. 2004, ApJ, 613, 956

Tagliaferri, G., Foschini, L., Ghisellini, G., et al. 2008, ApJ, 679, 1029

Tavecchio, F., Maraschi, L., Ghisellini, G., et al. 2007, ApJ, 665, 980

Treister, E. & Urry, C.M. 2005, ApJ, 630, 115

Treister, E. & Urry, C.M. 2006, ApJ, 652, L79

Treister, E., Urry, C.M., & Virani, S. 2009, ApJ, 696, 110

Ueda, Y., Akiyama, M., Ohta, K., & Miyaji, T. 2003, ApJ, 598, 886

Urry, C.M. 1998, AdSpR, 21, 89

Urry, C.M. 1999, in ASP Conf Ser. 159, BL Lac Phenomenon, ed. L.O. Takalo & A. Sillanpää (Turku: ASP), 3

Urry, C.M. & Padovani, P. 1991 ApJ, 371, 60

Urry, C.M. & Padovani, P. 1995, PASP, 107, 803

Urry, C.M., Padovani, P., & Stickel, M. 1991, ApJ, 382, 501

Urry, C.M. & Shafer, R.A. 1984, ApJ, 280, 569

Vecchi, A., Molendi, S., Guainazzi, M., Fiore, F. & Parmar, A. 1999, A&A, 349, L73

Venturi, T., Dallacasa, D., & Stefanachi, F. 2004, A&A, 422, 515

Vercellone, S., Donnarumma, I., Bulgarelli, A., et al. 2009, in AIP Conf. Proc. Vol. 1112, Science With the New Generation of High Energy Gamma-ray Experiments, ed. D. Bastieri & R. Rando (Abano Terme:AIP), 121

Watanabe, K., Hartmann, D.H., Leising, M.D., & The, L.-S. 1999, ApJ, 516, 285

Watanabe, S., Sato, R., Takahashi, T., et al. 2009, ApJ, 694, 294

Weidenspointner, G., Varendorff, M., Kappadath, S.C., et al. 2000, in AIP Conf. Proc. Vol. 510, The Fifth Compton Symposium, ed. M.L. McConnell & J.M. Ryan (Portsmouth, NH: AIP), 467

Willott, C.J., Rawlings, S., Blundell, K.M., Lacy, M. & Eales, S.A. 2001, MNRAS, 322, 536

Worsley, M., Fabian, A.C., Barcons, X., et al. 2004, MNRAS, 352, L28

Worsley, M., Fabian, A.C., Bauer, F.E., et al. 2005, MNRAS, 357, 1281

Yencho, B., Barger, A.J., Trouille, L., & Winter, L.M. 2009, ApJ, 698, 380

CHAPTER III

THE EVOLUTION AND EDDINGTON RATIO DISTRIBUTION OF COMPTON THICK AGN

3.1 Introduction

It is thought that all forms of active galactic nuclei (AGN) are variations of the same phenomenon, namely accreting supermassive black holes (Rees, 1984). The most basic observational description of AGN is their bolometric luminosity, L_{bol}, and the obscuring column density, $N_{\rm H}$, through which they are observed. AGN are known to radiate at luminosities $L_{bol} \approx 10^{40}$–10^{48} erg s^{-1}, but this is more physically described by the Eddington ratio, defined as L_{bol}/L_{Edd}, where $L_{Edd} \equiv 4\pi G M_{\bullet} m_p c/\sigma_T$ is the Eddington luminosity of a black hole with mass $M_{\bullet}$. Observed Eddington ratios range roughly ten orders of magnitude with a maximum of $\sim$1 (Cao & Xu, 2007). There is a similarly wide range of observed column densities ($20 \leq \log N_{\rm H} \lesssim 25$; e.g., Tueller et al., 2008).

The most widely accepted theory to explain the observed range of obscuration is known as the unified model and claims that the obscuration of an AGN is dependent solely on the orientation of the AGN with respect to the line of sight to the observer (e.g., Antonucci, 1993). However, there is evidence that suggests that Compton thick (CT) obscuration, when $\log N_{\rm H} \gtrsim 24$, is linked to an evolutionary phase during which the black hole and the host stellar spheroid accrete rapidly (e.g., Fabian 1999; Page et al., 2004; Rigopoulou et al., 2009). As the black hole grows, the outflow from the black hole strengthens and ejects the obscuring material, revealing an unobscured quasar. This outflow also halts the growth of the host spheroid causing the observed proportionality between black hole mass and host spheroid mass (e.g., Crenshaw et al., 2003; Page et al., 2004; Alexander et al., 2010). Galaxy merger simulations show that mergers between gas rich galaxies will cause gas to flow into the nuclear region, igniting a nuclear starburst and highly obscured, high Eddington ratio

quasar activity (e.g., Hopkins et al. 2006). Fabian et al. (2009) also show that if an AGN is accreting at close to Eddington, radiation pressure on dust will blow out any column density with $\log N_{\rm H} \lesssim 24$. Therefore, if an AGN is obscured and has a high Eddington ratio, it must be CT. Observational evidence also supports this evolutionary scenario. Page et al. (2004) found that star formation in the hosts of unobscured quasars has already peaked, whereas the hosts of obscured quasars are still undergoing massive amounts of star formation indicating that their galactic spheroids are still forming. Treister et al. (2009a) found that the space density of luminous CT AGN candidates evolves strongly at $z = 1.5$–2.5, so that the CT quasar population seems to peak at a slightly higher redshift than the population of unobscured quasars. This evolutionary theory is difficult to observationally test since the high levels of obscuration found in CT AGN make them nearly invisible below 10 keV in their rest-frame.

If being CT is an early evolutionary phase of powerful quasars, CT AGN should be very rare at $z \sim 0$; however, *Swift*/BAT and *INTEGRAL* have detected several CT AGN at $z < 0.025$ (Tueller et al., 2008; Malizia et al., 2010). According to black hole masses and X-ray luminosities reported by Gültekin et al. (2009), the two brightest CT AGN, the Circinus Galaxy and NGC 4945, have $\log \lambda = -2.0$ and $\log \lambda = -5.6$, respectively, where $\lambda \equiv L_{bol}/L_{Edd}$. Therefore the scenario where CT AGN are high Eddington ratio quasars does not completely describe the entire CT AGN population.

As the majority of the cosmic X-ray background (XRB) $\lesssim$ 10 keV has been resolved into AGN by deep observations by *ROSAT*, *Chandra*, and XMM-*Newton* (see Brandt & Hasinger, 2005), the XRB provides a complete census of AGN. Due to the observational constraints of highly obscured sources, CT AGN are difficult to study even in the local universe; thus, historically CT AGN have been invoked to augment the observed AGN population in population synthesis models to make these models properly fit the observed, but not resolved, peak of the XRB around 30 keV. As there is a dearth of observational information about CT AGN, previous population synthesis models have treated CT AGN as a simple extension of type 2 AGN (e.g., Ueda et al., 2003; Treister & Urry, 2005; Ballantyne et al., 2006; Gilli et al., 2007) however, if CT AGN are part of an evolutionary sequence,

then they would not evolve in the same manner as the less extremely obscured type 2 AGN. Indeed, fitting the XRB in that manner seems to over-predict the local observed space density of CT AGN (see Treister et al., 2009a).

In this chapter, the contributions of AGN with various Eddington ratios to the XRB are computed and CT AGN are modeled using a physically motivated Eddington ratio distribution. I then compare the model predictions with observed cumulative and decadal space densities and the *Swift*/BAT CT AGN $\log N$–$\log S$ relation. It is found that CT AGN are a composite population of AGN accreting at both very high Eddington ratios and very low Eddington ratios. When necessary, a ΛCDM cosmology is assumed with $h_0 = 0.7$, $\Omega_M = 0.3$, and $\Omega_\Lambda = 0.7$.

3.2 Calculations

3.2.1 Eddington Ratio Distribution

Following the method of Merloni (2010) and Merloni & Heinz (2008), with minor modifications described below, the Eddington ratio space density is calculated, $\Phi_\lambda\left(L_X, M_\bullet, z\right)$, in Mpc^{-3}, where L_X is the 2–10 keV luminosity. The bolometric correction from Marconi et al. (2004),

$$\log(L_{bol}/L_X) = 1.54 + 0.24\mathcal{L} + 0.012\mathcal{L}^2 - 0.0015\mathcal{L}^3, \tag{3.1}$$

where $\mathcal{L} = \log(L_{bol}/L_\odot) - 12$, is used to transform X-ray luminosities to bolometric luminosities. Marconi et al. (2004) derive this bolometric correction using an average intrinsic spectral energy distribution template for radio quiet AGN. The scatter in the bolometric correction is $\sim$0.1 dex, which is negligible in our analysis. The black hole mass function (BHMF) is derived from a Gaussian curve fit to the combined type 1 and type 2 AGN BHMF observed by Netzer (2009) at $z \sim 0.15$. As the Netzer (2009) BHMF is fractional, the Merloni (2010) and Merloni & Heinz (2008) method was modified to use only the space density from the Ueda et al. (2003) hard X-ray luminosity function (HXLF), instead of depending equally on the space density from the BHMF and the HXLF. Merloni & Heinz (2008) argue that black hole mergers will only have a perturbative effect on black hole growth as the uncertainties in the AGN bolometric luminosity function are larger than the

impact of black hole mergers on the local BHMF. Therefore, the evolution of the BHMF must satisfy the conservation equation (Small & Blandford, 1992):

$$\frac{\partial n_M(M_\bullet, t)}{\partial t} + \frac{\partial [n_M(M_\bullet, t)\langle \dot{M}(M_\bullet, t)\rangle]}{\partial M} = 0, \tag{3.2}$$

where n_M is the BHMF and $\langle \dot{M}(M_\bullet, t)\rangle$ is the average accretion rate at time t. Thus the BHMF is evolved by integrating this conservation equation forward and backward in time, using the observed BHMF at z 0.15 as the boundary condition. The critical Eddington ratio where the transition from radiatively efficient thin disk accretion to radiatively inefficient geometrically thick accretion is taken as $\log \lambda_{cr} = -2.0$ (Cao & Xu, 2007). For $\lambda > \lambda_{cr}$ the radiative efficiency is assumed to be $\epsilon_{rad} = 0.1$ and for $\lambda < \lambda_{cr}$, $\epsilon_{rad} = 0.1(\lambda/\lambda_{cr})^{1/2}$ (Merloni & Heinz, 2008).

3.2.2 Cosmic X-ray Background Model

The XRB model closely follows that described by Draper & Ballantyne (2009) with differences in the spectra of CT sources and low Eddington ratio sources, and $\Phi_\lambda(L_X, M, z)$ is input in place of a luminosity function. A torus reflection component, calculated using "reflion" (Ross & Fabian, 2005), is added to the CT AGN spectrum (cf., Gilli et al., 2007). For AGN with $\log \lambda < -2.0$, the reflection component is included only if the source is CT. In order to properly fit the XRB at higher energies, the power-law component of the $\log \lambda < -2.0$ spectrum is assumed to have a cut-off energy of 200 keV, otherwise a cut-off energy of 250 keV is used[1]. Most importantly, CT AGN are added at specific Eddington ratios which are chosen based on a physically motivated scenario instead of adjusting the normalization of the luminosity function to account for CT AGN as done with previous XRB models.

3.3 Results

In previous population synthesis models the number of CT AGN was assumed to be proportional to the number of type 2 AGN. In this original model I find 44% of all type 2 AGN

[1] If 250 keV is used as the cut-off energy for all sources the qualitative findings of this study do not change, but the fraction of CT AGN is reduced by ∼1%.

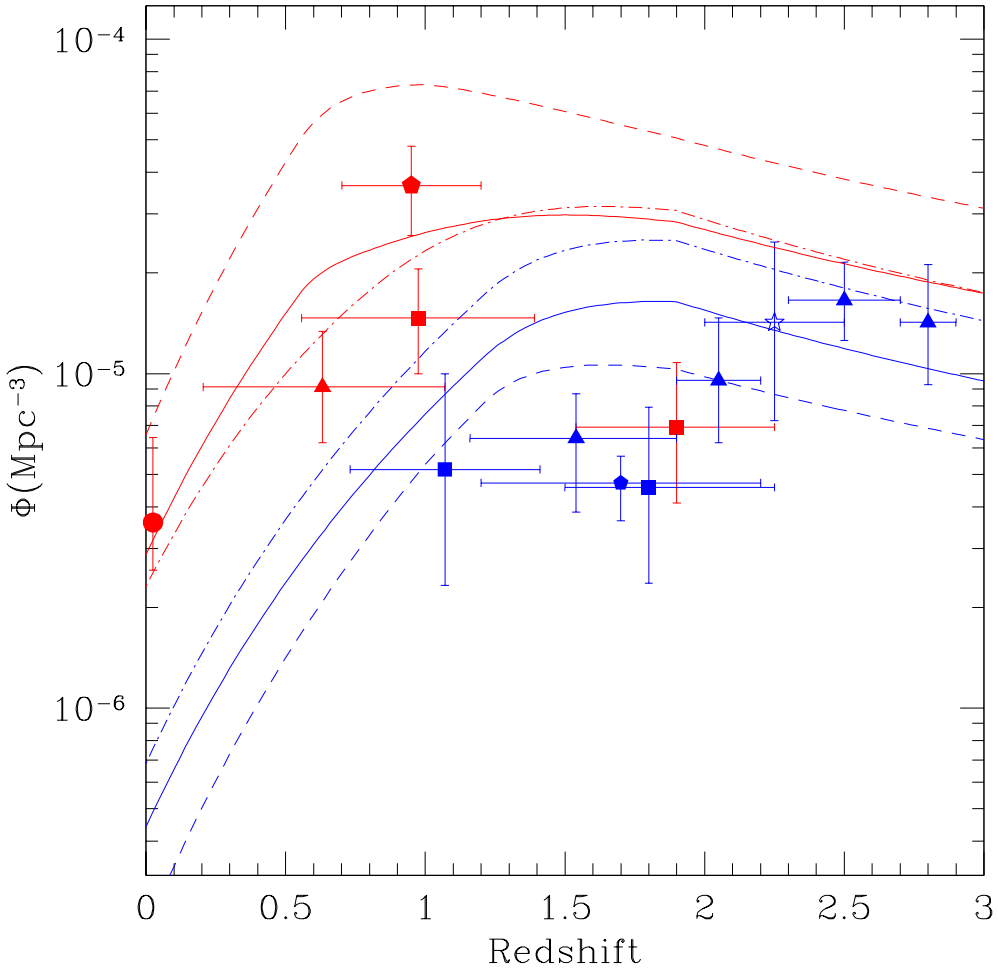

Figure 3.1: Cumulative CT AGN space density. Red points and lines denote CT AGN with $\log L_X > 43$ and blue points and lines denote CT AGN with $\log L_X > 44$. Solid lines show the composite model where CT AGN have either $\log \lambda < -2.0$ or $\log \lambda > -0.05$. The dashed lines show the original model where CT AGN are considered a simple extension of the Compton thin type 2 population. The dot-dashed lines show the scenario where all CT AGN have $\log \lambda > -0.05$. Data points are shown from several studies: triangles: Treister et al. (2009a); squares: Tozzi et al. (2006); stars: Alexander et al. (2008); pentagons: Fiore et al. (2009); circle: local *Swift*/BAT and INTEGRAL data point reported by Treister et al. (2009b) adjusted to reflect the flux-luminosity relation for CT AGN described by Rigby et al. (2009).

are CT, where the normalization is fixed by fitting the peak of the XRB ($EF_E \approx 44.2$ keV cm^{-2} s^{-1} str^{-1} at 30 keV). In figure 3.1 the cumulative space density is shown for CT AGN with $\log L_X > 43$ (red) and $\log L_X > 44$ (blue). The dashed line shows the predictions of the original model. The red circle shows the local *Swift*/BAT and INTEGRAL data originally reported by Treister et al. (2009b) and here has been corrected to account for the flux-luminosity relation for CT AGN described by Rigby et al. (2009). The original model significantly over-predicts the observed space density of CT AGN with $\log L_X > 43$ at all redshifts. The original model also over-predicts the observed space density of CT AGN with $\log L_X > 44$ at $1.5 < z < 2$, while under-predicting the $z > 2.5$ data points. The decadal CT AGN space density is shown in figure 3.2 where data and predictions for CT AGN with $\log L_X = 44$–45 are colored blue, and data and predictions for CT AGN with $\log L_X = 45$–46 are colored green. The dashed lines again show the predictions of the original model. This model agrees fairly well with the $\log L_X = 44$–45 and $\log L_X = 45$–46 data at low redshift, but under-predicts the density of high redshift sources. As seen in figure 3.3, the original model agrees fairly well with the *Swift*/BAT $\log N$–$\log S$ relation, where red lines denote the transmission dominated CT AGN number counts and dashed lines denote the original model. This model over-predicts the BAT number counts at the lowest flux levels but is in decent agreement with observations at the higher flux levels. A χ^2 test was performed using the cumulative CT AGN space density data points, the decadal CT AGN space density data points which are not lower limits, and the BAT CT AGN number counts data points, giving 32 degrees of freedom. The original model was found to have a reduced χ^2 of $\chi^2_{red} = 15$.

I then attempted to model the CT population as only including sources with $\log \lambda > -0.05$ independent of the fraction of type 2 AGN at any L_X and z. In order to match the peak of the XRB, ∼91% of these AGN at any time must be CT. As seen in figures 3.1, 3.2, and 3.3, where the predictions from this model are shown as the dot-dashed lines, this scenario under-predicted the observed local CT AGN space densities, over-predicted the *Swift*/BAT $\log N$–$\log S$ relation by a factor of 2.0 to 3.5, and resulted in $\chi^2_{red} = 25$. Thus, the CT population cannot be modeled as only including sources with very high Eddington

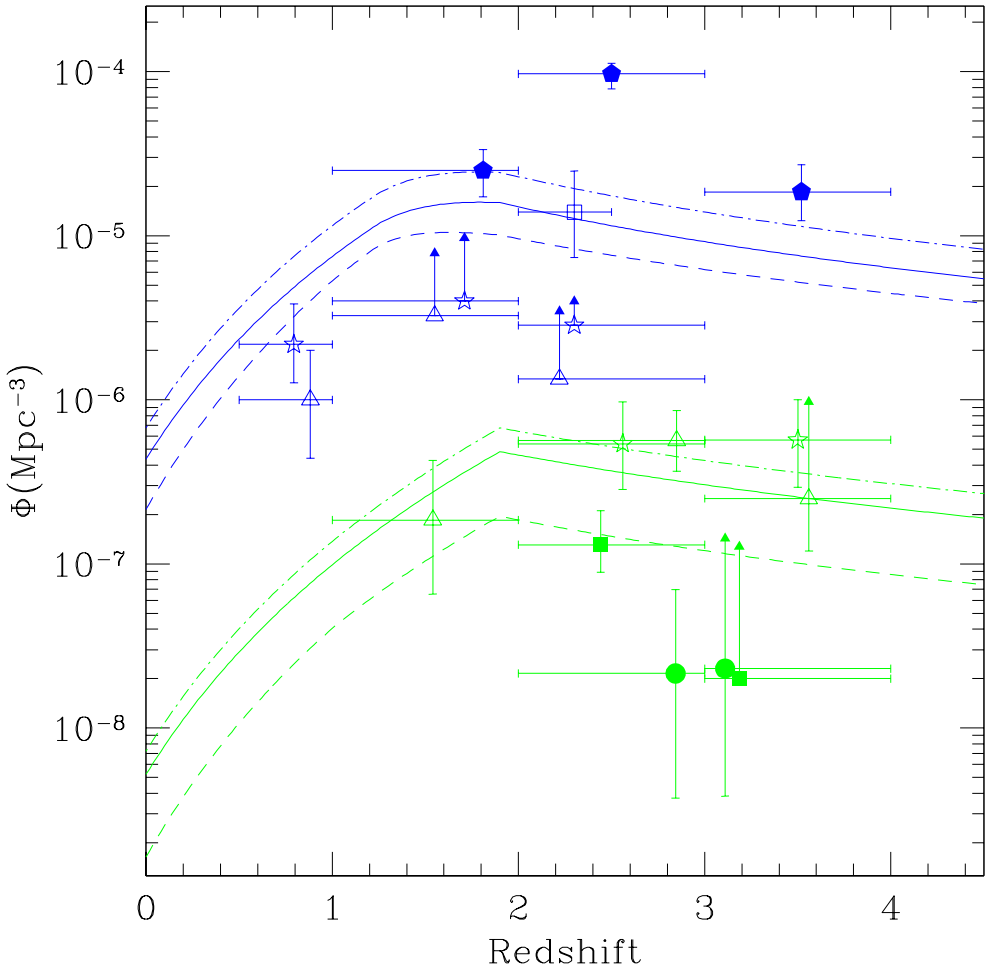

Figure 3.2: Decadal CT AGN space density. Blue points and lines denote CT AGN with $\log L_X = 44$–45 and green points and lines denote CT AGN with $\log L_X = 45$–46. Lines are the same style as in figure 3.1. Data points are shown from several studies: filled squares: Yan et al. (2007); circles: Martínez-Sansigre et al. (2006); stars: Polletta et al. (2006); triangles: Fiore et al. (2009); pentagons: Fiore et al. (2008); open squares: Alexander et al. (2008).

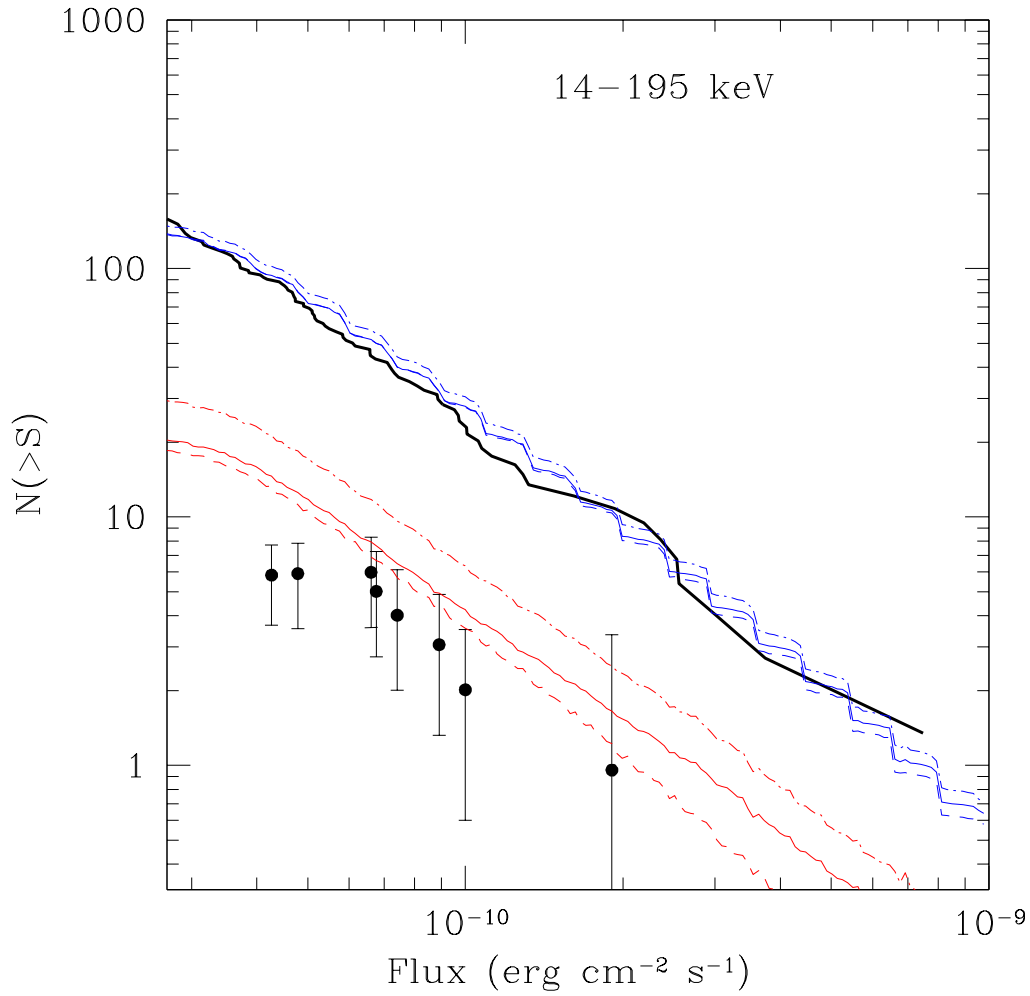

Figure 3.3: BAT number counts. Blue lines signify total AGN number counts and red lines signify transmission dominated CT AGN number counts. Colored lines are the same style as in figure 3.1. The black line shows the total AGN $\log N$–$\log S$ relation from Tueller et al. (2008) and the black data points show the CT $\log N$–$\log S$ data points from Treister et al. (2009b).

ratios.

The scenario where all CT AGN have $\log\lambda > -0.05$ failed to agree with local observations, and as local AGN are known to have low Eddington ratios (Ho, 2008), low Eddington ratio sources were then added to the CT AGN population model. In order to fit the peak of the XRB, while not overestimating the XRB in the 100–200 keV range, this composite model predicts ∼60% of AGN with $\log\lambda < -2.0$ and ∼86% of AGN with $\log\lambda > -0.05$, at any time and independent of the fraction of type 2 AGN, are CT. The XRB fit found using this composite model is shown in figure 3.4 with the contribution made by AGN accreting at different Eddington ratios plotted as separate lines. In this model the XRB is still dominated by obscured sources accreting at moderate Eddington ratios, i.e. type 2 Seyferts. The composite model predictions are shown as the colored solid lines in figures 3.1, 3.2, and 3.3. This model is in fairly good agreement with the observed space densities for CT AGN with $\log L_X > 43$ and $\log L_X > 44$, except for over-predicting the observed space density of CT AGN with $\log L_X > 44$ at $1.5 < z < 2$. The composite model predictions match the observed cumulative space densities better than the original model predictions. At $z \lesssim 1$, the composite model slightly over-predicts the space density of CT AGN with $\log L_X = 44$–45 and under-predicts the observed densities at $z \gtrsim 2.5$. For CT AGN with $\log L_X = 45$–46, this scenario agrees fairly well with observations. In general, the composite model is a better fit to the high luminosity, high redshift data than the original model. This scenario does over-predict the BAT number counts at the lowest flux levels, but is in decent agreement with observations at the higher flux levels. I find $\chi^2_{red} = 9.8$, indicating that the composite model is in better overall agreement with the observed CT AGN space densities and the *Swift*/BAT $\log N$–$\log S$ relation when compared to the original model, or one where all CT AGN have $\log\lambda > -0.05$.

Other models were investigated in which the CT population was assumed to be accreting at only low or moderate Eddington ratios. When the CT population was assumed to all be accreting at $\log\lambda < -2.0$ the model under-predicted the observed high luminosity CT space densities and slightly under-predicted the *Swift*/BAT $\log N$–$\log S$ relation. When $-2.0 < \log\lambda < -0.5$ accretion was assumed for the CT population the model over-predicted

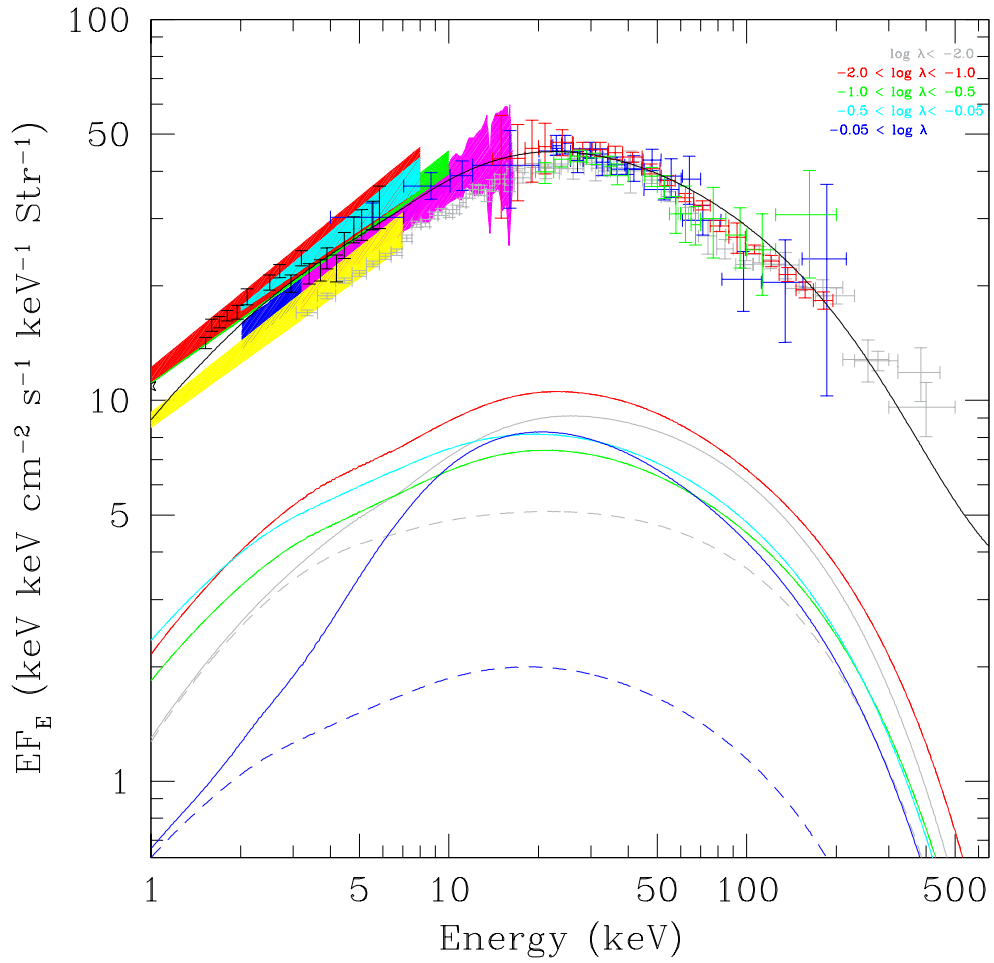

Figure 3.4: XRB fit using the composite model showing contributions of AGN accreting at different Eddington ratios. The solid black line shows the combined contribution of non-blazar AGN and blazars to the XRB. Colored lines show the contribution of AGN accreting at the color designated Eddington ratio, where dashed lines refer only to the Compton thin contribution and solid lines show the combined contribution of Compton thin AGN and CT AGN. Measurements from various instruments are shown as colored areas and data points; blue: *ASCA* GIS (Kushino et al., 2002); magenta: *Rossi X-ray Timing Explorer* (*RXTE*; Revnivtsev et al., 2003); green: XMM-*Newton* (Lumb et al., 2002); red: *BeppoSAX* (Vecchi et al., 1999); yellow: *ASCA SIS* (Gendreau et al., 1995); cyan: XMM-*Newton* (De Luca & Molendi, 2004); grey data: *HEAO*-1 (Gruber et al., 1999); blue data: *INTEGRAL* (Churazov et al., 2007); red data: *Swift*/BAT (Ajello et al., 2008); black data: *Swift*/XRT (Moretti et al., 2009); green data: *INTEGRAL* (Türler et al., 2010).

the observed local space density by a factor of 3.2 and significantly over-predicted the *Swift*/BAT $\log N$–$\log S$ relation. In conclusion, it is necessary to include both sources with $\log lambda < -2.0$ and $\log \lambda > -0.05$ to model the CT AGN population.

3.4 Discussion and Summary

It is found that current data suggests that the majority of AGN accreting at close to the Eddington limit are CT, in agreement with galaxy merger simulations (e.g., Hopkins et al., 2006) that show that mergers funnel gas into the central regions of galaxies igniting both starbursts and high Eddington ratio accretion onto the central black hole. These AGN are able to accrete rapidly because of a large abundance of gas and dust in the central region of the host bulge. This abundance of gas and dust naturally leads to a very high obscuring column density (Fabian, 1999). Furthermore, radiation pressure from a rapidly accreting AGN will blow out any dusty gas with $\log N_{\rm H} \lesssim 24$ (Fabian et al., 2009). Thus, in accordance with these findings, the vast majority of rapidly accreting, obscured AGN must be CT.

A new result is that the CT AGN population, in addition to including sources with $\log \lambda > -0.05$, also includes sources with $\log \lambda \lesssim -2.0$. While Ho (2008) explains that most observed low Eddington ratio sources tend to be unobscured, Terashima & Wilson (2003) find evidence for a population of highly obscured low Eddington ratio AGN. Indeed Malizia et al. (2010) find an obscuration-luminosity relation in their sample of *INTEGRAL* sources which claims that lower luminosity sources tend to be more obscured. As these observed lower luminosity sources are local, these AGN are likely to have low Eddington ratios. Since low Eddington ratio AGN are only weakly accreting, they will have very little effect on their environment. Therefore molecular clouds would be able to come deep into the core of the bulge without being affected. Indeed Terashima & Wilson (2003) find that the highly obscured low Eddington ratio sources in their sample might exhibit variable obscuration, as would be expected if the obscuration were due to molecular clouds near the black hole. Several studies have been conducted on so called "changing-look" AGN (see Bianchi et al., 2005 and references therein), which are AGN whose spectrum changes from

Compton thin to reflection dominated on the time scale of years. It is thought that the changes in the spectrum of these local, low luminosity AGN is due to either the nucleus being obstructed by a cloud with a CT column density or the nucleus switching off, so that the reflection dominated state is actually the echo of a previous accretion episode. Bianchi et al. (2005) find that it is most likely that the four AGN in their sample are in CT states. In a study of 82 low-ionization nuclear emission-line regions (LINERs), González-Martín et al. (2009) find about half of the LINERs in their sample appear to be CT and that there is a higher percentage of CT LINERs than CT Seyferts. The average Eddington ratio of the CT LINERs in the sample used by González-Martín et al. (2009) is $\log \lambda$ = -4.7. This finding is consistent with the composite model for CT AGN discussed here which finds that $\sim$60% of AGN with $\log \lambda < -2.0$ are CT.

It is clear that previous attempts to model the elusive CT AGN population as an extension of the Compton thin type 2 population fail to explain the observed CT AGN space density and $\log N$–$\log S$ relation. Treister et al. (2009b) suggest that CT AGN only contribute $\sim$10% of the XRB and that the normalization of the XRB is over-estimated by population synthesis models which predict a large population of CT AGN. However, changing the normalization of the XRB does not account for the strong evolution of CT AGN at z = 1.5–2.5 found by Treister et al. (2009a). Here it is assumed that CT AGN contribute $\sim$20% of the XRB based on the findings of Draper & Ballantyne (2009), but the composite model presented here does account for the strong evolution of CT AGN at high redshift while not overestimating the local CT AGN space density. Additionally, models which include CT sources with $-2.0 < \log \lambda < -0.5$ over-predict locally observed CT AGN space density. Models which only include CT sources with $\log \lambda < -2.0$ under-predict the density of high luminosity CT sources. If CT sources are assumed to only have $\log \lambda > -0.5$, the model over-predicts the observed $\log N$–$\log S$ relation. While observational evidence suggests that it is possible for CT AGN to accrete at $-2.0 < \log \lambda < -0.5$ (e.g., Mrk 3 Collins et al., 2009), this study shows that distribution of Eddington ratios of Compton thick AGN should have a minimum in the region $\log \lambda$ = -2.0– -0.5. A composite model, where the CT AGN population includes both sources accreting at close to Eddington and

sources accreting at <1% of Eddington, best explains observations.

As CT AGN are rare and difficult to observe due to high obscuration, it is difficult to use observations to directly decipher the physical phenomenon which gives rise to the extreme levels of obscuration found in CT AGN (e.g., Triester et al., 2009b; Rigby et al., 2009). Thus physical models of CT AGN must use indirect observational constraints, like observed space densities and number counts, to uncover the nature of the extreme obscuration of these sources. This chapter presents a model which constrains the physical parameter of the Eddington ratios of CT AGN to $\gtrsim$90% and $\lesssim$1%. Future studies will explore if there is a connection between these rapidly accreting CT AGN and the newly discovered class of highly obscured, geometrically buried AGN (e.g., Ueda et al., 2007; Imanishi, 2009; Brightman & Ueda, 2012). In the future the understanding of CT AGN will also be expanded through IR and sub-mm studies of the reprocessed radiation from CT AGN and very hard X-ray imaging with missions like *NuSTAR*.

3.5 References

Ajello, M., Greiner, J., Sato, G., et al. 2008, ApJ, 689, 666

Alexander, D.M., Chary, R.-R., Pope, A., et al. 2008, ApJ, 687, 835

Alexander, D.M., Swinbank, A.M., Smail, I., McDermid, R., & Nesvadba, N.P.H. 2010, MNRAS, 402, 2211

Antonucci, R., 1993, ARA&A, 31, 473

Ballantyne, D.R., Everett, J.E., & Murray, N. 2006, ApJ, 639, 740

Bianchi, S., Guainazzi, M., Matt, G., et al. 2005, A&A, 442, 185

Brandt, W.N. & Hasinger, G. 2005, ARA&A, 43, 827

Brightman, M. & Ueda, Y. 2012, MNRAS, 423, 702

Cao, Xinwu & Xu, Y.-D. 2007, MNRAS, 377, 425

Churazov, E., Sunyaev, R., Revnivtsev, M., et al. 2007, A&A, 467, 529

Collins, N.R., Kraemer, S.B., Crenshaw, D.M., Bruhweiler, F.C., & Meléndez, M. 2009, ApJ, 694, 765

Crenshaw, D.M., Kraemer, S.B., & George, I.M. 2003, ARA&A, 41, 117

De Luca, A. & Molendi, S. 2004, A&A, 419, 837

Draper, A.R. & Ballantyne, D.R. 2009, ApJ, 707, 778

Fabian, A.C. 1999, MNRAS, 308, L39

Fabian, A.C., Vasudevan, R.V., Mushotzky, R.F., Winter, L.M., & Reynolds, C.S. 2009, MNRAS, 385, L43

Fiore, F., Grazian, A., Santini, P., et al. 2008, ApJ, 672, 94

Fiore, F., Puccetti, S., Brusa, M., et al. 2009, ApJ, 693, 447

Gendreau, K.C., Mushotzky, R., Fabian, A.C., et al. 2007, PASJ, 47, L5

Gilli, R., Comastri, A., & Hasinger, G. 2007, A&A, 463, 79

González-Martín, O., Masegosa, J., Márquez, I., & Guainazzi, M. 2009, ApJ, 704, 1570

Gruber, D.E., Matteson, J.L., Peterson, L.E., & Jung, G.V. 1999, ApJ, 520, 124

Gültekin, K., Cackett, E.M., Miller, J.M., et al. 2009, ApJ, 706, 404

Ho, L., 2008, ARA&A, 46, 475

Hopkins, P.F., Hernquist, L., Cox, T.J., et al. 2006, APJS, 163, 1

Imanishi, M. 2009, ApJ, 694, 751

Kushino, A., Ishisaki, Y., Morita, U., et al. 2002, PASJ, 54, 327

Lumb, D.H., Warwick, R.S., Page, M., & De Luca, A. 2002, A&A, 389, 93

Malizia, A., Stephen, J.B., Bassani, L., et al. 2009, in Extreme Sky 2009, ed. B. McBreen, F. Labrun, & P. Giommi, (Otranto: INAF/IASF), 12, http://pos.sissa.it/cgi-bin/reader/conf.cgi?confid=96

Marconi, A., Risaliti, G., Gilli, R., et al. 2004, MNRAS, 351, 169

Martínez-Sansigre, A., Rawlings, S., Lacy, M., et al. 2006, MNRAS370, 1479

Merloni, A. 2010 in ASP Conf. Proc. Vol. 427, Accretion and Ejection in AGN: A Global View, ed. L. Maraschi, G. Ghisellini, R. Della Ceca& F. Tavecchio (Como:ASP), 11

Merloni, A. & Heinz, S. 2008, MNRAS, 388, 1011

Moretti, A., Pagani, C., Cusumano, G., et al. 2009, A&A, 493, 501

Netzer, H. 2009, ApJ, 695, 793

Page, M.J., Stevens, J.A., Ivison, R.J., & Carrera, F.J. 2004, ApJ, 611, L85

Polletta, M.d.C, Wilkes, B.J., Siana, B., et al. 2006, ApJ, 642, 673

Rees, M.J. 1984, ARA&A, 22, 471

Revnivtsev, M., Gilfanov, M., Sunyaev, R., Jahoda, K., & Markwardt, C. 2003, A&A, 411, 329

Rigby, J., Diamond-Stanic, A.M., & Aniano, G. 2009, ApJ, 700, 1878

Rigopoulou, D., Mainieri, V., Almaini, O., et al. 2009, MNRAS, 400, 1199

Ross, R.R. & Fabian, A.C. 2005, MNRAS, 358, 211

Small, T.A. & Blandford, R.D. 1992, MNRAS, 259, 725

Terashima, Y. & Wilson, A.S. 2003, ApJ, 583, 145

Tozzi, P., Gilli, R., Mainieri, V., et al. 2006, A&A, 451, 457

Treister, E., Cardamone, C.N., Schawinski, K., et al. 2009a, ApJ, 706, 535

Treister, E., Urry, C.M., & Virani, S. 2009b, ApJ, 696, 110

Treister, E. & Urry, C.M. 2005, ApJ, 630, 115

Tueller, J., Mushotzky, R.F., Barthelmy, S., et al. 2008, ApJ, 681, 113

Türler, M., Chernyakova, M., Courvoisier, T.J.-L., et al. 2010, A&A, 512, 49

Ueda, Y., Akiyama, M., Ohta, K., & Miyaji, T. 2003, ApJ, 598, 886

Ueda, Y., Eguchi, S., Terashima, Y., et al. 2007, ApJ, 664, L79

Vecchi, A., Molendi, S., Guainazzi, M., Fiore, F., & Parmar, A. 1999, A&A, 349, L73

Yan, L., Sajina, A., Fadda, D., et al. 2007, ApJ, 658, 778

CHAPTER IV

PROPERTIES AND EXPECTED NUMBER COUNTS OF ACTIVE GALACTIC NUCLEI AND THEIR HOSTS IN THE FAR INFRARED

4.1 Introduction

Thanks to the *Spitzer Space Telescope* and its imaging and spectroscopic instrument suite (Werner et al., 2004), it has recently been found that active galactic nuclei (AGN) can dominate the near and mid-infrared luminosity and make a significant contribution to the 8-1000 μm luminosity, L_{IR}, of AGN host galaxies (Houck et al., 2005; Yan et al., 2005; Weedman et al., 2006; Soifer et al., 2008, and references therein). Specifically, a large fraction of ultra-luminous infrared galaxies ($L_{IR} > 10^{12}$ L$_\odot$; ULIRGs) and luminous infrared galaxies ($L_{IR} > 10^{11}$ L$_\odot$; LIRGs) appear to host luminous AGN (e.g., Dey et al., 2008; Donley et al., 2008; Fiore et al., 2008, 2009; Yuan et al., 2010). In the far infrared (FIR) it is more difficult to determine the AGN contribution to the combined AGN and host observed flux as little is known about the AGN spectral energy distribution (SED) at these wavelengths. For the purposes of this study we define the FIR as 70-1000 μm.

The next several years will see a huge growth in high quality FIR and submillimeter spectral data due to telescopes like the *Herschel Space Observatory* and the Atacama Large Millimeter/submillimeter Array (ALMA). *Herschel*, launched in May 2009, offers unprecedented coverage of the FIR and submillimeter spectral regions (Pilbratt et al., 2010). *Herschel* carries two imaging photometers, the Photodetector Array Camera and Spectrometer (PACS) which has photometric bands at 70, 100, and 160 μm (Poglitsch et al., 2010) and the Spectral and Photometric Imaging Receiver (SPIRE) which has photometric bands at 250, 350, and 500 μm (Griffin et al., 2010). As one of the primary science goals of

Herschel is to study the evolution of galaxies (Pilbratt et al., 2010), three wide-area surveys of various depths are being undertaken. The PACS evolutionary probe (PEP) will cover ∼3 deg^2 and will observe some fields, such as the GOODS fields, down to the depth of the 100 and 160 μm confusion limits of a few mJy (Berta et al., 2010). The *Herschel* Multi-tiered Extragalactic Survey (HerMES) will observe ∼70 deg^2 with SPIRE, reaching 5σ depths of a couple mJy at 250 μm in some fields (Oliver et al., 2010; Roseboom et al., 2010). Observing ∼510 deg^2 with both PACS and SPIRE, the *Herschel* Atlas (H-ATLAS) survey is the largest open time survey being undertaken by *Herschel* (Eales et al., 2010). H-ATLAS will reach 5σ depths of 67 mJy at 100 μm and 53 mJy at 500 μm (Eales et al., 2010; Ibar et al., 2010; Pascale et al., 2010). The ground-based instrument Submillimeter Common-User Bolometer Array 2 (SCUBA-2) will operate at 450 and 850 μm and will offer an intermediate sensitivity and mapping speed between those of *Herschel* and ALMA (Holland et al., 2006). Also ground-based, ALMA is an imaging and spectroscopic instrument operating in the millimeter and submillimeter regime. The ALMA primer[1] notes that at full science operations, starting in late 2012, ALMA will have a 450 μm band (Band 9) with a continuum sensitivity of 0.69 mJy and a 350 μm band (Band 10) with a sensitivity of 1.1 mJy, along with bands at longer wavelengths[2]. The 450 μm band will be available for early science operations in mid 2011, albeit at reduced sensitivity. *Herschel*'s observing capabilities, and in particular the SPIRE deep and wide surveys at 250, 350 and 500 μm, will provide promising candidate targets for ALMA early science operations.

It is expected that AGN and their hosts will be readily detected in the FIR by *Herschel*. Hatziminaoglou et al. (2010) found that a third of their AGN sample had *Herschel* 5σ detections at 250 μm with $f_{250\mu m} > 12.8$ mJy, where $f_{250\mu m}$ is the 250 μm flux. The FIR flux from AGN and their hosts will be due to dust heated by a combination of AGN radiation and star formation. Observations suggest that only 3–9% of submillimeter galaxies are dominated by AGN emission in the submillimeter (Laird et al., 2010). However, a large portion of galaxies, nearly 50% of the galaxies in the infrared selected sample of Yuan

[1]available at http://www.almaobservatory.org/images/stories/publications

[2]Sensitivities are for an integration time of 60 seconds and a spectral resolution of 1.0 km/s.

et al. (2010), show strong infrared emission from both star formation and AGN activity. Consequently, the AGN contribution to the FIR emission of AGN hosts must be considered in order to not over-estimate star formation rates in AGN hosts.

As the FIR SED of AGN is expected to generally be dominated by star formation (e.g. Hatziminaoglou et al., 2010; Lutz et al., 2010), FIR observations will inform investigations of the star formation history of AGN hosts. By comparing the star formation history of AGN hosts and normal galaxies, the role of AGN in galaxy evolution will be constrained. Understanding AGN host star formation history is therefore an important tool in determining what processes trigger AGN. For example, Sanders et al. (1988) proposed that galaxy mergers trigger both intense starbursts and quasar activity. Recent observations and simulations support this model (Page et al., 2004; Hopkins et al., 2006; Rigopoulou et al., 2009; Draper & Ballantyne, 2010; Kelly et al., 2010). Page et al. (2004) found that type 2 AGN tend to have higher SFRs than type 1 AGN. Draper & Ballantyne (2010) found that a significant fraction of Compton thick (CT) AGN, AGN with an X-ray obscuring column density $N_H > 10^{24}$ cm^{-2}, are quasars which are accreting very rapidly, as predicted by simulations by Hopkins et al. (2006) and others. However, it appears that this model may only be applicable for the most powerful AGN and that Seyfert strength AGN may evolve more secularly (Ballantyne et al., 2006a; Hasinger, 2008; Lutz et al., 2010; Narayanan et al., 2010). In order to determine the applicability of the merger driven evolution and secular evolution models, the star formation history of AGN hosts must be accurately determined. This requires a robust method of identifying AGN hosts and the AGN contribution to the FIR emission.

FIR emission from AGN comes from the "torus" of dusty gas, which, according to the unified scheme, surrounds the central engine of all AGN (e.g., Antonucci, 1993). This dusty torus will absorb higher energy emission from the central engine of the AGN and re-radiate this energy in the infrared. The temperature of the dust, and therefore the peak wavelength of the infrared radiation, is dependent on the density of the obscuring gas and the distance of the obscuring gas from the central engine (e.g., Ballantyne et al., 2006b), among other parameters like the geometry of the obscuring torus (e.g., Hatziminaoglou et al., 2009). It

appears that the infrared SED of most X-ray selected AGN peaks in the mid-infrared (e.g., Elvis et al., 1994; Netzer et al., 2007). However, due to the large amount of dust required to reach CT levels of obscuration, it is expected that the clouds of dusty gas in CT AGN will have a greater spatial extent than in less obscured AGN. Therefore, CT AGN will have a significant reservoir of dusty gas which is cooler than most AGN-related dust clouds. This cooler dust component will cause CT AGN to be brighter in the FIR than unobscured AGN.

Indeed, studies suggest that bright galaxies detected in the FIR host a large number of heavily obscured, $N_H > 10^{23}$ cm^{-2}, and possibly CT AGN (e.g., Alexander et al., 2005b,a; Bongiovanni et al., 2010; Wilman et al., 2010). Mullaney et al. (2010) found that 45–75% of the 1 Ms CDF-S X-ray sources will be detected by *Herschel* at 100 μm and that deep infrared observations with *Herschel* will allow for a significant fraction of the CT AGN population to be identified. Also, since X-ray selection misses nearly half of all infrared identified AGN (Fu et al., 2010) it is expected that FIR telescopes like *Herschel* and ALMA will detect highly obscured AGN that are missed by the deep X-ray surveys. However, there is an open debate as to how many of these infrared AGN reach CT levels of obscuration. Fiore et al. (2009) find that up to 90% of sources with $f_{24} > 550$ μJy and $f_{24}/f_R > 1000$ are CT AGN, where f_{24} is the 24 μm flux and f_R is the R-band flux. Conversely, Georgantopolous et al. (2010) find a more moderate fraction of CT AGN for this population. When looking at similar infrared excess sources, Georgakakis et al. (2010) found no strong evidence suggesting that these sources host AGN with CT levels of obscuration. Therefore further study of the infrared properties of AGN are important in determining exactly how many CT AGN are hidden within dusty luminous infrared galaxies.

This chapter gives predictions for FIR AGN number counts, contribution to the CIRB, and luminosity density using a population synthesis model informed by constraints from the cosmic X-ray background (XRB) and deep X-ray surveys, including the Eddington ratio dependent CT fraction, f_{CT}, of the composite model investigated by Draper & Ballantyne (2010). The effect of various AGN host star formation scenarios are also investigated. The calculation of the model SEDs is discussed in §4.2. Predictions for bare AGN are presented in §4.3 followed by predictions for various host star formation scenarios in §4.4. In §4.5

and §4.6 the results are discussed and summarized. A ΛCDM cosmology is assumed as necessary, with $h_0 = 0.7$, $\Omega_m = 0.3$, and $\Omega_\Lambda = 0.7$ (Hinshaw et al., 2009).

4.2 Calculation of AGN SEDs

As the goal of this study is to make predictions of the average FIR properties of AGN, SEDs are used which are representative of an ensemble of AGNs at a given 2–10 keV luminosity, L_X, and z, instead of using a SED template based on observations of a statistically small set of AGNs. Since AGN IR emission is primarily due to the obscuring gas and dust re-radiating absorbed X-ray emission, photoionization simulations allow for the computation of the IR emission of an average AGN with a given L_X and N_H. Also, this SED computation method provides an opportunity to explore the parameter space of obscuring gas location, density distribution, and dust content, which, upon comparison with observations, may offer constraints for these physical parameters.

Similarly to Ballantyne et al. (2006b), the IR AGN SEDs are calculated using the photoionization code Cloudy version C08.00 (Ferland et al., 1998). Cloudy includes the complicated physics of radiative transfer through dusty gas and uses a physical dust model which takes into account silicate and graphite grains along with polycyclic hydrocarbons (PAHs). This technique does necessitate a simplification of the IR emitting region, which might actually be quite complex (e.g., Hatziminaoglou et al., 2009; Hönig et al., 2010). However, since the purpose of this study is to describe average properties of AGN, and not to model individual objects, this technique is an appropriate method of SED calculation. This assumption will be tested by comparing the model SEDs against real data in §4.2.3.

4.2.1 Cloudy Model Setup

Each Cloudy model is setup such that a constant AGN spectrum, characterized by L_X, is incident upon a cloud with inner radius r from the continuum source. The inner radius r is set to 10 pc. Compton thin clouds are assigned a uniform hydrogen density $n_H = 10^4$ cm^{-3}, as is typical of molecular clouds. In order to prevent the dust mass from becoming too large, the Compton thick clouds are assigned $n_H = 10^6$ cm^{-3}. Molecular clouds of this density are not uncommon and have been observed in the Large Magellanic Cloud (Rubio

et al., 2009) and in the Orion Nebula (Persson et al., 2007). Simulations were also run with $r = 1$ pc and $n_H = 10^4$ cm^{-3} for both Compton thin and CT clouds to test the sensitivity of the results to these assumptions, which is discussed later.

The Cloudy model input files are similar to those used by Ballantyne et al. (2006b), with the following improvements. Instead of using a constant α_{OX} for all AGN, the Steffen et al. (2006) α_{OX}-L_{2keV} relation is used here to determine α_{OX}. The most significant improvement made includes dividing the AGN population into Eddington ratio bins, high ($L/L_{Edd} > 0.9$, where L is the bolometric luminosity found using the bolometric correction by Marconi et al. (2004) and L_{Edd} is the Eddington luminosity), moderate ($0.9 < L/L_{Edd} < 0.01$), and low ($0.1 < L/L_{Edd}$), as described by Draper & Ballantyne (2010). Both the composite and original models of Draper & Ballantyne (2010) are investigated. The f_{CT} of the composite model is Eddington ratio dependent and finds that ∼86% of AGN accreting at greater than 90% of their Eddington rate and ∼60% of AGN accreting at less than 1% of their Eddington rate are Compton thick. The original model assumes Compton thick AGN are a simple extension of the Compton thin type 2 population and that ∼44% of type 2 AGN are Compton thick. Since the covering factor is set assuming the unified scheme holds, the covering factors are Eddington ratio dependent since f_{CT} is Eddington ratio dependent. For Compton thick objects the covering factor is set as the Compton thick fraction, f_{CT}. For objects with $22 \leq \log N_H < 24$ the covering factor is set as $(1.0 - f_{CT})f_2$ where f_2 is the type 2 fraction and is calculated as discussed in §2.2 of Draper & Ballantyne (2009). The covering factor for objects with $20 \leq \log N_H < 22$ is set to $(1.0 - f_{CT})(1.0 - f_2)$. As the covering factor is dependent on the Eddington ratio and varies from $z = 0$ to 1, Cloudy models had to be calculated as a function of z and L/L_{Edd} for each L_X and N_H.

There is evidence that different levels of obscuration in quasars might be related by an evolutionary scenario instead of by orientation effects (e.g., Sanders et al., 1988; Page et al., 2004; Draper & Ballantyne, 2010; Donley et al., 2010), and thus the covering factor need not be related to f_{CT} or f_2. Ballantyne et al. (2006b) found that the unified model assumption holds for lower luminosity quasars and Seyfert galaxies but does not seem to hold for high-luminosity quasars, possibly due to a different evolution for high luminosity, and therefore

high Eddington ratio, quasars. Here this issue is addressed by using the Eddington ratio dependent f_{CT} of the composite model, which takes into account the different evolution of high Eddington ratio quasars from the moderate and low Eddington ratio AGN.

4.2.2 The Model Grids

As this investigation of the FIR properties of AGN is informed by the constraints offered by the XRB and X-ray observations of AGN, SEDs are calculated as a function of $\log L_X$ and z. It is assumed that the redshift evolution of f_2 halts at $z = 1$, thus models are computed up to $z = 1$ and the $z = 1$ models are used at $z > 1$. Therefore, Cloudy models are computed for $z = 0$ to 1, in steps of 0.05, and $\log L_X = 41.5$ to 48, in steps of 0.25. For each luminosity and redshift, Cloudy models are calculated for each $\log N_H = 20.0$, 20.5, ..., 24.5, 25.0 cm^{-2}. Since the covering factor is Eddington ratio dependent, Cloudy models had to be calculated for each luminosity, redshift, and column density for each of the three Eddington ratio bins. This resulted in 18711 individual Cloudy models for each r investigated and an additional 5103 Cloudy models to investigate the sensitivity of results to the hydrogen density, n_H, of the Compton thick clouds.

As it is necessary to run 33 models for each (L_X, z) pair, it is computationally prohibitive to run models on a finer grid. Therefore, I have linearly interpolated between the SEDs to allow for a finer grid in the calculations. Thus eight SEDs are interpolated between consecutive $\log L_X$ model SEDs at a given z and two SEDs are interpolated between consecutive z model SEDs at a given L_X. A convergence test was conducted using twice as many steps in both L_X and z; it was found that the step size used here is adequate for convergence.

To create final SEDs from the 18711 Cloudy models, the method described by Ballantyne et al. (2006b) is used. For each Eddington ratio bin, the weighted average of the reflection components of each N_H is added to the net transmitted continua of each N_H to create the "unified SEDs". The final SEDs are calculated in three categories: type 1, type 2 but Compton thin (which will be referred to as "type 2"), and Compton thick, for each Eddington ratio bin. The type 1 SED is an average of the $20 \leq \log N_H < 22$ unified SEDs,

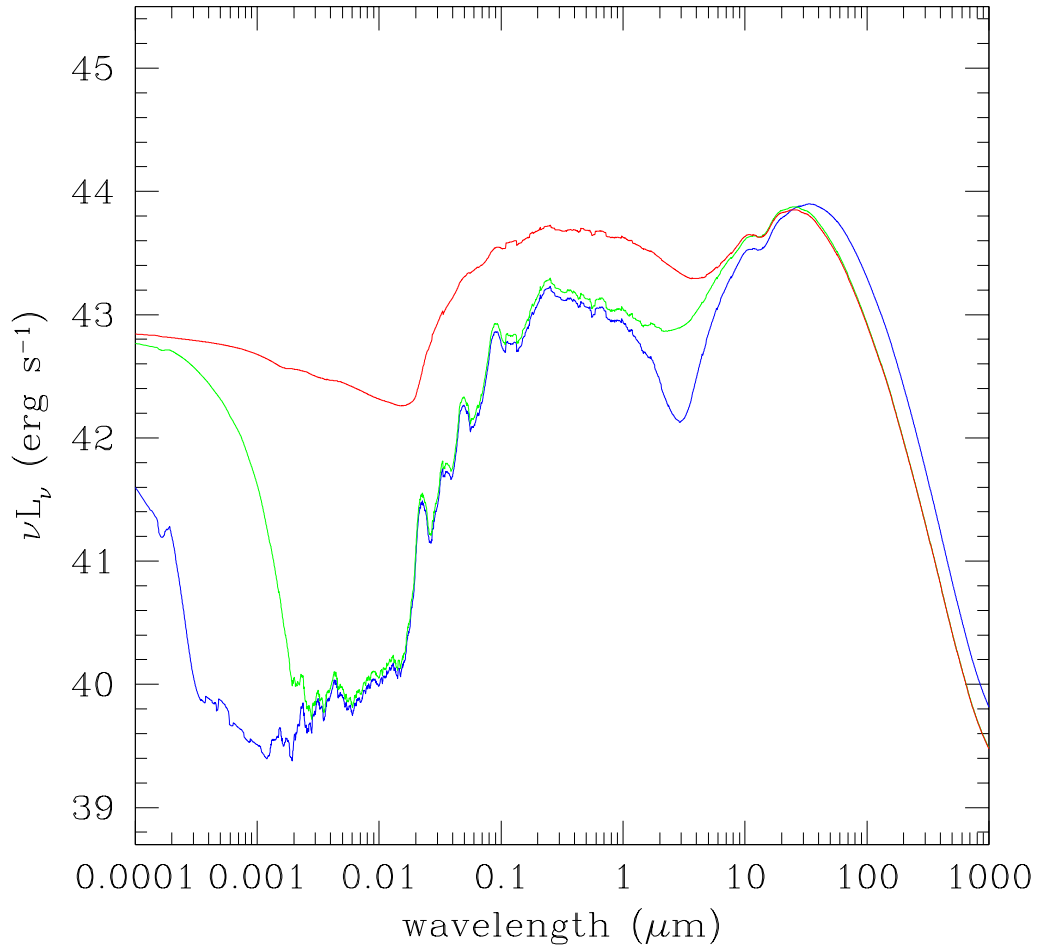

Figure 4.1: Rest frame SEDs for high Eddington ratio AGN ($L/L_{Edd} > 0.9$) with $\log L_X = 43$ and $z = 0.45$ ($f_{CT} = 0.86$ and $f_2 = 0.78$). The type 1 SED is shown in red, the type 2 SED is shown in green, while the Compton thick SED is shown in blue.

the type 2 SED is an average of the $22 \leq \log N_H < 24$ unified SEDs, and the CT SED is an average of the $24 \leq \log N_H$ unified SEDs. At this point, for each (L_X,z) pair there is a type 1, type 2, and Compton thick SED for each Eddington ratio bin. Figure 4.1 shows the rest frame $\log L_X = 43$ and $z = 0.45$ SEDs for the high Eddington ratio bin, which has $f_{CT} = 0.86$ and $f_2 = 0.78$.

4.2.3 Properties of AGN Model SEDs

The model SEDs were tested in the same manner as by Ballantyne et al. (2006b) to assure the assumptions used to compute the SEDs were appropriate and that the model SEDs are consistent with observed SED trends. As little is known about AGN FIR SEDs, these tests primarily investigate the mid-infrared properties of the model SEDs. The mid-infrared colors were examined and found to be consistent with the findings of Brand et al. (2006). The mid-infrared to X-ray flux ratio was considered as a function of N_H and no correlation was found, in agreement with observational data (Lutz et al., 2004; Rigby et al., 2004; Gandhi et al., 2009). Also, the fluxes were tested against and found to be consistent with expectations from local bright AGN, known as "Piccinotti AGNs" (see Alonso-Herrero et al., 2004). As the goal of this study is to make predictions which characterize an ensemble of AGNs, like number counts, the model SEDs are not compared against individual objects but against data which explores average properties of AGN SEDs. The model SEDs are found to be consistent with the observed AGN SED trends.

The model SEDs were also tested against the more recently discovered correlation between mid-infrared luminosity, $L_{12.3\mu m}$, and L_X for a sample of local Seyferts (Gandhi et al., 2009). Figure 4.2 compares the $z = 0.05$ model SEDs to the local best-fit correlation found by Gandhi et al. (2009). The model SEDs agree reasonably well with the correlation, especially the type 1 SEDs. At high luminosities the Compton thick SEDs appear to have a slight X-ray excess compared to the local Seyfert correlation. This is due to the Compton thick SEDs including more power radiated in the FIR, and consequently less power radiated in the mid-infrared, than the Compton thin SEDs. The $r = 1.0$ pc model SEDs do match the $L_{12.3\mu m}$ – L_X relation better than the $r = 10$ pc model SEDs; however, the $r = 10$ pc model SEDs best describe the general mid-infrared properties of an ensemble of AGN (see Ballantyne et al., 2006b). The fact that the $r = 1.0$ pc model SEDs fit this relation better than the $r = 10$ pc model SEDs shows that the distribution of gas and dust in the AGN dusty torus is an important effect in the mid-infrared. In order for the models used here to better approximate the Gandhi et al. (2009) relation, the geometry of the dusty torus should be carefully taken into account. The FIR SEDs are dominated by star formation, so

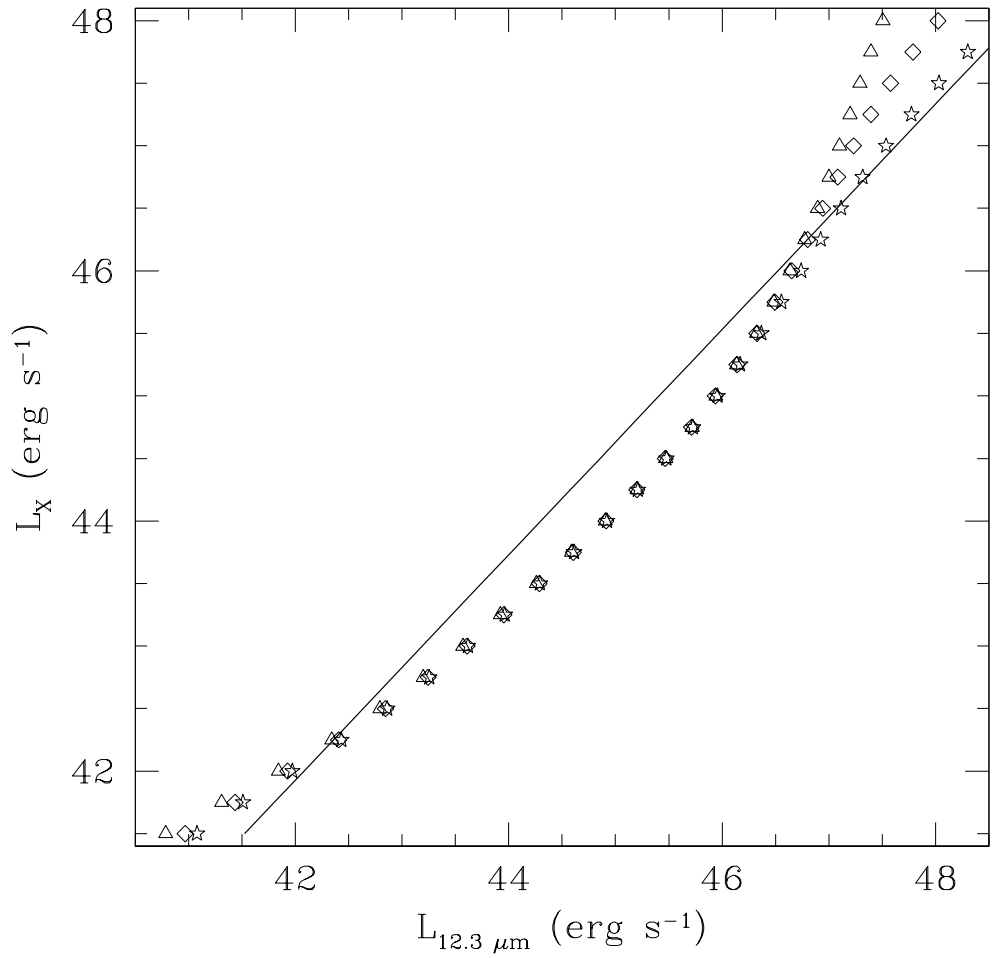

Figure 4.2: L_X versus $L_{12.3\mu m}$ for the high Eddington ratio ($L/L_{Edd} > 0.9$) model SEDs at $z = 0.05$. Type 1 SEDs are shown as stars, type 2 SEDs are shown as diamonds, and the Compton thick SEDs are shown as triangles. The black line is the best-fit line for the well-resolved sample of Gandhi et al. (2009).

the geometric details of the hot dust close to the central engine should not affect the results of this study. Also, as this study is focused on the integral properties of a large number of AGN, detailed modeling of the torus geometry is beyond the scope of this current study and is left for future work. Overall, the model SEDs are an appropriate representation of average AGN SEDs.

4.3 Predictions for Bare AGNs

In this section the predictions for differential number counts, the AGN contribution to the cosmic infrared background (CIRB), and luminosity density, based on the model SEDs with no contribution from the host galaxy, is presented. The population synthesis model last described by Draper & Ballantyne (2010) is used to incorporate the information about and the constraints on the AGN population from deep hard X-ray surveys and the XRB into infrared predictions.

4.3.1 Differential Number Counts

The number of sources per square degree with flux greater than S, $N(>S)$ is found by

$$\begin{aligned} N(>S) &= \frac{K_{sr}^{deg} c}{H_0} \\ &\times \int_{z_{min}}^{z_{max}} \int_{max(\log L_X^{min}, \log L_X^S)}^{\log L_X^{max}} \frac{d\Phi_\lambda(L_X,z)}{d\log L_X} \frac{d_l^2}{(1+z)^2[\Omega_m(1+z)^3+\Omega_\Lambda]^{1/2}} d\log L_X dz, \end{aligned} \tag{4.1}$$

where the factor $K_{sr}^{deg} = 3.05 \times 10^{-4}$ converts from sr^{-1} to deg^{-2}, $d\Phi_\lambda(L_X,z)/d\log L_X$ is the evolving Eddington ratio space density computed by Draper & Ballantyne (2010), in Mpc^{-3}, d_l is the luminosity distance, and $\log L_X^S$ is the 2–10 keV rest-frame luminosity corresponding to the observed-frame infrared flux S at redshift z. The differential number counts are found by taking the derivative of $N(>S)$ with respect to S, $dN(>S)/dS$. The differential number counts were also calculated directly. However, due to the coarseness of the L_X and z grid used, the differential number counts contained numerical artifacts at brighter fluxes. The predictions from the two calculation methods are in agreement; however, computing the integral number counts on a very fine flux grid and then taking the derivative with respect to flux minimizes the numerical noise found in direct calculation of the differential number counts.

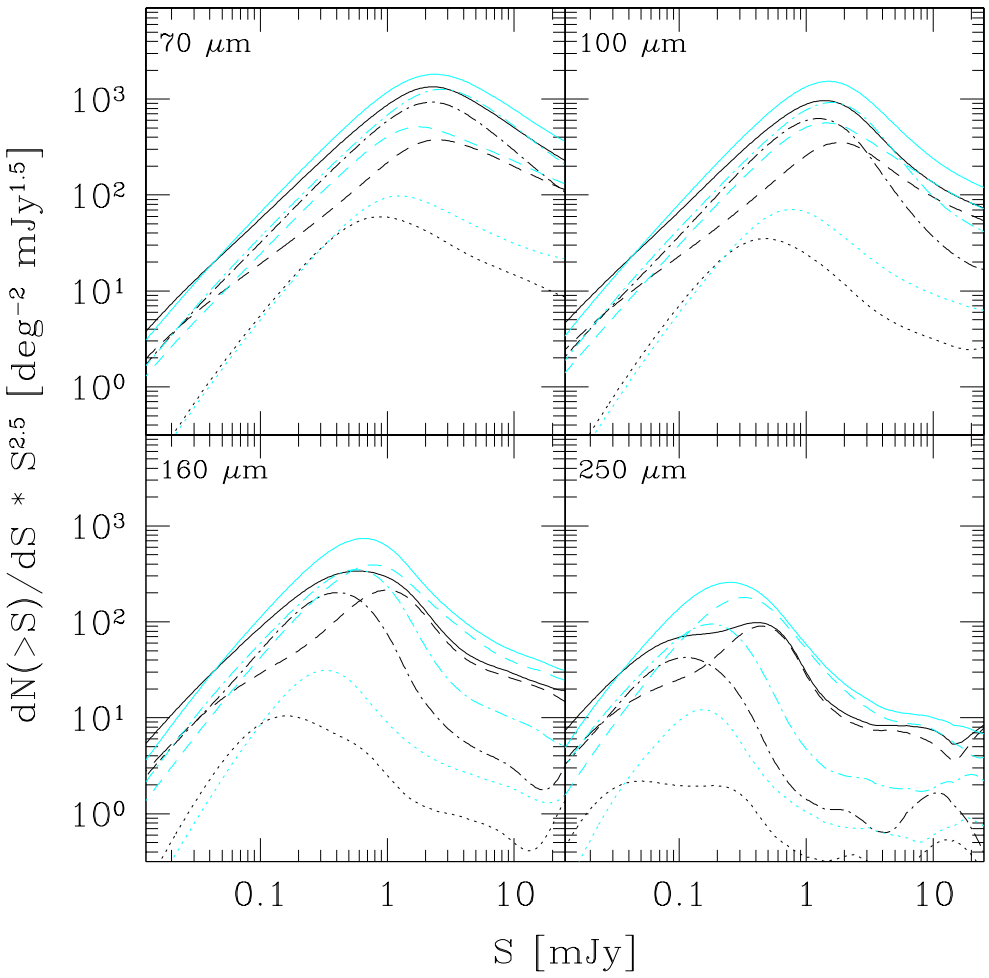

Figure 4.3: Euclidean normalized differential number counts for bare AGN at 70, 100, 160, and 250 μm. The black lines plot the predictions based on the composite model of Draper & Ballantyne (2010) and the cyan lines show the predictions for the original model. The dotted-lines are predictions for type 1 AGN, the dot-dashed lines are predictions for type 2 AGNs, and the dashed lines are predictions for Compton thick AGN.

The Euclidean normalized differential number counts for 70, 100, 160, and 250 μm are shown in figure 4.3[3]. Plots are not shown for the 350 and 500 μm bands because, as evident in figure 4.1, the flux due to the AGN is very small at such long wavelengths; for example, at 10 mJy the 500 μm band $dN(>S)/dS \approx 0.4$ AGN hosts mJy$^{1.5}$ deg^{-2}. The black lines show the predictions for the composite model and the cyan lines show the predictions for the original model. For ease in interpreting the figure, the low, moderate and high Eddington ratio bins have been combined and the total differential counts are shown (see §4.5.4 for a discussion about the contribution from the various Eddington ratio bins). As expected, the differential number counts for bare AGN are very small at long wavelengths because the AGNs tend to create hot dust. Therefore, long wavelengths can be used to investigate the star formation in AGN hosts. For both the original and composite models, CT AGN dominate the bright end of the differential counts, especially at wavelengths longer than 70 μm. In both models the type 2 AGN dominate at lower fluxes and the type 1 AGN contribute significantly less than their obscured counterparts at all wavelengths. The original model and composite model differential counts peak at about the same flux for each wavelength and have similar bright end slopes. However, the original model peaks above the composite model and declines faster on the lower flux level end.

It is important to consider the dependence of these predictions on the parameters of the distance of the inner edge of the cloud from the ionizing source, r, and the n_H of the CT clouds, $n_{H,CT}$. As seen in figure 4.4, when $r = 1$ pc the differential counts are greatly reduced at all FIR wavelengths because the dust is hot and radiating more energy in the mid-infrared. Contrastingly, when $r > 10$ pc the differential counts are enhanced due to the dust being farther from the illuminating source and therefore cooler. Similarly, when $n_{H,CT}$ $= 10^4$ cm^{-3} the differential counts are slightly enhanced in the FIR due to the greater spatial extent of the cloud. However, since the combined AGN and host SED will be dominated by star formation at longer wavelengths, and there is likely to be variation among individual

[3]Fluxes are calculated at the filter nominal wavelengths. Using the full filter transmission function to calculate the dN/dS provides a result which is within a factor of 1.05 of that obtained when calculating the flux at the filter nominal wavelength. Thus the error due to calculating the fluxes at the filter nominal wavelength instead of using the full filter profile is negligible compared to the uncertainties in the model and the measurements.

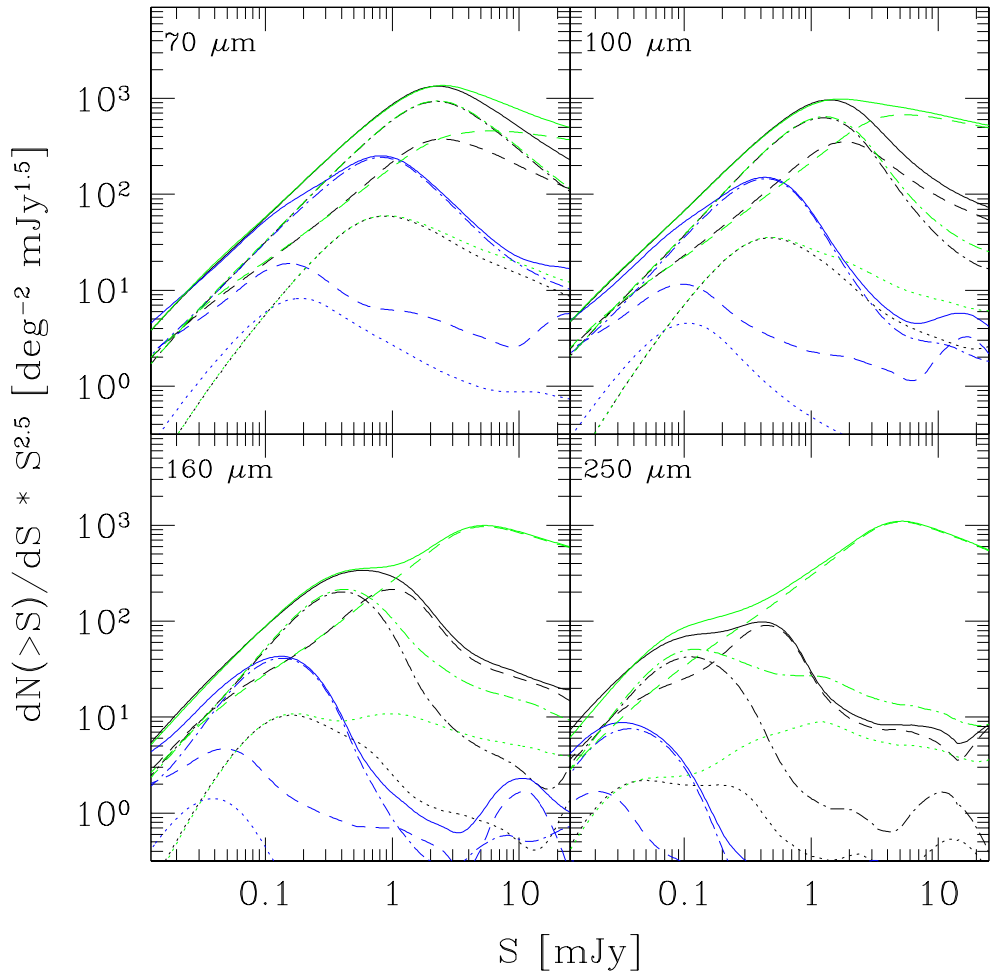

Figure 4.4: Comparison of Euclidean normalized differential number counts for bare AGN at 70, 100, 160, and 250 μm using the composite model. The blue lines are $r = 1$ pc and $n_{H,CT} = 10^6$ cm^{-3}, the black lines are $r = 10$ pc and $n_{H,CT} = 10^6$ cm^{-3}, and the green lines are r= 10 pc and $n_{H,CT} = 10^4$ cm^{-3}. The line styles are the same as in figure 4.3.

objects, the exact values for r and $n_{H,CT}$ used will have little effect on the final predictions.

4.3.2 CIRB

The AGN contribution to the CIRB is calculated similarly to population synthesis models looking at the XRB, but exchanging the X-ray spectrum with the infrared spectrum. Thus,

$$I_\nu(\nu) = \frac{c}{H_0}\int_{z_{min}}^{z_{max}}\int_{\log L_X^{min}}^{\log L_X^{max}} \frac{d\Phi_\lambda(L_X,z)}{d\log L_X} \times \frac{S_\nu(L_X,z)d_l^2}{(1+z)^2[\Omega_m(1+z)^3+\Omega_\Lambda]^{1/2}} d\log L_X dz, \quad (4.2)$$

where $S_\nu(L_X,z)$ is the observed-frame AGN model SED, in Jy sr^{-1}, computed with L_X at redshift z. As there is little knowledge about the SEDs of AGN in the FIR, there are very few constraints on the AGN contribution to the CIRB. Jauzac et al. (2010) claim that AGN contribute $\lesssim 10\%$ of the CIRB at $z < 1.5$, based on *Spitzer* observations in the GOODS and COSMOS fields. By extrapolating from XRB models to the CIRB using rough AGN SED templates, Silva et al. (2004) predict that bare AGN contribute ∼0.3% of the CIRB at 160 μm[4]. Using a method similar to the one described here, Ballantyne & Papovich (2007) predict that bare AGN contribute ∼0.9% of the CIRB at 160 μm. Here it is found that both the composite and original models predict that bare AGN contribute ∼0.9% of the CIRB at 160 μm. As seen in figure 4.5, type 2 AGN dominate the CIRB at lower wavelengths and at higher wavelengths CT AGN dominate the AGN contribution to the CIRB. At wavelengths greater than ∼100 μm the original model and the composite model predict very similar contributions of AGN to the CIRB. Below ∼100 μm the composite model predicts a higher contribution to the CIRB by AGNs than the original model.

4.3.3 Luminosity Density

The cosmic infrared luminosity density and its evolution are good indicators of the star formation rate density and the evolution of star formation in the universe. However, infrared luminosity density is significantly contaminated by AGN, thus making it important to understand the contribution of AGN to the infrared luminosity density and how the AGN contribution to the infrared luminosity density evolves. The 8–1000 μm AGN luminosity

[4]Here it is assumed the intensity of the CIRB at 160 μm is 12.84 nW m^{-2} sr^{-1} (Altieri et al., 2010).

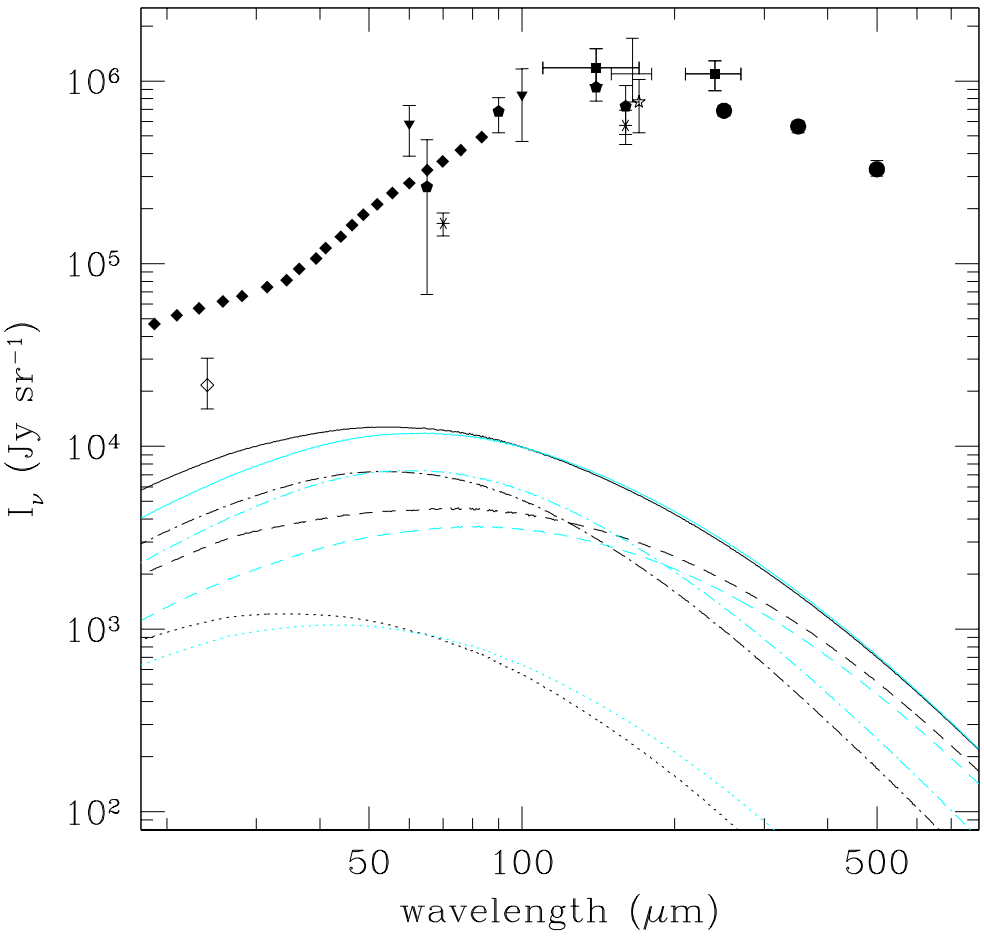

Figure 4.5: Bare AGN contribution to the CIRB. Line color and styles are the same as in figure 4.3. Data points are from a variety of instruments: the filled diamonds are from IACTS (Mazin & Raue, 2007); the open diamond is from MIPS (Papovich et al., 2004); the triangles are from DIRBE (Finkbeiner et al., 2000); the pentagons are from AKARI (Matsuura et al., 2010); the asterisks are from MIPS (Dole et al., 2006); the squares are from DIRBE (Hauser et al., 1998); the cross is from ISOPHOT (Juvela et al., 2009); the star is also from ISOPHOT (Lagache & Puget, 2000); and the circles are from BLAST (Patanchon et al., 2009).

density, ρ_{IR}, is calculated as

$$\rho_{IR}(z) = \int_{L_{IR,min}}^{L_{IR,max}} L_{IR} \frac{d\Phi_\lambda(L_{IR}, z)}{d \log L_{IR}} d \log L_{IR}, \tag{4.3}$$

where $d\Phi_\lambda / d \log L_{IR}$ is the evolving Eddington ratio space density calculated in Draper & Ballantyne (2010) in terms of the total infrared luminosity, i.e. a total infrared luminosity function for a population of AGN with a specific Eddington ratio, which is found using the relation

$$\frac{d\Phi_\lambda(L_{IR}, z)}{d(\log L_{IR})} = \frac{d\Phi_\lambda(L_X, z)}{d(\log L_X)} \frac{d(\log L_X)}{d(\log L_{IR})}. \tag{4.4}$$

As seen in figure 4.6, both the composite and original models are in agreement with observations by Goto et al. (2010a) at $z \approx 0.2$–0.8. For $z \gtrsim 1$ both models do not evolve fast enough to agree with the ρ_{IR} and ULIRG AGN infrared luminosity density, ρ_{IR}^{ULIRG}. However, both models are in fairly good agreement with the high redshift LIRG AGN luminosity density, ρ_{IR}^{LIRG}. Locally both the original and composite model under-predict the ρ_{IR} and over-predict the ρ_{IR}^{ULIRG}, but are in agreement with the ρ_{IR}^{LIRG}, as measured by Goto et al. (2010b). Due to the method used to separate the AGN and star forming galaxies in the samples of Goto et al. (2010a,b), there is an uncertainty of up to 50% due to the complication of galaxies whose infrared SED is not clearly dominated by AGN activity nor by star formation (Goto et al., 2010b). Also, by applying the same method of separating the contribution of AGN and star forming galaxies to the infrared luminosity density measured by Le Floc'h et al. (2005) using *Spitzer* 24 μm sources in the CDF-S, the local ρ_{IR}^{ULIRG} is $\sim$0.4 dex higher and in good agreement with local ρ_{IR}^{ULIRG} predicted here.

4.4 Accounting for Star Formation

The infrared SEDs of most AGN are dominated by star formation (e.g., Franceschini et al., 2010). Unless the AGN host galaxy can be spatially resolved, it is very difficult to separate the AGN emission from the star formation emission. Therefore it is important to consider how various AGN star formation scenarios will affect the predictions discussed above. In particular, a constant star formation rate is considered, keeping with the unified scheme. A star formation scenario consistent with the AGN evolution scenario discussed by Sanders

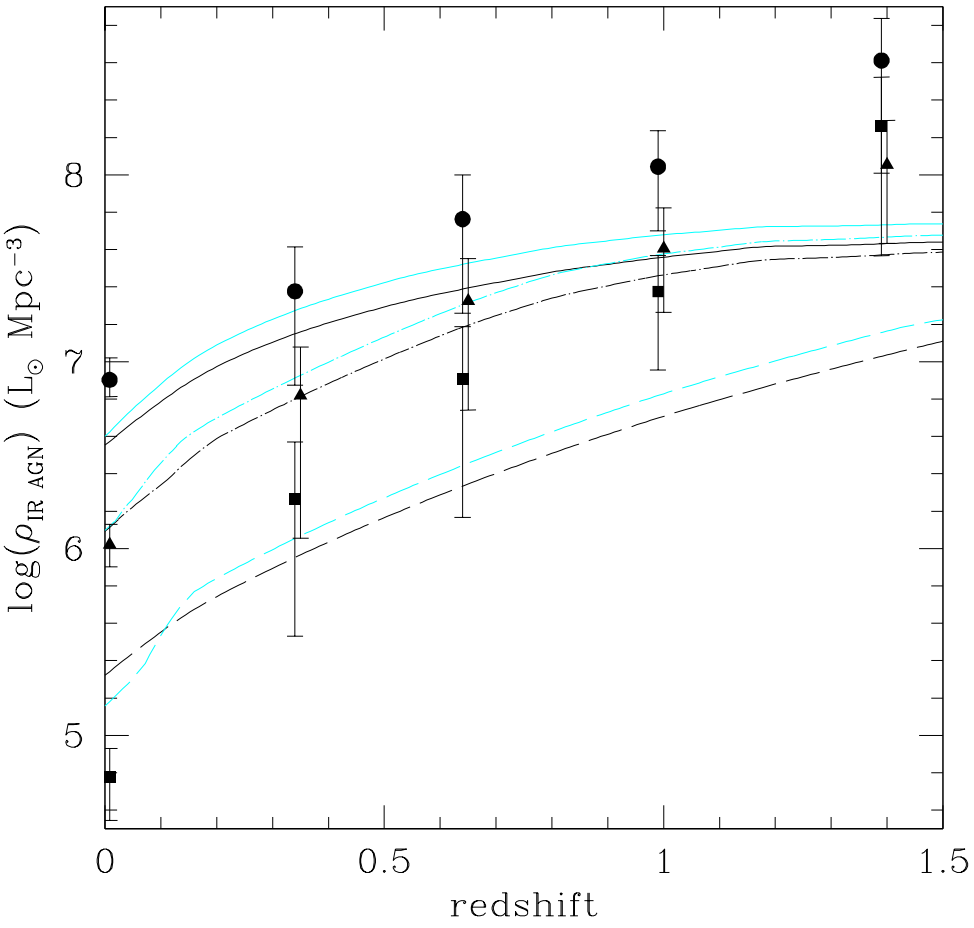

Figure 4.6: Infrared luminosity density of bare AGN with respect to redshift. Solid lines and circles refer to ρ_{IR}, dot-dashed lines and triangles refer to ρ_{IR}^{LIRG}, while dashed lines and squares refer to ρ_{IR}^{ULIRG}. The black lines show the composite model and the cyan lines show the original model. The $z = 0.0082$ data points are taken from Goto et al. (2010b) and the higher redshift data points are from the work of Goto et al. (2010a) in the AKARI NEP deep field.

et al. (1988) is also analyzed. Finally, star formation scenarios which include evolution of the SFR with redshift and AGN L_X are considered.

To calculate the star formation SED for a given SFR, a modified black body spectrum characterized by the dust emissivity, β, and the dust temperate, T_d, is used. The Kennicutt (1998) relation,

$$SFR = 4.5 \times 10^{-44} L_{IR}, \tag{4.5}$$

is used to determine L_{IR}, in erg s^{-1}, for a given SFR, in M$_\odot$ yr^{-1}, and the L_{IR}-T_d relation from Amblard et al. (2010),

$$T_d = T_0 + \alpha \log(L_{IR}/L_\odot), \tag{4.6}$$

is used to determine T_d. Using *Herschel* observations, Amblard et al. (2010) find T_0 = 20.5 K and $\alpha = 4.4$, using $\beta = 1.5$. Amblard et al. (2010) define L_{IR} as the 8–1100 μm luminosity, instead of the 8–1000 μm luminosity as done here; however, for the purposes of this work, the difference is negligible. The resulting star formation SEDs are in good agreement with the star formation templates presented by Rieke et al. (2009) at rest frame wavelengths greater than 50 μm. The star formation SEDs are then added to the model SEDs discussed above to create the AGN+SF SED. The calculations discussed in section §4.3 are repeated using the AGN+SF SEDs in place of the AGN model SEDs. Here, the predictions for the composite model are presented. A comparison of the predictions of the original and composite models is discussed in §4.5.2.

4.4.1 Constant Star Formation

The simplest star formation scenario is where AGN hosts have a constant SFR. Ballantyne & Papovich (2007) found that an average AGN SFR = 1.0 M$_\odot$ yr^{-1} reproduces the AGN contribution to the mid-infrared portion of the CIRB as measured by *Spitzer*; thus for the constant star formation model SFR = 1.0 M$_\odot$ yr^{-1}. In keeping with the unified scheme, all AGN have the same SFR regardless of spectroscopic type. The Euclidean normalized differential number counts for the constant star formation model are shown as the black lines in figures 4.7, 4.8, 4.9, 4.10, 4.11, and 4.12. At wavelengths shorter than 350 μm, the number counts increase steeply from 0.01 mJy to ∼1 mJy and then remain approximately

flat through ∼25 mJy. At wavelengths longer than 350 μm, the number counts turn over around 1 mJy and continue to decrease toward brighter flux levels. At all wavelengths the CT AGN dominate the bright end counts above ∼1 mJy, with type 2 AGN dominating at lower flux levels.

The black lines in figure 4.13 show the AGN contribution to the CIRB for the constant star formation model. In this star formation scenario, AGN contribute ∼4% of the CIRB at 160 μm. The AGN contribution to the CIRB is dominated by CT AGN above 100 μm and type 2 AGN also contribute significantly. The AGN contribution to the CIRB peaks at approximately the same wavelength as the CIRB itself peaks, ∼160 μm.

The ρ_{IR} is shown in figure 4.14, with the constant star formation model shown as the black lines. The ρ_{IR}^{ULIRG} is not increased over the bare AGN scenario, however, the total and LIRG AGN infrared luminosity densities are increased slightly. Thus the constant star formation model does not allow for rapid enough evolution with redshift to match the observed high redshift ρ_{IR}.

4.4.2 AGN Evolution Scenario

It has been suggested that, at least in the quasar regime, the level of obscuration observed in an AGN is connected to the evolutionary stage of the quasar (e.g., Sanders et al., 1988; Page et al., 2004; Ballantyne, 2008; Draper & Ballantyne, 2010). Galaxy merger simulations support the evolutionary scenario showing that gas rich mergers lead to a burst of star formation and intense, highly obscured black hole growth (e.g., Hopkins et al., 2006). In the AGN evolution scenario, high Eddington ratio CT AGN would be expected to have SFRs reaching into the ULIRG regime and type 2 AGN hosts would be expected to have more star formation that type 1 AGN hosts (e.g., Page et al., 2004). Following this prescription, I set the high Eddington ratio SFR = 175 $M_\odot$ yr^{-1}, the type 2 SFR = 2.0 $M_\odot$ yr^{-1}, and type 1 SFR = 0.5 $M_\odot$ yr^{-1}. The low Eddington ratio CT AGN are also given SFR = 0.5 $M_\odot$ yr^{-1} as these are weak AGN most likely obscured by molecular clouds in the host bulge or by dust lanes in the host galaxy (Martínez-Sansigre, 2009), and not by intense nuclear starbursts. This star formation scenario gives predictions which are only negligibly different

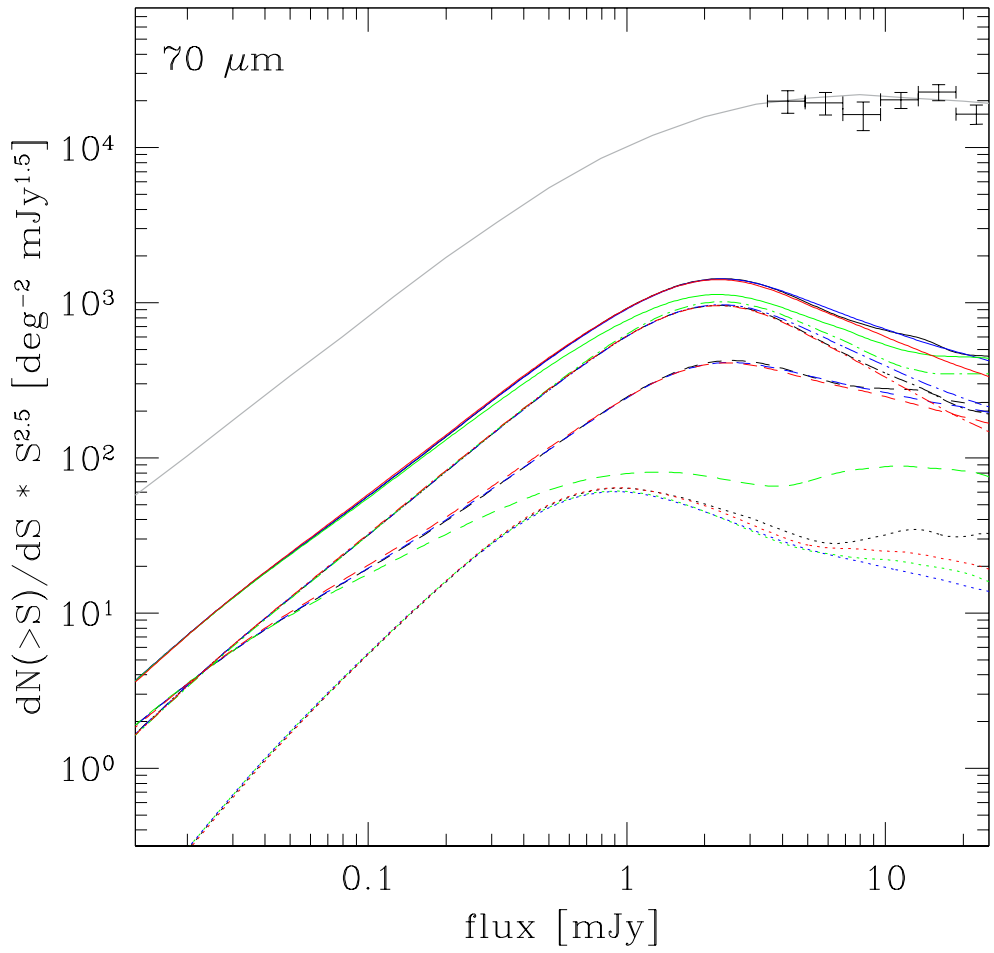

Figure 4.7: Euclidean normalized differential number counts for AGN and host star formation at 70 μm for the various star formation scenarios using the composite model. Constant star formation is shown as black. The AGN evolution star formation scenario is shown as green. Star formation with the redshift evolution found by Serjeant et al. (2010) is shown as red. The star formation scenario using the redshift and AGN L_X evolution by Wilman et al. (2010) is shown in blue. The line styles are the same as in figure 4.3. The grey line shows the best fit model galaxy differential number counts of Franceschini et al. (2010). *Spitzer* data points are from Béthermin et al. (2010).

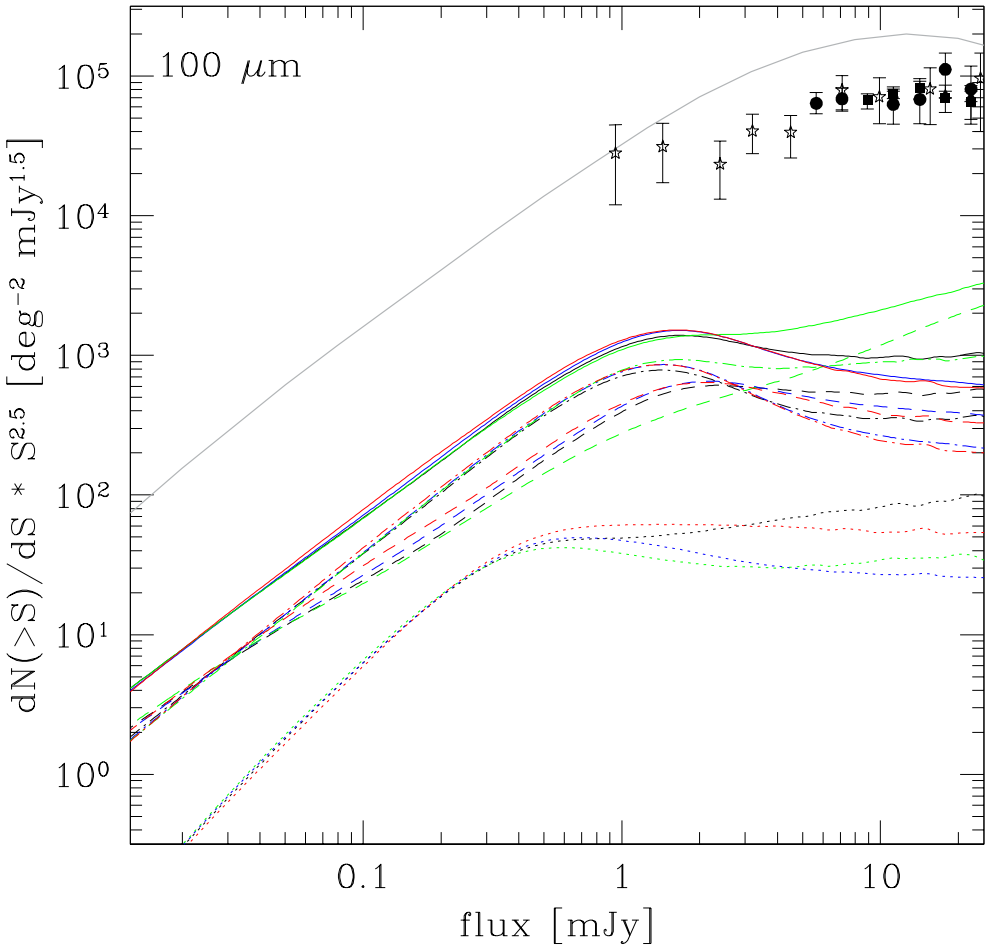

Figure 4.8: Euclidean normalized differential number counts for AGN and host star formation at 100 μm for the various star formation scenarios using the composite model. Lines are the same as in figure 4.7. *Herschel* data points are from Altieri et al. (2010) (stars) and Berta et al. (2010) (circles–GOODS-N, squares–Lockman XMM, and triangles–COSMOS).

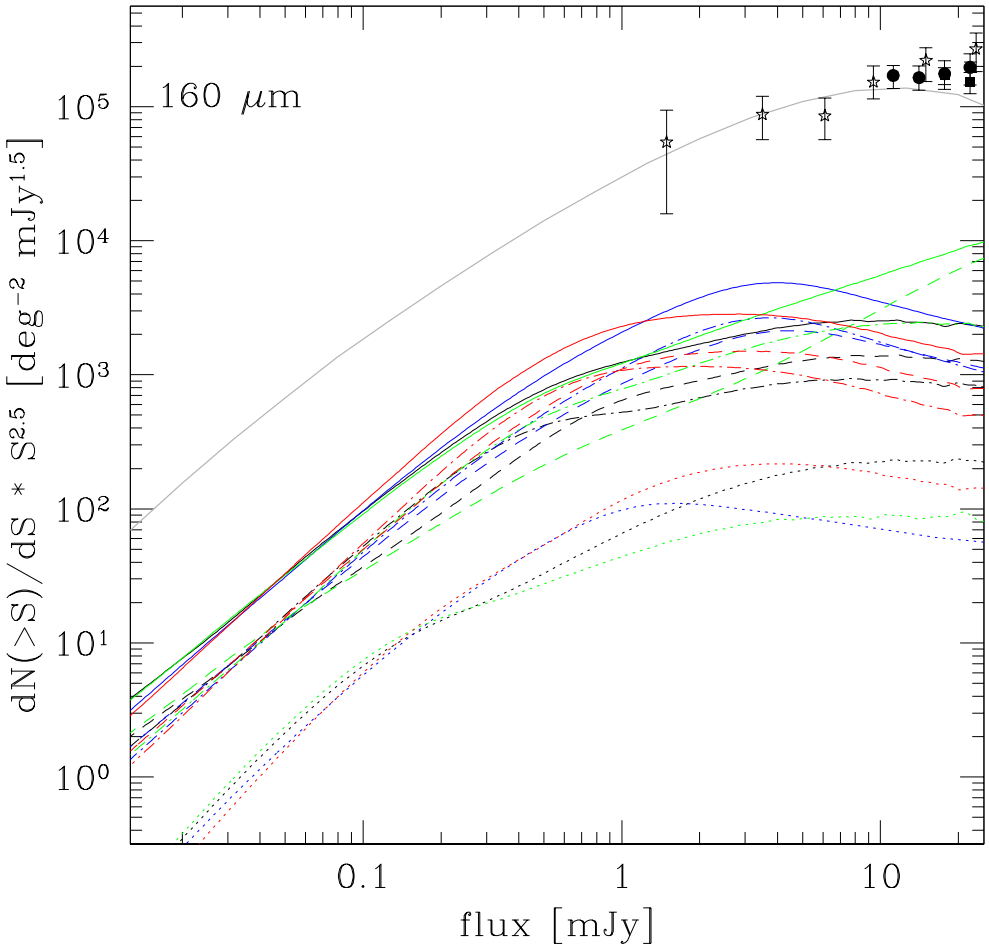

Figure 4.9: Euclidean normalized differential number counts for AGN and host star formation at 160 μm for the various star formation scenarios using the composite model. Line colors and styles are the same as in figure 4.7. Data points are the same as in figure 4.8.

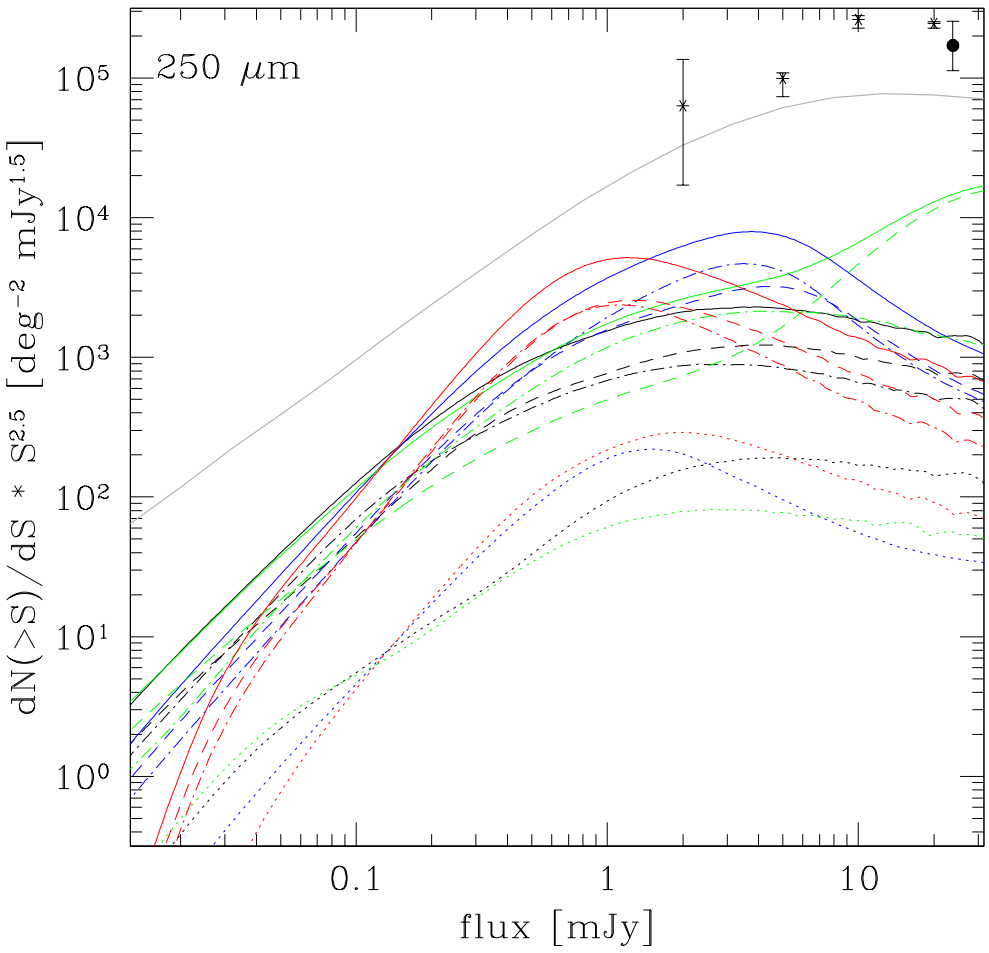

Figure 4.10: Euclidean normalized differential number counts for AGN and host star formation at 250 μm for the various star formation scenarios using the composite model. Line colors and styles are the same as in figure 4.7. Circles are data points from *Herschel* (Oliver et al., 2010) and asterisks show the multiply-broken power-law model of Glenn et al. (2010).

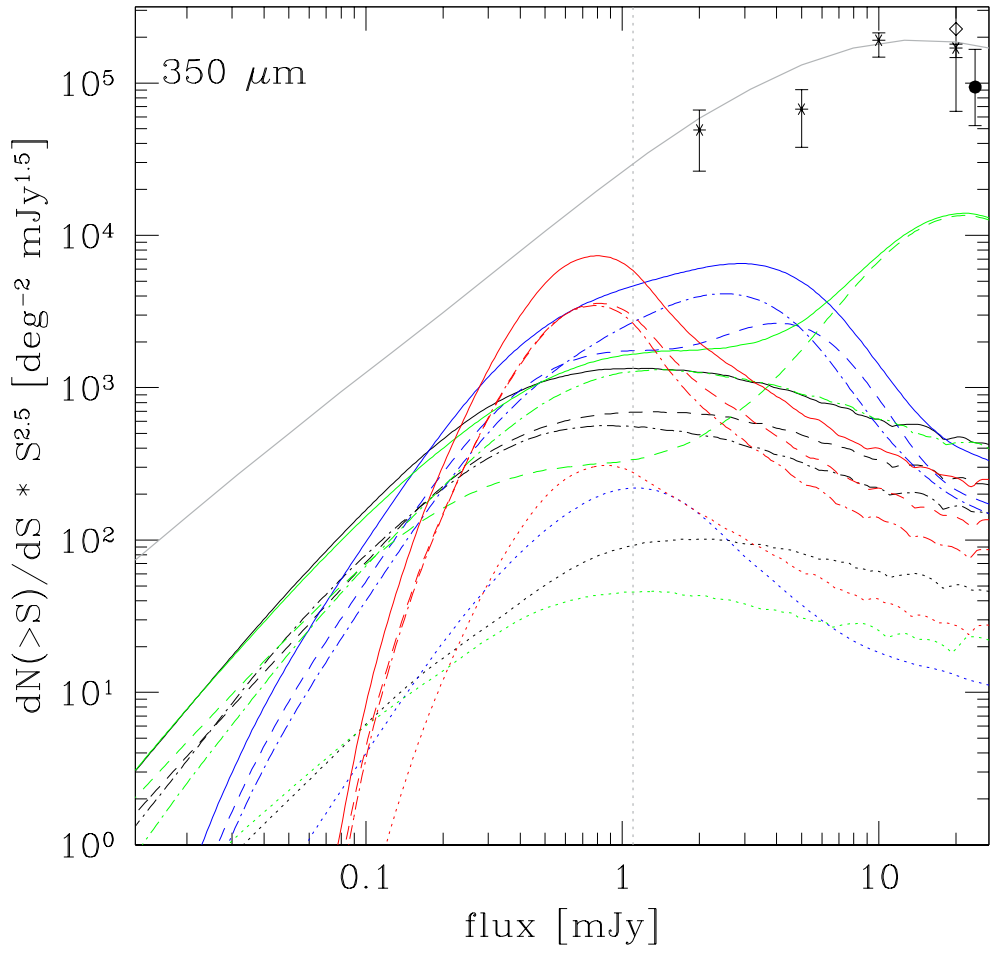

Figure 4.11: Euclidean normalized differential number counts for AGN and host star formation at 350 μm for the various star formation scenarios using the composite model. Line colors and styles are the same as in figure 4.7. Additionally, the dotted grey line shows the expected continuum sensitivity of ALMA for an integration time of 60 seconds and a spectral resolution of 1 km/s. Circles are data points from *Herschel* (Oliver et al., 2010), the diamond is from SHARC II (Khan et al., 2007), and asterisks show the multiply-broken power-law model of Glenn et al. (2010).

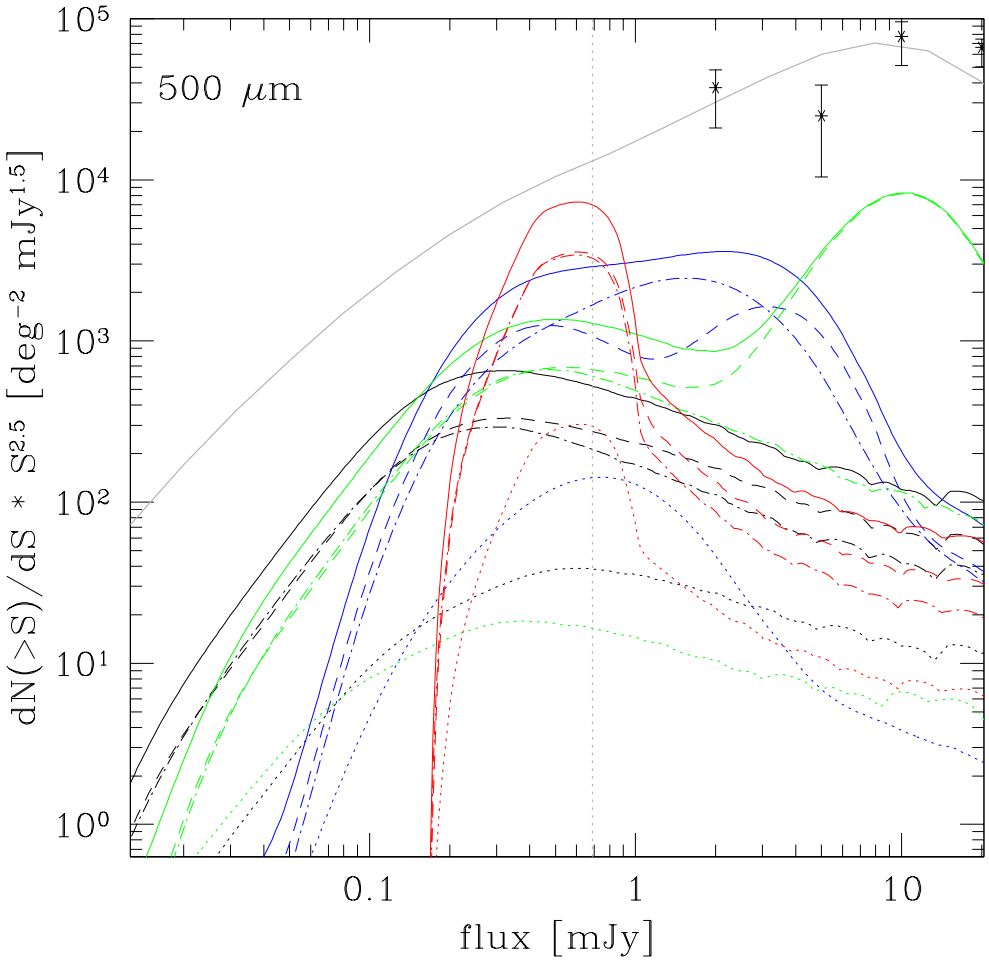

Figure 4.12: Euclidean normalized differential number counts for AGN and host star formation at 500 μm for the various star formation scenarios using the composite model. Line colors and styles are the same as in figure 4.11. Circles are data points from *Herschel* (Oliver et al., 2010) and asterisks show the multiply-broken power-law model of Glenn et al. (2010). At bright fluxes numerical artifacts are present due to the small number of sources in this flux region.

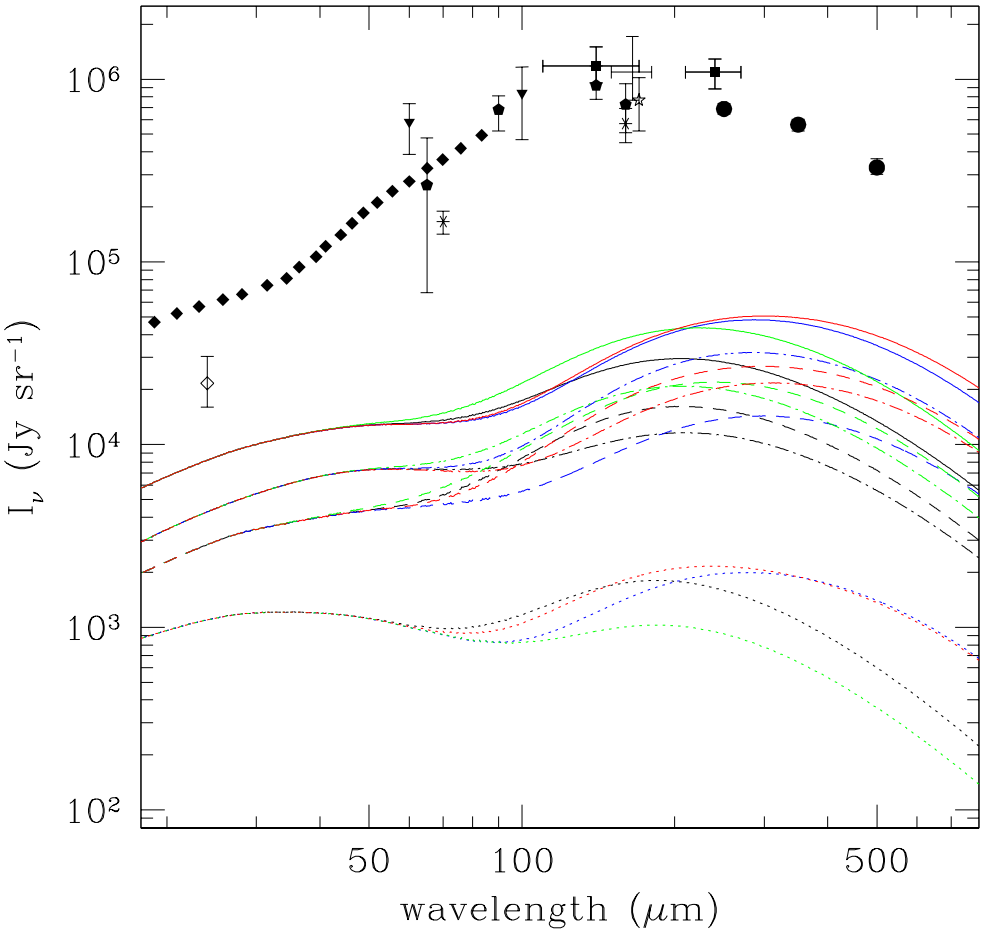

Figure 4.13: AGN and host star formation contribution to the CIRB for the various star formation scenarios using the composite model. Line colors are the same as in figure 4.8. The line styles are the same as in figure 4.3. Data points are the same as figure 4.5.

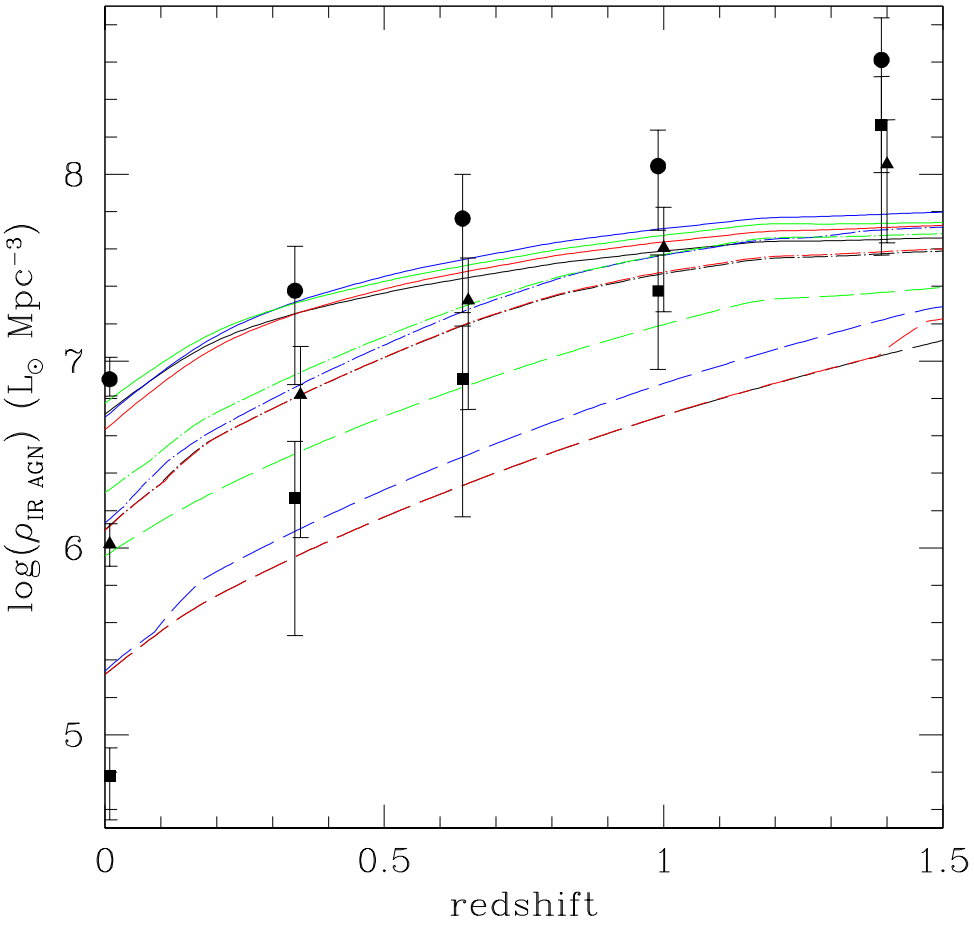

Figure 4.14: AGN and host star formation infrared luminosity density for the various star formation scenarios using the composite model. Line colors are the same as in figure 4.8. The line styles and data points are the same as figure 4.6.

from the scenario where all AGN have SFR = 1.0 $M_\odot$ yr^{-1} except for the high Eddington ratio CT AGN which have SFR = 175 $M_\odot$ yr^{-1}.

The Euclidean normalized differential counts for the AGN evolution scenario are shown as the green lines in figures 4.7, 4.8, 4.9, 4.10, 4.11, and 4.12. At all wavelengths the number counts rise as the flux level increases, leveling off around 1 mJy, and then continue to rise at least until the flux level of 10 mJy. CT AGN dominate at flux levels greater than ∼6 mJy and type 2 AGN dominate at lower flux levels for all wavelengths.

In figure 4.13, the AGN contribution to the CIRB for the AGN evolution scenario is shown in green. At 160 μm, AGN contribute ∼6% of the CIRB. CT AGN dominate the AGN contribution to the CIRB at wavelengths greater than ∼200 μm and type 2 AGN dominate below 200 μm. The peak of the AGN contribution to the CIRB is roughly at the same wavelength as the peak of the CIRB.

The green lines in figure 4.14 show the ρ_{IR} for the AGN evolution scenario. The total ρ_{IR} is in decent agreement with observations except at the highest redshift bin, which this model under-predicts. The local ρ_{IR}^{LIRG} and ρ_{IR}^{ULIRG} are over-predicted by this model but are in good agreement with observations at higher redshifts. However, the ρ_{IR}^{ULIRG} observations show a stronger redshift evolution than predicted by this model.

4.4.3 Evolution with Redshift

Also considered was the star formation redshift evolution found by Serjeant et al. (2010), where SFR $\propto (1.0+z)^{2.3}$. Serjeant et al. (2010) did find that the highest luminosity quasars had a much stronger redshift evolution, perhaps as strong as SFR $\propto (1.0+z)^{10}$. For simplicity the total volume-averaged star formation rate redshift evolution is used here, independent of the object luminosity. The local star formation rate is set such that SFR(z=0.0) = 0.5 $M_\odot$ yr^{-1}, in keeping with the average type 1 SFR found in a sample of local SDSS quasars by Kim et al. (2006). Following the unified scheme, the SFR is not dependent on spectroscopic type.

As shown by the red lines in figures 4.7, 4.8, 4.9, 4.10, 4.11, and 4.12, the Euclidean normalized differential number counts increase with increasing flux level until peaking at

$\sim$1 mJy. The number counts decrease at flux levels above $\sim$1 mJy, and, for wavelengths greater than 160 μm, the number counts decrease more steeply as the wavelength increases. CT AGN dominate the counts on the brighter side of the peak and type 2 AGN dominate the lower flux level side of the peak.

The star formation redshift evolution model contribution to the CIRB is shown in red in figure 4.13. The AGN contribution to the CIRB at 160μm is $\sim$5%. CT AGN dominate the AGN contribution to the CIRB at wavelengths greater than $\sim$100 μm, with type 2 AGN dominating at lower wavelengths. The AGN contribution to the CIRB for this model peaks at $\sim$320 μm, a significantly longer wavelength than the peak of the CIRB as a whole.

The ρ_{IR}^{LIRG} and ρ_{IR}^{ULIRG} for the star formation redshift evolution model are very similar to those for the constant star formation scenario, as shown by the red lines in figure 4.14. The total ρ_{IR} of the star formation redshift evolution model under-predicts the observed local ρ_{IR} but evolves more strongly with redshift than the constant star formation scenario.

4.4.4 Evolution with Redshift and AGN L_X

The final star formation scenario investigated here is the redshift and AGN L_X dependent star formation scenario used by Wilman et al. (2010), where

$$SFR \propto \sqrt{L_X/10^{43}}(1.0+z)^{1.6}. \tag{4.7}$$

Type 1 AGN are given the normalization constant 0.63 $M_\odot$ yr^{-1} and for type 2 AGN the normalization prefactor is increased to 2.0 $M_\odot$ yr^{-1} (Wilman et al., 2010). High Eddington ratio CT AGN are given the type 2 SFR and low Eddington ratio CT AGN are given the type 1 SFR, for the reasons discussed in §4.4.2.

The Euclidean normalized differential number counts for the redshift and AGN L_X dependent SFR model are shown as blue lines in figures 4.7, 4.8, 4.9, 4.10, 4.11, and 4.12 and are in decent agreement with the predictions made by Wilman et al. (2010) based on a simulation of the extragalactic radio sky. The differential number counts increase with increasing flux level until peaking at 1–3 mJy, depending on wavelength. The peak of the number counts appears to increase with wavelength, with the peak at $\sim$1 mJy at 100 μm and $\sim$3 mJy at 350 μm. The number counts decrease from the peak to the brighter flux

levels. At 100, 350, and 500 μm CT AGN dominate the number counts on the brighter side of the peak, but at 70, 160, and 250 μm type 2 AGN dominate except for at the brightest flux levels, $\gtrsim$10 mJy.

The blue lines in figure 4.13 show the AGN contribution to the CIRB for the redshift and AGN L_X dependent SFR model. This model predicts $\sim$5% of the CIRB at 160 μm is due to AGN. Type 2 AGN dominate the AGN contribution to the CIRB at all wavelengths and CT AGN make a significant contribution. For this model the AGN contribution to the CIRB peaks at $\sim$300 μm, which is significantly different from the peak of the total CIRB around 160 μm.

In figure 4.14 the ρ_{IR} for the redshift and L_X dependent SFR model is shown in blue. This model is in decent agreement with the ρ_{IR}^{LIRG} at all redshifts but over-predicts the local ρ_{IR}^{ULIRG} and under-predicts the local total ρ_{IR}. Both the total ρ_{IR} and ρ_{IR}^{ULIRG} predictions are in agreement with observations at moderate redshifts, but do not evolve strongly enough with redshift to be in agreement with observations at the highest redshift.

4.5 Discussion

I have presented predictions for observations of AGN and AGN hosts in the FIR *Herschel* bands based on the composite model by Draper & Ballantyne (2010). These findings demonstrate that while AGN may not contribute a large fraction of the CIRB, AGN will be significant FIR sources and care must be taken in FIR surveys to identify AGNs as such. Here the implications of these results are discussed in terms of AGN and AGN host demographics.

4.5.1 CT AGN

A substantial population of CT AGN are necessary for AGN population synthesis models to match the peak of the XRB at $\sim$30 keV (e.g., Ballantyne et al., 2006a; Treister et al., 2009b; Draper & Ballantyne, 2010). Due to the extreme levels of obscuration in CT AGN, these elusive sources are generally only observed in the very hard X-ray, $>$ 10 keV, or the infrared, especially the FIR. Using X-ray stacking methods, it has been shown that a large fraction of bright infrared excess sources ($f_{24}/f_R > 1000$) host heavily obscured AGN (e.g., Daddi

et al., 2007; Fiore et al., 2009; Treister et al., 2009a). However, it is uncertain how many of these highly obscured AGN are actually CT (see Georgakakis et al., 2010; Georgantopolous et al., 2010). Also, there is much debate over the prevalence of AGN in sources with more moderate infrared luminosities (e.g., Dey et al., 2008; Donley et al., 2008; Fiore et al., 2009; Treister et al., 2009a, 2010). Because CT AGN are generally not observable in the 2–10 keV band, AGN hard X-ray luminosity functions do not include CT AGN and therefore they must added in by hand to population synthesis models. In the population synthesis model used in this study, CT AGN are assumed to be accreting at either at $L/L_{Edd} > 0.9$ or $L/L_{Edd} < 0.01$, with f_{CT} independent of f_2, as found by Draper & Ballantyne (2010). Here predictions specifically for CT AGN in the FIR are discussed.

At all wavelengths and for all star formation scenarios, the differential number counts are dominated by CT AGN for fluxes $\gtrsim$ 1–10 mJy. Type 2 AGN dominate at lower fluxes. Moreover, CT AGN, should constitute a non-trivial fraction of *Herschel* sources. Depending on the star formation scenario considered, CT AGN could make up $\sim$10% of *Herschel* sources, even at 500 μm.

Depending on the star formation scenario, CT AGN are found to contribute <5% of the CIRB at 160 μm. For bare AGN, CT AGN dominate the AGN contribution to the CIRB at wavelengths $\gtrsim$ 200 μm. When star formation is included, CT AGN dominate the AGN contribution to the CIRB at wavelengths $\gtrsim$ 100 μm for all star formation scenarios, except the Wilman et al. (2010) model.

Comparing the predictions made here against the infrared luminosity density found by Le Floc'h et al. (2005), it is found that CT AGN and their hosts contribute $\sim$3% of the local infrared luminosity density from sources with $L_{IR} > 10^{10}$ L$_\odot$ and nearly one-fourth of the infrared luminosity density from sources in the ULIRG range. In the AGN evolution star formation scenario, CT AGN can account for all of the local ULIRG range luminosity density. At $z \sim 1$ the relative CT AGN contribution decreases significantly in all luminosity ranges. However, when taking into account the stronger evolution of the SFR in high luminosity sources found by Serjeant et al. (2010), CT AGN and their hosts can still contribute nearly a quarter of the infrared luminosity density in the ULIRG range at $z \sim 1$.

Showing that at higher redshifts CT AGN contribute less to the total infrared luminosity density, but may still contribute quite significantly to the brightest sources.

The FIR is an important wavelength range for observing CT AGN due to the large amount of cold dust which obscures CT AGN. The majority of AGN observed by *Herschel* will be CT. Depending on the star formation trends in CT AGN hosts, CT AGN and their hosts may constitute nearly $\sim$10% of *Herschel* sources at 500 μm. The relative contribution of CT AGN and their hosts to the ULIRG range infrared luminosity density is $\lesssim$25% and appears to be approximately constant over the redshift range $z = 0$–1. However, Hatziminaoglou et al. (2010) showed that AGN cannot be identified by their *Herschel*-SPIRE colors alone. Therefore finding CT AGN in the FIR will require either *Spitzer*-MIPS coverage of bright SPIRE sources (Hatziminaoglou et al., 2010) or X-ray stacking. Since the AGN and host differential number counts for both the composite and original models are dominated by CT AGN in the SPIRE bands, X-ray stacking of bright SPIRE sources is likely to disclose a large fraction of the CT AGN population.

4.5.2 Differences Between Original and Composite Model

The difference between the original model and the composite model is that in the composite model the CT AGN are put in specific, physically motivated Eddington ratio bins. Also, in the original model $f_{CT} \propto f_2$, but in the composite model f_{CT} is independent of f_2. In order to understand the effects of the differences between the two models, the predictions of the original and composite model are compared for the constant star formation scenario.

In the differential number counts, the differences between the composite and original models are small but not insignificant. At all wavelengths the original model has a steeper decline in the bright end counts than the composite model. The original model predicts that the number counts will be dominated by type 2 AGN except for at the brightest fluxes. Conversely, in the composite model the differential counts are dominated by CT AGN at every wavelength for fluxes $\gtrsim$ 1 mJy.

The original model predicts a smaller overall AGN contribution to the CIRB than the composite model. In the composite model, CT AGN dominate the AGN contribution to

the CIRB at wavelengths greater than 100 μm, but in the original model the type 2 AGN dominate the AGN contribution to the CIRB at all wavelengths.

The original and composite models make similar predictions as to the AGN contribution to the infrared luminosity density in all luminosity ranges. The difference between these two models is most noticeable in the contribution of CT AGN to the local ULIRG range luminosity density. The original model predicts that CT AGN contribute 4% of the local ULIRG infrared luminosity density. The composite model predicts that nearly one-fourth of the local ULIRG infrared luminosity density is due to CT AGN.

The overall predictions of the original and composite models are in agreement. To observationally determine which model best describes the CT AGN population, rigorous measurements of the CT AGN contribution to the local infrared luminosity density and/or accurate accounting of *Herschel* number counts to see whether CT AGN or type 2 AGN dominate the number counts will be needed.

4.5.3 Star Formation in AGN hosts

As seen in figures 4.7, 4.8, 4.9, 4.10, 4.11, and 4.12, the star formation scenario used greatly affects the predicted differential number counts. At wavelengths $\lesssim$ 250 μm, the faint end slope is similar for all the star formation models investigated here, but the bright end slope is highly dependent on the host star formation at all wavelengths. The differences between the various star formation scenarios becomes more prominent when observing at longer wavelengths. The constant star formation model peaks at $\sim$ 1 mJy and has a relatively flat bright end slope. The AGN evolution star formation model peaks at $\gtrsim$ 10 mJy with a knee at $\sim$ 1 mJy. The redshift only evolution model peaks around, or just short of 1 mJy. This model also has the steepest faint and bright end slopes of the star formation scenarios considered here. The Wilman et al. (2010) star formation model peaks between 1 and 10 mJy for wavelengths $\gtrsim$ 100 μm. The flux level of the peak in the differential counts may be an important tool in understanding the evolution of SFR in AGN hosts. This tool will be most effective when observing at longer wavelengths.

Dust obscured star formation is the primary progenitor of the CIRB with much debate

as to the contribution from AGN. Ballantyne & Papovich (2007) found that AGN and star formation in AGN hosts can account for ∼30% of the CIRB at 70 μm. Similarly, Mullaney et al. (2010) find that AGN contribute 5–25% of the CIRB at 70 μm. However, at longer wavelengths it appears the AGN contribution reduces to $\lesssim$10% (Jauzac et al., 2010; Lacey et al., 2010). In this work it was found that AGN and host star formation contribute ∼5% of the CIRB at 160 μm. However, when investigating the submillimeter properties of X-ray-selected AGN, Lutz et al. (2010) found the average AGN SFR to be ∼30 $M_\odot$ yr^{-1}, in which case AGN and their hosts would contribute ∼88% of the CIRB at 160 μm. Therefore, understanding the star formation trends in AGN hosts is necessary for understanding how significant the contribution of AGN and their hosts is.

The peak intensity of the CIRB occurs at ∼160 μm. The star formation scenarios investigated here which take into account the evolution of the SFR with redshift predict the peak of the AGN contribution to the CIRB occurs at ∼300μm. This suggests that the SFR of AGN hosts evolves differently with redshift than the SFR of normal galaxies. This effect could also be explained if the star formation SEDs used here are on average too cold, which is unlikely. If it is true that the SFR of AGN hosts evolves differently than the SFR of normal galaxies, this could offer important insights into the role of the AGN in the host galaxy evolution. At wavelengths shorter than the peak of the CIRB, the dominate contribution is from sources $z < 1$. Sources at $z > 2$ tend to dominate at wavelengths longer than 500 μm.

Another tool used to study different AGN host star formation scenarios is the infrared luminosity density. Using simulations, Hopkins et al. (2010) find that AGN contribute 1-5% of the total infrared luminosity density at all redshifts. Applying the classification scheme of Yuan et al. (2010) to AKARI sources, Goto et al. (2010b) find that AGN contribute ∼20% of the total infrared luminosity density, ∼40% of the luminosity density from sources in the LIRG range, and $\gtrsim$90% of the luminosity density of sources in the ULIRG range, regardless of redshift. When considering the infrared luminosity density as measured by Le Floc'h et al. (2005), it is found that the AGN and host galaxy contribution to the local infrared luminosity density is approximately a factor of 2 smaller than that found by Goto et al.

(2010b). At $z \sim 1$ the relative AGN contribution decreases to $\lesssim$5% for all luminosity ranges. Even when taking into account the stronger evolution of the SFR in high luminosity sources found by Serjeant et al. (2010), it appears that AGN and their hosts only contribute ∼25% of the infrared luminosity density in the ULIRG luminosity range at $z \sim 1$. The reduction in the AGN contribution to the ULIRG range infrared luminosity density by a factor of 2 between $z \sim 0$ and $z \sim 1$, is consistent with the findings of Sturm et al. (2010) that ULIRG level luminosities can be achieved without major mergers at higher redshifts, suggesting that the AGN fraction in the high redshift ULIRG population will be smaller than that found locally.

Determining the star formation history of AGN hosts is important in understanding why some galaxies host active supermassive black holes (SMBHs) and other galaxies host inactive SMBHs. The predictions presented here show that the flux level of the differential number counts peak in longer wavelength bands will be a helpful tool in determining the star formation history of AGN hosts. By comparing the peak wavelength of the AGN contribution to the CIRB to the peak wavelength of the CIRB, it is possible to determine if the star formation evolution of AGN hosts is different from that of normal galaxies. Also, at higher redshift AGN will have a smaller contribution to the ULIRG population, and that contribution will be dominated by CT AGN.

4.5.4 Eddington Ratio Breakdown

By using $d\Phi_\lambda(L_X, z)/d\log L_X$, the evolving Eddington ratio space density computed by Draper & Ballantyne (2010), instead of a traditional luminosity function, it is possible to make predictions for the contribution of AGN with different Eddington ratios. In figures 4.15 and 4.16 the composite model Euclidean normalized differential counts are shown for the AGN evolution star formation model at 160 and 500 μm with the relative contributions from the different Eddington ratio bins shown. The blue lines show the contribution from AGN with $L/L_{Edd} < 0.01$. The green lines show the contribution from AGN with $0.01 < L/L_{Edd} < 0.9$. The contribution from high Eddington ratio sources is shown in red. For all but the AGN evolution scenario, the number counts are dominated by low Eddington

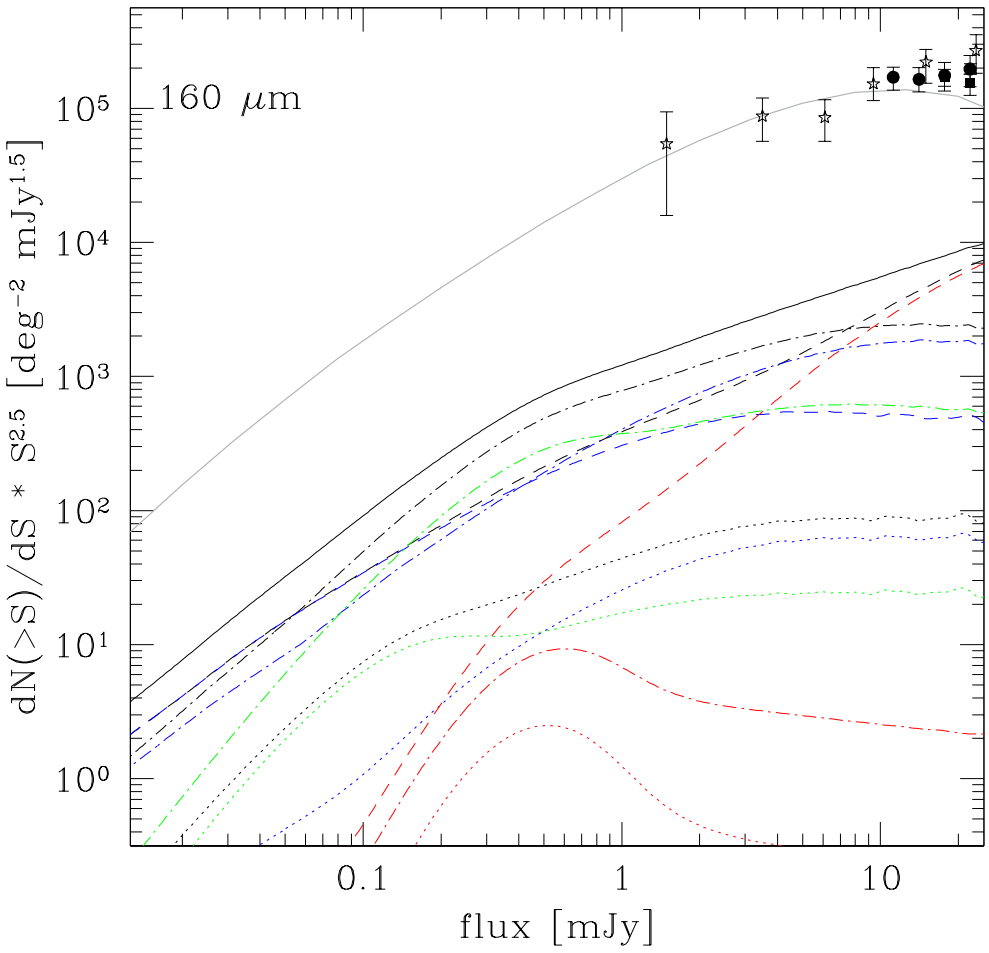

Figure 4.15: Euclidean normalized differential number counts for AGN and host star formation at 160 μm for the AGN evolution star formation model. Black lines show the total predictions for the composite model with the low Eddington ratio sources in blue, the mid Eddington ratio sources in green, and the high Eddington ratio sources in red. The line styles are the same as in figure 4.3. The solid grey lines shows the best fit model galaxy differential number counts of Franceschini et al. (2010). the Data points are the same as in figure 4.7.

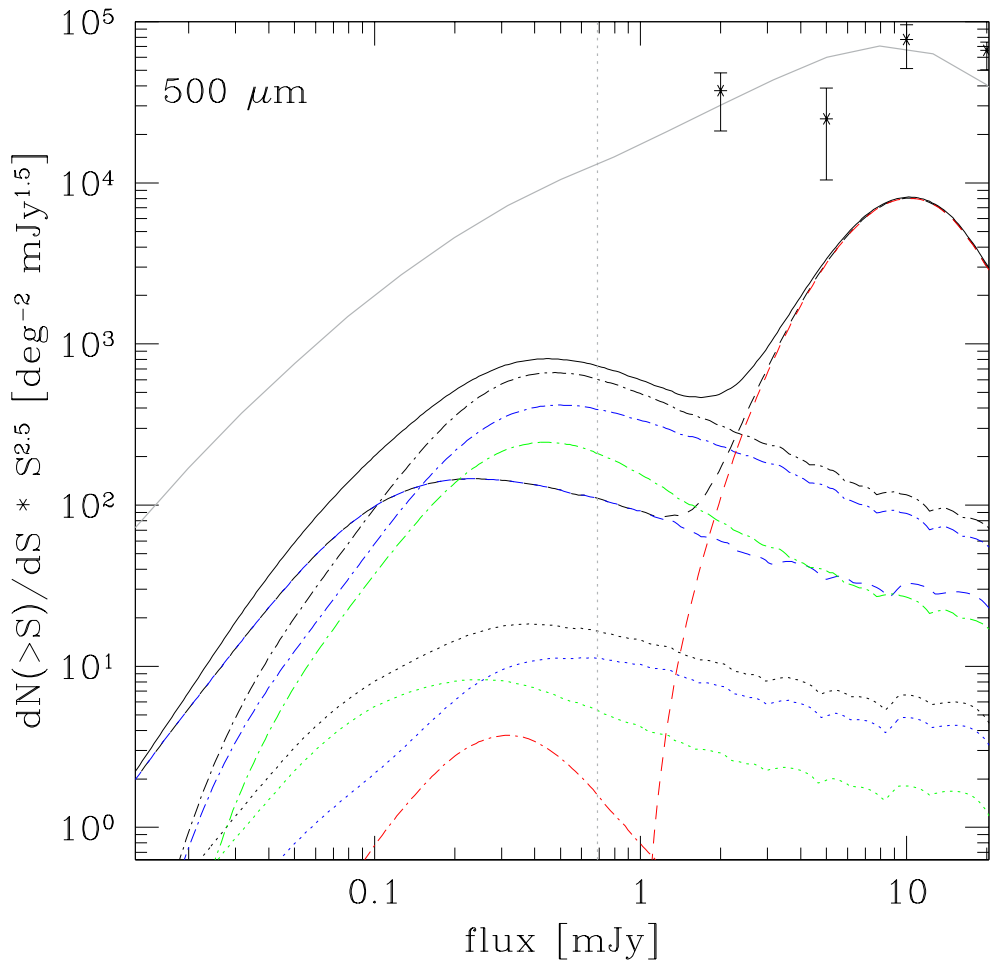

Figure 4.16: Euclidean normalized differential number counts for AGN and host star formation at 160 μm for the AGN evolution star formation model. Line colors and styles are the same as in figure 4.15 with the addition of the dotted grey line which shows the expected continuum sensitivity of ALMA for an integration time of 60 seconds and a spectral resolution of 1 km/s. Data points are the same as in figure 4.10. At bright fluxes numerical artifacts are present due to the small number of sources in this flux region.

ratio AGN at all flux levels, due to the high space density of low accretion rate AGN at all redshifts. As shown in figures 4.15 and 4.16, the AGN evolutionary scenario bright end counts are dominated by high Eddington ratio CT AGN because of the high star formation rate in these objects.

For all star formation scenarios the low Eddington ratio sources dominate the AGN contribution to the CIRB at wavelengths $\gtrsim 100$ μm. The AGN contribution to the infrared luminosity density is dominated by moderate Eddington ratio AGN at all luminosity levels for all star formation scenarios except the AGN evolution star formation model, where the high Eddington ratio sources dominate the ULIRG range. The star formation scenarios that do not include redshift evolution find that low Eddington ratio sources dominate the AGN contribution to the local infrared luminosity density.

4.5.5 Implications for *Herschel* and ALMA

The three wide area surveys conducted by *Herschel* will yield a large catalog of AGN host galaxies. Using the planned survey depths and areas as described in Section 2.1, the models discussed here predict the following numbers of AGN hosts to be observed by the *Herschel* wide field surveys. Not including the planned lensing cluster observations, PEP should observe 100-500 AGN hosts, depending on the star formation scenario, at 160 μm with 5σ significance. The portion of HerMES conducted during the *Herschel* science demonstration phase should provide 140-2100 AGN hosts, depending on the star formation scenario, with 5σ significance at 250 μm. The H-ATLAS survey will yield 250-4000 AGN hosts at 160 μm and 90-1200 AGN hosts at 350 μm with 5σ significance. The H-ATLAS observed AGN host counts drop to 30-230 in the 500 μm band. This catalog of sources will provide a robust sample to better constrain the star formation properties of AGN hosts.

Hatziminaoglou et al. (2010) showed that AGN cannot be differentiated from normal galaxies based only on their FIR colors; therefore, ALMA will only be able to offer supplementary data on AGN which are identified in other wavelength bands. The wide area surveys conducted by *Herschel* will provide many promising candidate targets for ALMA. The dotted grey lines in figures 4.11 and 4.12 show the sensitivity limit of the 350 and 450

μm ALMA bands, respectively, as quoted in section 2.1. Based on this projected sensitivity and the models presented here, the areal density of AGN hosts available to ALMA at 450 μm will be 300-1500 deg^{-2}, depending on the star formation scenario, for an integration time of only 60 seconds. Therefore, using ALMA to conduct follow up observations on X-ray selected AGN should be an efficient way to study star formation in AGN host galaxies. As discussed in section 4.5.3, the differential number counts for different star formation scenarios seem to peak at different flux levels. These peak fluxes become more differentiated at higher wavelengths. By providing deeper submillimeter observations of *Herschel* sources and X-ray selected AGN, ALMA should be able to determine the evolution of star formation in AGN hosts. This will allow the determination of the wavelength where the AGN contribution to the CIRB peaks, and therefore whether the star formation in AGN hosts evolves differently than in normal galaxies. Furthermore, since ALMA will be taking spectra, measurements such as gas velocity, abundances, and temperature can be made. This will allow ALMA to not only determine the evolution of star formation in AGN hosts, but also to probe the physical structure of AGN host galaxy star formation.

4.5.6 Evolution of AGN

From deep X-ray surveys it is known that high luminosity quasars and moderate luminosity AGN evolve differently with respect to redshift (e.g., Ueda et al., 2003). This would suggest that quasars and Seyferts are caused by processes with different time scales. Also, it appears that the Seyfert population is well described by the unified scheme, but the high luminosity AGN population may not follow the unified model (e.g., Ballantyne et al., 2006b; Lutz et al., 2010). A picture is starting to surface where the most powerful AGN are triggered by major mergers as explored in the simulations by Hopkins et al. (2006) and others, but most AGN are triggered by less violent processes (Ballantyne et al., 2006a). This picture is taken into account here by using the composite model of Draper & Ballantyne (2010) to describe the CT AGN fraction as Eddington ratio dependent. The difference in triggering process will also affect the star formation within the host galaxy. Mergers will engender not only AGN activity but also bursts of star formation, where as the more secular evolution

experienced by moderate power AGN will induce moderate, constant star formation.

This AGN evolution scenario was further explored here with the AGN evolution star formation scenario. In this scenario, high Eddington ratio CT AGN hosts were assigned SFR = 175 $M_\odot$ yr^{-1}. The differential counts for this star formation scenario show a large peak $\gtrsim$ 10 mJy. However, the high Eddington CT AGN account for $>$ 100% of the local ULIRG range infrared luminosity density measured by Le Floc'h et al. (2005). If the SFR in high Eddington ratio CT AGN hosts is reduced to 100 $M_\odot$ yr^{-1}, then AGN will contribute 80% of the local ULIRG range infrared luminosity density, with a larger contribution to the local LIRG range infrared luminosity density. The prominent peak in the differential counts at $\sim$ 10 mJy persists, despite the reduced SFR in high Eddington ratio CT AGN. Therefore, a test of the AGN evolution scenario will be if the observed differential counts feature a strong bright end peak, possibly with a knee at moderate fluxes. As a large fraction of the sources contributing to this peak will be CT AGN, the AGN samples used for this test will have to be chosen very carefully.

4.6 Summary

FIR observations by telescopes like *Herschel* and ALMA will provide important insights on many questions about AGN and their hosts. Determining the flux level at which the differential AGN and host number counts peak will offer crucial constraints to the star formation history of AGN hosts, especially when observing at wavelengths at $\sim$500 μm. The predictions presented here show that it is likely that the SFR in AGN hosts evolves differently than the SFR in normal galaxies, as indicated by the peak wavelength of the AGN contribution to the CIRB being significantly longer than the peak wavelength of the CIRB. Understanding how the SFR evolution in active galaxies differs from quiescent galaxies will provide clues on the triggering mechanisms of AGN and how the AGN interacts with the host galaxy. FIR observations will also allow the AGN evolution scenario to be tested by comparing SFRs in bright AGN with different levels of obscuration. The relative contributions of AGN with various levels of obscuration to the bright end differential counts will also be an important test of the major merger trigger model. Applying X-ray stacking

techniques to bright 350 or 500 μm sources, especially sources with a hot dust component in the SED, will be an efficient way of finding CT AGN.

4.7 References

Alexander, D.M., Bauer, F. E., Chapman, S. C., et al. 2005a, ApJ, 632, 736

Alexander, D.M., Smail, I., Bauer, F.E., et al. 2005b, Nature, 434, 738

Alonso-Herrero, A., Pérez-González, P.G., Rigby, J., et al. 2004, ApJS, 154, 155

Altieri, B., Berta, S., Lutz, D., et al. 2010, A&A, 518, L17

Amblard, A., Cooray, A., Serra, P., et al. 2010, A&A, 518, L9

Antonucci, R. 1993, ARA&A, 31, 473

Ballantyne, D.R. & Papovich, C. 2007, ApJ, 660, 988

Ballantyne, D.R. 2008, ApJ, 685, 787

Ballantyne, D.R., Everett, J.E., & Murray, N. 2006a, ApJ, 639, 740

Ballantyne, D.R., Shi, Y., Rieke, G.H., et al. 2006b, ApJ, 653, 1070

Berta, S., Magnelli, B., Lutz, D., et al. 2010, A&A, 518, L30

Béthermin, M., Dole, H., Beelen, A., & Aussel, H. 2010, A&A, 512, 78

Bongiovanni, Á., Oteo, I., Cepa, J., et al. 2010, A&A, 519, L4

Brand, K., Dey, A., Weedman, D., et al. 2006, ApJ, 644, 143

Buchanan, C.L., Gallimore, J.F., O'Dea, C.P., et al. 2006, AJ, 132, 401

Daddi, E., Alexander, D.M., Dickinson, M., et al. 2007, ApJ, 670, 173

Dey, A., Soifer, B.T., Desai, V., et al. 2008, ApJ, 677, 943

Dole, H., Lagache, G., Puget, J.-L., et al. 2006, A&A, 451, 417

Donley, J.L., Rieke, G.H., Alexander, D.M., Egami, E., Pérez-González, P.G. 2010, ApJ, 719, 1393

Donley, J.L., Rieke, G.H., Pérez-González, P.G., & Barro, G. 2008, ApJ, 687, 111

Draper, A.R. & Ballantyne, D.R. 2009, ApJ, 707, 778

Draper, A.R. & Ballantyne, D.R. 2010, ApJ, 715, L99

Eales, S., Dunne, L., Clements, D., et al. 2010, PASP, 122, 499

Elvis, M., Wilkes, B.J., McDowell, J.C., et al. 1994, ApJS, 95, 1

Ferland, G.J., Korista, K.T., Verner, D.A., et al. 1998, PASP, 110, 761

Finkbeiner, D.P., Davis, M., & Schlegel, D.J. 2000, ApJ, 544, 81

Fiore, F., Grazian, A., Santini, P., et al. 2008, ApJ, 672, 94

Fiore, F., Puccetti, S., Brusa, M., et al. 2009, ApJ, 693, 447

Franceschini, A., Rodighiero, G., Vaccari, M., et al. 2010, A&A, 517, 74

Fu, H., Yan, L., Scoville, N.Z., et al. 2010, ApJ, 722, 653

Gandhi, P., Horst, H., Smette, A., et al. 2009, A&A, 502, 457

Georgakakis, A., Rowan-Robinson, M., Nandra, K., et al. 2010, MNRAS, 406, 420

Georgantopolous, I., Rovilos, E., Xilouris, E.M., Comastri, A., & Akylas, A., 2011, A&A, 526, 86

Glenn, J., Conley, A., Béthermin, M., et al. 2010, MNRAS, 409, 109

Goto, T., Takagi, T., Matsuhara, H., et al. 2010a, A&A, 514, 6

Goto, T., Arnouts, S., Inami, H., et al. 2010b, MNRAS, 410, 573

Griffin, M.J., Abergel, A., Abreu, A., et al. 2010, A&A, 518, L3

Hasinger, G. 2008, A&A, 490, 905

Hatziminaoglou, E., Fritz, J., & Jarrett, T.H., 2009, MNRAS, 399, 1206

Hatziminaoglou, E., Omont, A., Stevens, J.A., et al. 2010, A&A, 518, L33

Hauser, M.G., Arendt, R.G., Kelsall, T., et al. 1998, ApJ, 508, 25

Hinshaw, G., Weiland, J.L., Hill, R.S., et al. 2009, ApJS, 180, 225

Holland, W., MacIntosh, M., Fairley, A., et al. 2006, SPIE, 6275, 45

Hönig, S.F., Kishimoto, M., Gandhi, P., et al. 2010, A&A, 515, 23

Hopkins, P.F., Hernquist, L., Cox, T.J., et al. 2006, ApJS, 163, 1

Hopkins, P.F., Younger, J.D., Hayward, C.C., Narayanan, D., & Hernquist, L. 2010, MNRAS, 402, 1693

Houck, J.R., Soifer, B.T., Weedman, D., et al. 2005, ApJ, 622, L105

Ibar, E., Ivison, R.J., Cava, A., et al. 2010, MNRAS, 409, 38

Jauzac, M., Dole, H., Le Floc'h, E., et al. 2011, A&A, 525, 52

Juvela, M., Mattila, K., Lemke, D., et al. 2009, A&A, 500, 763

Kelly, B.C., Vestergaard, M., Fan, X., et al. 2010, ApJ, 719, 1315

Kennicutt, R.C. 1998, ARA&A, 36, 189

Khan, S.A., Shafer, R.A., Serjeant, S., et al. 2007, ApJ, 665, 973

Kim, M., Ho, L.C., Im, M. 2006, ApJ, 642, 702

Lacey, C. G., Baugh, C. M., Frenk, C. S., et al. 2010, MNRAS, 405, 2

Laird, E.S., Nandra, K., Pope, A., & Scott, D. 2010, MNRAS, 401, 2763

Lagache, G. & Puget, J.L. 2000, A&A, 355, 17

Laor, A. & Draine, B.T. 1993, ApJ, 402, 441

Le Floc'h, E., Papovich, C., Dole, H., et al. 2005, ApJ, 632, 169

Lutz, D., Mainieri, V., Rafferty, D., et al. 2010, ApJ, 712, 1287

Lutz, D., Maiolino, R., Spoon, H.W.W., & Moorwood A.F.M. 2004, A&A, 389 93

Marconi, A., Risaliti, G., Gilli, R., et al. 2004, MNRAS, 351, 169

Martínez-Sansigre, A., Karim, A., Schinnerer, E., et al. 2009, ApJ, 706, 184

Matsuura, S., Shirahata, M., Kawada, M., et al. 2010, ApJ, 737, 2

Mazin, D. & Raue, M. 2007, A&A, 471, 439

Mullaney, J. R., Alexander, D. M., Huynh, M., Goulding, A. D., & Frayer, D. 2010, MNRAS, 401, 995

Narayanan, D., Dey, A., Hayward, C.C., et al. 2010, MNRAS, 407, 1701

Netzer, H., Lutz, D., Schweitzer, M., et al. 2007, ApJ, 666, 806

Oliver, S.J., Wang, L., Smith, A.J., et al. 2010, A&A, 518, L21

Page, M.J., Stevens, J.A., Ivison, R.J., Carrera, F.J. 2004, 611, L85

Papovich, C., Dole, H., Egami, E., et al. 2004, ApJS, 154, 70

Parra, R., Conway, J.E., Aalto, S., et al. 2010, ApJ, 720, 555

Pascale, E., Auld, R., Dariush, A., et al. 2010, MNRAS, 415, 911

Patanchon, G., Ade, P.A.R., Bock, J.J., et al. 2009, ApJ, 707, 1750

Persson, C.M., Olofsson, A.O.H., Koning, N., et al. 2007, A&A, 476, 807

Pilbratt, G.L., Riedinger, J.R., Passvogel, T., et al. 2010, A&A, 518, L1

Poglitsch, A., Waelkens, C., Geis, N., et al. 2010, A&A, 518, L2

Rieke, G.H., Alonso-Herrero, A., Weiner, B.J., et al. 2009, ApJ, 692, 556

Rigby, J.R., Rieke, G.H., Maiolino, R., et al. 2004, ApJS, 154, 160

Rigopoulou, D., Mainieri, V., Almaini, O., et al. 2009, MNRAS400, 1199

Roseboom, I.G., Oliver, S.J., Kunz, M., et al. 2010, MNRAS, 409, 48

Rubio, M., Paron, S., & Dubner, G. 2009, A&A, 505, 177

Sanders, D.B., Soifer, B.T., Elias, J.H., et al. 1988, ApJ, 325, 74

Serjeant, S., Bertoldi, F., Blain, A.W., et al. 2010, A&A, 518 L7

Silva, L., Maiolino, R., & Granato, G.L. 2004, MNRAS, 355, 973

Soifer, B.T., Helou, G., & Werner M. 2008, ARA&A, 46, 201

Steffen, A.T., Strateva, I., Brandt, W.N., et al. 2006, AJ, 131, 2826

Sturm, E., Verma, A., Graciá-Carpio, J., et al. 2010, A&A, 518, L36

Treister, E., Cardamone, C.N., Schawinski, K., et al. 2009a, ApJ, 706, 535

Treister, E., Urry, C.M., Schawinski, K., Cardamone, C.N., & Sanders, D.B. 2010, ApJ, 722, L238

Treister, E., Urry, C.M., & Virani, S. 2009b, ApJ, 696, 110

Ueda, Y., Akiyama, M., Ohta, K., & Miyaji, T. 2003, ApJ, 598, 886

Veilleux, S., Kim, D.-C., Sanders, D. B., Mazzarella, J. M., & Soifer, B. T. 1995, ApJS, 98, 171

Weedman, D.W., Le Floc'h, E., Higdon, S.J.U., Higdon, J.L., & Houck, J.R. 2006, ApJ, 638, 613

Weingartner, J.C. & Murray, N. 2002, ApJ, 580, 88

Werner, M.W., Roellig, T.L., Low, F.J., et al. 2004, ApJS, 154, 1

Wilman, R.J., Jarvis, M.J., Mauch, T., Rawlings, S., & Hickey, S. 2010, MNRAS, 405, 447

Yan, L., Chary, R., Armus, L., et al. 2005, ApJ, 628, 604

Yuan, T.-T., Kewley, L.J., & Sanders, D.B. 2010, ApJ, 709, 884

CHAPTER V

THE YOUNG, THE OLD, AND THE DUSTY: STELLAR POPULATIONS OF AGN HOSTS

5.1 Introduction

It is known that all massive galaxies have a central supermassive black hole (SMBH) (e.g., Kormendy & Richstone, 1995). Yet it is unknown why only a small fraction of these SMBHs are actively accreting as active galactic nuclei (AGN). Several theories attempt to explain the fueling mechanism of AGN: major mergers (e.g., Sanders et al., 1988; Hopkins et al., 2006), minor mergers and gravitational instabilities within the host galaxy (e.g., Crenshaw et al., 2003; Kormendy & Kennicutt, 2004; Pierce et al., 2007; Shapiro et al., 2008), nuclear starbursts (e.g., Davies et al., 2007; Ballantyne, 2008), supernova explosions within nuclear starbursts (e.g., Chen et al., 2009; Kumar & Johnson, 2010), and collisions of warm halo clouds with the nuclear region (McKernan et al., 2010b). Given the large range of observed AGN properties, it is likely that different fueling mechanisms come into play for different AGN populations. Current observations suggest that powerful quasars are triggered by major mergers but moderate luminosity AGN are more likely to be triggered by stochastic fueling incidents (Ballantyne et al., 2006a; Hasinger, 2008; Hopkins & Hernquist, 2009; Lutz et al., 2010). However, it is not yet clear which fueling mechanisms are dominant in which portions of the AGN population.

The unified model of AGN (Antonucci, 1993) explains the different observed levels of AGN obscuration as a simple geometric effect. This model assumes that the central engines of all AGN are identical and the level of obscuration is dependent on the line of sight between the observer and the central engine. Thus type 2 AGN are obscured by column densities $N_H \gtrsim 10^{22}$ cm^{-2}, because the observer is looking through the dusty torus, in contrast to type 1 AGN which are unobscured ($N_H < 10^{22}$ cm^{-2}) because the observer is looking down

the throat of the dusty torus. Since the central engines are identical, it is expected that, on average, the host galaxies of various spectral types of AGN will be similar. However, different black hole fueling mechanisms are likely to lead to different relationships between the various spectral types of AGN. In the major merger AGN fueling paradigm, the AGN is triggered while deeply embedded in gas and dust and thus when the AGN first turns on, it is highly obscured. Eventually the radiation pressure pushes away the remaining gas and dust revealing an unobscured quasar (e.g., Page et al., 2004; Hopkins et al., 2006; Rigopoulou et al., 2009). In the major merger paradigm, type 1 and type 2 AGN have host galaxies which are in different evolutionary stages. Conversely, in the nuclear starburst fueling paradigm, type 1 and type 2 AGN hosts can be similar since on average the unified model can hold (Ballantyne, 2008). This shows that tests of the unified model can be used to explore which processes are viable options for AGN fueling and in which sections of the AGN population different mechanisms are relevant.

Classifying the host galaxies of Compton thick (CT) AGN, AGN with $N_H \gtrsim 10^{24}$ cm^{-2}, is of special interest. It is expected that a large fraction of AGN with CT levels of obscuration are in a young evolutionary stage characterized by rapid black hole and host bulge growth (Sanders et al., 1988; Fabian, 1999; Hopkins et al., 2006; Fabian et al., 2009; Draper & Ballantyne, 2010; Treister et al., 2010). Thus, understanding the host properties of CT AGN may offer special insight into the AGN triggering process and the formation of massive galaxies. Large samples of CT AGN are difficult to identify because, by definition, CT AGN suffer from extreme levels of obscuration (e.g., Ghisellini et al., 1994). Therefore, previous studies of AGN host galaxies have not been able to study the stellar populations of CT AGN.

Galaxy optical colors are often described in terms of the red sequence and the blue cloud, where objects located on the red sequence are characterized by massive older stellar populations and objects on the blue cloud are less massive and have young stellar populations and current star formation. Between the red sequence and the blue cloud is a lightly populated region referred to as the green valley. Some studies find that AGN feedback is connected to the shut down of host star formation (e.g., McKernan et al., 2010a; Bluck et al., 2011)

and thus certain types of AGN hosts preferentially reside in the green valley (e.g., Hickox et al., 2009; Griffiths & Stern, 2010; Wold et al., 2010; Smolčić & Riechers, 2011). Thus AGN activity is potentially a stage in galaxy evolution where feedback from the AGN could shut down star formation, causing the host galaxy to age from the blue cloud, across the green valley, and onto the red sequence (Faber et al., 2007; Schawinski et al., 2007). However, other studies find that the colors of an AGN and its host are more closely related to the amount of available obscuring material rather than the evolutionary stage of the host stellar population (Brusa et al., 2009; Georgakakis et al., 2009; Cardamone et al., 2010; Rovilos et al., 2011). Indeed, Cardamone et al. (2010) show that AGN are intrinsically bimodal in color and that many AGN which appear to be on the red sequence are actually located in the blue cloud once dust extinction is taken into account. Thus further investigation is necessary to establish the nature of AGN host galaxy stellar populations and the role of AGN feedback in regulating star formation. This point is especially salient as several possible AGN fueling mechanisms include either causal or concurrent star formation. Some studies even show that AGN obscuration may in part be due to nuclear starburst disks (e.g., Thompson et al., 2005; Davies et al., 2007; Ballantyne, 2008). In order to understand how host galaxy processes affect the central SMBH and the role of the central SMBH in host galaxy evolution, the nature of stellar populations of AGN hosts must be well understood.

As AGN hosts exhibit size-able object-to-object variability, it is difficult to elucidate trends in the AGN population by fitting individual objects. Thus, in order to study larger trends in AGN–host galaxy interactions, the average stellar properties of a large ensemble of AGN hosts is investigated here. To this end the stellar synthesis models of Bruzual & Charlot (2003) are used to explore the stellar populations of AGN hosts. As in previous studies (Ballantyne et al., 2006b; Draper & Ballantyne, 2011), the AGN SEDs are calculated using the photoionization code Cloudy (Ferland et al., 1998). The cosmic X-ray background (XRB) synthesis modeling framework is used to characterize the AGN population. The model SEDs are then used to move the XRB framework into other wavelength regions. This allows the space density and evolution of AGN host galaxies to be determined by the most comprehensive census of AGN activity. By comparing these models against various

observations in the optical through mid-infrared (mid-IR) spectral ranges, constraints are placed on the average stellar populations of type 1, Compton thin type 2 (here referred to simply as type 2), and CT AGN at various redshifts. In Section 5.2 the AGN spectral model and stellar population model are described. Section 5.3 presents the results of the model. In Sections 5.4 and 5.5 the results are discussed and summarized. AB magnitudes are used, unless otherwise stated, and $h = 0.7$, $\Omega_\Lambda = 1 - \Omega_M = 0.7$ is assumed as necessary.

5.2 The Model

5.2.1 Methodology

In order to study the average properties of AGN host galaxy stellar populations, a model is created which combines knowledge of AGN space density and evolution from deep X-ray surveys and XRB population synthesis models with stellar population studies. A model SED is computed which includes the emission from the AGN, the host galaxy stellar population, and ongoing dust enshrouded star formation. This AGN and host SED covers the wide spectral range of hard X-ray to mid-IR. The calculation of the AGN model SED is discussed in Section 5.2.3 and the details of the host stellar population model SED calculation are discussed in Section 5.2.4. To account for dust enshrouded star formation, the templates of Rieke et al. (2009) are used, which extend from 5 μm to 30 cm, and are determined by averaging empirical SEDs of local purely star forming galaxies. While dust enshrouded star formation may contribute to the galaxy SED at wavelengths shorter than 5 μm, generally the near IR AGN and host SEDs are dominated by either emission from the AGN or the Bruzual & Charlot (2003) portion of the host SED. Examples of the rest frame AGN and host SEDs are shown in Figure 5.1, where the dot-dashed lines show AGN SEDs, the dashed lines show stellar population SEDs, and the dotted lines show the Rieke et al. (2009) templates.

A Gaussian stellar mass (M_*) distribution was used with $M_*^{min} = 10^{9.5}$ $M_\odot$ and $M_*^{max} = 10^{12}$ $M_\odot$. The average M_* was set at $10^{10.9}$ $M_\odot$ with a standard deviation of 0.4 dex, in agreement with the sample of X-ray selected, $z \sim 1$ AGN hosts presented by Pierce et al. (2010). It is assumed that the mass-to-light ratio of the host galaxy is constant within

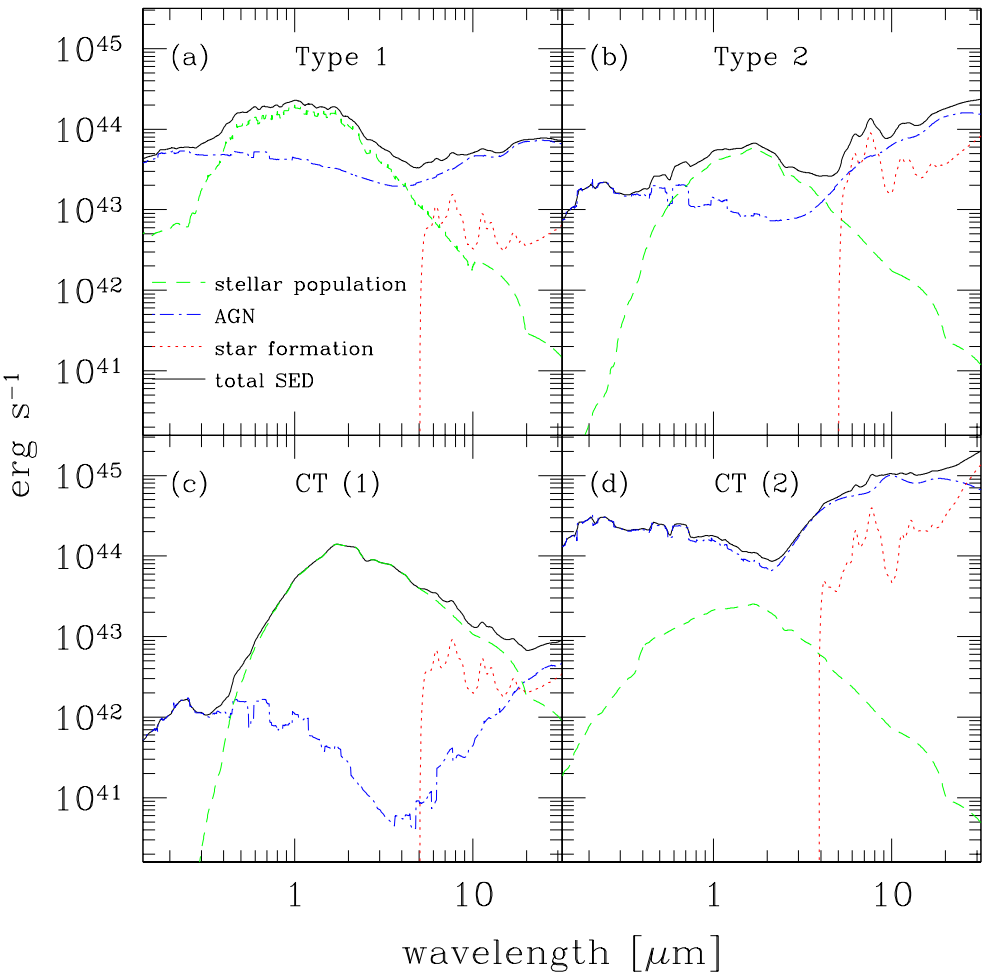

Figure 5.1: Smoothed AGN and host rest frame SEDs. Solid lines show the total AGN and host SED. Dot-dashed lines show AGN SEDs, dashed lines show Bruzual & Charlot (2003) stellar population model SEDs, and dotted lines show Rieke et al. (2009) dusty star formation templates. (a) type 1 AGN with $L_X = 10^{43}$ erg s^{-1}, a stellar population of $M_* = 10^{11}$ M$_\odot$ with 90% of M_* in a 4.5 Gyr old stellar population and 10% of M_* in a 2 Gyr old stellar population with $E(B-V) \approx 0.25$, and the $L_{IR} = 10^{10}$ L$_\odot$ dusty star formation template, corresponding to SFR ≈ 2 M$_\odot$ yr^{-1}. (b) type 2 AGN with $L_X = 10^{43}$ erg s^{-1}, the same stellar population as in (a) but with $E(B-V) \approx 0.50$, and the $L_{IR} = 10^{11}$ L$_\odot$ template, corresponding to SFR ≈ 17 M$_\odot$ yr^{-1}. (c) low Eddington ratio CT AGN with $L_X = 10^{42}$ erg s^{-1}, a 4.5 Gyr old stellar population of $M_* = 10^{12}$ M$_\odot$ with $E(B-V) \approx 1.0$, and SFR ≈ 1 M$_\odot$ yr^{-1}, corresponding to the $L_{IR} = 10^{9.75}$ L$_\odot$ template. (d) high Eddington ratio CT AGN with $L_X = 10^{44}$ erg s^{-1}, a 0.3 Gyr old stellar population of $M_* = 10^{10}$ M$_\odot$ with $E(B-V) \approx 0.50$, and the $L_{IR} = 10^{12}$ L$_\odot$ template, or SFR ≈ 175 M$_\odot$ yr^{-1}.

each waveband and thus the host galaxy flux scales linearly with the host M_*. Therefore, the stellar population SED is calculated for $M_* = 1$ $M_\odot$ and then re-normalized to $M_* = 10^{9.5}$ – 10^{12} $M_\odot$ before the stellar population and AGN SEDs are combined. Creating host SEDs at several masses in the AGN host mass spectrum allows the consideration of AGN and host colors for hosts of various masses. When considering space densities, however, it is important to consider not only the range of AGN host masses but also the probability that an AGN host be a certain M_*. The space density calculations presented are therefore weighted sums across the mass spectrum of AGN hosts where the weight is determined by the Gaussian M_* distribution described above. Specifically, when calculating luminosity functions and number counts the weighted sum over the Gaussian M_* distribution is used; however, when considering flux-flux plots, only the range of M_* is used. In agreement with current observational results, the M_* distribution used does not evolve with redshift (Bluck et al., 2011).

A variety of broad band data from the optical through mid-IR is used to constrain the host models. These model constraints are described in Section 5.2.5, and include mid-IR number counts, the J band AGN and host space density as a function of redshift and the absolute J band magnitude, M_J, and the type 1 AGN and host B band luminosity function. First, it is assumed that the unified model (e.g., Antonucci, 1993) holds and therefore, since all AGN are essentially the same system viewed along different lines of sight, there is only one class of AGN host galaxies.

5.2.2 XRB Synthesis Model

It is known that the XRB encodes the accretion history of SMBHs and as such is a powerful tool for scientific inquiry into accretion processes (Fabian & Barcons, 1992). The XRB synthesis model framework can be used in wavelength regions outside of the X-ray spectral region by modeling the SEDs of AGN and their host galaxies. Thus the advances in XRB synthesis modeling (e.g., Risaliti et al., 1999; Ballantyne et al., 2006a; Gilli et al., 2007; Treister et al., 2009b; Draper & Ballantyne, 2009) can be used to further the understanding of AGN at all wavelengths. Particularly, XRB synthesis models provide constraints on the

distribution of N_H, the fraction of type 2 AGN, f_2, and the fraction of CT AGN, f_{CT}. Here a simple N_H distribution is assumed where type 1 AGN are evenly distributed among $\log N_H$ = 20.0, 20.5, 21.0, 21.5, type 2 AGN are evenly distributed among $\log N_H$ = 22.0, 22.5, 23.0, 23.5, and CT AGN are evenly distributed among $\log N_H$ = 24.0, 24.5, 25.0. Ballantyne et al. (2006a) showed that this N_H distribution is consistent with XRB observations and provides results which are negligibly different from the observed N_H distribution of Risaliti et al. (1999) (Ballantyne et al., 2006a,b). The shape of the XRB combined with deep X-ray surveys has also been used to constrain f_2 (e.g., Ballantyne et al., 2006a). At a given L_X and redshift, $f_2 \propto (1+z)^a (\log L_X)^{-b}$ where $a = 0.4$ (Ballantyne et al., 2006a) and $b = 4.7$. The normalization of f_2 is set such that at $z = 0$ and $\log L_X = 41.5$, the type 2 to type 1 ratio is 4:1 (see Section 2.2 of Draper & Ballantyne, 2009).

Both the original and the composite model of CT AGN evolution of Draper & Ballantyne (2010) are considered. The original, non-evolving model assumes that CT AGN are a simple extension of the Compton thin type 2 AGN population and that, when assuming the Ueda et al. (2003) hard X-ray luminosity function, ∼44% of all obscured AGN are CT. In this model there is a population of CT AGN which are nearly as common as Compton thin type 2 AGN and which are in all ways similar to Compton thin type 2 AGN except for the presence of more obscuration along our line of sight. Contrastingly, the composite model assumes that CT AGN are a population of AGN distinct from the Compton thin type 2 AGN population. Simulations show that gas rich galaxy mergers will cause dust and gas to be funneled into the nuclear region of the galaxy, triggering star formation and accretion onto the central SMBH (e.g., Hopkins et al., 2006). Due to the large reservoir of material, the SMBH will accrete very rapidly and be very highly obscured (Fabian, 1999; Fabian et al., 2008, 2009). Thus it is expected that CT AGN are high Eddington ratio sources. Draper & Ballantyne (2010) found that if all CT AGN are rapidly accreting sources, than the local space density of CT AGN is under-predicted, and thus a population of low Eddington ratio CT AGN are necessary to explain the observed space density of CT AGN. These low accretion rate CT AGN are likely obscured by molecular clouds within the host bulge. Observational evidence of this low luminosity CT AGN population has been found in the local universe (Terashima

& Wilson, 2003; González-Martín et al., 2009). Furthermore, Draper & Ballantyne (2010) showed that if CT AGN have moderate Eddington ratios, the space density of CT AGN with $L_X > 10^{43}$ erg s^{-1} at $z \gtrsim 0$ is greatly over-predicted. Therefore, the evolving model of CT AGN has an Eddington ratio dependent f_{CT} with ∼86% of all AGN which are accreting at >90% of their Eddington rate being CT and ∼60% of all AGN which are accreting at <1% of their Eddington rate being CT. In this model CT AGN are a distinct population of AGN associated with specific stages of AGN evolution and f_{CT} evolves with both L_X, the AGN 2–10 keV luminosity, and redshift. Both the evolving model and the non-evolving model are consistent with the XRB and the local space density of CT AGN with $L_X > 10^{43}$ erg s^{-1} (Draper & Ballantyne, 2010).

5.2.3 AGN SEDs

In order to compute the model AGN SEDs, the photoionization code Cloudy version C08.00 (Ferland et al., 1998) is used, following the same procedure as in Section 2 of Draper & Ballantyne (2011). These SEDs cover the wavelength range of very hard X-ray through far-IR and include the transmitted AGN emission, the diffuse emission emitted along the line of sight by the obscuring material around the AGN, and the reflected emission off the inner face of the obscuring cloud. The inner radius of the obscuring material is assumed to be ∼10 pc. As in Draper & Ballantyne (2011), the obscuring clouds are assigned neutral hydrogen densities, n_H, in agreement with typical molecular clouds; the Compton thin clouds have $n_H = 10^4$ cm^{-3} and the Compton thick clouds have $n_H = 10^6$ cm^{-3}.

5.2.4 Host Galaxy Stellar Population Model

The host galaxy stellar populations are modeled using GALAXEV [1] (Bruzual & Charlot, 2003). This model calculates stellar population SEDs over the wavelength range of 91Å–160 μm. Using an isochrone synthesis technique, GALAXEV can evolve stellar populations with three stellar evolution library options. The stellar evolution models of the "Padova 1994" library and the stellar spectra of the STELIB/BaSeL 3.1 semi-empirical library are

[1] available at http://www. cida.ve/ bruzual/bc2003

Table 5.1: Ages of stellar populations in Gyr for various redshift bins.

	Type 1 and Type 2 AGN host		Low Eddington ratio CT AGN host[¶]	
z	YSP[†] ($0.1M_*$)	DSP[‡] ($0.9M_*$)	YSP[†] ($0.1M_*$)	DSP[‡] ($0.9M_*$)
$z < 0.5$	2.0	7.0	4.5	10
$0.5 < z < 1$	2.0	7.0	4.5	7.0
$1 < z < 2$	2.0	4.5	4.5	4.5
$2 < z < 3$	2.0	2.0	2.0	2.0
$3 < z$	1.0	1.0	1.0	1.0

[¶] The Low Eddington ratio CT AGN hosts are only relevant in the evolving model. The age of the stellar population of the evolving model high Eddington ratio CT AGN hosts is the same in all z bins and is shown in the bottom row of Table 5.2.
[†] Younger Stellar Population
[‡] Dominant Stellar Population

utilized in this study. GALXEV models can be computed for six different metallicities in the range $Z = 0.005\mathrm{Z}_\odot$ - $2.5\mathrm{Z}_\odot$. Both the Salpeter (1955) and Chabrier (2003) initial mass functions (IMFs) are available in the GALAXEV code. Here solar metallicity (Kauffmann et al., 2007; Silverman et al., 2009) and the Chabrier (2003) IMF (Silverman et al., 2009) are assumed. The sensitivity of the results to these assumptions is assessed in Section 5.3. GALAXEV also allows for a variety of star formation histories, including constant star formation rate, instantaneous bursts, and exponentially declining star formation rate. An exponentially declining star formation history (Kauffmann et al., 2007; Silverman et al., 2009) with an e-folding time of 0.5 Gyr is used here. This star formation history allows for a simple parametrization of the average age of the stellar population while not requiring the entire stellar population to be a single age. GALAXEV does not include re-radiation of energy absorbed by dust; however, the majority of this re-emission by cool dust occurs at wavelengths longer than those considered here.

The stellar population SEDs are computed in four different redshift bins: $z < 1$, $1 < z < 2$, $2 < z < 3$, and $3 < z < 5$, where z is the redshift. It is assumed that the host galaxy has a dominate stellar population (DSP) which is slightly younger than the average age of the universe in each redshift bin, and M_* is given by the Gaussian distribution described in

Table 5.2: Summary of the AGN host stellar population parameters for the working model of this study. The SFRs in parenthesis refer to the average SFR of the enhanced star formation sources.

AGN population	Stellar population age (Gyr)	$E(B-V)$ $z<1$	$E(B-V)$ $z>1$	SFR ($M_\odot$ yr^{-1})
Type 1 AGN	col 2 & 3 Table 5.1	0.25	0.05	2.0 (20)
Unified/type 2 AGN	col 2 & 3 Table 5.1	0.25	0.5	2.0 (20)
Non-evolving model CT AGN				
w/o enhanced star formation sources	1.0	1.0	1.0	10
w/ enhanced star formation sources	col 2 & 3 Table 5.1	0.25	0.5	2.0 (20)
Evolving model CT AGN				
Low Eddington ratio CT AGN	col 4 & 5 Table 5.1	1.0	1.0	1.0
High Eddington ratio CT AGN	0.3	0.6	0.6	175

Section 5.2.1. A younger stellar population (YSP) which accounts for $\sim 0.1 M_*$ (Kauffmann et al., 2007; Shi et al., 2009) is also included. The age of the YSP is selected such that $D_n(4000\text{Å}) \approx 1.5$ (Kauffmann et al., 2003; Silverman et al., 2009), using $D_n(4000\text{Å}) = f_{RC}/f_{BC}$, where f_{RC} is the flux in the 4000–4100 Å wavelength range and f_{BC} is the flux in the 3850–3950 Å wavelength range (Balogh et al., 1999). For the stellar population models used here, $D_n(4000\text{Å}) \approx 1.5$ corresponds to a stellar population age of $\sim$2 Gyr. The age of the YSP and DSP in each redshift bin is summarized in Table 5.1. At $z > 2$, the older and younger stellar populations are the same age and thus at $2 < z < 3$ the entire stellar population is 2 Gyr old and at $3 < z < 5$ the entire stellar population is 1 Gyr old. Extinction due to dust, as described by $E(B-V)$, is allowed to vary between redshift bins, but not within redshift bins. While in some objects the AGN emission is likely to be extincted by extended dust structures within the host galaxy (e.g., Martínez-Sansigre et al., 2010), this is not true for all objects. As this study focuses on modeling the average properties of AGN and their hosts, a detailed modeling of the complex geometry of obscuring material in individual sources is beyond the scope of this work. Thus, it is assumed here that all of the extinction suffered by the AGN emission occurs within a few tens of parsecs of the central engine. The dust which extincts the stellar population is not allowed to further extinct the AGN emission.

5.2.5 Model Constraints

A variety of data in a broad range of spectral regions was used to constrain the stellar population models. The number counts are computed at 3.6, 5.7, 8.0 and 24 μm and compared to the AGN observed by *Spitzer Space Observatory* in the GOODS fields with $f_{2-8} \gtrsim 1 \times 10^{-16}$ erg s^{-1} cm^{-2}, where f_{2-8} is the 2–8 keV flux (Treister et al., 2006). This X-ray flux limit is taken into consideration in the number counts calculated here, thus the number counts presented are computed for the same population probed by the observational data points. These number counts are dominated by type 2 AGN and their hosts and therefore are primarily useful to constrain the type 2 AGN host population. The number of sources at wavelength λ per square degree with flux greater than S, $N_\lambda(> S)$, is

found by

$$\begin{aligned} N_\lambda(>S) &= \frac{K_{sr}^{deg} c}{H_0} \\ &\times \int_{z_{min}}^{z_{max}} \int_{max(\log L_X^{min}, \log L_X^S)}^{\log L_X^{max}} \frac{d\Phi(L_X,z)}{d\log L_X} \frac{d_l^2}{(1+z)^2[\Omega_m(1+z)^3+\Omega_\Lambda]^{1/2}} d\log L_X dz, \end{aligned} \tag{5.1}$$

where $K_{sr}^{deg} = 3.05 \times 10^{-4}$ deg^2 sr^{-1}, $d\Phi/d\log L_X$ is the hard X-ray luminosity function of Ueda et al. (2003) or, when referring to the evolving model, is the evolving Eddington ratio space density calculated by Draper & Ballantyne (2010), in units of Mpc^{-3}, d_l is the luminosity distance, and $\log L_X^S$ is the 2–10 keV rest-frame luminosity which corresponds to the observed-frame flux S at redshift z.

As the number counts are dominated by type 2 AGN and their hosts, a separate data set must be used to constrain the type 1 AGN host stellar populations. The most obvious choice is the optical luminosity function for type 1 Seyferts and QSOs and their hosts. Using the X-ray luminosity function, the type 1 AGN and host B band luminosity function, $d\Phi_B/d(mag_B)$ can be calculated using the following equation:

$$\frac{d\Phi_B}{d(mag_B)} = (1.0 - f_2) \times \frac{d\Phi}{d(\log L_X)} \frac{d(\log L_X)}{d(mag_B)}. \tag{5.2}$$

This luminosity function is considered in three redshift bins — $z < 0.4$, $1.0 < z < 1.55$, and $1.55< z < 2.1$.

Further constraints were considered in order to rule out possible degeneracies between stellar population age and extinction due to absorption by dust. The first of these additional constraints was the AGN and host J band space density as a function of redshift in several M_J bins. First, the AGN and host J band luminosity function, $d\Phi_J/d(mag_J)$, must be calculated. This is done in the same manner as $d\Phi_B/d(mag_B)$ above. Therefore,

$$\frac{d\Phi_J(M_J,z)}{d(mag_J)} = A \times \frac{d\Phi}{d(\log L_X)} \frac{d(\log L_X)}{d(mag_J)}. \tag{5.3}$$

The normalization constant A depends on the AGN spectral type being considered. For type 1 AGN, $A = (1.0 - f_2)$, while for type 2 AGN, $A = f_2$, and for CT AGN, $A = f_{CT}$. For comparison with the J band AGN and host space density measured by Assef et al. (2011), $d\Phi_J/d(mag_J)$ is then binned into six M_J bins.

Additionally, the optical colors were considered in the form of the U-B versus M_B color-magnitude diagram (CMD). Also, it is well documented that AGN and their hosts tend to have X-ray to optical flux ratios of 0±1 (e.g. Alexander et al., 2001; Brandt et al., 2001; Rovilos et al., 2010), with CT AGN hosts generally falling below this ratio. Here the ratio between the soft X-ray flux, $f_{0.5-2}$, and the R band flux, f_R, $\log(f_{0.5-2}/f_R) = 0\pm1$ is used to ensure that the absolute optical fluxes are in agreement with observations.

5.2.6 Procedure

With all the necessary ingredients in place, I begin by assuming that the unified model holds, and therefore, on average, type 1, type 2, and CT AGN hosts are identical. The AGN space density, N_H distribution, type 1/type 2 AGN ratio, and f_{CT} are set by the XRB model used. The age of the stellar populations is assigned such that the dominant stellar population age is slightly less than the mean Hubble time in each redshift bin and a younger stellar population is assigned the age corresponding to the average observed $D_n(4000$ Å) for AGN host galaxies. The stellar population ages are summarized in Table 5.1. The host M_* distribution is Gaussian within the observed AGN host M_* range. The only free parameters are the host galaxy dust enshrouded star formation rate and the extinction due to dust. These two free parameters are used to fit the near and mid-IR AGN and host number counts. The dust enshrouded star formation rate is determined by cycling through the Rieke et al. (2009) templates in order of increasing infrared luminosity in steps corresponding to a change in SFR of $\sim$1 $M_\odot$ yr^{-1}, until the 24 μm number counts are over-estimated at all flux levels. The template of the highest luminosity to not over-estimate the mid-IR number counts is selected as the best fit template. The dust extinction in the Bruzual & Charlot (2003) models is set using the total effective V band optical depth obscuring young stars, τ_V. SEDs are created with τ_V = 0.0, 1.0, 2.0, 5.0, 7.5, 10, 15, 20, and 25. This corresponds to $E(B-V)$ = 0.0 - $\sim$1.0, with the exact values of $E(B-V)$ depending on the age of the stellar population. The $E(B-V)$ with a reduced χ^2, χ^2_{red}, closest to 1.0, with respect to the 35 number counts data points at 3.6 μm, 5.7 μm, 8.0 μm, and 24 μm, is selected as the best fit model. The resulting model is then compared to

the suite of optical and near IR observations described in Section 5.2.5 in order to evaluate the appropriateness of the model fit to observations. In this manner the average AGN host galaxy properties are elucidated without the complications which arise from object-to-object variability. Next, the assumption of the unified model is tested by considering the specific constraints for different spectral types. Multiple star formation scenarios and the evolution of f_2 are also considered.

5.3 Results

5.3.1 Unified Model of AGN Hosts

In this section, it is assumed that the unified model holds and therefore type 1, type 2, and CT AGN have, on average, identical host galaxies. First, the maximum dust enshrouded star formation rate (SFR) allowed by the near and mid-IR number counts for X-ray selected AGN observed by *Spitzer* in the GOODS fields, as reported by Treister et al. (2006), is determined. Figure 5.1 shows that the mid-IR emission is due primarily to the AGN and dust enshrouded star formation; therefore, fitting the 24 μm number counts can be used to set an upper limit on the average AGN host dust enshrouded SFR. In order to not over-estimate the AGN and host mid-IR number counts, the average AGN host must have a SFR $\lesssim 2$ M$_\odot$ yr^{-1}. This SFR is consistent with the findings of Ballantyne et al. (2006b), who found that an AGN host SFR ≈ 1 M$_\odot$ yr^{-1} provides a good fit to *Spitzer*'s measurement of the AGN contribution to mid-IR portion of the cosmic infrared background, and is similar to the SFR of local normal spiral galaxies (e.g., Lee et al., 2009). According to the Kennicutt (1998) relation, this SFR corresponds to an infrared star formation luminosity $L_{IR} \approx 10^{10}$ L$_\odot$.

Next, the dust content of the average AGN host galaxy is fixed by fitting the near IR AGN and host number counts. It is found that if the average AGN host has $E(B-V) \approx 0.5$, the near IR number counts are under-predicted. However, if the average AGN host has $E(B-V) \approx 0.4$, the near and mid-IR number counts are over-predicted. As it is known that higher redshift galaxies tend to be dustier than local galaxies (e.g., Dunne et al., 2003; Santini et al., 2010), it is assumed that $z < 1$ AGN hosts contain less dust than $z > 1$ AGN

hosts. If the average AGN host at $z < 1$ has $E(B-V) \approx 0.25$ and the average $z > 1$ AGN host has $E(B-V) \approx 0.5$, the predicted number counts are in good agreement with the near and mid-IR number counts observations, with $\chi^2_{red} = 1.2$. If the average $z < 1$ AGN host has $E(B-V) < 0.25$, the mid-IR number counts are over-predicted. In contrast, the model constraints are not very sensitive to the age of the older, dominant stellar population, which can be changed by $\sim$ 1 Gyr with only minor effects. The age of the younger stellar mass population is constrained to within $\sim$0.5 Gyr.

This unified model of AGN hosts is also in good agreement with the other model constraints. The J band AGN and host space density is in decent agreement with observations, as shown in Figure 5.2. The data points in Figure 5.2 show the results of Assef et al. (2011). At $z < 0.75$ the IR and X-ray selected AGN sample of Assef et al. (2011) was chosen using a specific selection criterion for optically extended sources. As the models used here do not account for the spatial extent of the AGN host galaxies, this exact selection criterion cannot be replicated. This gives rise to an obvious discrepancy between the model predictions presented here and the observed J band space density reported by Assef et al. (2011). Thus at $z < 0.75$ the AGN and host space density is over-predicted in magnitude bins of medium brightness and under-predict the fainter magnitude bins. Type 2 AGN hosts dominate the J band space density at $M_J >$ -26 for $z \gtrsim 0.75$, with type 1 AGN hosts dominating the brightest magnitude bins.

According to Figure 6 of Pierce et al. (2010), type 1 and type 2 AGN tend to be found in the 0.55 < U-B < 1.4 and -23.5 < M_B < -19 region of the CMD. This region of the CMD is well populated by the model adopted here as many combinations of AGN L_X and host galaxy M_* fit this criteria. Furthermore, the AGN and hosts fit the expected $\log(f_{0.5-2}/f_R)$ ratio, as shown by the green triangles in Figure 5.3. Thus the unified model of AGN hosts explains the average trends of AGN and host observations in the optical through mid-IR spectral regions.

In order to understand how well constrained these findings are, the same procedure is followed using a supersolar metallicity, $Z = 2.5Z_\odot$, a subsolar metallicity, $Z = 0.2Z_\odot$, and the Salpeter (1955) IMF. In all of these scenarios, it is found that the stellar ages described

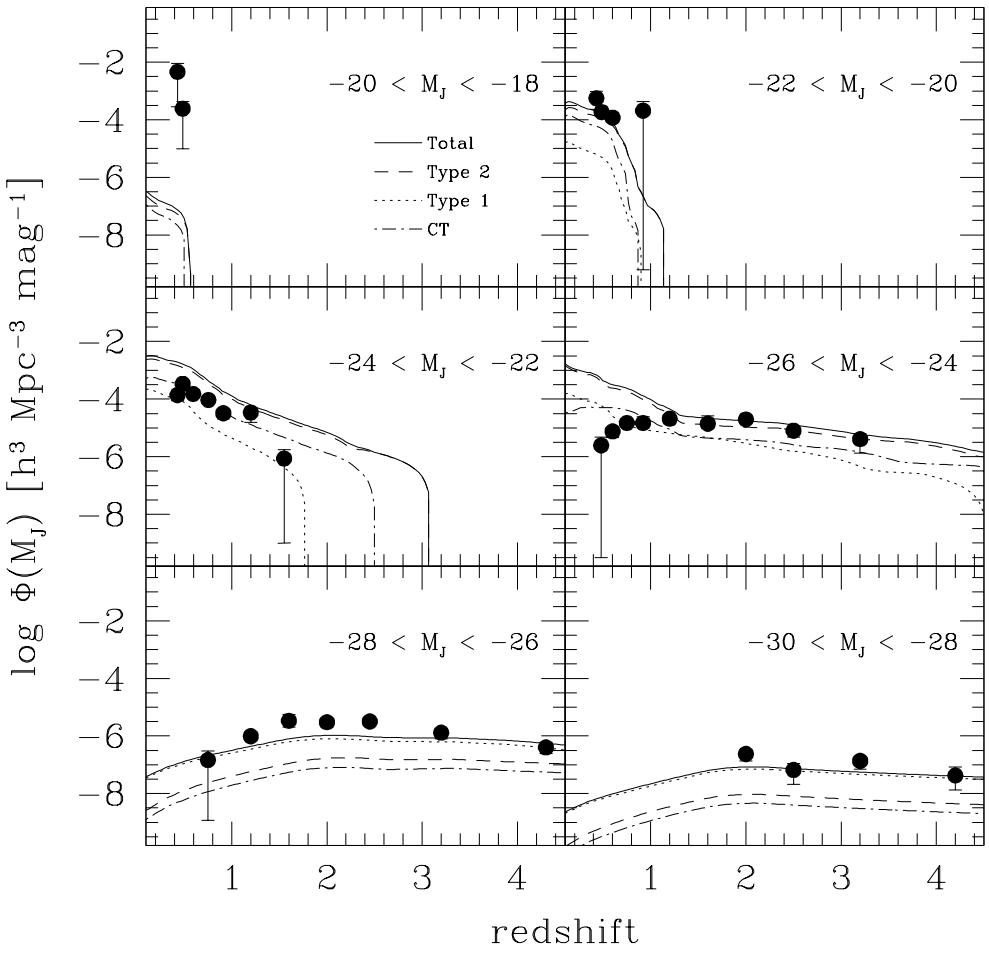

Figure 5.2: J band space density for AGN and hosts for the unified AGN host model. The black lines show the AGN and host J band space density for the model host galaxies described in row 2 of Table 5.2. The solid lines show the total AGN and host J band space density while the dotted lines show the space density for type 1 AGN and hosts, dashed lines show the space density for type 2 AGN and hosts, and dot-dashed lines show the CT AGN and host space density. Data from the mid-IR and X-ray selected AGN sample of Assef et al. (2011) is also shown. The obvious discrepancy at $z < 0.75$ between the model presented here and the observations reported by Assef et al. (2011) are primarily due to a selection criterion used by Assef et al. (2011) for optically extended sources at $z < 0.75$ which cannot be replicated here as the models do not contain information of the spatial extent of the host galaxies.

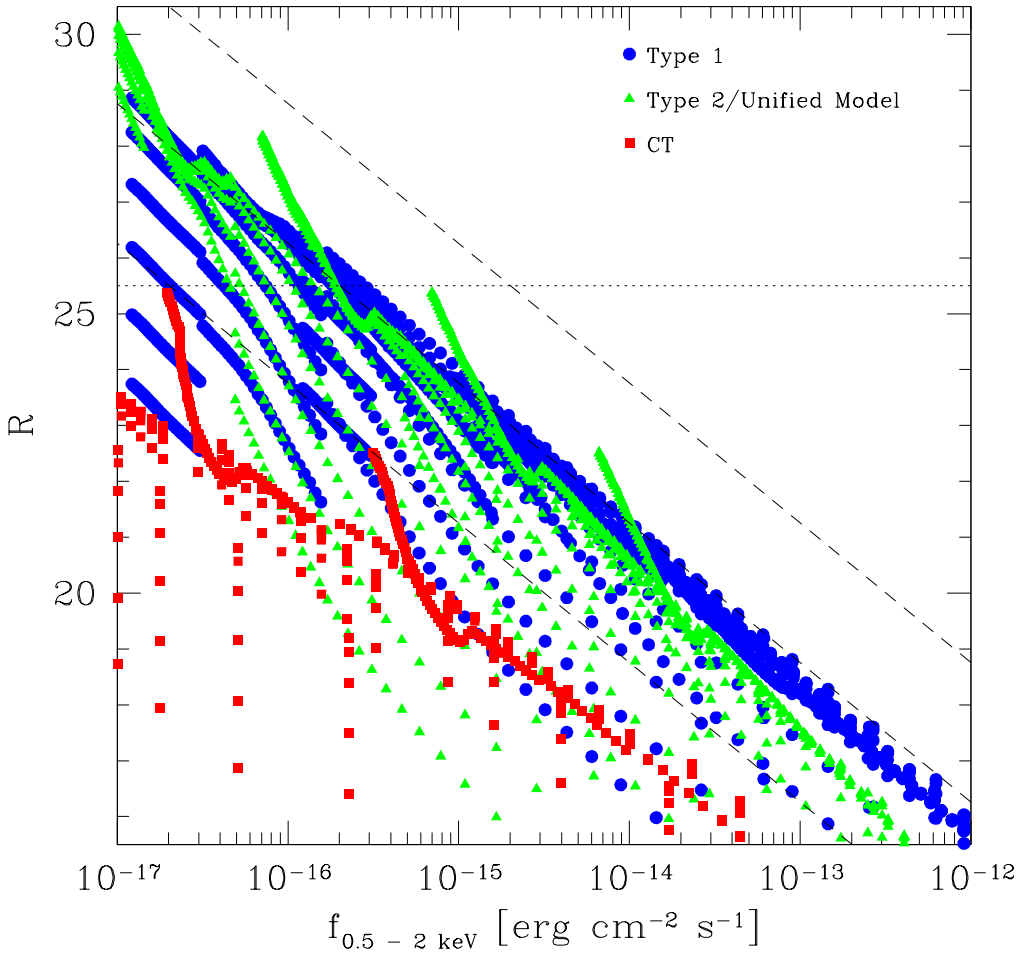

Figure 5.3: Soft X-ray flux versus R band magnitude for AGN and hosts for the non-evolving model. AGN and hosts are shown for $L_X < 10^{45}$ erg s^{-1}, $z < 3$, and $M_* = 10^{9.5}$, 10^{10}, $10^{10.5}$, 10^{11}, $10^{11.5}$, and 10^{12} M$_\odot$. The green triangles show the unified AGN hosts model and type 2 AGN and hosts, blue circles show type 1 AGN and hosts, and red squares show non-evolving model CT AGN and hosts. The model host galaxies shown here are described by the parameters in the first three rows of Table 5.2. The dashed lines show the empirical relationship $\log(f_{0.5-2keV}/f_R) = 0\pm1$. The horizontal dotted line marks $R = 25.5$, above which the source is considered an optically faint X-ray AGN.

Table 5.3: $E(B-V)$ for the different IMFs and metallicities considered. The first row summarizes the working model of this chapter.

Model		Unified/type 2 AGN host		Type 1 AGN host	
IMF	Metallicity	$z<1$	$z>1$	$z<1$	$z>1$
Chabrier (2003)	$Z_{\odot}$	0.25	0.5	0.25	0.05
Chabrier (2003)	$0.2Z_{\odot}$	0.3	0.5	0.3	0.1
Chabrier (2003)	$2.5Z_{\odot}$	0.2	0.7	0.1	0.05
Salpeter (1955)	$Z_{\odot}$	0.1	0.1	0.1	0.0

in Section 5.2.4 are able to fit the model constraints well; however different $E(B-V)$ values are necessary. The columns labeled "Unified/type 2 AGN host" in Table 5.3 summarize the $E(B-V)$ values for the different models considered. As the Rieke et al. (2009) templates are independent of the GALAXEV stellar population models, the average AGN host dust enshrouded SFR is not affected by changing the metallicity or IMF of the host galaxy stellar population.

Overall, the near and mid-IR AGN and host number counts, as well as the J band space density, optical colors, and X-ray to optical ratio of AGN and their hosts are in good agreement with observations if type 1, type 2, and CT AGN have, on average, similar host galaxies. Also, the near and mid-IR number counts require AGN hosts at $z>1$ be dustier than AGN hosts at $z<1$. I now investigate if this finding holds when spectral type specific model constraints are considered.

5.3.2 Type 1 AGN Hosts

In order to study the host galaxies of type 1 AGN, I begin by calculating the type 1 AGN contribution to the type 1 AGN and host B band luminosity function. The predicted AGN only B band luminosity function is shown as the dot-dashed lines in Figure 5.4, where black lines and data refer to $z<0.4$, blue lines and data refer to $1.0<z<1.55$, and red lines and data refer to $1.55<z<2.1$. The χ^2_{red} takes into account the 50 B band type 1 AGN and host B band luminosity function data points shown in Figure 5.4. When only the AGN contribution to the B band luminosity function is considered, $\chi^2_{red}=14$. It is clear that except for at the very brightest magnitudes, a contribution from the host galaxy is necessary

in order to fit the observed type 1 AGN and host B band luminosity function.

If the same stellar population described in Section 5.3.1 is used to calculate the type 1 AGN and host B band luminosity function, the predicted $z > 1$ luminosity functions are not in agreement with observations. The unified model gives a $\chi^2_{red} = 13$ fit to the B band luminosity function. This is shown by the dashed lines in Figure 5.4. For the $z < 0.4$ type 1 AGN and hosts, the lower limit $E(B-V)$ of the unified AGN host model B band luminosity function (solid black line in Figure 5.4) is in decent agreement with observations. As the type 2 AGN hosts are constrained by the IR AGN and host number counts as described in Section 5.3.1, this suggests that at $z < 1$, AGN hosts can be described by the unified AGN host model, but at $z > 1$ the unified AGN host model cannot properly predict the type 1 AGN and host B band luminosity function. Thus at $z > 1$, type 1 and type 2 AGN must be hosted by two distinct galaxy populations. The lowest χ^2_{red} with respect to the B band luminosity function is found when type 1 AGN hosts have $E(B-V) \approx 0.05$ at $z > 1$. For this model $\chi^2_{red} = 4.3$, which is not formally a good fit to the data points, but is dominated by the over-prediction of the two faintest Croom et al. (2004) data points at both $1.0 < z < 1.55$ and $1.55 < z < 2.1$. If these points are not included $\chi^2_{red} = 2.5$. As these data points refer to observations of faint AGN at high redshift, it is likely that the observational sample is not complete at these fluxes. Thus, at $z < 1$ type 1 and type 2 AGN hosts are similarly dusty. However, at $z > 1$, type 1 AGN hosts are less dusty than type 2 AGN hosts. Also, on average, it appears that type 1 and type 2 AGN hosts have similarly aged stellar populations, at least at $z < 2$, where the model can be well constrained.

The type 1 AGN host stellar population described above is in good agreement with the other model constraints considered. Figure 5.5 shows the number counts for type 1 AGN and their hosts as dotted lines. This model has a $\chi^2_{red} = 1.3$ with respect to the observed number counts. For the unified model, a $\chi^2_{red} = 1.2$ was found with respect to the IR number counts; thus reducing the dust extinction in type 1 AGN hosts at $z > 1$ has little effect on the total IR number counts. Type 1 AGN and hosts make a considerable contribution to the shorter wavelength number counts, but at mid-IR wavelengths they make a minimal contribution. Again shown as dotted lines, Figure 5.6 demonstrates that type 1 AGN and

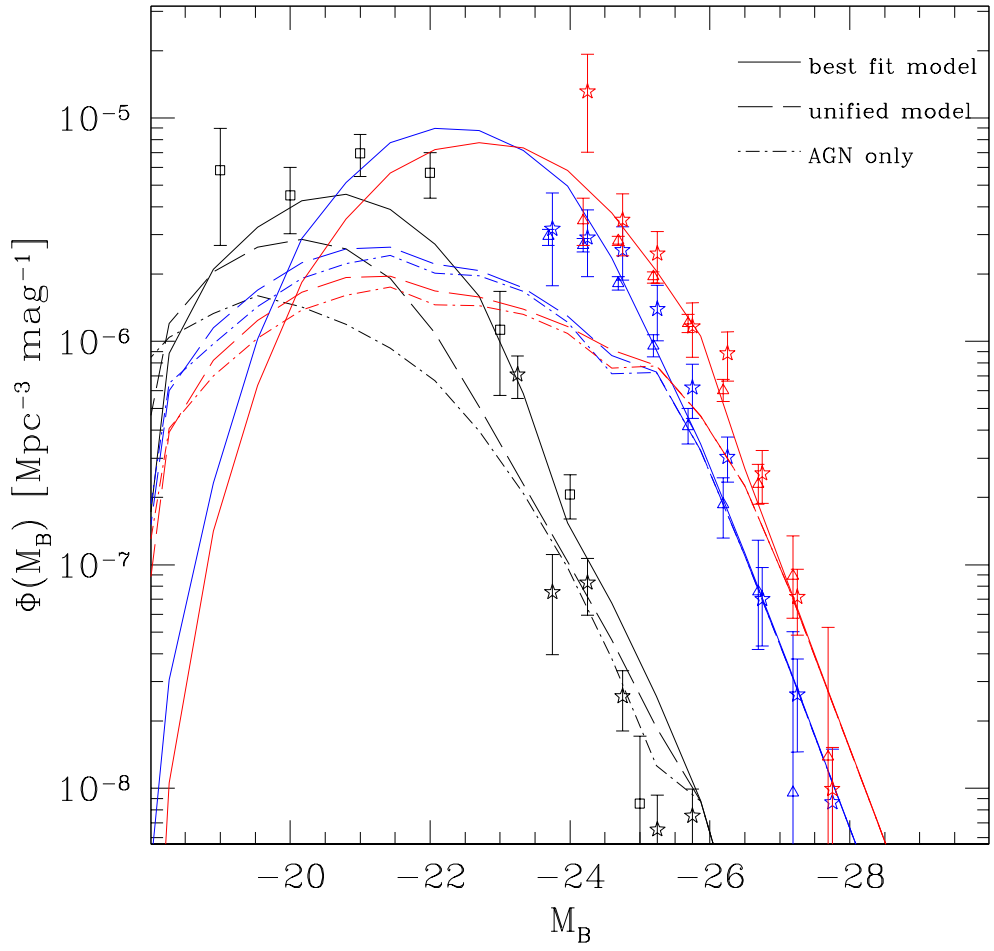

Figure 5.4: Type 1 AGN and host B band luminosity function. Different colors show the luminosity function in different redshift bins. Black lines and data refer to $z < 0.4$, blue lines and data refer to $1.0 < z < 1.55$, and red lines and data refer to $1.55 < z < 2.1$. The blue and red dashed lines show the luminosity function for the unified AGN host model as summarized in row one of Table 5.2. The black dashed line shows the dustiest average AGN host at $z < 1$ allowed by the unified AGN host model, $E(B-V) \approx 0.4$. The solid lines show the type 1 AGN host best fit model as summarized in row 2 of Table 5.2. The AGN contribution to the luminosity function is shown as the dot-dashed lines. Data points show various type 1 AGN and host B band luminosity functions from the literature: squares are from Della Ceca et al. (1996), triangles are from Croom et al. (2004), and stars are the $q_0 = 0.5$ luminosity function from Hartwick & Schade (1990) converted to the cosmology used here.

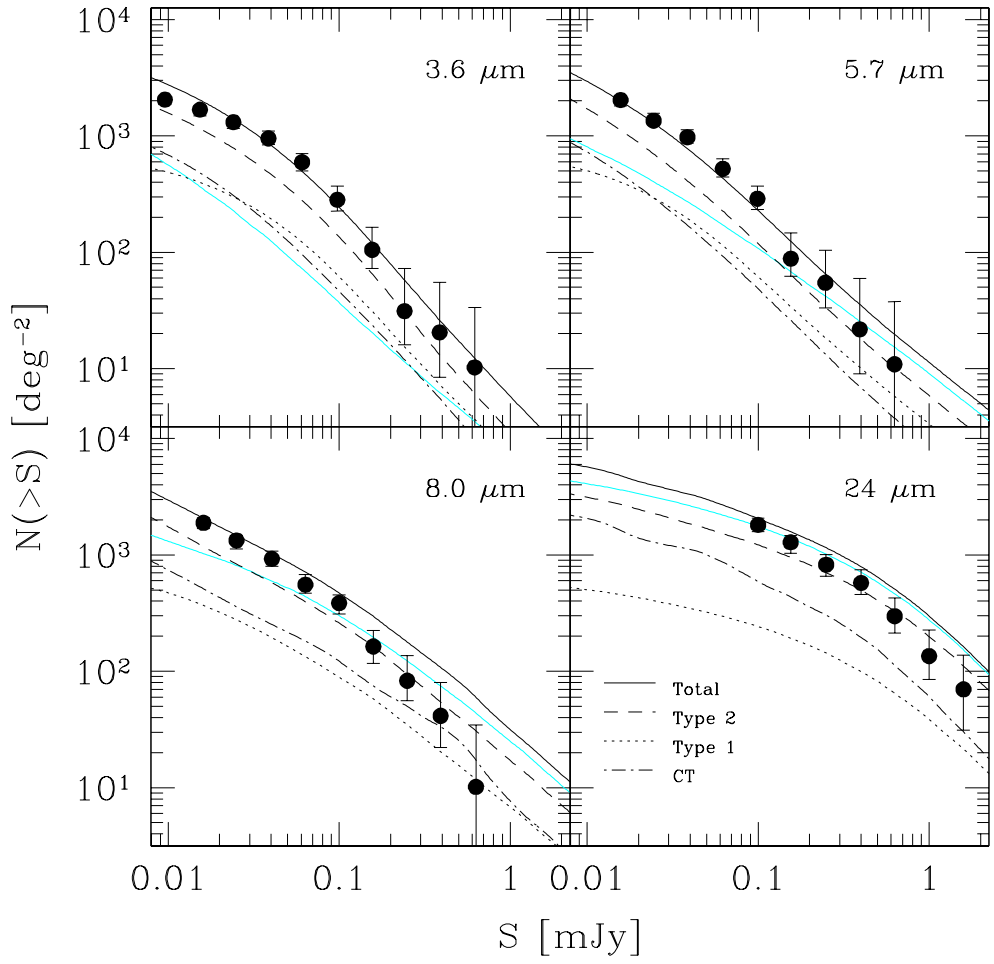

Figure 5.5: Near and mid-IR number counts for AGN and hosts for the non-evolving model with $f_{2-8} > 1 \times 10^{-16}$ erg s^{-1} cm^{-2}. The cyan lines show the predicted number counts for AGN alone. The black lines show the AGN and host number counts for the model host galaxies described by the first three rows of Table 5.2. The solid lines show the total AGN and host number counts while the dotted lines show the counts for type 1 AGN and hosts, dashed lines show the counts for type 2 AGN and hosts, and dot-dashed lines show the CT AGN and host counts. Data is from *Spitzer* observations of X-ray selected AGN in the GOODS fields (Treister et al., 2006).

hosts dominate the J band space density for M_J < -26 and make a significant contribution in the -26 < M_J < -24 magnitude bin. However, at fainter absolute magnitudes, the type 1 AGN hosts make only a nominal contribution to the J band AGN and host space density.

The region of the CMD where type 1 AGN and their hosts tend to be found, as shown by the upside down triangles in Figure 6a of Pierce et al. (2010), is -23.5 < M_B < -19 and 0.55 < U-B < 1.4. This region of the CMD is well populated by a variety of AGN L_X and host M_* model combinations. The majority of type 1 AGN and host model SEDs used here are in agreement with the $\log(f_{0.5-2}/f_R)$ ratio, as exhibited by the blue circles in Figure 5.3. At fainter soft X-ray fluxes it appears that the type 1 AGN and hosts fall below the expected ratio. These sources are located at $z > 2.0$ where the observed R band flux measures rest frame UV emission. Due to the observed frame R band filter redshifting out of optical wavelengths, it is unclear whether the $\log(f_{0.5-2}/f_R) = 0 \pm 1$ relation should hold at high redshift. These high redshift type 1 AGN and hosts can be brought into agreement with $\log(f_{0.5-2}/f_R) = 0 \pm 1$ by increasing the extinction due to dust in the host stellar population or by increasing the age of the host stellar population. Thus if the locally observed $\log(f_{0.5-2}/f_R)$ ratio holds at high redshift, this suggests that at the peak of quasar activity, type 1 AGN hosts either had older stellar populations than type 2 AGN hosts at the same redshift or were dustier than $1.0 < z < 2.0$ type 1 AGN hosts. If the stellar populations of type 1 AGN hosts at $z > 2$ are older than the stellar populations of type 2 AGN hosts at the same epoch, this implies an evolutionary scenario where recently triggered AGN are obscured and then blow out the obscuring gas and dust in order to reveal an unobscured AGN and an older host. It is also possible that, since the fraction of gas rich galaxies at $z > 2$ is larger than at $1 < z < 2$ (Dahlen et al., 2007), type 1 AGN hosts located at $z > 2$ contain more dust than type 1 AGN hosts located at $1 < z < 2$. Both of these possibilities are consistent with quasars being triggered by major mergers, which is expected to be the dominate quasar fueling mechanism at $2 < z < 3$.

When considering the subsolar metallicity, supersolar metallicity and Salpeter (1955) IMF models, the values for $E(B-V)$ which supply the best fit for the type 1 AGN and host B band luminosity function change, but the general trend that type 1 and type 2 AGN

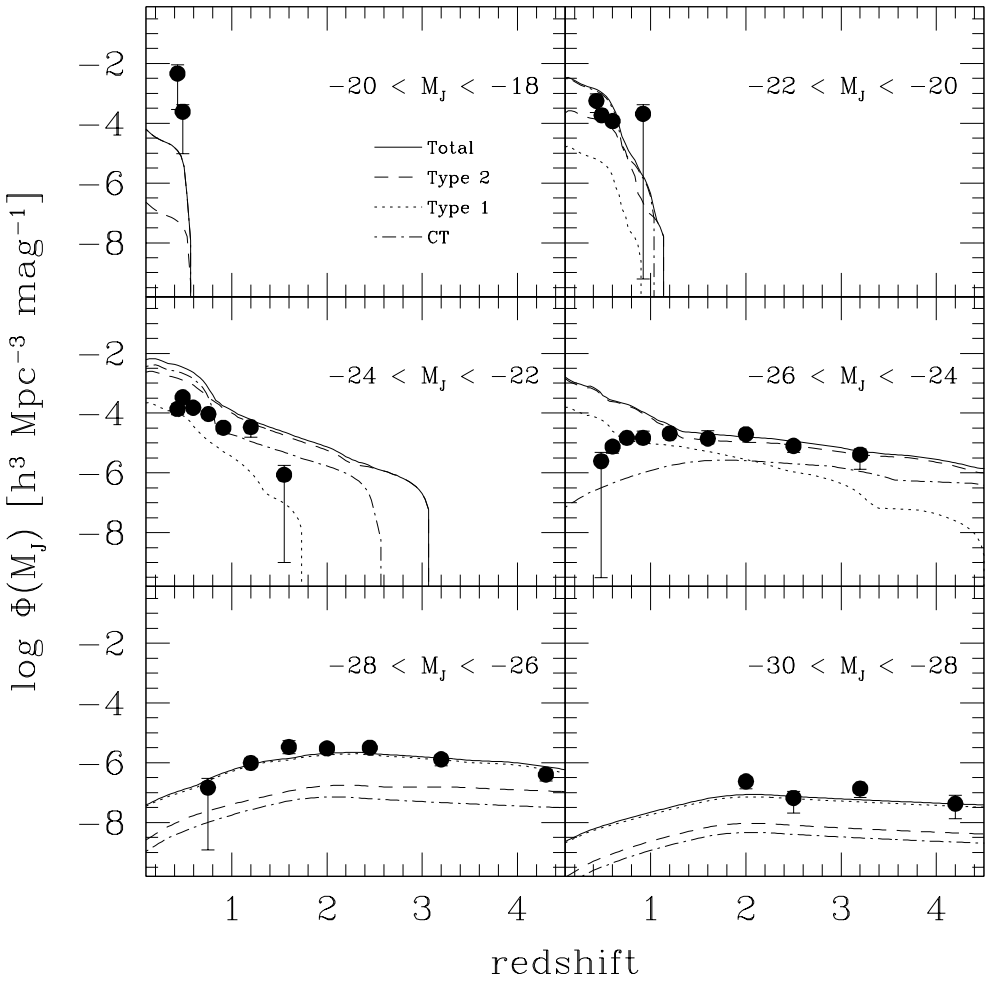

Figure 5.6: J band space density for AGN and hosts for the non-evolving model. The black lines show the AGN and host J band space density for the model host galaxies described in the first three rows of Table 5.2. The solid lines show the total AGN and host J band space density while the dotted lines show the space density for type 1 AGN and hosts, dashed lines show the space density for type 2 AGN and hosts, and dot-dashed lines show the CT AGN and host space density. Data points are the same as in Figure 5.2.

host stellar populations are similar at $z < 1$ and different at $z > 1$ remains. The $E(B-V)$ values for type 1 AGN hosts in the different models are shown in the columns labeled "Type 1 AGN host" in Table 5.3. In all models the type 1 AGN hosts are similar in dust content to the type 2 AGN at $z < 1$ and the type 1 AGN hosts are less dusty than the type 2 AGN hosts at $z > 1$. Thus, regardless of the metallicity or IMF, type 1 and type 2 AGN hosts are similar at $z < 1$ and intrinsically different at $z > 1$.

5.3.3 Star Formation in AGN Hosts

The emission due to obscured star formation is taken into account using the Rieke et al. (2009) star formation templates. The mid-IR AGN and host number counts suggest that the average AGN host has a dust obscured SFR ≈ 2 M$_\odot$ yr^{-1}, the same SFR as normal local spiral galaxies (e.g., Lee et al., 2009). However, recent studies suggest that a larger, but still modest, AGN host SFR is expected (e.g., Lutz et al., 2010; Melbourne et al., 2011). Furthermore, studies also find that the AGN host SFR tends to increase with redshift (Lutz et al., 2010), AGN luminosity (Thompson et al., 2009), or both (Serjeant & Hatziminaoglou, 2009; Serjeant et al., 2010). As several AGN fueling mechanisms, such as the starburst disk model of Ballantyne (2008), require processes related to star formation, it is important to consider if it is possible for AGN hosts to have average SFR $\gtrsim 2$ M$_\odot$ yr^{-1}. Thus several SFR evolutions are considered here.

The Wilman et al. (2010) SFR evolution depends on both AGN L_X and redshift, finding

$$SFR \propto \sqrt{L_X/10^{43}}(1.0+z)^{1.6}. \tag{5.4}$$

When the Wilman et al. (2010) SFR evolution is used, the average $z < 1$ SFR must still be $\lesssim 2$ M$_\odot$ yr^{-1} in order to not over-predict the mid-IR number counts. However samples of AGN hosts with average SFRs an order of magnitude higher than this ($\sim$ 18-41 M$_\odot$ yr^{-1}) have been observed (Lutz et al., 2010; Melbourne et al., 2011; Seymour et al., 2011). In order to explain these observations, a population of enhanced star formation sources are considered. The normalization factor for the proportionality in equation 5.4 is set such that the average SFR for AGN hosts at $z < 1$ is $\sim$20 M$_\odot$ yr^{-1}. In order to not over-estimate

the faint end of the 24 μm number counts, enhanced star formation sources can account for at most $\sim$15% of the AGN population.

Similar fractions of enhanced star formation sources are found using other SFR evolutions. Serjeant et al. (2010) used *Herschel Space Observatory* observations of type 1 SDSS selected quasars to study the evolution of SFR in quasar hosts, finding that AGN host SFR displays strong luminosity dependent evolution with redshift. This leads to a SFR evolution of the form

$$SFR \propto (1.0 + z)^{\alpha}, \tag{5.5}$$

where $\alpha \approx$ -1.9I_{AB} - 42, where I_{AB} is the absolute I band magnitude of the quasar. If the average $z < 1$ SFR is set at $\sim$20 M$_{\odot}$ yr^{-1}, enhanced star formation sources can at most be $\sim$5% of the AGN population.

If AGN host SFR does not evolve with luminosity, and instead only evolves with redshift, then the average AGN host SFR can be considerably higher. If the average AGN host SFR redshift evolution found by Serjeant et al. (2010) for moderate luminosity AGN, SFR $\propto (1.0+z)^{2.3}$, is applied to all AGN hosts, an average $z < 1$ SFR $\approx$ 16 M$_{\odot}$ yr^{-1} for both type 1 and type 2 AGN is in good agreement with the mid-IR AGN and host number counts, with $\chi^2_{red} = 1.3$. This average SFR corresponds to SFR(z=0.0) = 0.5 M$_{\odot}$ yr^{-1}, which is in excellent agreement with Kim et al. (2006) who, using a sample of local type 1 SDSS quasars, found that the average local AGN host SFR $\approx$ 0.5 M$_{\odot}$ yr^{-1}. Furthermore, in the redshift only SFR evolution, for an average $z < 1$ SFR $\approx$ 20 M$_{\odot}$ yr^{-1}, $\sim$80% of AGN hosts can be enhanced star formation sources.

Thus, if the AGN host SFR evolution is dependent on luminosity, either through luminosity evolution or luminosity dependent redshift evolution, enhanced star formation sources are $\sim$5-15% of the AGN population, but if AGN host SFR only evolves with redshift, the average AGN host SFR can be up to $\sim$16 M$_{\odot}$ yr^{-1}. This finding is fully consistent with the 15 μm AGN luminosity function at $z \sim 0.7$ observed by Fu et al. (2010). Furthermore, Lutz et al. (2010) find that for moderate luminosity AGN, the SFR does not evolve with L_X and that only at the highest quasar luminosities does the AGN host SFR seem to depend on the AGN luminosity. Therefore, the fraction of enhanced star formation sources found

here is a lower limit to the true fraction of enhanced star formation sources.

5.3.4 CT AGN Hosts

Observational and theoretical evidence suggests that CT levels of obscuration of an AGN may be due to an evolutionary stage where the SMBH and host bulge are both in a phase of rapid growth (e.g. Sanders et al., 1988; Fabian, 1999; Page et al., 2004; Ballantyne, 2008; Fabian et al., 2009; Draper & Ballantyne, 2010; Nardini & Risaliti, 2011). According to galaxy merger simulations, gas rich mergers will ignite a burst of star formation and rapid black hole growth (e.g. Hopkins et al., 2006). In this scenario, it is expected that CT AGN hosts would be a subset of the ultraluminous infrared galaxy (ULIRG) population, characterized by $L_{IR} > 10^{12}$ $L_{\odot}$, where L_{IR} is the 8–1000 μm luminosity. In order to test this scenario, an attempt is made to model the CT AGN hosts with stellar populations similar to those found in ULIRGs hosting AGNs. Rodríguez Zaurín et al. (2010) find that ULIRGs hosting AGNs have an average stellar population age of $\sim$0.3 Gyr which dominates the stellar mass of the galaxy with an average $M_* \approx 10^{10.8}$ $M_{\odot}$ and standard deviation of $\sim$0.35 dex and an average $E(B-V) \approx 0.6$. This scenario is tested using both the non-evolving and evolving models described in Section 5.2.2.

Due to the observational challenges of identifying CT AGN, there is no data set specific to the optical or near infrared properties of CT AGN hosts. Thus the near and mid-IR AGN number counts measured from an X-ray flux limited sample of AGN, with $f_{2-8} \gtrsim 1 \times 10^{-16}$ erg s^{-1} cm^{-2} (Treister et al., 2006), are used to place limits on the average CT AGN host galaxy. The X-ray flux limit of the *Spitzer* GOODS AGN sample is taken into account in the number counts calculation. Thus, despite the fact that a large fraction of CT AGN are missed by deep X-ray surveys (Hasinger, 2008), the dot-dashed lines in Figures 5.5 and 5.7 show the CT AGN which would have been selected by the Treister et al. (2006) selection criteria. The J band space density, X-ray to optical flux ratio, and optical colors are also used to ensure the model CT AGN hosts are consistent with observations of the AGN population as a whole.

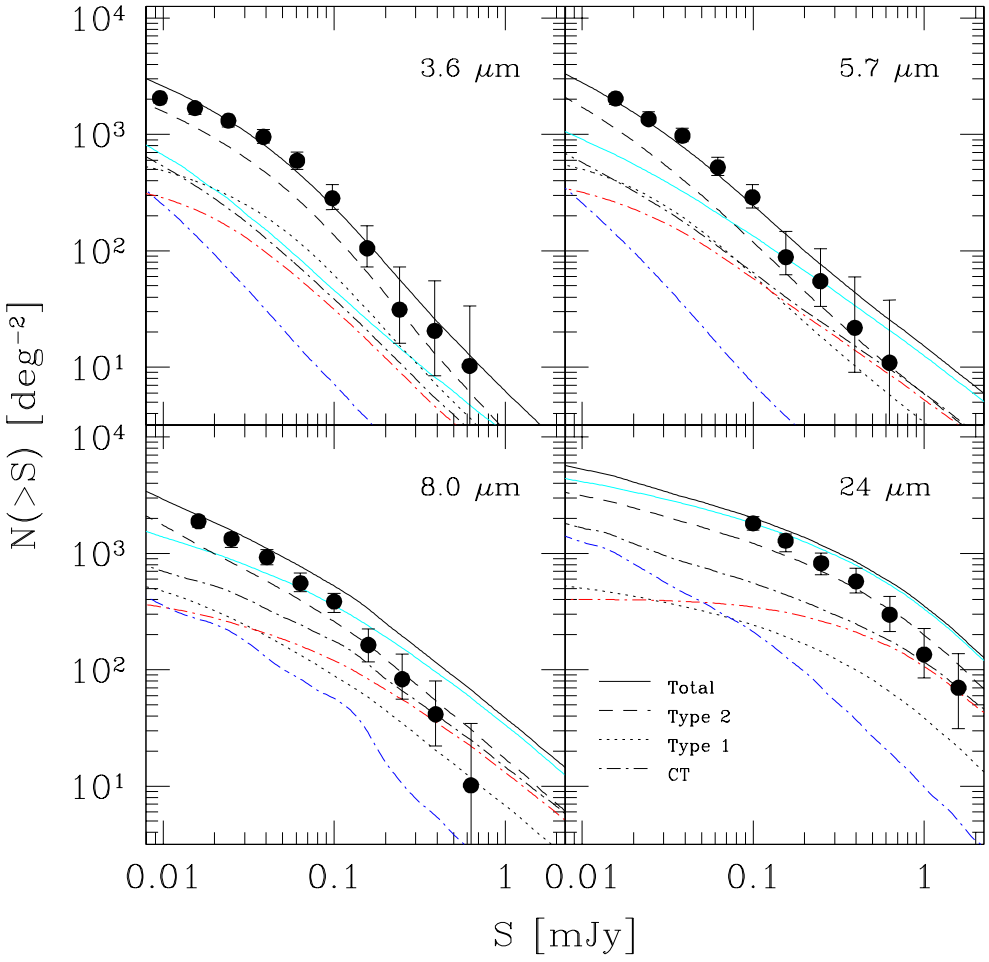

Figure 5.7: Near and mid-IR number counts for AGN and hosts for the evolving model with $f_{2-8} > 1 \times 10^{-16}$ erg s^{-1} cm^{-2}. As in Figure 5.5, the cyan solid lines show the predicted number counts for AGN alone, the black solid lines show the total AGN and host number counts, the black dotted lines show the counts for type 1 AGN and hosts, and the black dashed lines show the counts for type 2 AGN and hosts. The type 1 and type 2 AGN hosts are the same as in Figure 5.5. The black dot-dashed lines show the total CT AGN and host number counts for the evolving model. The low Eddington ratio CT AGN hosts are shown by the blue dot-dashed lines and the high Eddington ratio CT AGN hosts are shown by the red dot-dashed lines. The evolving model CT AGN host galaxies are summarized in Table 5.2. The data shown is the same as in Figure 5.5.

5.3.4.1 Non-evolving Model

The non-evolving model of Draper & Ballantyne (2010) assumes that CT AGN evolve like less obscured type 2 AGN. In order to match the peak of the XRB at ∼30 keV, it is required that ∼44% of obscured AGN are CT. When the CT AGN host stellar populations are modeled in agreement with the findings of Rodríguez Zaurín et al. (2010), the IR number counts are greatly over-predicted. This suggests that on average, CT AGN in the non-evolving model cannot be hosted by ULIRGs. In fact, when using the non-evolving model, the average CT AGN host cannot even be a luminous infrared galaxy (LIRG), which is characterized by $L_{IR} > 10^{11}$ $L_{\odot}$. In order for the near and mid-IR number counts to not be over-predicted at the faint end, the average non-evolving model CT AGN host must have $L_{IR} \lesssim 10^{10.75}$ $L_{\odot}$, corresponding to a star formation rate of $\lesssim 10$ $M_{\odot}$ yr^{-1}, according to the Kennicutt (1998) relation. The youngest the non-evolving model CT AGN host average stellar population can be, and not over-predict the mid-IR number counts, is ~ 1 Gyr old which requires $E(B-V) \approx 1.0$. The contribution of the non-evolving model CT AGN and their hosts to the near and mid-IR number counts is shown as the dot-dashed line in Figure 5.5.

In the non-evolving model, CT AGN dominate the low redshift, faint M_J region of the J band space density. Figure 5.6 shows the CT AGN and host contribution to the J band space density as the dot-dashed lines. As expected by the higher dust content, CT AGN hosts occupy a region of the CMD which is on average slightly redder and fainter than the type 1 and type 2 AGN hosts. The CT AGN tend to lie below the $\log(f_{0.5-2}/f_R)$ ratio, as the majority of the soft X-ray flux of CT sources is absorbed by the CT obscuring material. Figure 5.3 shows the $\log(f_{0.5-2}/f_R)$ ratio of CT AGN and their hosts as red squares. Changing the metallicity or IMF used for the host galaxy stellar population does not change these results.

When the enhanced star formation sources are considered, the CT AGN hosts must be similar to the type 2 AGN hosts, regardless of host galaxy stellar population metallicity and IMF. Similarly, when the redshift evolution of AGN host SFR is included, the CT AGN hosts must be similar to the type 2 AGN hosts. Thus, if f_{CT} does not evolve with AGN

Eddington ratio, then CT AGN and their hosts are expected to be a simple extension of the less obscured type 2 AGN population. This would require that AGN triggered by mergers be a small minority of the quasar population.

5.3.4.2 Evolving Model

The evolving model allows CT AGN to evolve independently of the less obscured type 2 AGN. Instead, f_{CT} is assumed to be Eddington ratio dependent. In order to fit the peak of the XRB at ∼30 keV, the local CT AGN space density, and the $z > 1$ IR CT AGN space density, it is found that ∼86% of AGN with Eddington ratios >0.9 are CT, ∼60% of AGN with Eddington ratios < 0.01 are CT, and ∼0% of AGN with intermediate Eddington ratios are CT.

As AGN with weaker accretion rates are observed to have older stellar populations (Kauffmann et al., 2003, 2004, 2007), the low Eddington ratio AGN are assumed to have the same mass distribution as the type 1 and type 2 AGN but an older stellar population and very little star formation. The age of the low Eddington ratio CT AGN host stellar populations are summarized in Table 5.1. If the low Eddington ratio CT AGN hosts have the same $E(B-V)$ as the type 1 and type 2 AGN hosts, the near and mid-IR number counts are over-predicted. Increasing the dust in the low Eddington ratio CT AGN hosts to $E(B-V) \approx 1.0$ brings the model predictions into agreement with the faint end of the IR number counts, as shown by the blue dot-dashed lines in Figure 5.7. The larger amount of dust in the CT AGN hosts as compared to the type 2 AGN hosts makes sense as only galaxies containing a large amount of dust will be able to host an AGN with CT levels of obscuration.

In the evolving model, the high Eddington ratio CT AGN hosts should be galaxies in a phase of rapid star formation and black hole growth. Therefore, the high Eddington ratio CT AGN hosts should be LIRGs or ULIRGs. Indeed it is found that if the stellar populations of the high Eddington ratio CT AGN hosts have $L_{IR} = 10^{12}$ $L_{\odot}$ from star formation, $E(B-V) \approx 0.6$, with a stellar population of age ∼0.3 Gyr which dominates M_*, in agreement with the average stellar population of ULIRGs which host an AGN (Rodríguez

Zaurín et al., 2010), the near and mid-IR number counts predictions are in agreement with deep observations. The high Eddington ratio CT AGN and host number counts are shown as the red dot-dashed lines in Figure 5.7. The over-prediction at the bright end of the number counts is due to the incompleteness of the survey at bright fluxes. As the GOODS fields cover only 0.1 deg^2 (Treister et al., 2006), GOODS misses bright, rare objects. If the stellar population is assumed to be younger than ∼0.3 Gyr, the number counts are over-predicted. Similarly if the $E(B-V) < 0.6$ or if the average $M_* > 10^{11}$ M$_\odot$, the number counts are over-predicted. Thus, the stellar population described here is the upper limit for how bright the high Eddington ratio CT AGN hosts can be without over-predicting the IR number counts.

The CT AGN host galaxies are also in good agreement with the other model constraints considered here. The CT AGN host contribution to the J band space density is shown as the dot-dashed lines in Figure 5.8, where the red lines refer to the high Eddington ratio CT AGN and their hosts and the blue lines refer to the low Eddington ratio CT AGN and their hosts. As expected the high Eddington ratio sources dominate the CT AGN and host contribution in the brighter magnitude bins while the low Eddington ratio sources dominate at the fainter magnitude bins. The optical colors are also in agreement with observations. The low Eddington ratio CT AGN hosts are on average redder and fainter than the type 1 and type 2 AGN hosts, while the high Eddington ratio CT AGN hosts are on average as bright or slightly brighter than the type 1 and type 2 AGN hosts but on average a little redder than the type 1 and type 2 AGN hosts. As with the non-evolving model, most of the CT AGN hosts lie below the empirical average $\log(f_{0.5-2}/f_R)$ ratio, as expected by the high levels of soft X-ray absorption fundamental to CT AGN. In Figure 5.9 the f_R versus $f_{0.5-2}$ for CT AGN and their hosts are shown as the red squares with the low Eddington ratio objects shown as filled red squares and the high Eddington objects shown as open red squares. The same result is found when the host galaxy IMF or metallicity is varied.

As the high Eddington ratio CT AGN are a small fraction of the overall AGN population, the evolving model CT AGN hosts are not affected by the consideration of the enhanced star formation sources. Thus the CT AGN hosts of the evolving model are in agreement

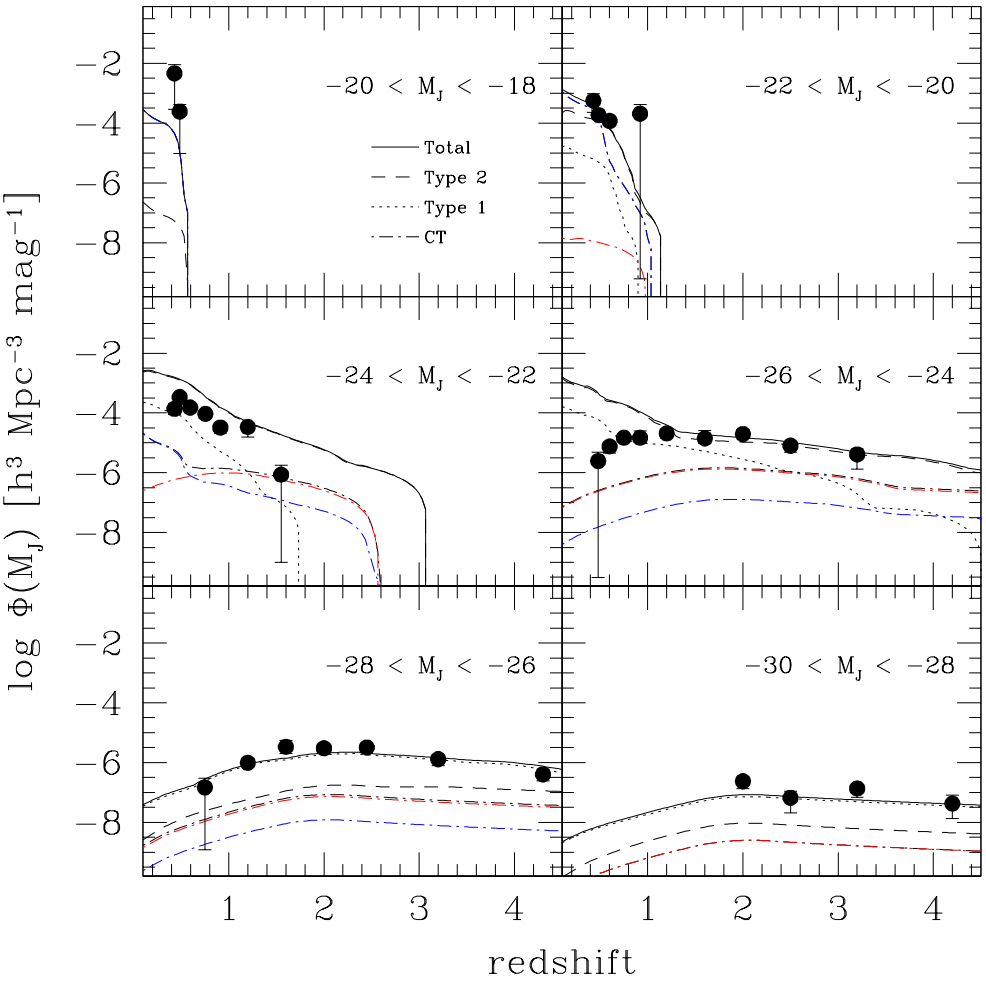

Figure 5.8: J band space density for AGN and hosts for the evolving model. The solid lines show the total AGN and host J band space density. The dotted lines show the type 1 AGN and hosts space density and the dashed lines show the type 2 AGN and hosts space density. The type 1 and type 2 AGN hosts have the same stellar populations as in Figure 5.6. The black dot-dashed lines show the total CT AGN and host J band space density for the evolving model. The low Eddington ratio CT AGN hosts, shown by the blue dot-dashed lines, and the high Eddington ratio CT AGN hosts, shown by the red dot-dashed lines, are described in Table 5.2. Data points are the same as in Figure 5.2.

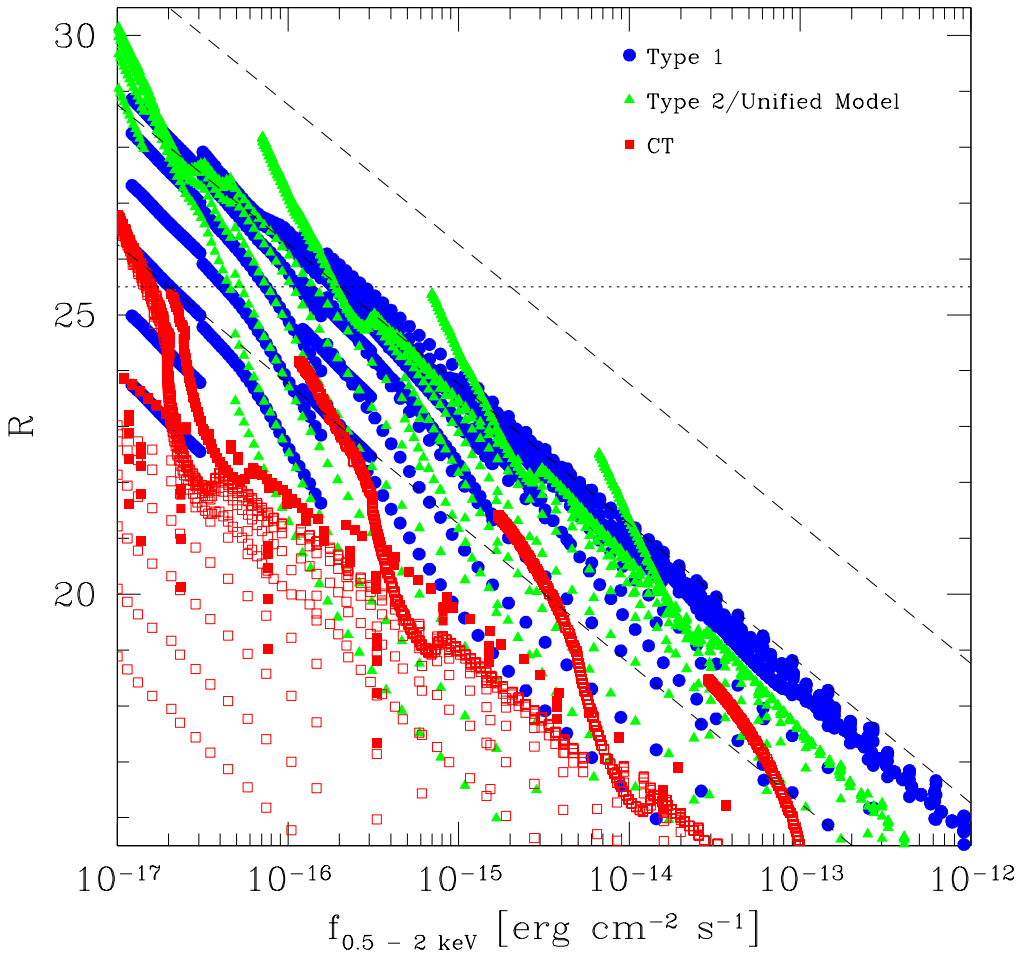

Figure 5.9: Soft X-ray flux versus R band magnitude for AGN and hosts for the evolving model. AGN and hosts are shown for $L_X < 10^{45}$ erg s^{-1}, $z < 3$, and $M_* = 10^{9.5}$, 10^{10}, $10^{10.5}$, 10^{11}, $10^{11.5}$, and 10^{12} M$_\odot$. The blue circles show type 1 AGN and hosts and green triangles show type 2 AGN and hosts. The type 1 and type 2 AGN hosts are the same as in Figure 5.3. The red squares show CT AGN and hosts. The red filled squares show the low Eddington ratio CT AGN and hosts, while the open red squares show the high Eddington ratio CT AGN and hosts. The evolving model CT AGN host galaxies are described in Table 5.2. The horizontal dotted line again marks $R = 25.5$, above which the source is considered an optically faint X-ray AGN.

with the AGN evolution scenario where major mergers trigger nuclear starbursts and highly obscured AGN activity.

5.3.5 Evolution of f_2

The evolution of f_2, the type 2 AGN fraction, is important for understanding the AGN life cycle and how AGN and their host galaxies interact (e.g., Ballantyne et al., 2006a). In the unified model, f_2 is the covering factor of the dusty torus, and thus the evolution of f_2 shows a fundamental evolution of the torus parameters (Ballantyne et al., 2006b). Several studies suggest that f_2 evolves with L_X and possibly also with redshift (e.g., Ueda et al., 2003; Simpson, 2005; Ballantyne et al., 2006a; Hasinger, 2008; Fabian et al., 2009; Winter et al., 2009). However, other studies find that it is not necessary for f_2 to evolve with L_X (e.g., Lawrence & Elvis, 2010) nor with redshift (e.g., Gandhi & Fabian, 2003; Treister & Urry, 2005) in order to explain observations. Indeed, it is found that the number counts and J band space density can be fit with a constant f_2. For $z < 0.4$, the type 1 AGN and host B band luminosity function can also be satisfactorily fit with a constant f_2. However, fitting the type 1 AGN and host B band luminosity function at $z \gtrsim 1$ requires that f_2 is not constant. If f_2 is constant, the best fit $\chi^2_{red} > 7.0$ and the type 1 AGN and host B band luminosity function predicts a considerably larger population of B band magnitude, $m_B \sim 23$, $1 < z < 2$ type 1 AGN than observed. Thus, it is found that in order to fit the type 1 AGN and host B band luminosity function at $z > 1$, f_2 must evolve with L_X.

The argument for evolution of f_2 with redshift is less conclusive. Figure 5.10 shows the type 1 AGN and host B band luminosity function assuming that f_2 does not evolve with redshift, which gives $\chi^2_{red} = 6.5$. When f_2 does evolve with redshift, the best fit $\chi^2_{red} = 4.3$. While the χ^2_{red} for both the evolving and the non-evolving f_2 models do not represent formal good fits to the observed data points, the model in which f_2 does evolve with redshift provides a better fit to the data. In the scenario where f_2 does not evolve with redshift, it is necessary that at higher redshift the type 1 AGN host galaxies be dustier than locally. This is in contrast to the scenario where f_2 does evolve with redshift and type 1 AGN hosts are less dusty at higher redshift compared to the local population. In order to not over-predict

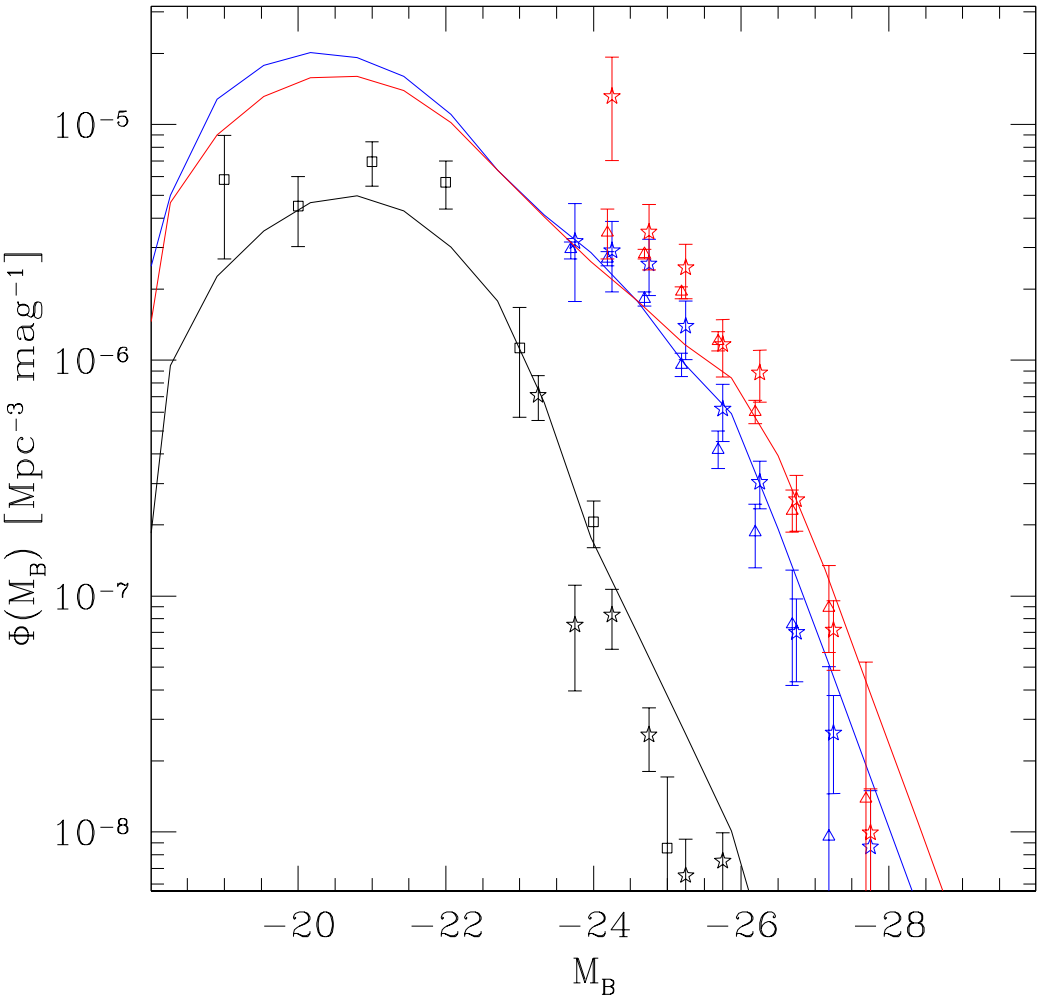

Figure 5.10: Type 1 AGN and host B band luminosity function when f_2 is assumed to not evolve with z. Colors and data points are the same as in Figure 5.4. The $z < 1$ type 1 AGN hosts have $E(B-V) \approx 0.25$ and at higher redshift the type 1 AGN hosts have $E(B-V) \approx 0.4$, in contrast to the case where f_2 does evolve with z and type 1 AGN hosts have a lower $E(B-V)$ at higher z than locally.

the IR number counts, the type 2 AGN hosts must also be dustier at higher redshift than locally. Assuming that f_2 does not evolve with redshift has minimal affect on the J band space density, optical colors, and $\log(f_{0.5-2}/f_R)$ ratio.

A comparison of Figure 5.4 and Figure 5.10, suggests that f_2 not only evolves with L_X, but also with redshift. Also, the model where f_2 evolves with both L_X and redshift provides a better fit to the type 1 AGN and host B band luminosity function has measured by χ^2_{red}. As neither the evolving nor non-evolving f_2 models provide a formally good fit to the observed luminosity function, the possibility that f_2 does not evolve with redshift cannot be conclusively ruled out; however, the evolution of the B band type 1 AGN and host luminosity function suggests that f_2 does evolve with redshift. In order to fit the type 1 AGN and host B band luminosity function f_2 must evolve with L_X.

5.3.6 Summary of Results

Using a variety of optical and near and mid-IR data, this work constrains the stellar populations of AGN host galaxies. Table 5.2 summarizes the average AGN host galaxy for different AGN spectral types. It is found that at $z < 1$ type 1 and type 2 AGN hosts are similar, but at $z > 1$ type 1 AGN hosts are less dusty than type 2 AGN hosts. The majority of AGN have an average SFR $\lesssim 2$ $M_\odot$ yr^{-1}, however there is evidence of a population of enhanced star formation sources which account for $\gtrsim$ 5–15% of the AGN population and has SFR ≈ 20 $M_\odot$ yr^{-1}. Also, it is found that if CT AGN evolve like type 2 AGN, then CT AGN hosts are similar to type 2 AGN hosts and if CT levels of obscuration are indicative of specific evolutionary stages in the AGN life cycle, then CT AGN hosts are also in specific evolutionary stages. Furthermore, it is shown that f_2 evolves with L_X and f_2 is likely to evolve with redshift.

5.4 Discussion

5.4.1 Hosts of CT AGN

For both the evolving and non-evolving models, the CT AGN host stellar populations suffer from at least as much dust extinction as the type 2 AGN host stellar populations. Observations suggest that at least some of the observed extinction of heavily obscured AGN

may be due to extended dust structures or molecular clouds within the host galaxy (Brand et al., 2007; Polletta et al., 2008; Martínez-Sansigre et al., 2010), so it is expected that the stellar populations of CT AGN will be enshrouded in dust. It is within the limits imposed by the model constraints for the high Eddington ratio CT AGN hosts to have an average $E(B-V)$ which is in agreement with ULIRGs hosting AGN (Rodríguez Zaurín et al., 2010).

The AGN evolution scheme, in which mergers trigger large nuclear starbursts and AGN activity, claims that the AGN activity will initially be very highly obscured while the black hole grows very rapidly. As the black hole grows, the radiation pressure on surrounding dusty gas will increase until the AGN feedback blows out the obscuring material and halts the star formation in the host nuclear region (Sanders et al., 1988; Page et al., 2004; Rigopoulou et al., 2009; Hopkins et al., 2006). In this scheme CT AGN should have young stellar populations and possibly high levels of on going star formation. The non-evolving model places a lower limit on the stellar population age of 1 Gyr. However, when the enhanced star formation sources are included, the non-evolving model CT AGN hosts have similar stellar ages to the type 2 AGN hosts, in contrast to the expectations of the AGN evolution scheme. For the high Eddington ratio CT AGN in the evolving model, the lower limit on the stellar population age is 0.3 Gyr, the average stellar age of ULIRGs hosting an AGN (Rodríguez Zaurín et al., 2010). The low Eddington ratio CT AGN hosts of the evolving model can be of similar age as the type 1 and type 2 AGN, but the near and mid-IR predicted number counts are in better agreement with the observations if these AGN hosts have slightly older stellar populations than the average type 1 and type 2 AGN hosts. It has been demonstrated that galaxies hosting AGN with lower [OIII] luminosities have larger values for $D_n(4000$ Å$)$ compared to galaxies hosting AGN with high [OIII] luminosities (Kauffmann et al., 2003, 2004, 2007). Thus it is expected that AGN with lower Eddington ratios are in hosts with older stellar populations, in agreement with the findings of this study.

The stellar populations of CT AGN hosts for the evolving model and the non-evolving model are in agreement with the expectations from the AGN evolution scheme. The non-evolving model finds that the average CT AGN host has recently ($\gtrsim$1 Gyr ago) undergone

a large burst of star formation, but that current star formation rates are more modest. The evolving model finds that high Eddington ratio CT AGN hosts have recently ($\gtrsim$0.3 Gyr ago) undergone a large burst of star formation and that current star formation rates may also be elevated. If the enhanced star formation sources are included, the non-evolving model AGN hosts have stellar populations of similar age as the type 2 AGN, and thus are in better agreement with the orientation based unified model than with the AGN evolution scheme. The evolving model CT AGN hosts are consistent with the AGN evolution scheme regardless of the inclusion of the enhanced star formation sources.

In summary, the non-evolving model CT AGN hosts are a simple extension of the type 2 AGN host population while the evolving model CT AGN are consistent with the paradigm where major mergers cause both intense starbursts and AGN activity. In the evolving model, low Eddington ratio CT AGN hosts will appear as galaxies with old and dusty stellar populations while the high Eddington ratio CT AGN hosts will appear as IR bright starburst galaxies.

5.4.2 Enhanced Star Formation in AGN Hosts

It is found that $\sim$5-15% of AGN hosts can be enhanced star formation sources with an average SFR $\approx$ 20 $M_{\odot}$ yr^{-1}, a factor of 10 higher than the majority of AGN hosts. This is expected to be a lower limit of the fraction of enhanced star formation sources as some sources may have such highly embedded star formation that the majority of the reprocessed emission due to star formation is at wavelengths longer than 24 μm. Observations at longer wavelengths, such as in the far-IR with the *Herschel* or the millimeter/sub-mm regime with the Atacama Large Millimeter/submillimeter Array (ALMA), are necessary for uncovering the evolution of star formation rates in AGN hosts (Draper & Ballantyne, 2011). Even deep radio observations are a useful tool in determining the highly embedded star formation rates of AGN hosts (Ballantyne, 2009). Indeed, by stacking sub-mm observations of X-ray selected AGN, Lutz et al. (2010) found that the average AGN host SFR $\approx$ 30 $M_{\odot}$ yr^{-1}. Furthermore, Lutz et al. (2010) found that the AGN host SFR evolves strongly with redshift but with evidence of luminosity dependent evolution only for the highest luminosity AGN.

In the scenario where AGN host SFRs are not luminosity dependent, it is found that more than half of AGN hosts can be enhanced star formation sources.

The fact that the mid-IR AGN and host number counts are over-predicted by an average SFR > 2 $M_{\odot}$ yr^{-1}, despite observational evidence that there is a population of AGN with an average SFR an order of magnitude higher than this upper limit, suggests that there are two populations of AGN. The majority of AGN hosts, at least at $z < 1$, have SFRs similar to local spiral galaxies and $\gtrsim$5-15% of AGN hosts have markedly higher SFRs. The existence of these two populations of AGN hosts can be interpreted in two complimentary ways. The first interpretation is that the AGN hosted by galaxies with enhanced SFRs are being fueled by different mechanisms than the lower star formation objects. At $z < 1$, the lower star formation objects are likely dying quasars which were triggered by major mergers while the enhanced star formation objects are likely Seyferts which are both fueled and obscured by circumnuclear starburst disks, as investigated by Ballantyne (2008). The other interpretation is that all AGN are fueled by processes related to nuclear starbursts, whether those starbursts are triggered by mergers or through secular processes, and on average, the nuclear starburst phase overlaps with the active AGN phase for $\gtrsim$5-15% of the AGN lifetime. Further exploration of these two populations of AGN hosts is necessary to determine the processes which trigger and fuel AGN activity.

5.4.3 Methods for Finding CT AGN

It is well documented that the integrated emission of AGN observed in deep X-ray surveys is insufficient to account for the intensity of the XRB at $\sim$30 keV and that the shape of the XRB necessitates that the missing population of AGN be highly obscured (e.g., Ballantyne et al., 2006a; Draper & Ballantyne, 2009; Treister et al., 2009b). Given the uncertainties of the normalization of the XRB and the AGN hard X-ray luminosity functions, different models predict vastly different numbers of missing CT AGN (e.g., Gilli et al., 2007; Draper & Ballantyne, 2009; Treister et al., 2009b). As these highly obscured AGN are missed in deep X-ray surveys (Hasinger, 2008), it is important to consider other methods to identify the elusive CT AGN population.

One possibility is that the majority of X-ray bright optically inactive galaxies (XBONGs) host CT AGN (Fiore et al., 2008, 2009; Treister et al., 2009a; Rovilos et al., 2010). XBONGs are X-ray sources found in deep surveys which have no optical counterparts with $R \lesssim 25.5$ and make up a substantial portion of deep survey X-ray sources (Aird et al., 2010). It is thought that these sources are either heavily obscured AGN and/or high redshift quasars (Alexander et al., 2001; Mainieri et al., 2005; Rovilos et al., 2010). Considering the sources above the dotted horizontal line in Figures 5.3 and 5.9 suggests that a small fraction of optically faint X-ray sources may be CT AGN, but the majority of this population is $z \gtrsim 1$ type 2 AGN. Thus it is unlikely that XBONGs host the majority of the missing CT AGN population.

Another method used to identify CT AGN candidates is to search for infrared bright sources which have an infrared excess, usually defined by $f_{24}/f_R \gtrsim 1000$, where f_{24} is the 24 μm flux (e.g. Polletta et al., 2006; Alexander et al., 2008; Donley et al., 2008; Fiore et al., 2008, 2009; Treister et al., 2009a). Some concern has been raised that this method will also pick out lower redshift type 2 AGN masquerading as high redshift CT AGN (Georgakakis et al., 2010). Therefore, the population of AGN selected by the infrared excess criteria is investigated.

Fiore et al. (2008) suggest that using the criteria $f_{24}/f_R \gtrsim 1000$ and R - $K > 4.5$ selects a distinct class of sources, the majority of which are CT AGN. However, according to both the evolving and non-evolving model CT AGN and host SEDs developed here, the Fiore et al. (2008) criteria selects low to moderately X-ray bright AGN at moderate to high redshift. The vast majority of the selected AGN are obscured, but a significant fraction are still Compton thin. Similarly, Donley et al. (2008) find that the Fiore et al. (2008) criteria is likely to select dusty star forming templates and low X-ray flux AGN. However, Donley et al. (2008) find no evidence that the selected AGN are CT.

A more effective method of identifying CT AGN candidates is based on the selection criteria of Polletta et al. (2008): $f_{24}/f_R \gtrsim 1000$ and $f_{24} > 1.0$ mJy. Furthermore, it appears that samples with a lower f_{24} limit, such as $f_{24} > 700$ μJy or even $f_{24} > 550$ μJy, also contain a large fraction of highly obscured AGN (Donley et al., 2010, and references

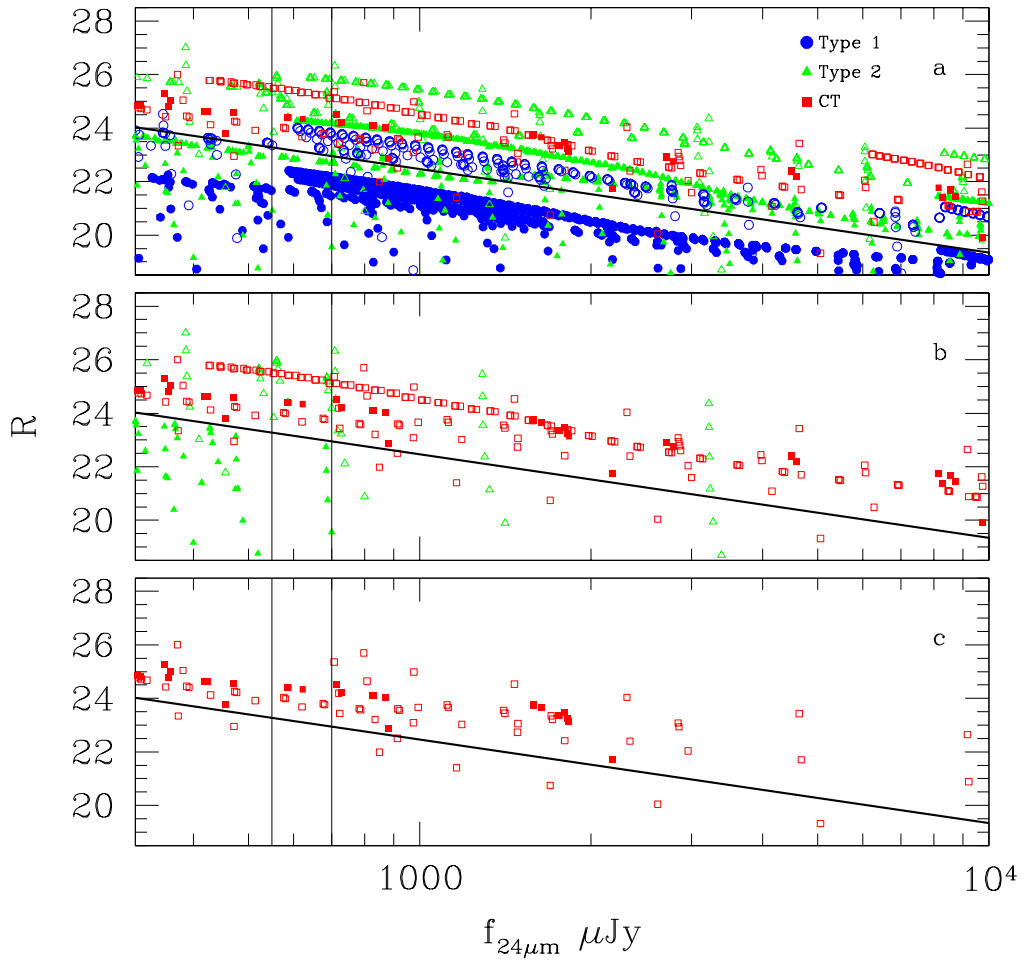

Figure 5.11: R versus f_{24} for evolving model AGN with $L_X = 10^{42}$, $10^{43.5}$, 10^{45} and $10^{46.5}$ erg s^{-1}, $z < 5$, and $M_* = 10^{10}$, 10^{11}, and 10^{12} M$_\odot$ for various soft X-ray flux ranges. Panel a shows all AGN regardless of $f_{0.5-2}$, panel b shows all AGN with $f_{0.5-2} < 10^{-15}$ erg s^{-1} cm^{-2}, and panel c shows all AGN with $f_{0.5-2} < 10^{-16}$ erg s^{-1} cm^{-2}. The blue circles show the type 1 AGN and the green triangles show the type 2 AGN. The open points mark the enhanced star formation objects. The red filled squares show the low Eddington ratio CT AGN and the open red squares show the high Eddington ratio CT AGN. The thick black line shows where $f_{24}/f_R = 1000$, therefore the area of interest is above the thick line. The vertical lines mark $f_{24} = 550$ μJy and $f_{24} = 700$ μJy.

therein). Fainter samples of infrared bright galaxies are found to be predominately powered by star formation rather than by AGN (e.g., Pope et al., 2008). Figure 5.11a shows that representatives of all spectral types of AGN can be found with $f_{24}/f_R \gtrsim 1000$ and $f_{24} > 550$ μJy. These sources will be located at all redshifts. However, the majority of type 1 and type 2 AGN are bright in the soft X-ray. For both the evolving and non-evolving models, the vast majority of infrared excess AGN with $f_{24} > 550$ μJy and $f_{0.5-2} < 10^{-15}$ erg cm^{-2} s^{-1} are CT AGN, as shown in Figure 5.11b. Figure 5.12b, which shows the redshift distribution of the CT AGN with $f_{0.5-2} < 10^{-15}$ erg cm^{-2} s^{-1}, illustrates that these X-ray faint CT AGN are located at all redshifts. For the evolving model the vast majority of these CT AGN are high Eddington ratio sources. This criteria will select a small number of type 2 AGN with enhanced star formation, but the majority of sources selected in this manner are indeed CT.

If an infrared excess AGN has $f_{0.5-2} \lesssim 10^{-16}$ erg cm^{-2} s^{-1} and $f_{24} > 550$ μJy, than the AGN is CT and located at $z \lesssim 2$. This is true for both the evolving and non-evolving models. An interesting consequence of this is that a size-able population of $z > 2$ CT AGN should have $10^{-15} > f_{0.5-2} > 10^{-16}$ erg s^{-1} cm^{-2}. According to the evolving model, nearly all of the $f_{0.5-2} \lesssim 10^{-16}$ erg cm^{-2} s^{-1} sources are high Eddington ratio sources and according to the non-evolving model these low X-ray flux sources are nearly all enhanced star formation sources. It is therefore expected that X-ray stacking of IR bright sources with $f_{24}/f_R \gtrsim 1000$ and low soft X-ray flux will yield a large fraction of the $z \lesssim 2$ high luminosity CT AGN population. This shows that combining observations in multiple spectral regions, such as mid-IR, optical, and X-ray observations, is the most efficient way of identifying CT AGN candidates.

Identifying and characterizing the elusive CT AGN population is a necessary part of understanding the history of accretion and galaxy evolution. However, due to the observational challenges of studying highly obscured sources, multi-wavelength investigations are necessary to identify and understand the nature of CT AGN.

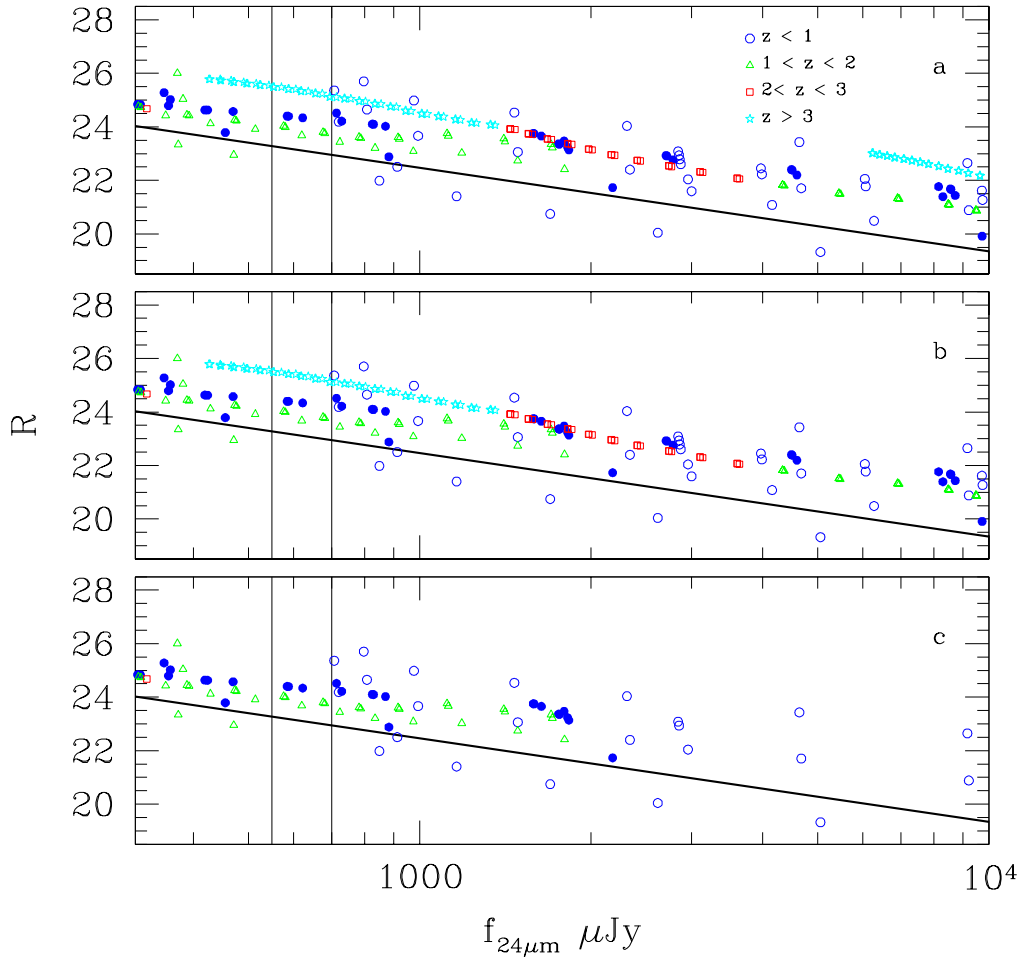

Figure 5.12: Redshift distribution of R versus f_{24} for CT AGN with $L_X = 10^{42}$, $10^{43.5}$, 10^{45} and $10^{46.5}$ erg s^{-1} and $M_* = 10^{10}$, 10^{11}, and 10^{12} M$_\odot$ using the evolving model for various soft X-ray flux ranges. Panel a shows all CT AGN regardless of $f_{0.5-2}$, panel b shows the CT AGN with $f_{0.5-2} < 10^{-15}$ erg s^{-1} cm^{-2}, and panel c shows the CT AGN with $f_{0.5-2} < 10^{-16}$ erg s^{-1} cm^{-2}. Point styles designate AGN in different redshift ranges. Blue circles show AGN with $z < 1$, green triangles show AGN with $1 < z < 2$, red squares show AGN with $2 < z < 3$, and cyan stars show AGN with $z > 3$. The filled points show the low Eddington ratio CT AGN and the open points show the high Eddington ratio CT AGN. The thick black line shows where $f_{24}/f_R = 1000$, therefore the area of interest is above the thick line. The vertical lines mark f$_{24}$ = 550 μJy and f$_{24}$ = 700 μJy.

5.4.4 Implications for the Unified Model and AGN Fueling Mechanisms

Several recent studies suggest that there are two distinct processes which lead to AGN activity, secular evolution and merger events (e.g., Ballantyne et al., 2006a; Hasinger, 2008; Hopkins & Hernquist, 2009; Lutz et al., 2010). In the latter paradigm, quasar activity is activated by galaxy mergers which cause gas and dust to be funneled into the nuclear region (e.g., Sanders et al., 1988; Fabian, 1999; Page et al., 2004; Hopkins et al., 2006), whereas moderate luminosity AGN are fueled by gravitational instabilities internal to the host galaxy or through minor interactions (e.g., Crenshaw et al., 2003; Kormendy & Kennicutt, 2004; Pierce et al., 2007; Shapiro et al., 2008). It is probable that if different forms of AGN activity are caused by contrasting fueling mechanisms, the relationship between various AGN spectral types may be different for the high and moderate luminosity populations.

This study finds that the average type 1 and type 2 AGN hosts have similar stellar populations and similar levels of dust attenuation at $z < 1$. At $z > 1$ type 1 and type 2 AGN hosts appear to be fundamentally different. Even though the high redshift type 1 and type 2 hosts have similar stellar populations, the type 1 AGN and host B band luminosity function requires that type 1 AGN hosts have significantly lower levels of dust extinction than what is required for type 2 AGN hosts to be in agreement with the observed near and mid-IR number counts. At $z > 1$, type 1 AGN hosts are intrinsically less dusty than type 2 AGN hosts. This suggests that the orientation based unified model works well for describing the local Seyfert population, but may not be appropriate for the high redshift, high luminosity quasar population. This conclusion is consistent with the findings of several other recent studies (e.g., Ballantyne et al., 2006b; Hopkins & Hernquist, 2009; Draper & Ballantyne, 2010; Lutz et al., 2010; Trump et al., 2011). For galaxies which are evolving secularly, the unified model appears to be an apt description. However, the violent growth experienced by black holes and their host bulges during major merger events does not appear to fit into the orientation based unified scheme.

It is likely that different AGN fueling mechanisms will result in different relationships between AGN spectral types. In the merger scenario, young AGN are highly obscured and old quasars are unobscured (e.g., Sanders et al., 1988; Fabian, 1999; Page et al., 2004;

Hopkins et al., 2006). Different spectral types of AGN fueled by secular processes related to nuclear starbursts are expected to be in agreement with the orientation based unified model due to the disky nature of the nuclear starburst which is likely to both fuel and obscure the AGN (e.g., Ballantyne, 2008). In the evolving model, it is found that mergers can play a strong role in fueling high L_X, $z > 1$ quasars. However, in the non-evolving model, when the enhanced star formation sources are considered, it appears that the dominant fueling mechanism is not mergers. Instead, the difference between spectral types may only be that some galaxies have less dust and gas than others at $z > 1$. In the non-evolving f_{CT} model, it appears that secular processes are the dominate AGN fueling mechanism at all redshift. For both the evolving and non-evolving model, at $z < 1$ the processes which lead to AGN activity are most likely secular. However, the findings of this study suggest that the dominant AGN fueling process changes at $z \sim 1$, since at $z < 1$ the average type 1 and type 2 AGN hosts are more similar than at higher redshift. In order to understand the mechanisms which trigger and fuel AGN, it is important for future studies to pay careful attention to which fueling mechanisms are dominant in different subsets of the AGN population.

Thus, it has been shown that the relationship between different AGN spectral types is a helpful tool for understanding the dominant processes responsible for triggering and fueling AGN activity. It is found that at $z < 1$ the orientation based unified model holds, suggesting that the dominant AGN fueling mechanisms at $z < 1$ are secular processes. At $z > 1$, the orientation based unified model does not seem to hold. The evolving CT AGN model suggests that at $z > 1$ mergers are an important AGN fueling mechanism; however, the non-evolving CT AGN model suggests that even at $z > 1$ the dominant AGN fueling mechanisms are secular processes and that mergers play only a minor role in fueling AGN at all redshifts.

5.4.5 L_X and redshift Evolution of f_2

Understanding the evolution of f_2 is an important step in understanding the nature of AGN obscuration and the interplay between an AGN and it's host galaxy. If f_2 evolves with AGN L_X, this suggests that the obscuring material is close enough to the central engine that dust

sublimation (Lawrence, 1991) and/or radiation pressure fed winds (Königl & Kartje, 1994) affect portions of the obscuring material. If f_2 evolves with redshift this would indicate that the evolution of the obscuring material is somehow connected to the evolution of the host galaxy (Ballantyne et al., 2006b). While most model constraints used in this study are not very sensitive to the evolution of f_2, the type 1 AGN and host B band luminosity function does prove to be a valuable test of the evolution of f_2. This study finds that f_2 must evolve with AGN L_X and that f_2 probably evolves with redshift.

If f_2 does not evolve with L_X, the predicted $1 < z < 2$ type 1 AGN and host B band luminosity functions are not in agreement with observations. Using the host galaxy stellar population age and $E(B-V)$ as free parameters does not allow for an appropriate fit to the data. The over-prediction of $m_B \sim 23$ sources at $1 < z < 2$ is not due to observational bias as $m_B \sim 23$ is significantly brighter than the depth of B band coverage accessible to surveys (e.g., B band 5σ level for COSMOS is $m_B = 26.7$; Scoville et al., 2007). Lawrence & Elvis (2010) argue that f_2 does not evolve with L_X and that apparent evolution of f_2 with L_X is due to X-ray observational biases. However, the $z > 1$ type 1 AGN and host B band luminosity function data used here is based on optical selection criteria (Hartwick & Schade, 1990; Croom et al., 2004). The Della Ceca et al. (1996) type 1 AGN and host B band luminosity function does use a sample defined through X-ray selection, and the $z < 0.4$ predicted type 1 AGN and host B band luminosity function is in reasonable agreement with observation even if f_2 does not evolve with L_X. This suggests that X-ray observational biases do not create an artificial evolution of f_2 with L_X. Therefore, at least for $z > 1$, f_2 must evolve with L_X.

While this study cannot rule out the possibility that f_2 is constant with redshift, the findings of this study suggest that f_2 does evolve mildly with redshift. While some studies suggest that f_2 must evolve with redshift (e.g. La France et al., 2005; Ballantyne et al., 2006a,b; Treister & Urry, 2006), the evidence is still tentative. If AGN are fueled by different mechanisms, one might assume that the type 1/type 2 ratio will be different for the different mechanisms. Therefore, if different mechanisms dominate during different epochs, the type 1/type 2 ratio should also include some redshift evolution. It is possible that the slower

secular evolution processes of Seyfert galaxies do not require evolution of f_2 with redshift or that the evolution is very mild, since this form of galaxy evolution is governed by stochastic processes. However, in the quasar regime, where AGN fueling is initiated by major mergers, a stronger evolution of f_2 with redshift may be necessary. Indeed, the type 1 AGN and host B band luminosity function which is least well fit by a non-evolving f_2 is the highest redshift bin considered, which is the redshift bin closest to the peak of quasar activity. While this study does not conclusively show that f_2 evolves with redshift, the findings presented here suggest that f_2 does exhibit some evolution with redshift.

It is found that f_2 evolves with L_X and f_2 is likely to evolve with redshift. This suggests that the obscuring medium is close enough to the central engine to be affected by dust sublimation (Lawrence, 1991) and/or radiation pressure fueled winds (Königl & Kartje, 1994). Also, the type 1 AGN and host B band luminosity function is an excellent X-ray independent tool to test the fraction of type 1 AGN predicted by X-ray observations.

5.5 Summary

By applying observational constraints at optical through mid-IR wavelengths to AGN host stellar population models, the average stellar properties of AGN hosts have been constrained and hard X-ray through mid-IR SEDs have been developed which include emission from the AGN and the host galaxy stellar population and dust enshrouded star formation. The findings of this study are summarized as follows.

•Type 1 and type 2 AGN hosts have similar stellar populations at $z < 1$.

•At $z > 1$, type 1 and type 2 AGN hosts have stellar populations of similar age, but type 1 AGN hosts are intrinsically less dusty than type 2 AGN hosts.

•The orientation based unified model provides a good description of the $z < 1$ Seyfert population. The unified model does not seem to hold at $z > 1$, where quasar activity triggered by major mergers becomes more prevalent.

•Multi-wavelength data is consistent with the paradigm in which (high Eddington ratio) CT AGN have recently undergone intense star formation. In the non-evolving model the AGN activity does not start until the starburst is $\gtrsim$1 Gyr old and the stellar population

is highly obscured by dust. In the evolving model, it is possible that the average high Eddington ratio CT AGN host galaxy is a LIRG or ULIRG, with the AGN activity starting one average $\gtrsim$0.3 Gyr after the starburst.

•$\gtrsim$5-15% of the type 1 and type 2 AGN population may have enhanced levels of star formation, with average SFR $\approx$ 20 $M_{\odot}$ yr^{-1}.

•If the enhanced star formation sources are included, the evolving model CT AGN hosts are unaffected, but the non-evolving model CT AGN hosts are not consistent with the AGN evolution scheme and instead are consistent with the orientation based unified scheme. Thus, if CT AGN are similar to type 2 AGN, then CT AGN host galaxies are similar to type 2 AGN host galaxies; however, if CT AGN are a distinct population of AGN in a special evolutionary stage, then the host galaxies of CT AGN are also in a special evolutionary stage.

•In order to fit the type 1 AGN and host B band luminosity function it is necessary for f_2 to evolve with L_X. However, future work studying the dependence of f_2 on redshift is necessary to elucidate the connection between AGN and their hosts. Understanding the redshift evolution of f_2 will offer insight into how AGN are fueled and the nature of AGN obscuration.

•While the actual values of $E(B-V)$ depend on the metallicity and IMF used in the Bruzual & Charlot (2003) host galaxy population synthesis model, the qualitative findings of this study are independent of, and robust against the uncertainties in, the host galaxy metallicity and IMF.

5.6 References

Aird, J., Nandra, K., Laird, E.S., et al. 2009, MNRAS, 401, 2531

Alexander, D.M., Brandt, W. N., Hornschemeier, A. E., et al. 2001, AJ, 122, 2156

Alexander, D.M., Chary, R.-R., Pope, A., et al. 2008, ApJ, 687, 835

Antonucci, R., 1993 ARA&A, 31, 473

Assef, R.J., Kochanek, C.S., Ashby, M.L.N., et al. 2011, ApJ, 728, 56

Ballantyne, D.R., Everett, J.E., & Murray, N. 2006a, ApJ, 639, 740

Ballantyne, D.R., Shi, Y., Rieke, G.H., et al. 2006b, ApJ, 653, 1070

Ballantyne, D.R. 2008, ApJ, 685, 787

Ballantyne, D.R. 2009, ApJ, 698, 1033

Balogh, M.L., Morris, S.L., Yee, H.K.C., Carlberg, R.G., & Ellingson, E. 1999, ApJ, 527, 54

Bluck, A.F.L., Conselice, C.J., Almaini, O., et al. 2011, MNRAS, 410, 1174

Brand, K., Dey, A., Desai, V., et al. 2007, ApJ, 663, 204

Brandt, W.N., Hornschemeier, A.E., Alexander, D.M., et al. 2001, AJ, 122, 1

Brusa, M., Fiore, F., Santini, P., et al. 2009, A&A, 507, 1277

Bruzual, G. & Charlot, S. 2003, MNRAS, 344, 1000

Cardamone, C.N., Urry, C.M., Schawinski, K., et al. 2010, ApJ, 721, L38

Chabrier, G. 2003, PASP, 115, 763

Chen, Y.-M., Wang, J.-M., Yan, C.-S., Hu, C., & Zhang, S. 2009, ApJ, 695, L130

Crenshaw, D.M., Kraemer, S.B., & Gabel, J.R. 2003, AJ, 126, 1690

Croom, S. M., Smith, R. J., Boyle, B. J., et al. 2004, MNRAS, 349, 1397

Dahlen, T., Mobasher, B., Dickinson, M., et al. 2007, ApJ, 654, 172

Davies, R.I., Müller Sánchez, F., Genzel, R., et al. 2007, ApJ, 671, 1388

Della Ceca, R., Zamorani, G., Maccacaro, T., Setti, G., & Wolter, A. 1996, ApJ, 465, 650

Donley, J.L., Rieke, G.H., Alexander, D.M., Egami, E., & Pérez-González, P.G. 2010, ApJ, 719, 1393

Donley, J.L., Rieke, G.H., Pérez-González, P.G., & Barro, G. 2008, ApJ, 687, 111

Draper, A.R. & Ballantyne D.R. 2009, ApJ, 707, 778

Draper, A.R. & Ballantyne D.R. 2010, ApJ, 715, L99

Draper, A.R. & Ballantyne D.R. 2011, ApJ, 729, 109

Dunne, L., Eales, S.A., & Edmunds, M.G. 2003, MNRAS, 341, 589

Faber, S.M., Willmer, C.N.A., Wolf, C., et al. 2007, ApJ, 665, 265

Fabian, A.C. 1999, MNRAS, 308, L39

Fabian, A.C. & Barcons, X. 1992, ARA&A, 30, 429

Fabian, A.C., Vasudevan, R.V., Gandhi, P. 2008, MNRAS, 385, L43

Fabian, A.C., Vasudevan, R.V., Mushotzky, R.F., Winter, L.M., & Reynolds, C.S. 2009, MNRAS, 394, L89

Ferland, G.J., Korista, K.T., Verner, D.A., et al. 1998, PASP, 110, 761

Fiore, F., Grazian, A., Santini, P., et al. 2008, ApJ, 672, 94

Fiore, F., Puccetti, S., Brusa, M., et al. 2009, ApJ, 693, 447

Fu, H., Yan, L., Scoville, N.Z., et al. 2010, ApJ, 722, 653

Gandhi, P. & Fabian, A.C. 2003, MNRAS, 339, 1095

Georgakakis, A., Clements, D.L., Bendo, G., et al. 2009, MNRAS, 394, 533

Georgakakis, A., Rowan-Robinson, M., Nandra, K., et al. 2010, MNRAS, 406, 420

Ghisellini, G., Haardt, R., & Matt, G. 1994, MNRAS, 267, 743

Gilli, R., Comastri, A., Hasinger, G. 2007, A&A, 463, 79

González-Martín, O., Masegosa, J., Márquez, I., & Guainazzi, M. 2009, ApJ, 704, 1570

Griffiths, R.L. & Stern, D. 2010, AJ, 140, 533

Hartwick, F.D.A & Schade, D. 1990, ARA&A, 28, 437

Hasinger, G. 2008, A&A, 490, 905

Hickox, R.C., Jones, C., Forman, W.R., et al. 2009, ApJ, 696, 891

Hopkins, P.F. & Hernquist, L. 2009, ApJ, 694, 599

Hopkins, P.F., Hernquist, L., Cox, T.J., et al. 2006, ApJS, 163, 1

Kauffmann, G., Heckman, T. M., Budavári, T., et al. 2007, ApJS, 173, 357

Kauffmann, G., Heckman, T.M., Tremonti, C., et al. 2003, MNRAS, 346, 1055

Kauffmann, G., White, S.D.M., Heckman, T.M., et al. 2004, MNRAS, 353, 713

Kennicutt, R.C. 1998, ARA&A, 36, 189

Kim, M., Ho, L.C., Im, M. 2006, ApJ, 642, 702

Königl, A. & Kartje, J.F. 1994, ApJ, 434, 446

Kormendy, J. & Kennicutt, R.C. 2004, ARA&A, 42, 603

Kormendy, J. & Richstone, D. 1995, A&A, 33, 581

Kumar, P. & Johnson, J.L. 2010, MNRAS, 404, 2170

La Franca, F., Fiore, F., Comastri, A.,et al. 2005, ApJ, 635, 864

Lawrence, A. 1991, MNRAS, 252, 586

Lawrence, A. & Elvis, M. 2010, ApJ, 714, 561

Lee, J.C., Gil de Paz, A., Tremonti, C., et al. 2009, ApJ, 706, 599

Lutz, D., Mainieri, V., Rafferty, D., et al. 2010, ApJ, 712, 1287

Mainieri, V., Rosati, P., Tozzi, P., et al. 2005, A&A, 437, 805

Martínez-Sansigre, A., Karim, A., Schinnerer, E., et al. 2010, ApJ, 706, 184

McKernan, B., Ford, K.E.S., & Reynolds, C.S. 2010a, MNRAS, 407, 2399

McKernan, B., Maller, A., & Ford, K.E.S. 2010b, ApJ, 718, L83

Melbourne, J., Peng, C.Y., Soifer, B.T., et al. 2011, AJ, 141, 141

Nardini, E. & Risaliti, G. 2011, MNRAS, 415, 619

Page, M.J., Stevens, J.A., Ivison, R.J., & Carrera, F.J. 2004, ApJ, 611, L85

Pierce, C.M., Lotz, J.M., Laird, E.S., et al. 2007, ApJ, 660, L19

Pierce, C.M., Lotz, J.M., Salim, S., et al. 2010, MNRAS, 408, 139

Polletta, M., Weedman, D., Hönig, S., et al. 2008, ApJ, 675, 960

Polletta, M.d.C., Wilkes, B.J., Siana, B., et al. 2006, ApJ, 642, 673

Pope, A., Bussmann, R.S., Dey, A., et al. 2008, ApJ, 689, 127

Rieke, G.H., Alonso-Herrero, A., Weiner, B.J., et al. 2009, ApJ, 692, 556

Rigopoulou, D., Mainieri, V., Almaini, O., et al. 2009, MNRAS, 400, 1199

Risaliti, G., Maiolino, R., & Salvati, M. 1999, ApJ, 522, 157

Rodríguez Zaurín, J., Tadhunter, C.N., & González Delgado, R.M. 2010, MNRAS, 403, 1317

Rovilos, E., Fotopoulou, S., Salvato, M., et al. 2011, A&A, 529, 135

Rovilos, E., Georgantopoulos, I., Akylas, A., & Fotopoulou, S. 2010, A&A, 522, 11

Salpeter, E.E. 1955, ApJ, 121, 161

Sanders, D.B., Soifer, B.T., Elias, J.H., et al. 1988, ApJ, 325, 74

Santini, P., Maiolino, R., Magnelli, B., et al. 2010, A&A, 518, L154

Schawinski, K., Thomas, D., Sarzi, M., et al. 2007, MNRAS, 382, 1415

Scoville, N., Abraham, R.G., Aussel, H., et al. 2007, ApJS, 172, 38

Serjeant, S., Bertoldi, F., Blain, A.W., et al. 2010, A&A, 518, L7

Serjeant, S. & Hatziminaoglou, E. 2009, MNRAS, 397, 265

Seymour, N., Symeonidis, M., Page, M.J., et al. 2011, MNRAS, 413, 1777

Shapiro, K.L., Genzel, R., Förster Schreiber, N.M., et al. 2008, ApJ, 682, 231

Shi, Y., Rieke, G.H., Ogle, P., Jiang, L., & Diamond-Stanic, A.M. 2009, ApJ, 703, 1107

Silverman, J.D., Kovač, K., Knobel, C., et al. 2009, ApJ, 695, 171

Simpson, C. 2005, MNRAS, 360, 565

Smolčić, V. & Riechers, D.A. 2011, ApJ, 730, 64

Terashima, Y., & Wilson, A.S. 2003, ApJ, 583, 145

Thompson, G.D., Levenson, N.A., Uddin, S.A., & Sirocky, M.M. 2009, ApJ, 697, 182

Thompson, T.A., Quataert, E., & Murray, N. 2005, ApJ, 630, 167

Treister, E., Cardamone, C.N., Schawinski, K., et al. 2009a, ApJ, 706, 535

Treister, E., Natarajan, P., Sanders, D.B., et al. 2010, Science, 328, 600

Treister, E., & Urry, C.M., 2005, ApJ, 630, 115

Treister, E. & Urry, C.M., 2006, ApJ, 652, L79

Treister, E., Urry, C.M., Van Duyne, J., et al. 2006, ApJ, 640, 603

Treister, E., Urry, C.M., & Virani, S., 2009b, ApJ, 696, 110

Trump, J.R., Impey, C.D., Brandon, C.K., et al. 2011, ApJ, 733, 60

Ueda, Y., Akiyama, M., Ohta, K., & Miyaji, T. 2003, ApJ, 598, 886

Wilman, R.J., Jarvis, M.J., Mauch, T., Rawlings, S., & Hickey, S. 2010, MNRAS, 405, 447

Winter, L.M., Mushotzky, R.F., Reynolds, C.S., & Tueller, J. 2009, ApJ, 690, 1322

Wold, I., Sheinis, A.I., Wolf, M.J., & Hooper, E.J. 2010, MNRAS, 408, 713

CHAPTER VI

A TALE OF TWO POPULATIONS: THE CONTRIBUTION OF MERGER AND SECULAR PROCESSES TO THE EVOLUTION OF ACTIVE GALACTIC NUCLEI

6.1 Introduction

In less than a decade it was determined that not only do all massive galaxies harbor a supermassive black hole at their center (Kormendy & Richstone, 1995), but also that the evolution of the galaxy is intrinsically linked to the growth of the central black hole (e.g., Magorrian et al., 1998; Tremaine et al., 2002). However, the mechanism responsible for the co-evolution of a supermassive black hole and its host galaxy is still under investigation. As accreting supermassive black holes, generally referred to as active galactic nuclei (AGN), can, over their lifetime, radiate an amount of energy comparable to the binding energy of their host galaxy (e.g., Silk & Rees, 1998; Fabian, 1999; Alexander et al., 2010), it is expected that this AGN feedback will affect star formation in the host galaxy (e.g., Fabian, 1999; Hopkins et al., 2006a; Lagos et al., 2008; Trichas et al., 2009; Bertone et al., 2010; Hambrick et al., 2011; Hocuk & Spaans, 2011). Galaxy wide processes can also affect the central supermassive black hole. For example, theoretical and observational evidence suggests that AGN can be triggered by major mergers of massive gas rich galaxies (e.g., Sanders et al., 1988; Hernquist et al., 1989; Carlberg, 1990; Kauffmann & Haehnelt, 2000; Hopkins et al., 2006a) or by secular processes not connected to major mergers, such as supernova winds, stellar bars, cold-flow accretion, interactions with other massive galaxies or satellite galaxies, or minor mergers (e.g., Crenshaw et al., 2003; Kormendy & Kennicutt, 2004; Vittorini et al., 2005; Davies et al., 2007; Pierce et al., 2007; Chen et al., 2009; Kumar & Johnson, 2010; Bournaud et al., 2011; Orban de Xivry et al., 2011).

Simulations show that mergers of gas rich galaxies cause gas and dust to lose angular momentum and fall into the central regions of the galaxy (e.g., Barnes & Hernquist, 1996). The resulting nuclear gas reservoir will be consumed by star formation in the host bulge and accretion flows onto the resident supermassive black hole (Hopkins et al., 2006a,b). According to the galaxy evolution model explored by Hickox et al. (2009), AGN feedback will then evolve the AGN host galaxy across the color-magnitude diagram (CMD) from the massive end of the blue cloud, through the green valley, and onto the red sequence (but see Schawinski et al. 2009 and Cardamone et al. 2010). Secular processes, such as supernova explosions, stellar bars, minor mergers and interactions, will also release angular momentum from gas and dust leading to a similar reservoir of gas in the central region of the galaxy (e.g., Crenshaw et al., 2003; Davies et al., 2007; Chen et al., 2009; Orban de Xivry et al., 2011). Despite mergers and secular mechanisms both leading to the accumulation of gas and dust deep in the galactic potential well, mergers and secular processes have very different galaxy wide effects and roles in galaxy evolution. Major mergers are violent processes which, as with the Antennae galaxies, can destroy galactic structure, causing the merger remnant to relax into a bulge-dominated system (e.g., Hopkins & Hernquist, 2006). Secular evolution, however, is not likely to disturb the morphology or large-scale structure of the host galaxy (see Georgakakis et al., 2009). Despite the systemic differences between galaxy evolution and AGN activity due to major mergers and secular processes, it is difficult to observationally determine which mechanism is responsible for a given AGN; tidal tails are often faint, bulge-dominated systems can be re-triggered by secular processes, and the timescales for AGN activity tend to be longer than the timescales for a merger remnant galaxy to dynamically relax (Schawinski et al., 2010a).

Despite the observational difficulties in determining how a particular AGN has been triggered, there is observational evidence that major mergers are not the dominant AGN triggering mechanism, at least not at $z \lesssim 2$. By determining the Sérsic indices of massive galaxies at $z = 2$–3, Weinzirl et al. (2011) found that ∼65% of AGN hosts at this redshift range have Sérsic indices indicative of disky morphologies. Observations also show that in the redshift ranges $z = 1.5$–3 (Schawinski et al., 2011) and $z = 1.5$–2.5 (Kocevski et

al., 2012), the majority of moderate luminosity AGN are hosted by disk galaxies. By considering galaxy pairs at $z \lesssim 2$, Williams et al. (2011) find that the wet major merger rate is too low to account for the majority of AGN activity at $z \lesssim 2$. When investigating AGN in zCOSMOS, Silverman et al. (2011) found that ∼20% of moderate luminosity AGN at $0.25 < z < 1.05$ are in close pairs, and thus were likely triggered by galaxy interactions. Cisternas et al. (2011) argue that AGN are as likely as quiescent galaxies to show signs of a recent merger at $z < 1$, and thus mergers cannot be connected to AGN activity at this redshift range. Georgakakis et al. (2009) investigate the morphology of AGN hosts and find that AGN hosted by disk galaxies contribute ∼25% of the AGN luminosity density at $z \approx 0.8$. They conclude, therefore, that a large fraction of $z \sim 1$ AGN are triggered by mechanisms unrelated to major mergers. Cardamone et al. (2010) found that when AGN host galaxy colors are corrected for dust extinction, there is a bi-modality of AGN host galaxy colors at $z \sim 1$, suggesting that there are two modes of AGN activity at this redshift range. When modeling the AGN population by considering mergers of massive dark matter halos, Shen (2009) find that secular AGN activity is necessary at $z < 0.5$ to account for the observed AGN population. Koss et al. (2010) recently found that ∼20% of *Swift*/BAT AGN at $z < 0.05$ are hosted by galaxies with disturbed morphologies indicative of a recent major merger and an additional 6% of *Swift*/BAT AGN are in close pairs suggesting these AGN were triggered by galaxy interactions. Thus, it appears that both major mergers and secular processes must contribute to the AGN activity observed at $z \lesssim 2$. If secular triggers dominate the AGN population at $z \lesssim 2$, current understanding of the stochastic fueling of secular mechanisms is insufficient to explain the high luminosity of quasars observed at $z \lesssim 2$ (Hopkins & Hernquist, 2006). However, Bournaud et al. (2011) recently showed that, at least at high redshift, it is possible for cold-flow accretion to trigger moderate luminosity AGN with occasional bright episodes. Thus, phenomenological models of the AGN population may provide an important tool for understanding the importance of merger and secularly triggered AGN at various redshift and luminosity ranges.

Here, a model of the AGN population is calculated using an empirically motivated space density of AGN triggered at each redshift and a theoretical AGN light curve. It is considered

whether major mergers or secular mechanisms alone can account for the observed AGN hard X-ray luminosity function (HXLF), AGN number counts, black hole space density, and the X-ray background (XRB) spectrum. In Section 6.2 the details of the AGN model, including the triggering rate, light curve, and black hole mass functions utilized, are described. Section 6.3 explains the calculations completed to compare the model against observations. I then consider the model results if AGN are a single population (Section 6.4) or two populations (Section 6.5). The results are discussed and summarized in Sections 6.6 and 6.7. A ΛCDM cosmology is assumed with $H_0 = 70$ km s^{-1} Mpc^{-1} and $\Omega_\Lambda = 1.0$ - $\Omega_M = 0.7$.

6.2 The AGN Population Model

In order to model the evolution of the AGN HXLF, three ingredients are necessary. To determine the space density of triggered AGN, an empirically based major merger rate is used. Once triggered, the AGN Eddington ratio, $\lambda = L_{bol}/L_{Edd}$, where L_{bol} is the bolometric luminosity and L_{Edd} is the Eddington luminosity, is evolved using a theoretically motivated light curve. The active black hole mass function (ABHMF) and the Marconi et al. (2004) bolometric correction are then used to convert from Eddington ratio to 2–10 keV luminosity, L_X. These three ingredients are described in detail below.

6.2.1 Triggering Rate

In order to determine the space density of AGN triggered at each redshift, the space density of gas rich massive galaxies at redshift z must be calculated. First, the minimum stellar mass of a massive galaxy, M_*^{min}, at z is derived by parametrizing the median mass of ultra-luminous infrared galaxies (ULIRGS) as a function of redshift (Treister et al., 2010a), which gives

$$M_*^{min}(z) = 5 \times 10^{11}(1.0+z)^{-1.5} M_\odot. \tag{6.1}$$

The space density of massive galaxies at z, $N_{gal}(M_* > M_*^{min}(z))$, in Mpc^{-3}, can then be calculated by integrating the stellar mass function from $M_*^{min}(z)$ to $M_*^{max} = 10^{12.5}$ M$_\odot$, such that

$$N_{gal}(M_* > M_*^{min}(z)) = \int_{M_*^{min}(z)}^{M_*^{max}} \frac{d\Phi_{gal}(M_*, z)}{d\log M_*} d\log M_*, \tag{6.2}$$

where $d\Phi_{gal}/d\log M_*$ is the stellar mass function (SMF) of Pérez-González et al. (2008) for $z \lesssim 4$. The dependence of the results on the SMF is considered in Sections 6.4.1 and 6.4.2. To determine the space density of gas rich massive galaxies, the fraction of gas rich galaxies at z, $f_g(z)$, must be determined. Considering observations of the GOODS fields (Dahlen et al., 2007), Treister et al. (2010a) find that $f_g(z)$ can be parametrized as

$$f_g(z) = \begin{cases} 0.11(1+z)^{2.0} & z \leq 2 \\ 1 & z > 2 \end{cases} . \tag{6.3}$$

Thus the space density, in Mpc^{-3}, of potential AGN host galaxies at redshift z is $f_g(z)N_{gal}(M_* > M_*^{min}(z))$.

The space density of AGN triggered by a merger at redshift z is then calculated by multiplying the space density of potential AGN host galaxies at z by the fraction of massive galaxies which will undergo a merger at z. Following Hopkins et al. (2010a), who derive the major merger rate per galaxy per Gyr, $d^2\Psi/dt\ dN$, from simulations and observational constraints, $d^2\Psi/dt\ dN$ is parametrized as

$$\frac{d^2\Psi}{dt\, dN} = A(M_*^{min})(1.0+z)^{\beta(M_*^{min})}, \tag{6.4}$$

where

$$A(M_*) = 0.02\left[1 + \left(\frac{M_*}{2\times 10^{10} M_\odot}\right)^{1/2}\right] \mathrm{Gyr}^{-1} \tag{6.5}$$

and

$$\beta(M_*) = 1.65 - 0.15\log\left(\frac{M_*}{2\times 10^{10} M_\odot}\right). \tag{6.6}$$

Here the major merger is said to occur upon the coalescence of the two similarly massive galaxies (Hopkins et al., 2010b). By assuming that every major merger leads to an AGN event, with a negligible time delay between the merger and the triggering of the AGN activity, the space density of AGN triggered by major mergers, dN_{merg}, at redshift z is

$$dN_{merg}(z) = \frac{d^2\Psi}{dN dt}\, N_{gal}(M_* > M_*^{min}(z))\, f_g(z)\, dt\, \mathrm{Mpc}^{-3}. \tag{6.7}$$

The rate at which AGN are triggered through secular processes, such as galaxy interactions, cold gas accretion, and internal disk instabilities, is calculated in a similar manner.

For AGN triggered by secular processes, $M_*^{min}(z) = 5 \times 10^9$ M$_\odot$, in agreement with the findings of Schawinski et al. (2010b). The fractional rate of massive gas rich galaxies which are triggered through secular processes every Gyr, f_{sec}, is assumed to be constant with redshift. Yamada et al. (2009) found that the fraction of galaxies with $M_* > 10^{11}$ M$_\odot$ hosting AGN, which are triggered through both secular processes and mergers, is $\sim$0.3. As the fraction of AGN triggered by secular processes is poorly constrained observationally, and galaxies with $M_* > 5 \times 10^9$ M$_\odot$ are considered, the constraint $f_{sec} \ll 0.3$ Gyr^{-1} is used. The specific value of f_{sec} is set by calculating the predicted AGN HXLF and minimizing a χ^2 test which compares against the observed HXLF. The space density of AGN triggered by secular mechanisms, dN_{sec}, at redshift z is then

$$dN_{sec}(z) = f_{sec}\, N_{gal}(M_* > M_*^{min}(z))\, f_g(z)\, dt\, \mathrm{Mpc}^{-3}. \tag{6.8}$$

6.2.2 AGN Light Curve

Once the AGN has been triggered, its Eddington ratio is used to parametrize the accretion as a function of time since the AGN was triggered. While there is evidence that AGN are an intermittent phenomenon, Treister et al. (2010a) show that quasars can grow most of their black hole mass in a single, merger triggered event. Therefore, a single-peaked light curve is assumed.

Based on hydrodynamical simulations, Hopkins & Hernquist (2009) suggest

$$\lambda(t) = \left[1 + (|t|/t_Q)^{1/2}\right]^{-2/\beta}, \tag{6.9}$$

where $t = t_{on} - t_Q$, where t_{on} is the time since the AGN was triggered, $t_Q = t_0 \eta^\beta / (2\beta \ln 10)$, and t_0, η, and β are fitting parameters which describe the quasar lifetime, maximum Eddington ratio, and light curve slope, respectively[1].

[1]For completeness, a wide variety of light curves were tested, including a constant λ, a monotonic linearly increasing or decreasing λ, a monotonic exponentially increasing or decreasing λ, a linearly increasing followed by a linearly decreasing λ, and an exponentially increasing followed by an exponentially decreasing λ. However, these light curve models were unable to match the shape of the AGN HXLF.

6.2.3 Active Black Hole Mass Function and Its Evolution

By combining the triggering rate and light curve, the space density of AGN with Eddington ratio λ can be calculated at any redshift $z \lesssim 4$. However, to compute model predictions that can be compared to observational constraints, the black hole mass must be used to convert Eddington ratios into bolometric luminosities. Once the bolometric luminosity is computed, the Marconi et al. (2004) bolometric correction is used to determine L_X. The distribution of black hole masses is determined by the fractional active black hole mass function (ABHMF) at z, which describes the fraction of active black holes at redshift z with black hole mass $M_\bullet$.

Two ABHMFs are considered. The first ABHMF is a Gaussian fit to the combined type 1 and type 2 AGN ABHMF at $z \sim 0.15$ observed by Netzer (2009). The second ABHMF considered is a Schechter function with the same slope and critical mass, M_{crit}, as the black hole mass function described by Merloni & Heinz (2008). Both ABHMFs are considered over the range $\log(M_\bullet^{min}/M_\odot) = 5.95$ and $\log(M_\bullet^{max}/M_\odot) = 10.55$. A black hole with $M_\bullet < M_\bullet^{min}$ would need to accrete at Eddington ratio $\lambda \gtrsim 0.1$ to achieve $\log L_X \gtrsim 41.5$. According to the light curve used here, the vast majority of the AGN lifetime is spent at $\lambda < 0.1$. Therefore, black holes with $M_\bullet < M_\bullet^{min}$ are expected to only make a very small contribution to the observed AGN population (Marconi et al., 2004; Merloni & Heinz, 2008). Black holes with $M_\bullet > M_\bullet^{max}$, correspond to $\ll 0.1\%$ of all active black holes according to both the Merloni & Heinz (2008) and Netzer (2009) ABHMFs, in agreement with the maximum black hole mass derived by Natarajan & Treister (2009).

Both the Merloni & Heinz (2008) and Netzer (2009) ABHMFs are derived using scaling relationships to determine black hole masses. These scaling relationships have an intrinsic scatter of $\sim$0.3 dex (Peterson & Bentz, 2006; Merloni & Heinz, 2008; Netzer, 2009). This leads to an uncertainty in the calculated L_X of a factor $\sim 2 \times \lambda$. For the majority of sources, $\lambda < 0.1$, thus the uncertainty introduced by the ABHMF is a smaller part of the error budget than the uncertainty in the major merger rate, which is a factor $\sim$2.

For both ABHMFs two redshift evolutions are investigated. The first ABHMF evolution

uses the continuity equation (Small & Blandford, 1992; Merloni & Heinz, 2008)

$$\frac{\partial n_M(M_\bullet, t)}{\partial t} + \frac{\partial [n_M(M_\bullet, t)\langle \dot{M}(M_\bullet, t)\rangle]}{\partial M} = 0, \tag{6.10}$$

where n_M is the ABHMF and $\langle \dot{M}(M_\bullet, t)\rangle$ is the average accretion rate of black holes with mass $M_\bullet$ at time t. By integrating this conservation equation forward and backward in time, using the observed ABHMF as the boundary condition, the ABHMF can be evolved to any redshift z. This evolution assumes that black hole growth occurs through accretion and that binary mergers are not the primary mechanism of black hole growth (e.g., Volonteri et al., 2003). The second ABHMF evolution considered is based on the observations of Labita et al. (2009) who found that the maximum black hole mass of the quasar population increases with redshift. Thus, $M_\bullet^{crit}(z) = M_\bullet^{crit}(0)(1.0+z)^{1.64}$. In order to compare the two considered evolutions, a power law is fit to $M_\bullet^{crit}(z)$ of the Merloni & Heinz (2008) ABHMF evolved with the continuity equation and it is found that $M_\bullet^{crit}(z) \approx M_\bullet^{crit}(0)(1.0+z)^{0.5}$. For both ABHMFs, the ABHMF is re-normalized at each redshift so that integrating over all black hole masses gives 1.

With the observationally determined AGN triggering rate, theoretical Eddington ratio evolution, and the ABHMF in place, the AGN population at $z < 4$ can be fully modeled[2]. To determine the light curve fitting parameters, t_0, β, and η, the AGN population model must be compared to observational constraints.

6.3 Calculations and Observational Constraints

In order to constrain the light curve parameters, the AGN population model is compared against the HXLF at five different redshifts, the black hole mass density as a function of redshift, the *Swift/BAT* 15–55 keV AGN counts, the 2–10 keV AGN counts, and the XRB spectrum. The methods used to calculate these quantities are described below.

[2]AGN triggered at $z > 4$ make only a minor contribution to the $z \lesssim 2$ AGN population. Therefore, if the AGN triggered at $z > 4$ are included, the results of this study do not change.

6.3.1 AGN HXLF

The HXLF, $d\Phi_X(L_X, z)/d\log L_X$, is computed at five different redshifts, $z = 2.3$, 1.2, 0.6, 0.3, and 0.1. The HXLFs observed by Ueda et al. (2003), La Franca et al. (2005), Silverman et al. (2008), Aird et al. (2010), and Ueda et al. (2011) are each presented in different redshift bins. Therefore, the predicted HXLF is computed at the central redshift of each of the Ueda et al. (2003) redshift bins.

The bolometric AGN luminosity function at redshift z, $d\Phi(L_{bol}, z)/d\log L$, is computed by integrating over the space density of AGN triggered at redshift z_t and, at redshift z, have black hole mass $M_\bullet$ and Eddington ratio λ such that the bolometric luminosity is L_{bol}. Thus,

$$\frac{d\Phi(L_{bol}, z)}{d\log L} = \int_{M_\bullet^{min}}^{M_\bullet^{max}} n_M(M_\bullet, z) d\log M_\bullet \int_z^4 \Phi_\lambda(M_\bullet, z) dz_t, \tag{6.11}$$

where $\log(M_\bullet^{min}/M_\odot) = 5.95$, $\log(M_\bullet^{max}/M_\odot) = 10.55$, z_t is the triggering redshift, and

$$\Phi_\lambda(M_\bullet, z) = \begin{cases} \frac{dN(z_t)}{d\log L} & \lambda(z, z_t) L_{Edd}(M_\bullet) = L_{bol} \\ 0 & \text{otherwise} \end{cases}, \tag{6.12}$$

where dN is either dN_{merg} or dN_{sec}. The Marconi et al. (2004) luminosity dependent bolometric correction is then used to convert L_{bol} to L_X.

As the observed HXLF only includes Compton thin AGN, the Compton thick AGN are removed from the calculated HXLF by assuming that one-third of all obscured AGN are Compton thick in agreement with the fraction of Compton thick AGN necessary for the Ueda et al. (2003) observed HXLF to be in agreement with the peak of the XRB at ~ 30 keV (Draper & Ballantyne, 2009, 2010; Ballantyne et al., 2011). The fraction of Compton thin obscured sources, f_2, is assumed to be a function of luminosity and redshift such that $f_2 \propto (1+z)^a (\log L_X)^{-b}$, where $a = 0.4$ (Ballantyne et al., 2006; Treister & Urry, 2006) and $b = 4.7$. The normalization factor is determined by assuming the type 2 to type 1 AGN ratio is 4:1 at $z = 0$ and $\log L_X = 41.5$. Thus, the space density of Compton thick AGN also depends on L_X and, in Mpc^{-3} dex^{-1}, is $(f_2/2)\ d\Phi_X/d\log L_X$.

According to both the Marconi et al. (2004) and Vasudevan et al. (2009) bolometric corrections, to achieve $L_X = 10^{46.5}$ erg s^{-1} it is necessary to have a black hole with mass

$\approx 10^{10.7}$ – $10^{10.9}$ $M_\odot$ accreting at its Eddington rate. Both the Gaussian fit to the Netzer (2009) and the Merloni & Heinz (2008) ABHMF, predict the fraction of active black holes with mass $\sim 10^{11}$ $M_\odot$ is ~ 0, in agreement with the black hole mass upper limit derived by Natarajan & Treister (2009). This strongly suggests that AGN with $L_X \gtrsim 10^{46}$ erg s^{-1} are accreting at super-Eddington rates. The light curve model used allows for $0 \lesssim \lambda \lesssim 1$. Therefore, super-Eddington accretion cannot be taken into account. Thus, the models presented here will necessarily under-predict the $L_X > 10^{46}$ erg s^{-1} observed HXLF data points. For completeness, the HXLF data points at $L_X > 10^{46}$ erg s^{-1} are still taken into account when performing the χ^2 fitting[3].

6.3.2 Black Hole Mass Density

To calculate the black hole mass density, the Sołtan (1982) argument is used. Thus, the black hole mass density at redshift z, $\rho_\bullet(z)$, is calculated as

$$\rho_\bullet(z) = \int_z^\infty \frac{dt}{dz} dz \int_0^\infty \frac{1-\epsilon}{\epsilon c^2} L_{bol} \frac{d\Phi(L,z)}{d\log L} d\log L \tag{6.13}$$

where $\epsilon = 0.1$ is the radiative efficiency, c is the speed of light, and $d\Phi(L,z)/d\log L$ is the AGN luminosity function (Yu & Tremaine, 2002; Marconi et al., 2004; Treister et al., 2011) [4]. The contribution of Compton thick AGN to the black hole mass density is included. The predicted black hole mass density is compared to the local black hole mass density observed by Shankar et al. (2009) and the $z \sim 2$ black hole mass density observed by Treister et al. (2010b).

6.3.3 X-ray Background Spectrum

The XRB spectrum model closely follows that described by Draper & Ballantyne (2009). Instead of inputting the observed luminosity function, the HXLF calculated as described in Section 6.3.1 is used. Also, a torus reflection component (Gilli et al., 2007) is included

[3]Exclusion of the three data points at $L_X > 10^{46}$ erg s^{-1} changes the reduced χ^2 values by $\lesssim 0.1$ and does not affect the determination of the light curve parameters.

[4]It is expected that at Eddington ratios $\lambda \lesssim 10^{-2}$, AGN accretion flows become radiatively inefficient and the radiative efficiency decreases with λ (e.g., Cao & Xu, 2007). If Equation 1 of Merloni & Heinz (2008) is used to characterize ϵ, the calculated local black hole mass density changes by $< 5\%$ since the majority of black hole growth occurs during radiatively efficient accretion.

which is computed using "reflion" (Ross & Fabian, 2005). The Type 2 fraction, f_2, is determined as in Section 6.3.1. The Compton thick fraction, f_{CT}, is defined as the ratio of the number of Compton thick AGN to the number of Compton thin type 2 AGN, and is set to $f_{CT} = 0.5$, in agreement with the f_{CT} necessary for the Ueda et al. (2003) HXLF to be in agreement with the XRB spectrum and the local Compton thick AGN space density (Draper & Ballantyne, 2009, 2010; Ballantyne et al., 2011). The unabsorbed type 1 sources are evenly distributed over column densities $\log N_H = 20.0$, 20.5, 21.0, and 21.5. The Compton thin type 2 sources are distributed equally over $\log N_H = 22.0$, 22.5, 23.0, and 23.5. The contribution of Compton thick AGN to the XRB is included. To do so, it is assumed that Compton thick sources evolve similarly to less obscured AGN and are evenly distributed over $\log N_H = 24.0$, 24.5, and 25.0.

The AGN number counts in the 2–10 keV and 15–55 keV bands are also calculated. This is done by using the same AGN spectra, f_2, and f_{CT} as in the XRB model described above, including the contribution of Compton thick AGN, and by using the HXLF calculated as in Section 6.3.1.

6.3.4 Summary of Free Parameters

The light curve fitting parameters— t_0, which is related to the AGN lifetime, η, which is related to the peak Eddington ratio, and β, which determines the slope of the light curve— are determined by comparing the resulting models against the observed HXLF, evolving black hole space density, XRB spectrum, and AGN number counts. The fractional rate of massive galaxies which are triggered by secular processes each Gyr, f_{sec}, is also determined by comparing against observational constraints.

The focus of this study is not to fit the AGN light curve parameters, but to investigate the contribution to the AGN population of AGN triggered by major mergers and AGN triggered by secular processes. Therefore, a minimization algorithm is not used. Instead, the best fit parameters for the AGN light curve are determined by considering models with $t_0 = 1.0 \times 10^7$, 5.0×10^7, 1.0×10^8, 2.5×10^8, 5.0×10^8, 7.5×10^8, and 1.0×10^9 yrs. Hopkins & Hernquist (2006) found that their model results were not very dependent on η,

so the values $\eta = 0.2$, 0.4, 1.0, 2.5, and 3.0 are considered. Steps of 0.05 in the range from 0.05 to 1.0 are used to determine β. For f_{sec} the values 0.0, 0.005, 0.01, 0.02, and 0.05 Gyr^{-1} are investigated. The best fit parameters for each model are determined by minimizing a χ^2 test which takes into account the 127 HXLF data points for $z = 2.3$, 1.2, 0.6, 0.3, and 0.1 presented by Ueda et al. (2003), La Franca et al. (2005), Silverman et al. (2008), Aird et al. (2010), and Ueda et al. (2011). By comparing against the observed AGN HXLF, black hole mass density, XRB spectrum, and AGN number counts, the model is fully constrained, allowing for some conclusions to be reached about the AGN light curve parameters. The model sensitivity to the light curve parameters is discussed in Section 6.6.1.

6.4 One Population

6.4.1 Major Merger Triggered Quasars

First, it is assumed that all AGN are triggered by major mergers, thus, $f_{sec} = 0.0$. The best fit to the HXLF is found using the Merloni & Heinz (2008) ABHMF with the Labita et al. (2009) evolution, $t_0 = 2.5 \times 10^8$ yrs, $\beta = 0.7$, and $\eta = 2.5$, similar to that found by Cao (2010). When compared to the 127 data points from the Ueda et al. (2003), La Franca et al. (2005), Silverman et al. (2008), Aird et al. (2010), and Ueda et al. (2011) observed HXLFs in the 5 redshift ranges considered, this model has a reduced χ^2, $\chi^2_{red} = 2.4$. If t_0 is changed by 0.5×10^8 yrs, β is changed by 0.05, or η is changed by 0.5, the resulting χ^2_{red} will increase by $\sim 0.1 - 0.2$. The light curve fitting parameters are summarized in Table 6.4.1. As shown by the dot-dashed red lines in Figure 6.1, this model provides a relatively good fit to the observed HXLF at $z \gtrsim 1$; however, at $z < 1$, this model has $\chi^2_{red} = 2.6$ for 85 data points. The space density of major mergers at $z < 1$ is too low to explain the space density of observed AGN in this redshift range. This model is in agreement with the observed local black hole mass density (Shankar et al., 2009) and the $z \sim 2$ observed black hole mass density (Treister et al., 2010b). However, this model significantly under-predicts the XRB spectrum as well as the 2–10 keV and 15–55 keV AGN number counts. Thus, despite major merger triggered AGN being able to account for the integrated black hole growth, merger triggered AGN cannot account for the space density of the entire AGN

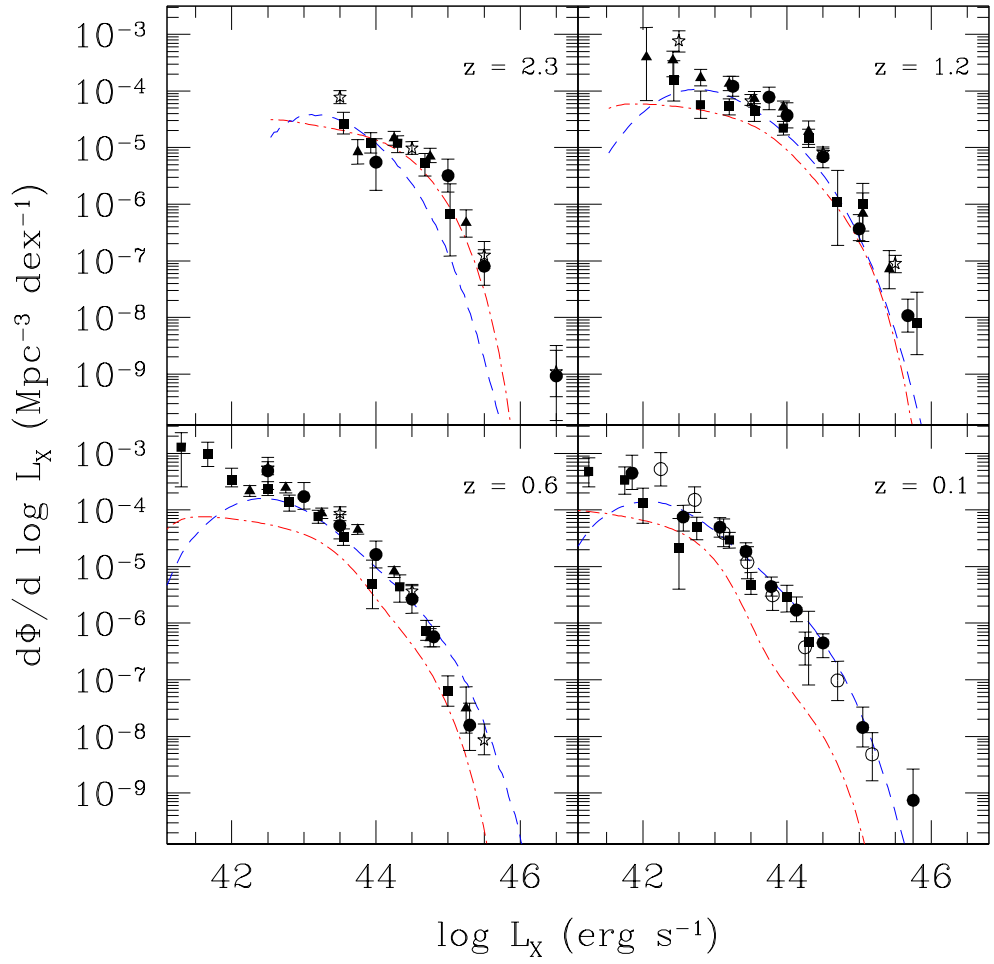

Figure 6.1: Best fit one population models compared against the observed HXLF. The dot-dashed red lines show the HXLF from the best fit major merger trigger only model and the dashed blue lines show the HXLF from the best fit secular processes trigger only model. The data points show measurements of the HXLF by Ueda et al. (2003; filled circles), La Franca et al. (2005; stars), Silverman et al. (2008; triangles), Aird et al. (2010; squares), and Ueda et al. (2011; open circles).

Table 6.1: Summary of derived model free parameters.

Model	Merger Triggered AGN			Secularly Triggered AGN			
	t_0 (yr)	β	η	t_0 (yr)	β	η	f_{sec} (Gyr^{-1})
One Population Models							
Mergers only	2.5×10^8	0.7	2.5	-	-	-	0.0
Secular only	-	-	-	2.5×10^8	0.8	0.4	0.02
Two Population Models							
N09 w/ Eq. 6.10	2.5×10^8	0.7	0.4	5×10^8	0.5	2.5	0.005
N09 w/ L09	1×10^8	0.5	1.0	2.5×10^8	0.6	2.5	0.005
MH08 w/ Eq. 6.10	2.5×10^8	0.8	2.5	5×10^8	0.7	2.5	0.01
MH08 w/ L09	2.5×10^8	0.7	2.5	5×10^8	0.8	2.5	0.005
Two Population Mixed ABHMF Model							
Mixed ABHMF	2.5×10^8	0.7	2.5	2.5×10^8	0.8	2.5	0.01

MH08 refers to the Merloni & Heinz (2008) ABHMF, N09 refers to the Netzer (2009) ABHMF, and L09 refers to the Labita et al. (2009) ABHMF evolution. The mixed ABHMF model uses the MH08 ABHMF with L09 evolution for the merger triggered AGN and the N09 ABHMF with the continuity equation (Eq. 6.10) evolution for the secularly triggered AGN.

population. Specifically, major mergers cannot account for the $z \lesssim 1$ AGN population.

The finding that major mergers are not capable of accounting for the $z \lesssim 1$ AGN population is robust against several assumptions. To test the dependence of the merger triggered AGN only model on the SMF, the $z = 1.3$–3 SMF presented by Marchesini et al. (2009) and the $z = 0.1$ SMF presented by Cole et al. (2001) are used to define an evolving SMF. When using the combined Cole et al. (2001) and Marchesini et al. (2009) SMF, the merger triggered AGN only model is not able to account for the space density of AGN at $z \lesssim 1$, with minimum $\chi^2_{red} = 3.6$. Similarly, if the minimum mass of a potential AGN host galaxy (M_*^{min}) is reduced, the merger only model cannot supply a decent fit to the observational constraints.

6.4.2 Secularly Triggered AGN

Next, the scenario where all AGN are triggered by secular processes is considered. For this model, the best fit to the HXLF is found when using the Netzer (2009) ABHMF with the continuity equation evolution, $t_0 = 2.5 \times 10^8$ yrs, $\beta = 0.8$, $\eta = 0.4$, and $f_{sec} = 0.02$ Gyr^{-1}. This model has $\chi^2_{red} = 2.1$ for 127 data points. If t_0 is changed by $\sim 0.5 \times 10^8$ yrs,β is changed by 0.05, or f_{sec} is changed by 0.01 Gyr^{-1}, the resulting χ^2_{red} will change by ~ 0.2. If η is changed by ~ 0.5 the resulting χ^2_{red} will increase by ~ 0.1. As shown

by the blue dashed lines in Figure 6.1, this model under-predicts the space density of low L_X AGN at $z \lesssim 1$ and under-predicts high L_X sources at $z \gtrsim 1$. Furthermore, this model significantly under-predicts the local black hole mass density, the XRB, and the 2–10 keV number counts. This model slightly over-predicts the *Swift*/BAT 15–55 keV number count and is inconsistent with the findings of Koss et al. (2010) that ∼20% of *Swift*/BAT AGN host galaxies have disturbed morphology indicative of a recent major merger. Thus, secular processes alone are not sufficient to account for the entire AGN population. Specifically, secular processes are not able to account for the AGN population at $z \gtrsim 0.5$. When the minimum mass of a potential AGN host galaxy is reduced or the evolving SMF defined by combining the Cole et al. (2001) and Marchesini et al. (2009) SMFs is used, the secular evolution only model still cannot account for the $z \gtrsim 0.5$ AGN population, with minimum $\chi^2_{red} = 2.0$. It is found that AGN triggered by secular mechanisms alone cannot explain the observed AGN population.

Neither merger triggered AGN nor secularly triggered AGN alone are able to account for the entire AGN population. Reducing the minimum mass of potential AGN host galaxies and using the combined Cole et al. (2001) and Moretti et al. (2009) SMF does not change this result. The space density of major mergers at $z < 1$ is too low to account for the low redshift AGN population but can account for the local space density of black holes. In contrast, AGN triggered by secular mechanisms are not able to account for the build up of the black hole mass density over cosmic time. Thus, the possibility that AGN are triggered by both major mergers and secular processes is investigated.

6.5 Two Populations

As neither the major merger triggered AGN nor the secularly triggered AGN can alone account for the entire AGN population, a two population model in which AGN are assumed to be triggered by both secular processes and major mergers is now considered. First, the major merger triggered AGN light curve is determined by finding the lowest χ^2 fit to the $z = 2.3$ HXLF using only the major merger triggered portion of the AGN population. Thus,

the maximum possible contribution from major mergers is assumed[5]. The light curve of the secularly triggered AGN is constrained by the minimum total χ^2 fit to all 127 HXLF data points. Both the Merloni & Heinz (2008) and Netzer (2009) ABHMFs and the Labita et al. (2009) and continuity equation (Eq. 6.10) ABHMF evolutions are considered. It is assumed that merger triggered and secularly triggered AGN may have different light curves; thus, the light curve parameters for AGN triggered by mergers and AGN triggered by secular processes are considered separately.

First, both the AGN triggered by major mergers and AGN triggered by secular processes are modeled using the same ABHMF and evolution for both populations of AGN. The best fit parameters for these models are summarized by the middle section of Table 6.4.1. Despite these models providing decent fits to the observed HXLF data points, the models were not in agreement with the other observational constraints, as summarized by the middle section of Table 6.5. However, this exercise did demonstrate that the $z \lesssim 0.5$ AGN population is fairly well described using the Netzer (2009) ABHMF with the continuity equation evolution (Eq. 6.10) and the $z \gtrsim 1$ AGN population can be described by using the Merloni & Heinz (2008) ABHMF with the Labita et al. (2009) evolution. Therefore, a mixed ABHMF and evolution model was investigated.

Since the Netzer (2009) ABHMF with continuity equation evolution works well at low redshift, where secular evolution is expected to dominate, and the Merloni & Heinz (2008) ABHMF with Labita et al. (2009) evolution works well at high redshift, where major merger triggered AGN are expected to dominate, a hybrid model is calculated. Using the Merloni & Heinz (2008) ABHMF with the Labita et al. (2009) evolution, the best fit parameters for the merger triggered AGN in this model are $t_0 = 2.5 \times 10^8$ yrs, $\beta = 0.7$, and $\eta = 2.5$. Using the Netzer (2009) ABHMF with the continuity equation evolution (Eq. 6.10), the AGN triggered by secular mechanisms are best described by the parameters $t_0 = 2.5 \times 10^8$ yrs, $\beta = 0.8$, $\eta = 0.4$, and $f_{sec} = 0.01$ Gyr^{-1}. This model does moderately well at describing the AGN HXLF, with $\chi^2_{red} = 1.4$, as shown in Figure 6.2. Also, this model is in agreement

[5]If the maximum contribution from secularly triggered AGN is assumed, an appropriate fit to the HXLF can be found ($\chi^2_{red} = 1.7$), but this model cannot account for the observed local black hole mass density.

Table 6.2: Summary of model fits to the observational constraints.

Model	d.o.f.[a]	chi^2_{red}[b]	$\rho_\bullet$[c]	XRB[d]	2–10 keV[e]	15–55 keV[f]
One Population Models						
Mergers only	123	2.4	$\surd$	×	×	×
Secular only	122	2.1	×	×	×	×
Two Population Models						
N09 w/ Eq. 6.10	119	1.5	×	×	$\surd$	$\surd$
N09 w/ L09	119	1.4	×	×	$\surd$	$\surd$
MH08 w/ Eq. 6.10	119	1.7	×	×	×	×
MH08 w/ L09	119	1.5	$\surd$	×	×	×
Two Population Mixed ABHMF Model						
Mixed ABHMF[g]	119	1.4	$\surd$	$\surd$	$\surd$	$\surd$

[a] The number of degrees of freedom for the χ^2 test reported in column χ^2_{red}.

[b] The quoted χ^2_{red} refers to the 127 HXLF data points plotted in Figure 6.1.

[c] A × in this column denotes that, when considering the two black hole space density data points, $\chi^2 > 4.0$ for the designated model.

[d] A × in this column denotes that this model either over or under-predicts the XRB by more than 25% in the 10–50 keV band.

[e] A × in this column denotes that, this model either over or under-predicts the the 2–10 keV observed number counts shown in Figure 6.5 by more than 25% at all fluxes.

[f] A × in this column denotes that, this model either over or under-predicts the 15–55 keV observed $\log N$–$\log S$ shown in Figure 6.6 by more than 25% at all fluxes.

[g] The mixed ABHMF model uses the MH08 ABHMF with L09 evolution for the merger triggered AGN and the N09 ABHMF with the continuity equation (Eq. 6.10) evolution for the secularly triggered AGN.

with the local black hole mass density observed by Shankar et al. (2009) and the $z \sim 2$ black hole mass density observed by Treister et al. (2010b), which, as shown in Figure 6.3, is dominated by black hole growth triggered by major mergers. Figure 6.4 shows that this model is also in agreement with the observed XRB spectrum. The mixed ABHMF model is in decent agreement with the 2–10 keV AGN number counts as shown in Figure 6.5. Figure 6.6 shows that the mixed ABHMF model is in good agreement with the *Swift*/BAT 15–55 keV AGN number count observed by Ajello et al. (2009). Furthermore, at the *Swift*/BAT survey flux limit of 7.6×10^{-12} erg cm^{-2} s^{-1}, this study finds that merger triggered AGN account for $\sim$20% of 15–55 keV number count, in agreement with the findings of Koss et al. (2010). Thus, this mixed ABHMF model provides the best overall fit to the observational constraints.

The largest discrepancy between the mixed ABHMF model and the observational constraints, is the HXLF at $L_X \lesssim 10^{42}$ erg s^{-1}, specifically at $z = 0.6$. Due to the tendril nature of cosmic structure, narrow fields, which tend to provide the high z, low L_X AGN detections, will observe over dense regions when one of these tendrils passes through the observed field. This cosmic variance may cause the number counts and HXLFs observed in different fields to vary slightly (Brandt & Hasinger, 2005). Observations of AGN with $L_X \lesssim 10^{42}$ erg s^{-1} and $z \sim 0.6$ can only be conducted in the *Chandra* deep fields, which are known to have significant field-to-field variation (Cowie et al., 2002). As the slope of the low L_X end of the HXLF is still fairly uncertain, cosmic variance is most likely to affect the low L_X end of the observed HXLF.

When both merger triggered and secularly triggered AGN are considered, models which use the Netzer (2009) ABHMF are in agreement with observations at $z < 0.5$, but not at high redshift. In contrast, models which use the Merloni & Heinz (2008) ABHMF for both merger and secularly triggered AGN over-predict the black hole mass density. In order to explain both high and low redshift observations, it is necessary that merger triggered and secularly triggered AGN have different ABHMFs which evolve differently with redshift. The mass distribution of black holes triggered by secular processes is, therefore, intrinsically different than the mass distribution of black holes triggered by mergers, in agreement with

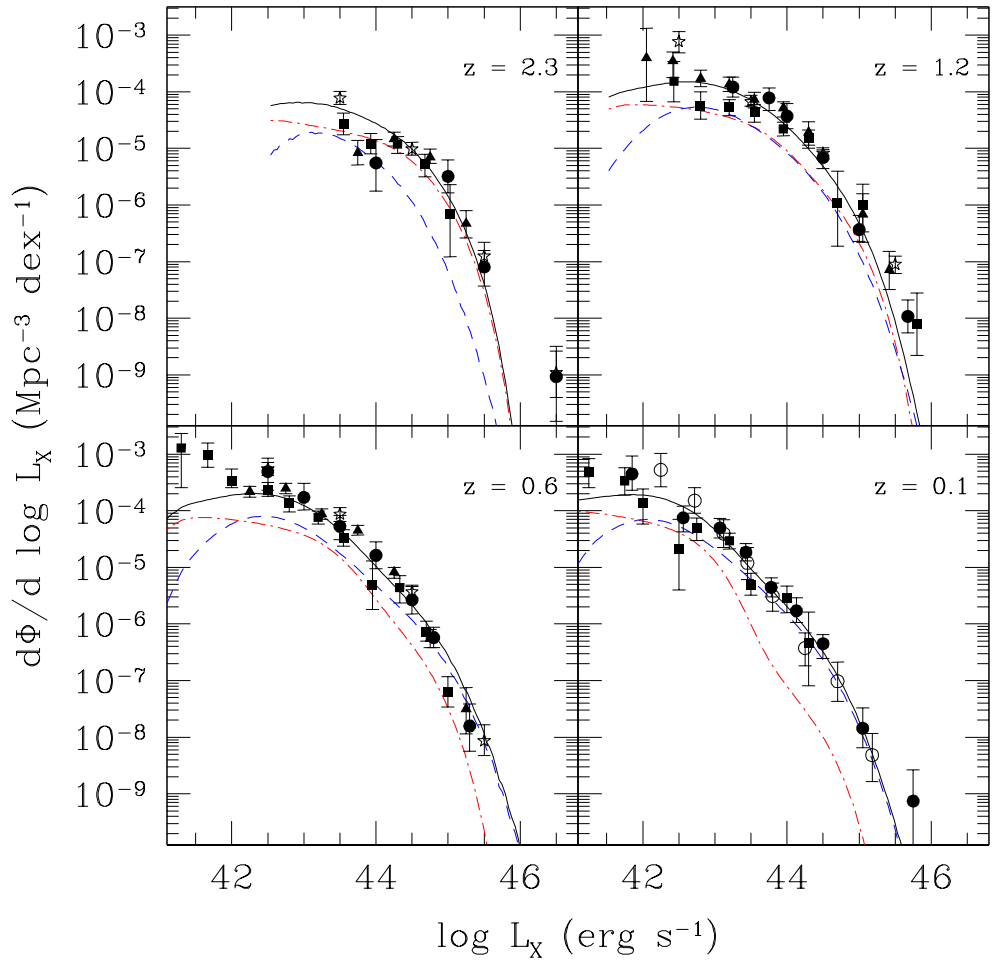

Figure 6.2: The HXLF predicted by the mixed ABHMF model, which has $\chi^2_{red} = 1.4$. The solid black line is the total AGN HXLF. The dot-dashed red lines show the contributions from AGN triggered by mergers and the dashed blue lines show the contribution from AGN triggered by secular mechanisms. The data points are the same as in Figure 6.1.

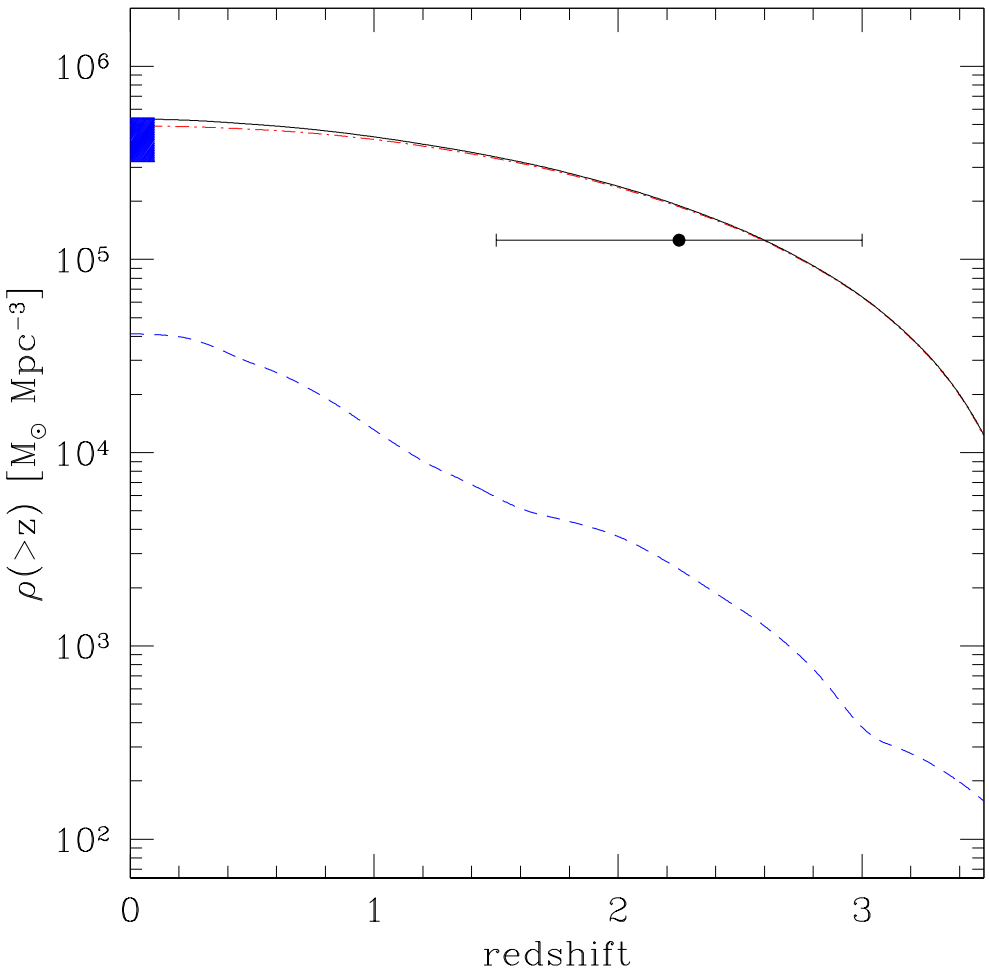

Figure 6.3: The black hole mass density with respect to redshift, predicted by the mixed ABHMF model. The line styles are the same as in Figure 6.2. The $z \sim 0$ shaded region is the local black hole mass density observed by Shankar et al. (2009) and the $z \sim 2$ data point is the black hole mass density observed by Treister et al. (2010b).

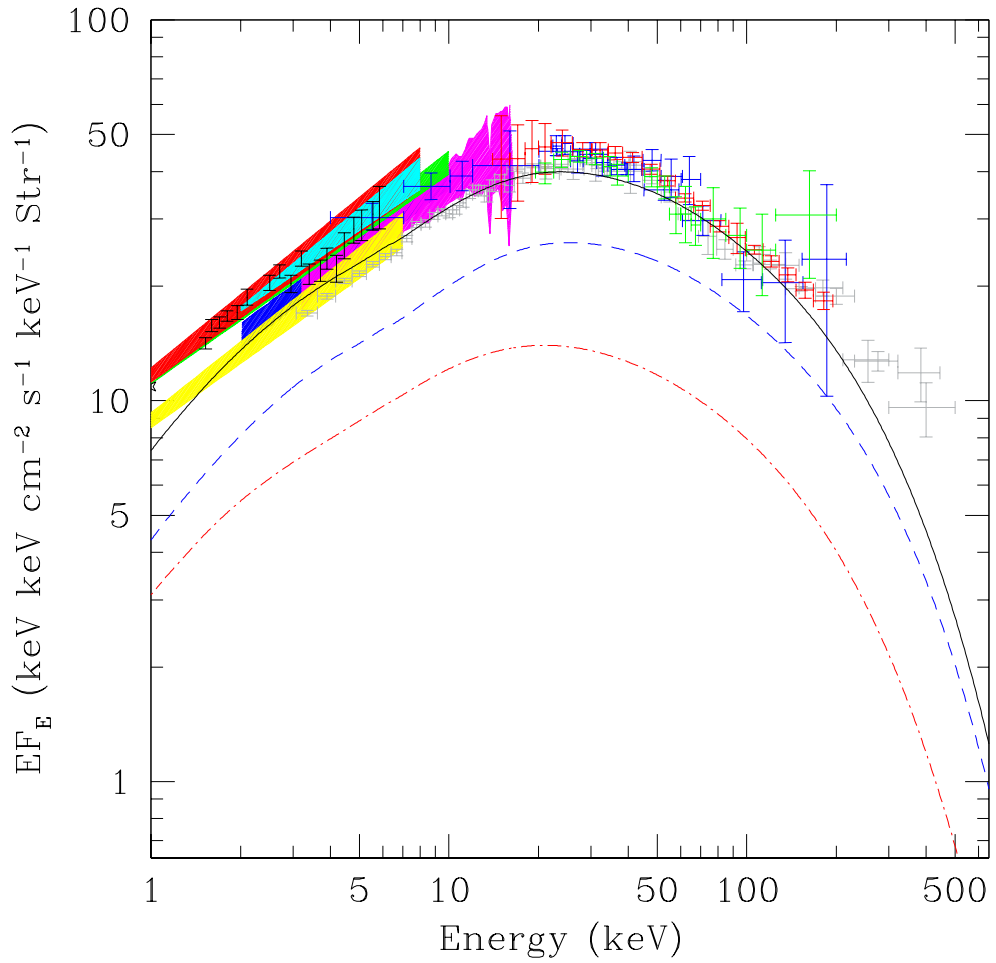

Figure 6.4: The XRB spectrum predicted by the mixed ABHMF model. The line styles are the same as in Figure 6.2. Colored regions and data points show measurements from various instruments; blue: *ASCA* GIS (Kushino et al., 2002); magenta: *Rossi X-ray Timing Explorer* (*RXTE*; Revnivtsev et al., 2003); green: XMM-*Newton* (Lumb et al., 2002); red: *BeppoSAX* (Vecchi et al., 1999); yellow: *ASCA SIS* (Gendreau et al., 1995); cyan: XMM-*Newton* (De Luca & Molendi, 2004); grey data: *HEAO*-1 (Gruber et al., 1999); blue data: *INTEGRAL* (Churazov et al., 2007); red data: *Swift*/BAT (Ajello et al., 2008); black data: *Swift*/XRT (Moretti et al., 2009); green data: *INTEGRAL* (Türler et al., 2010).

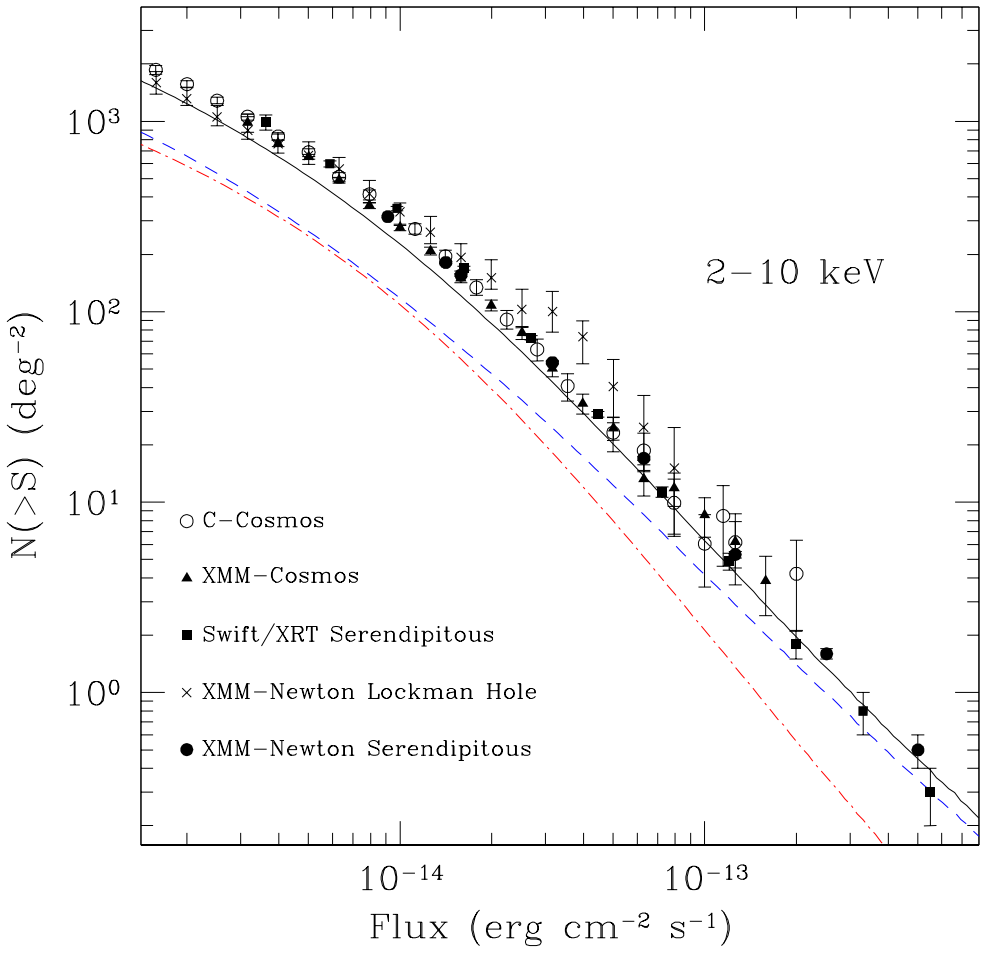

Figure 6.5: The 2–10 keV AGN $N(>S)$ predicted by the mixed ABHMF model. The line styles are the same as in Figure 6.2. The plotted data show observed the number counts from various surveys: C-COSMOS (Elvis et al., 2009), XMM-COSMOS (Cappelluti, 2009), *Swift*/XRT Serendipitous (Puccetti et al., 2011), XMM-*Newton* Lockman Hole (Brunner et al., 2008), and XMM-*Newton* Serendipitous (Mateos et al., 2008).

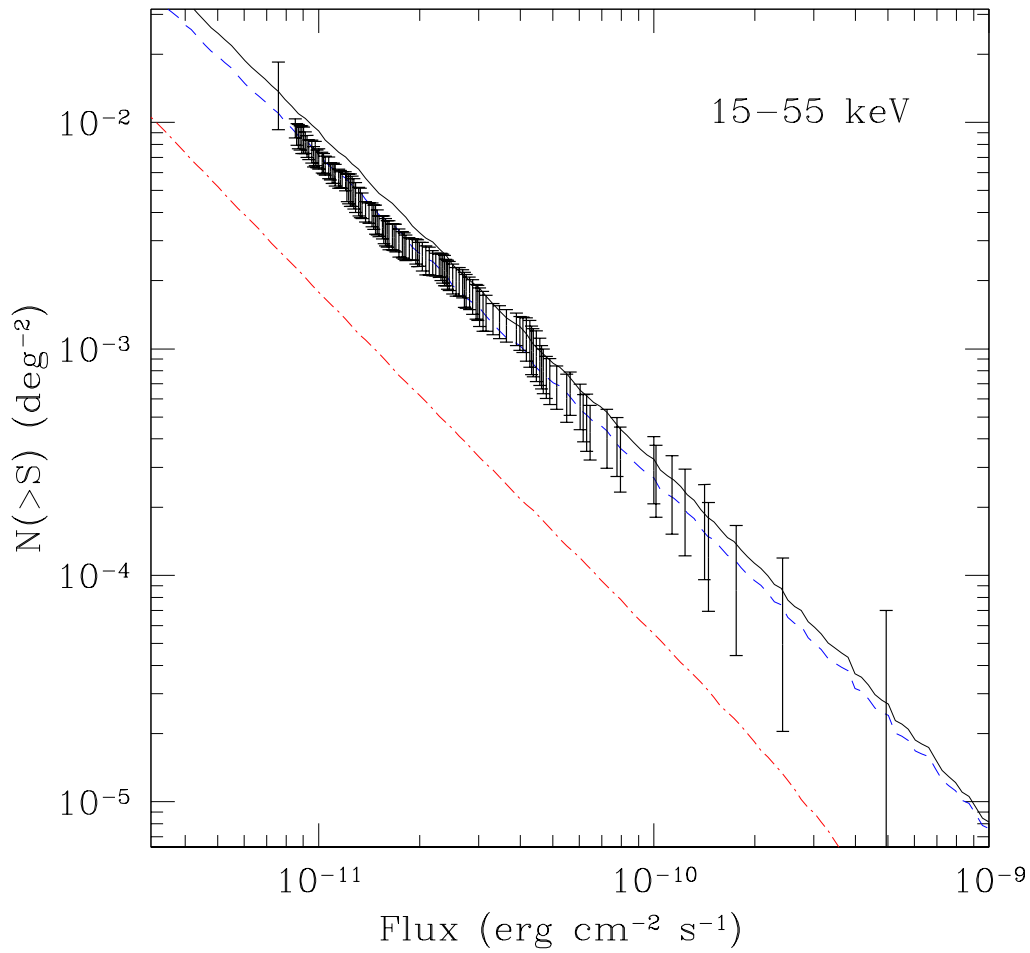

Figure 6.6: The 15–55 keV AGN $N(> S)$ predicted by the mixed ABHMF model. The line styles are the same as in Figure 6.2. The data points show the 15-55 keV AGN $\log N$–$\log S$ relation observed by *Swift*/BAT (Ajello et al., 2009).

the findings of Schawinski et al. (2010b).

6.6 Discussion

An observationally based AGN triggering rate and a theoretical AGN light curve is used to model the AGN population. By considering the HXLF at five different redshifts, the black hole mass density, the XRB spectrum, and the AGN number counts in the 2–10 and 15–55 keV bands, it is determined that neither merger triggered AGN nor AGN triggered by secular processes can alone account for the entire AGN population. Two populations are necessary to describe the observed evolution and space density of AGN. Furthermore, it is found that the ABHMF of merger triggered AGN evolves more rapidly and has a higher average black hole mass than the ABHMF of secularly triggered AGN.

6.6.1 AGN Light Curve Model

The AGN light curve model used has three parameters, t_0, β, and η. The η parameter is related to the peak Eddington ratio of the light curve. The AGN population model is least sensitive to η, however, it is found that $\eta \gtrsim 1.0$ provides the best fit to the observational constraints, suggesting that short periods of super-Eddington accretion are likely in a significant fraction of the AGN population. The AGN population model is moderately dependent on the time scale parameter, t_0. If this time scale is too short, the AGN fade too quickly, and the space density of low luminosity AGN is severely under-predicted. Thus, t_0 is most important for the normalization of the AGN HXLF. The shape of the HXLF is primarily controlled by the slope of the light curve, which is controlled by the β parameter. The AGN population model is most sensitive to β. Changing β by 0.1 can cause the resulting HXLF shape to change substantially. The primary goal of this study is to investigate if it is necessary that AGN be triggered by both mergers and secular processes or if a single mechanism can account for the entire AGN population, not to determine the best fit AGN light curve parameters. However, the observational constraints used in this study do provide interesting restrictions on the AGN light curve parameters.

Hopkins & Hernquist (2009) point out that different models of the AGN light curve predict different light curve slopes, β. Therefore, the AGN light curve fit provides information about the physical conditions in the vicinity of the accretion disk. For example, self-regulated models, where the black hole accretion is feedback limited, predict $\beta = 0.3$ – 0.8. Meanwhile, if AGN are fueled by mass loss from a nuclear star cluster, $\beta = 0.9$ – 1.0. Models in which the fuel supply of a Shakura & Sunyaev (1973) accretion disk is suddenly cut off, predict $\beta = 0.80 - 0.84$. In all of the best fit merger triggered AGN models presented here, $\beta = 0.7$, suggesting that for merger triggered AGN, the accretion is feedback limited. Also, for the best fit model presented here, η, the parameter related to light curve peak Eddington ratio, is much smaller for AGN triggered by secular mechanisms than for AGN triggered by major mergers.

6.6.2 Two Populations of AGN

Here, it is assumed that every major merger triggers an AGN and major mergers can account for the AGN population at $z = 2.3$, thus this analysis is an upper limit for the contribution of major merger triggered AGN. Indeed, when Schawinski et al. (2012) studied the morphology of 28 dust obscured galaxies (DOGs) at $z \sim 2$, they found the majority of the DOGs had disky morphologies, suggesting that if these galaxies host AGN, the AGN was triggered by secular processes. Here, it is found that at $z \lesssim 2$, a significant fraction of all AGN are triggered through secular mechanisms. Figure 6.7 shows the space and luminosity density of AGN with $\log L_X > 42$, 43, and 44, which are triggered by mergers and secular processes as a function of redshift for the mixed ABHMF model. At all three luminosity ranges, the luminosity density and space density of AGN is dominated by major merger triggered AGN at $z \gtrsim 1.5$ and secularly triggered AGN at $z \lesssim 1.5$. By varying model parameters, it is found that the minimum redshift at which major mergers can dominate AGN trigger is $z \sim 1$. This finding is in agreement with Georgakakis et al. (2009), who found that ∼30% of the AGN space density and ∼25% of the AGN luminosity density at $z \sim 1$ is due to AGN hosted by disk dominated hosts, implying that secular processes are responsible for at least one quarter of the AGN luminosity density at $z \sim 1$. It is found that

merger triggered AGN account for ∼20% of the space density of $\log L_X > 43$ AGN at $z < 0.05$, consistent with findings of Koss et al. (2010). Thus, AGN hosted by disk dominated galaxies are a significant fraction of the AGN population by $z \sim 1$, indicating that secular evolution is an important mode of galaxy evolution at this redshift.

Similarly, Draper & Ballantyne (2011b) found that for AGN at $z \lesssim 1$ the host galaxies of obscured and unobscured AGN are, on average, the same, suggesting that at $z \lesssim 1$ AGN and galaxy evolution is controlled by secular processes. However, at $z \gtrsim 1$, the host galaxies of unobscured AGN are intrinsically less dusty than the host galaxies of obscured AGN at similar redshifts, suggesting a fundamental change in the mechanisms which control AGN activity at $z \sim 1$ (Draper & Ballantyne, 2011b). Indeed, Figure 6.2 shows that, at $z \lesssim 1$, AGN triggered through secular processes dominate even the high L_X end of the HXLF, while fading major merger triggered AGN dominate the low L_X end of the HXLF. These findings are also in agreement with the conclusions of a variety of recent observational studies which found that secular processes are an important form, and possibly the dominate form, of galaxy evolution at $z \lesssim 2$ (Georgakakis et al., 2009; Allevato et al., 2011; Cisternas et al., 2011; Schawinski et al., 2011; Williams et al., 2011). Indeed, according to the HXLF, it is found that AGN triggered by secular processes can account for the entire AGN population with $\log L_X > 43$ at $z \lesssim 0.5$. Hopkins & Hernquist (2006) suggest that secularly triggered AGN are not cosmologically important; however, the findings of this study illustrate that AGN triggered by secular mechanisms are necessary to describe the AGN population and dominate the space density of AGN with $\log L_X > 43$ at $z \lesssim 1.5$.

The findings of Schawinski et al. (2010b) suggest that this fundamental change in AGN activity at $z \sim 1.5$ is due to cosmic downsizing. By studying AGN black hole masses as a function of host galaxy morphology for AGN observed by the Sloan Digital Sky Survey (SDSS), Schawinski et al. (2010b) find that it is preferentially the least massive black holes in less massive early type galaxies (stellar mass $M_* \sim 10^{10}$ $M_\odot$) which are currently active. In contrast, the black holes which are currently active in late type galaxies are preferentially the most massive black holes hosted by more massive late type host galaxies ($M_* \sim 10^{11}$ $M_\odot$). A stellar disk generally indicates that a galaxy has not undergone a major merger or

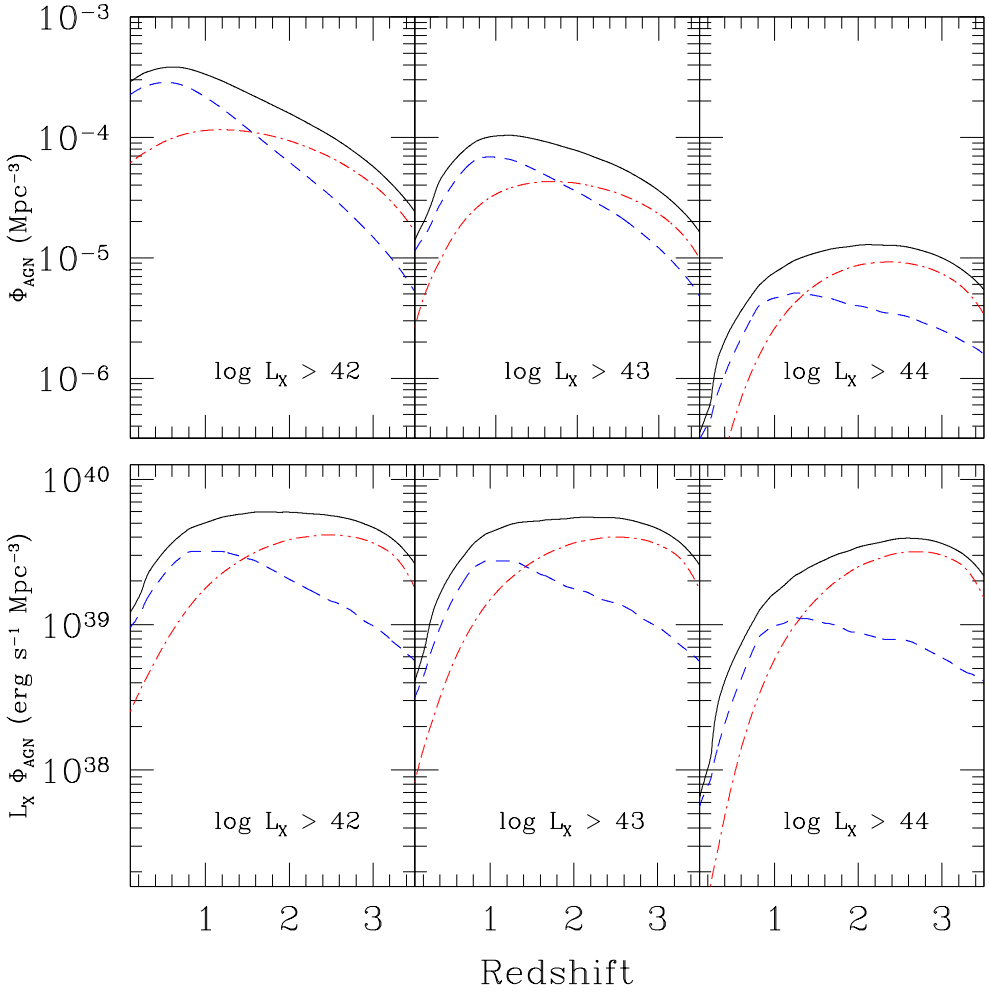

Figure 6.7: The space and luminosity density of AGN as a function of redshift predicted by the mixed ABHMF model. The top row shows the space density of AGN for $\log L_X >$ 42, 43, and 44. The bottom row shows the luminosity density of AGN for $\log L_X > 42$, 43, and 44. The line styles are the same as in Figure 6.2.

that the last major merger experienced by the galaxy was long enough ago that a disk had time to reform, $\gtrsim$ 500 Myr (Hota et al., 2011). Therefore it can be assumed that, for AGN hosted by late type galaxies, the current episode of AGN activity was triggered by secular processes. Schawinski et al. (2010b) suggest that the early type galaxy hosts in their sample may be smaller versions of the mode of galaxy evolution experienced by massive ellipticals at high redshift. Thus, the early type host galaxies in the sample of Schawinski et al. (2010b) may host downsized versions of major merger triggered AGN. Thus, it appears that the dominance of major mergers in galaxy evolution began to decline by $z \sim 2$ and is continuing to decline, in agreement with the theory of cosmic downsizing. Meanwhile, the importance of secular evolution increased as the importance of major mergers decreased, until secular evolution became the dominate form of galaxy evolution at $z \sim 1.5$. Since we are still early in the era of secularly dominated galaxy evolution, it is the more massive systems which are currently undergoing secularly triggered AGN activity. Cosmic downsizing would therefore predict that as the era of secular dominance continues, AGN triggered through secular processes will become more common in lower mass systems.

6.6.3 ABHMF and Evolution

It is found that AGN triggered by major mergers at $z < 4$ have, on average, more massive central black holes than AGN triggered by secular processes, at least at high redshift. Locally, it appears that merger triggered AGN and secularly triggered AGN have similar black holes masses (Schawinski et al., 2010b), necessitating that the ABHMF of merger triggered AGN evolves differently than the ABHMF of secularly triggered AGN. The ABHMF of AGN triggered by secular mechanisms appears to evolve in a manner consistent with the continuity equation (Eq. 6.10), which describes the evolution of the combined active and quiescent black hole mass function (e.g., Small & Blandford, 1992; Merloni & Heinz, 2008). However, if the ABHMF of merger triggered AGN evolves following the continuity equation, then at $z \gtrsim 1$ the average active black hole mass is too small to account for the high L_X end of the HXLF. In contrast, if the Labita et al. (2009) ABHMF evolution is used to evolve the ABHMF of secularly triggered AGN, then the low L_X end of the $z \lesssim 1$ HXLF is

significantly under-predicted. Thus, it appears that not only are both secular processes and major mergers important mechanisms for triggering the $z < 2$ AGN population, but these two mechanisms trigger different populations of black holes and these two populations have different redshift evolution.

It is not surprising that the ABHMF of merger triggered AGN evolves differently from the secularly triggered ABHMF and the quiescent black hole mass function. The major merger rate evolves strongly with redshift and galaxy mass (Hopkins et al., 2010a). Thus, it is expected that the ABHMF of AGN triggered by major mergers would also evolve strongly with redshift (e.g., Treister et al., 2011). In contrast, the rate of AGN being triggered by secular evolution, f_{sec}, is assumed to be constant with redshift. Therefore, it is expected that the ABHMF for AGN triggered by secular processes will be less redshift dependent than the ABHMF for merger triggered AGN. Also, as the majority of supermassive black holes at any redshift are quiescent, the combined quiescent and active black hole mass function evolves more slowly with redshift than the merger triggered ABHMF. Thus, it is expected that the merger triggered ABHMF will evolve more strongly with redshift than the ABHMF of secularly triggered AGN or of the combined active and quiescent black hole mass function.

6.6.4 The Connection Between Compton Thick AGN and Mergers

Observational and theoretical evidence suggests that Compton thick AGN are AGN which were recently triggered by a mechanism which has caused a large amount of gas and dust to be funneled into the nuclear regions of the host galaxy (e.g., Fabian, 1999; Page et al., 2004; Fabian et al., 2008, 2009; Draper & Ballantyne, 2010; Treister et al., 2010a; Draper & Ballantyne, 2011b). Due to the large amount of gas and dust required for the rapid AGN fueling and high column density necessary for an AGN to be Compton thick, the most likely triggering process is a wet major merger (Sanders et al., 1988; Hopkins et al., 2006a), though Weinzirl et al. (2011) argue that Compton thick levels of obscuration are also possible in instances of clumpy cold-flow accretion onto the host galaxy. Here, $f_{CT} = 0.0$ for the secularly triggered AGN and calculate f_{CT} for the merger triggered AGN as

described in Section 6.3.1. If it is assumed that Compton thickness is an evolutionary phase which only merger triggered AGN experience, the χ^2_{red} of the mixed ABHMF increases by 0.1 and the model is still in agreement with the observed black hole space density, XRB spectrum, and the 2–10 keV and 15–55 keV number counts. Therefore, the hypothesis that Compton thick AGN are an evolutionary stage of merger triggered AGN is fully consistent with the model presented here.

6.7 Summary

By combining an observationally motivated AGN triggering rate and a theoretically motivated AGN light curve, an AGN population synthesis model is developed which can track the evolution of AGN triggered by mergers and secular processes. The light curve parameters are constrained by comparing model predictions against the observed AGN HXLF. The observed space density of supermassive black holes, AGN number counts, and XRB spectrum are also considered. The results of this study are summarized below.

• Neither AGN triggered by major mergers nor AGN triggered by secular mechanisms alone are capable of accounting for the entire observed AGN population at $z \lesssim 2$. This finding is independent of the SMF used or the potential AGN host galaxy minimum mass.

• The dominant AGN triggering mechanism switches from major mergers at $z \gtrsim 1.5$ to secular mechanisms by $z \sim 1$. This is a natural consequence of both the major merger rate and fraction of gas rich galaxies increasing with redshift. However, both major mergers and secular processes are important triggering mechanisms for AGN over the entire redshift range considered, especially at moderate luminosities. .

• The black hole mass density is dominated by black hole growth triggered by major mergers over the entire redshift range considered.

• The space density and luminosity density of AGN with $\log L_X > 42$, 43, and 44 is dominated by AGN triggered by major mergers at $z \gtrsim 1.5$ and by AGN triggered by secular processes at $z \lesssim 1.5$.

• The XRB is dominated by emission from AGN triggered by secular mechanisms.

• The ABHMF of AGN triggered by major mergers is different from the ABHMF of

AGN triggered by secular mechanisms. At high redshift, the average black hole triggered by major mergers is more massive than the average black hole triggered by secular processes, which is consistent with cosmic downsizing.

• The evolution of the ABHMF of AGN triggered by major mergers is also different from the evolution of the ABHMF of AGN triggered through secular mechanisms, with the ABHMF of major merger triggered AGN evolving more rapidly with redshift than the ABHMF of AGN triggered by secular processes. The observed evolution of Labita et al. (2009) appears to describe the evolution of the merger triggered AGN ABHMF well. In contrast, the continuity equation (Eq. 6.10) describes the evolution of the ABHMF for secularly triggered AGN. This finding is consistent with the strong redshift evolution of the major merger rate.

• The findings of this study are not changed if Compton thick AGN are an evolutionary stage only experienced by major merger triggered AGN.

6.8 References

Ajello, M., Greiner, J., Sato, G., et al. 2008, ApJ, 689, 666

Ajello, M., Costamante, L., Sambruna, R.M., et al. 2009, ApJ, 699, 603

Alexander, D.M., Swinbank, A.M., Smail, I., McDermid, R., Nesvadba, N.P.H. 2010, MNRAS, 402, 2211

Allevato, V., Finoguenov, A., Cappelluti, N., et al. 2011, ApJ, 736, 99

Aird, J., Nandra, K., Laird, E.S., et al. 2010, MNRAS, 401, 2531

Ballantyne, D.R., Draper, A.R., Madsen, K.K., Rigby, J.R., & Treister, E. 2011, ApJ, 736, 56

Ballantyne, D.R., Everett, J.E., Murray, N. 2006, ApJ, 639, 740

Barnes, J.E. & Hernquist, L. 1996, ApJ, 471, 115

Bertone, S., Schaye, J., Booth, C.M., et al. 2010, MNRAS, 408, 1120

Bournaud, F., Dekel, A., Teyssier, R., et al. 2011, ApJ, 741, L33

Brandt, W.N. & Hasinger G. 2005, ARA&A, 43, 827

Brunner, H., Cappelluti, N., Hasinger, G., et al. 2008, A&A, 479, 283

Brusa, M., Fiore, F., Santini, P., et al. 2009, A&A, 507, 1277

Cao, X. 2010, ApJ, 725, 388

Cao, X. & Xu, Y.-D. 2007, MNRAS, 377, 425

Cappelluti, N., Brusa, M., Hasinger, G., et al. 2009, A&A, 497, 635

Cardamone, C.N., Urry, C.M., Schawinski, K., et al. 2010, ApJ, 721, L38

Carlberg, R.G. 1990, ApJ, 350, 505

Chen, Y.-M., Wang, J.-M., Yan, C.-S., Hu, C., & Zhang, S. 2009, ApJ, 695, L130

Churazov, E., Sunyaev, R., Revnivtsev, M., et al. 2007, A&A, 467, 529

Cisternas, M., Jahnke, K., Inskip, K.J., et al. 2011, ApJ, 726, 57

Cole, S., Norberg, P., Baugh, C.M., et al. 2001, MNRAS, 326, 255

Cowie, L.L., Garmire, G.P. Bautz, M.W., et al. 2002, ApJ, 566, L5

Crenshaw, D.M., Kraemer, S.B., & Gabel, J.R. 2003, AJ, 126, 1690

Dahlen, T., Mobasher, B., Dickinson, M., et al. 2007, ApJ, 654, 172

Davies, R.I., Müller Sánchez, F., Genzel, R., et al. 2007, ApJ, 671, 1388

De Luca, A. & Molendi, S. 2004, A&A, 419, 837

Draper, A.R. & Ballantyne, D.R., 2009, ApJ, 707, 778

Draper, A.R. & Ballantyne, D.R., 2010, ApJ, 715, L99

Draper, A.R. & Ballantyne, D.R., 2011a, ApJ, 729, 109

Draper, A.R. & Ballantyne, D.R., 2011b, ApJ, 740, 57

Elvis, M., Civano, F., Vignali, C., et al. 2009, ApJS, 184, 158

Fabian, A.C. 1999, MNRAS, 308, L39

Fabian, A.C., Vasudevan, R.V., & Gandhi, P. 2008, MNRAS, 385, L43

Fabian, A.C., Vasudevan, R.V., Mushotzky, R.F., Winter, L.M., & Reynolds, C.S. 2009, MNRAS, 394, L89

Gendreau, K.C., Mushotzky, R., Fabian, A.C., et al. 1995, PASJ, 47, L5

Georgakakis, A., Coil, A.L., Laird, E.S., et al. 2009, MNRAS, 397, 623

Gilli, R., Comastri, A., Hasinger, G. 2007, A&A, 463, 79

Gruber, D.E., Matteson, J.L., Peterson, L.E., & Jung, G.V. 1999, ApJ, 520, 124

Hambrick, D.C., Ostriker, J.P., Naab, T., Johansson, P.H. 2011, ApJ, 738, 16

Hernquist, L. 1989, Nature, 340, 687

Hickox, R., Jones, C., Forman, W.R., et al. 2009, ApJ, 696, 891

Hocuk, S. & Spaans, M. 2011, A&A, 536, 41

Hopkins, P.F., Bundy, K., Croton, D., et al. 2010a, ApJ, 715, 202

Hopkins, P.F., Croton, D., Bundy, K., et al. 2010b, ApJ, 724, 915

Hopkins, P.F. & Hernquist, L. 2009, ApJ, 298, 1550

Hopkins, P.F. & Hernquist, L. 2006, ApJS, 166, 1

Hopkins, P.F., Hernquist, L., Cox, T.J., et al. 2006a, ApJS, 163, 1

Hopkins, P.F., Somerville, R.S., Hernquist, L. 2006b, ApJ, 652, 864

Hota, A., Sirothia, S.K., Ohyama, Y., et al. 2011, MNRAS, 417, L36

Kauffmann, G. & Haehnelt, M. 2000, MNRAS, 311, 576

Kocevski, D.D., Faber, S.M., Mozena, M., et al. 2012, ApJ, 744, 148

Kormendy, J. & Kennicutt, R.C. 2004, ARA&A, 42, 603

Kormendy, J. & Richstone, D. 1995, ARA&A, 33, 581

Koss, M., Mushotzky, R., Veilleux, S., & Winter, L. 2010, ApJ, 716, L125

Kumar, P. & Johnson, J.L. 2010, MNRAS, 404, 2170

Kushino, A., Ishisaki, Y., Morita, U., et al. 2002, PASJ, 54, 327

Labita, M., Decarli, R., Treves, A., & Falomo, R. 2009, MNRAS, 399, 2099

La Franca, F., Fiore, F., Comastri, A., et al. 2005, ApJ, 635, 864

Lagos, C.D.P., Cora, S.A., & Padilla, N.D. 2008, MNRAS, 388, 587

Lumb, D.H., Warwick, R.S., Page, M., & De Luca, A. 2002, A&A, 389, 93

Magorrian, J., Tremaine, S., Richstone, D., et al. 1998, AJ, 115, 2285

Malizia, A., Stephen, J.B., Bassani, L., et al. 2009, MNRAS, 399, 944

Marchesini, D., van Dokkum, P.G., Förster Schreiber, N.M., et al. 2009, ApJ, 701, 1765

Marconi, A., Risaliti, G., Gilli, R., et al. 2004, MNRAS, 351, 169

Mateos, S., Warwick, R.S., Carrera, F.J., et al. 2008, A&A, 492, 51

Merloni, A. & Heinz, S. 2008, MNRAS, 308, 1011

Moretti, A., Pagani, C., Cusumano, G., et al. 2009, A&A, 493, 501

Natarajan, P. & Treister, E. 2009, MNRAS, 393, 838

Netzer, H. 2009, ApJ, 695, 793

Orban de Xivry, G., Davies, R., Schartmann, M., et al. 2011, MNRAS, 417, 2721

Page, M.J., Stevens, J.A., Ivison, R.J., & Carrera, F.J. 2004, ApJ, 611, L85

Pérez-González, P.G., Rieke, G.H., Villar, V., et al. 2008, ApJ, 675, 234

Pierce, C.M., Lotz, J.M., Laird, E.S., et al. 2007, ApJ, 660, L19

Peterson, B.M. & Bentz, M.C. 2006, New Astronomy Reviews, 50, 796

Puccetti, S., Capalbi, M., Giommi, P., et al. 2011, A&A, 528, 122

Revnivtsev, M., Gilfanov, M., Sunyaev, R., Jahoda, K., & Markwardt, C., 2003, A&A, 411, 329

Ross, R.R. & Fabian, A.C. 2005, MNRAS, 358, 211

Sanders, D.B., Soifer, B.T., Elias, J.H., et al. 1988, ApJ, 325, 74

Schawinski, K., Dowlin, N., Thomas, D., Urry, C.M., & Edmondson, E. 2010a, ApJ, 714, L112

Schawinski, K., Simmons, B.D., Urry, C.M., Treister, E., & Glikman, E. 2012, MNRAS, in press (arXiv:1206:4063)

Schawinski, K., Treister, E., Urry, C.M., et al. 2011, ApJ, 727, L31

Schawinski, K., Urry, C.M., Virani, S., et al. 2010b, ApJ, 711, 284

Schawinksi, K., Virani, S., Simmons, B., et al. 2009, ApJ, 692, L19

Shakura, N.I. & Sunyaev, R.A. 1973, A&A, 24, 337

Shankar, F., Weinberg, D.H., & Miralda-Escudé, J. 2009, ApJ, 690, 20

Shen, Y. 2009, ApJ, 704, 89

Silk, J. & Rees, M.J. 1998, A&A, 331, L1

Silverman, J.D., Green, P.J., Barkhouse, W.A., et al. 2008, ApJ, 679, 118

Silverman, J.D., Kampczyk, P., Jahnke, K., et al. 2011, ApJ, 743, 2

Small, T.A. & Blandford, R.D. 1992, MNRAS, 259, 725

Sołtan, A. 1982, MNRAS, 200, 115

Treister, E., Natarajan, P., Sanders, D.B., et al. 2010a, Science, 328, 600

Treister E., Schawinski, K., Volonteri, M., Natarajan, P., & Gawiser, E. 2011, Nature, 474, 356

Treister, E., Urry, C.M., Schawinski, K., et al. 2010b, ApJ, 722, L238

Treister, E., Urry, C.M., Virani, S. 2009, ApJ, 696, 110

Treister, E. & Urry, C.M. 2006, ApJ, 652, L79

Tremaine, S., Gebhardt, K., Bender, R., et al. 2002, ApJ, 574, 740

Trichas, M., Georgakakis, A., Rowan-Robinson, M., et al. 2009, MNRAS, 399, 663

Türler, M., Chernyakova, M., Courvoisier, T. J.-L., et al. 2010, A&A, 512, 49

Ueda, Y., Akiyama, M., Ohta, K., & Miyaji, T. 2003, ApJ, 598, 886

Ueda, Y., Hiroi, K., Isobe, N., et al.2011, PASJ, in press 63, 937

Vasudevan, R.V., Mushotzky, R.F., Winter, L.M., & Fabian, A.C. 2009, MNRAS, 399, 1553

Vecchi, A., Molendi, S., Guainazzi, M., Fiore, F., & Parmar, A. 1999, A&A, 349, L73

Vittorini, V., Shankar, F. & Cavaliere, A. 2005, MNRAS, 363, 1376

Volonteri, M., Haardt, F., & Madau, P. 2003, ApJ, 582, 559

Weinzirl, T., Jogee, S., Conselice, C.J., et al. 2011, ApJ, 743, 87

Williams, R.J., Quadri, R.F., & Franx, M. 2011, ApJ, 738, L25

Yamada, T., Kajisawa, M., Akiyama, M., et al. 2009, ApJ, 699, 1354

Yu, Q. & Tremaine, S. 2002, MNRAS, 335, 965

CHAPTER VII

THE MERGER-TRIGGERED ACTIVE GALACTIC NUCLEI CONTRIBUTION TO THE ULTRALUMINOUS INFRARED GALAXY POPULATION

7.1 Introduction

In the 1980s astronomers discovered a new class of infrared selected galaxies known as ultraluminous infrared galaxies (ULIRGs) and characterized by $L_{IR} > 10^{12}$ $L_{\odot}$, where L_{IR} is the 8–1000 μm luminosity (e.g., Houck et al., 1984; Soifer et al., 1984,b; Houck et al., 1985). Another important topic during this time period was the study of the evolution of quasars (e.g., Schmidt & Green, 1983), a class of active galactic nuclei (AGN) where accretion onto the supermassive black hole at the center of a massive galaxy gives rise to $L_X > 10^{44}$ erg s^{-1}, where L_X is the 2–10 keV luminosity. ULIRGs and quasars have similar bolometric luminosities (10^{45}–10^{46} erg s^{-1}) and optical observations suggest many ULIRGs have nuclear sources of non-thermal ionizing radiation and disturbed morphologies (Sanders et al., 1988a). Thus, Sanders et al. (1988a) suggested that when two gas rich galaxies merge, gas and dust will fall into the nucleus of the resulting galaxy, triggering a massive starburst and a quasar.

Thirty years later, the connection between ULIRGs, AGN, and major mergers is still an area of active research. Recent simulations show that, indeed, gas rich major mergers are capable of triggering large starbursts and bright AGN (e.g., Hopkins et al., 2006a; Younger et al., 2009; Hopkins et al., 2010b; Narayanan et al., 2010). By looking for ULIRGs with strong X-ray emission or a power-law spectra in the *Spitzer Space Telescope* IRAC bands, studies have shown that AGN are common in ULIRGs (e.g., Hopkins et al., 2006a; Armus et al., 2007; Younger et al., 2009; Donley et al., 2010; Hopkins et al., 2010b; Narayanan et al., 2010). Furthermore, both the fraction of ULIRGs that host AGN and the fraction of

ULIRGs whose bolometric luminosities are dominated by AGN emission, appear to increase strongly with luminosity (e.g., Veilleux et al., 2002; Pearson, 2005; Gruppioni et al., 2005; Brand et al., 2006; Donley et al., 2010; Nardini et al., 2010). Morphological studies have shown that a significant fraction of ULIRGs have disturbed morphologies, suggesting the galaxy has recently undergone a merger or interaction (e.g. Donley et al., 2010; Kartaltepe et al., 2010; Nardini et al., 2010). Additionally, Veilleux et al. (2002) showed that the fraction of ULIRGs triggered by major mergers increases with luminosity. Thus, it is expected that a significant fraction of ULIRGs host AGN and were triggered by gas rich major mergers. However, these studies tend to focus on ULIRGs with $z \lesssim 1$.

Far-infrared observations by the *Herschel Space Telescope* have opened a new window on the $z \gtrsim 1$ ULIRG population. Interestingly, *Herschel* observations show that at high redshift major mergers are not necessary to trigger ULIRGs (Sturm et al., 2010). Analyzing *Herschel* observations of the Boötes field, Melbourne et al. (2012) point out that $\lesssim$30% of optically-faint $z \sim 2$ ULIRGs show obvious signs of a recent merger. Deep *Herschel* observations of the Great Observatories Origins Deep Survey (GOODS) and the Cosmological Evolution Survey (COSMOS) fields find that most $z \gtrsim 1$ ULIRGs are not in a starburst mode of star formation (Elbaz et al., 2011; Rodighiero et al., 2011). Instead, the increased gas fraction in high redshift galaxies allows normal secular star formation to power ULIRGs (e.g., Daddi et al., 2008; Elbaz et al., 2011; Rodighiero et al., 2011; Melbourne et al., 2012). Recent cosmological simulations confirm these observational results, finding that more than half of high redshift ULIRGs can be accounted for through mechanisms other than major mergers (Niemi et al., 2012). These results indicate that at high redshift the AGN-ULIRG connection may be quite different than the connection observed locally.

Draper & Ballantyne (2012) computed an AGN population model that constrains the space density and Eddington ratio evolution of AGN triggered by major mergers by considering the hard X-ray luminosity function (HXLF), X-ray AGN number counts, the X-ray background, and the local mass density of supermassive black holes. Thus, a model of the major merger population can be computed by combining this description of the evolving luminosity function of merger-triggered AGN with the Hopkins et al. (2010b) model for the

time evolution of merger-triggered starbursts. Similarly, a model merger spectral energy distribution (SED) can be calculated by combining AGN infrared spectra computed with the photoionization code CLOUDY (Ferland et al., 1998) with the Rieke et al. (2009) star formation templates. This method is used here to determine the maximum contribution of mergers to the ULIRG population at $z \lesssim 1.5$. A ΛCDM cosmology is assumed with $H_0 = 70$ km s^{-1} Mpc^{-1} and $\Omega_\Lambda = 1.0 - \Omega_M = 0.7$.

7.2 Calculations

7.2.1 AGN Model

The evolving HXLF of major merger-triggered AGN presented by Draper & Ballantyne (2012) is used to determine the space density and luminosity distribution of merger-triggered AGN. Draper & Ballantyne (2012) combined an observationally motivated major merger rate (Hopkins et al., 2010a; Treister et al., 2010) and a theoretical AGN light curve (Hopkins & Hernquist, 2009) to determine the contribution of major merger-triggered AGN to the HXLF. Hopkins & Hernquist (2009) parametrize the AGN light curve as

$$\lambda(t) = \left[1 + \left(\frac{|t - t_Q|}{t_Q}\right)^{1/2}\right]^{-2/\beta}, \tag{7.1}$$

where $\lambda(t)$ is the AGN Eddington ratio at time t years after the AGN was triggered, $t_Q = t_0\eta^\beta/(2\beta \ln 10)$, and t_0, η, and β are parameters describing the AGN lifetime, peak Eddington ratio, and light curve slope, respectively. Draper & Ballantyne (2012) find that the best fit to the observed HXLF, X-ray AGN number counts, X-ray background, and mass density of supermassive black holes is achieved when $t_0 = 2.5 \times 10^8$ yrs, $\eta = 2.5$, and $\beta = 0.7$ for AGN triggered by mergers. It is assumed that all mergers trigger AGN and therefore this model provides an upper limit to the contribution of major mergers to the AGN population.

Here, this merger-triggered AGN HXLF is converted to an infrared luminosity function using AGN SEDs computed using CLOUDY version C08.00 (Ferland et al., 1998) as described in Section 2 of Draper & Ballantyne (2011). These SEDs cover the sub-mm to very hard X-ray wavelength regimes and incorporate the direct emission from the AGN, the diffuse

emission radiated along the line of sight by the obscuring material around the AGN, and the emission reflected off the inner surface of the obscuring cloud. As in Draper & Ballantyne (2011), the neutral hydrogen density of the clouds is assigned such that Compton thin clouds have $n_H = 10^4$ cm^{-3} and Compton thick (CT) clouds have $n_H = 10^6$ cm^{-3}, in accordance with the observed densities of typical molecular clouds. The inner radius of the obscuring material is assumed to be ∼10 pc. As we compare against observations of an ensemble of sources, instead of fitting individual sources, a simple AGN torus model is appropriate for this study. Moreover, as discussed in Section 7.3, the infrared emission of ULIRGs is dominated by star formation processes, thus the results presented here are not dependent on the torus model used.

7.2.2 Starburst Model

The evolving star formation rate, $\dot{M}_*(t)$, of the merger-triggered starburst is determined using the model of Hopkins et al. (2010b). Thus,

$$\frac{dt}{d\dot{M}_*} = t_* \ln(10) \exp\left(\frac{-\dot{M}_*}{M_{sb}/t_*}\right), \tag{7.2}$$

where $t_* = 0.1$ Gyr is the timescale of the merger-triggered starburst and M_{sb} is the total mass of stars born during the merger-triggered starburst. Once $\dot{M}_*$ is determined, L_{IR} due to star formation is calculated using (Hopkins et al., 2010b)[1]

$$L_{IR} = 1.1 \times 10^{10} \left[\frac{\dot{M}_*}{1 M_\odot yr^{-1}}\right] L_\odot. \tag{7.3}$$

In order to combine the AGN and starburst models, the time delay between the triggering of the starburst and the triggering of the AGN must be considered. Observational studies and simulations show that λ tends to peak ∼100 Myr after $\dot{M}_*$ peaks (Davies et al., 2007; Schawinski et al., 2007, 2009; Rodríguez Zaurín et al., 2010; Wild et al., 2010; Hopkins, 2012). Therefore, the starburst is triggered such that the time delay between the peak star formation rate, $\dot{M}_*^{peak}$, and the peak AGN Eddington ratio, λ^{peak}, $\Delta t = 100$ Myr. Scenarios where $\Delta t = 0$ and 1 Gyr are also considered. Once the merger occurs, the AGN

[1]Using the Kennicutt (1998) conversion factor, 5.8 $\times 10^9$ $L_\odot/(M_\odot$ yr$^{-1})$, yields an infrared luminosity density ∼10% lower.

light curve of Equation 7.1 and the star formation rate evolution of Equation 7.2 determine the evolution of the system.

Thus, the space density of major mergers at redshift z is set by the merger rate. The starburst model is triggered at $z + \Delta z$, where Δz is the appropriate change in redshift for Δt at z. The corresponding AGN is triggered at z. The evolution of the starburst is governed by Equation 7.2 and the AGN luminosity evolves according to Equation 7.1. The infrared luminosity of the merger remnant galaxy is then determined using the AGN SEDs calculated with CLOUDY and the Rieke et al. (2009) starburst SED templates. The Rieke et al. (2009) templates are based on the SEDs of local, pure star forming galaxies and include poly-cyclic aromatic hydrocarbon (PAH) emission features. Figure 7.1 shows an example SED at four different times, t, after the major merger: before $\dot{M}_*$ reaches $\dot{M}_*^{peak}$ (upper left), $\dot{M}_* \approx \dot{M}_*^{peak}$ (upper right), $\lambda \approx \lambda^{peak}$ (lower left), and after λ reaches λ^{peak} (lower right). With the merger-triggered AGN HXLF, $d\Phi_X/d(\log L_X)$, and merger SEDs set, the merger infrared luminosity function, $d\Phi_{IR}/d(\log L_{IR})$, is calculated as

$$\frac{d\Phi_{IR}(L_{IR}, z)}{d(\log L_{IR})} = \frac{d\Phi_X(L_X, z)}{d(\log L_X)} \frac{d(\log L_X)}{d(\log L_{IR})}, \tag{7.4}$$

where L_X and L_{IR} are computed using the combined AGN-starburst SEDs. The infrared luminosity density, Ψ, is then computed as

$$\Psi_{merger}(z) = \int_{L_{IR}^{min}}^{L_{IR}^{max}} L_{IR} \frac{d\Phi_{IR}(L_{IR}, z)}{d(\log L_{IR})} d(\log L_{IR}), \tag{7.5}$$

where $L_{IR}^{min} = 10^8$ $L_\odot$ and $L_{IR}^{max} = 10^{13.5}$ $L_\odot$. To calculate the ULIRG Ψ_{merger}, L_{IR}^{min} is increased to 10^{12} $L_\odot$. The Ψ_{merger} calculated here is then compared with the infrared luminosity density of AGN and their host galaxies, Ψ_{AGN}, measured by Goto et al. (2010, 2011) and the total infrared luminosity density, Ψ_{total}, measured by Le Floc'h et al. (2005).

The major merger rate is set by parametrizing observations and simulations (Hopkins et al., 2010a; Treister et al., 2010) and the AGN light curve parameters are set by fitting observations of the AGN HXLF (Draper & Ballantyne, 2012). The evolution of the merger-triggered starburst model is parametrized by fitting results of simulations (Hopkins et al., 2010b). This leaves only M_{sb} and Δt as free parameters. We explore $9.0 \leq \log M_{sb}/\mathrm{M}_\odot \leq 11$ in steps of 0.25, assuming all mergers result in a similar value of M_{sb}. The values $\Delta t = 0$, 100

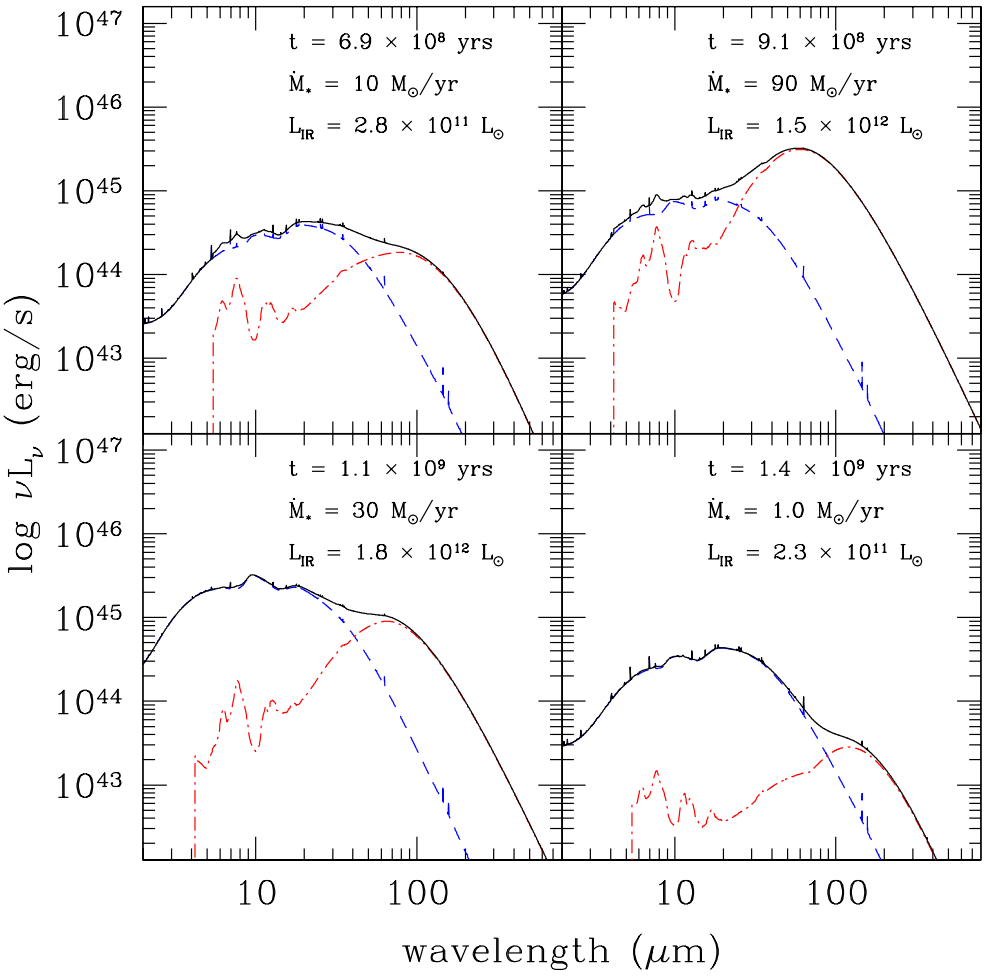

Figure 7.1: Infrared SEDs of an AGN-starburst galaxy with black hole mass $M_\bullet = 10^8$ $M_\odot$ and obscuring column density $N_H \sim 10^{23}$ cm^{-2}, at various times after being triggered by a major merger. The dashed blues lines show the AGN infrared SEDs computed with CLOUDY and the red dot-dashed lines show the Rieke et al. (2009) starburst SEDs. The solid black lines show the SED of the AGN-starburst galaxy. In the upper left plot, the AGN and starburst both contribute approximately half of L_{IR}. The upper right plot shows the SED at $\dot{M}_* \approx \dot{M}_*^{peak}$, and thus the starburst dominates L_{IR}. The lower left plot shows the SED at $\lambda \approx \lambda^{peak}$. The AGN dominates L_{IR} in both of the bottom plots.

Myr, and 1 Gyr are considered. The maximum ULIRG Ψ_{merger}/Ψ_{AGN} and $\Psi_{merger}/\Psi_{total}$ are then investigated.

7.3 Results

In order to prevent over-predicting the maximum Ψ_{merger}, we consider the 24 μm number count of X-ray selected AGN following Equation 1 of Draper & Ballantyne (2011). If $M_{sb} \gtrsim 10^{10.25}$ M$_\odot$ the bright end of the 24 μm number count is over-predicted by a factor $\gtrsim$2. These same models also over-predict the local ULIRG Ψ_{total}. Thus, $10^{10.25}$ M$_\odot$ is an upper limit on the average M_{sb} for the population of major mergers. Figure 7.2 shows the number count for mergers with $\Delta t = 100$ Myr and $M_{sb} = 10^{10}$ M$_\odot$. As the observed number count is from the GOODS fields (Treister et al., 2006), it is not surprising that the model slightly over-predicts the bright end of the observed count since GOODS is a narrow field survey and likely misses bright, rare sources which are better accounted for by wide field surveys.

Figure 7.3 shows the maximum ULIRG Ψ_{merger}/Ψ_{AGN} and ULIRG $\Psi_{merger}/\Psi_{total}$ that does not significantly over-predicting the 24 μm number count. For the model shown in Figure 7.3, $\Delta t = 100$ Myr and $M_{sb} = 10^{10}$ M$_\odot$. The top left frame of Figure 7.3 shows that mergers can account for the local ULIRG Ψ_{AGN}, however, as shown in the lower left frame, $\Psi_{merger}/\Psi_{total} \lesssim 0.26$ for local ULIRGs. Interestingly, if we remove the starburst from our SEDS, we find that emission from AGN alone can contribute $\lesssim$20% of the local ULIRG Ψ_{AGN}. Thus, we confirm that the L_{IR} of ULIRGs hosting AGN tends to be dominated by star formation.

If $M_{sb} = 10^{10}$ M$_\odot$, major mergers can account for the local ULIRG Ψ_{AGN} for $\Delta t = 0$ and 1 Gyr. Thus, the ability for mergers to account for the local AGN ULIRG population is not strongly dependent on Δt. The local ULIRG $\Psi_{merger}/\Psi_{total}$ reduces to $\sim$0.20 for both $\Delta t = 0$ and 1 Gyr. If $\Delta t = 100$ Myr and $M_{sb} \lesssim 10^{9.75}$ M$_\odot$, mergers cannot account for the local population of ULIRGs hosting AGN. Observations and simulations suggest that M_{sb} is proportional to the galaxy stellar mass, M_*, such that $M_{sb}(M_*) = fM_*$ with the fraction f on the order of, but $<$0.1 (Hopkins et al., 2010b; Zavala et al., 2012). If we

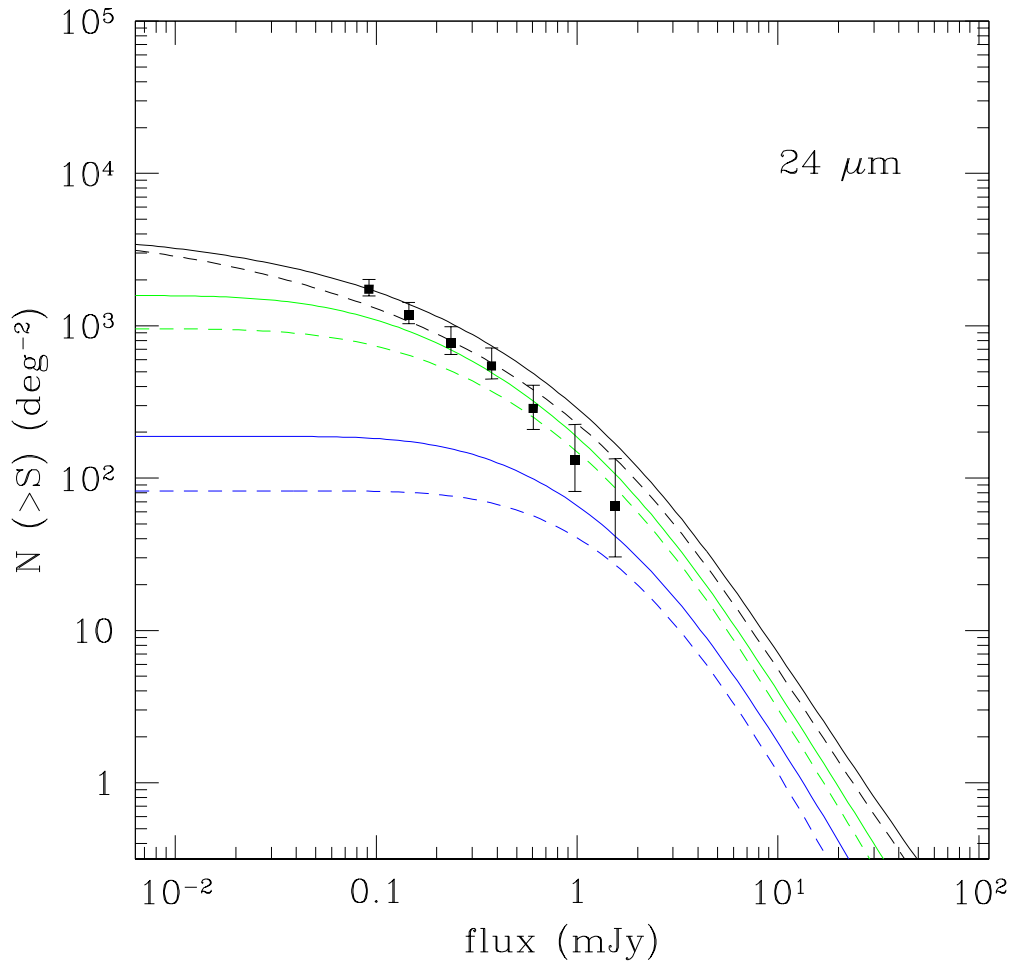

Figure 7.2: 24 μm number counts for mergers with $\Delta t = 100$ Myr, $M_{sb} = 10^{10}$ M$_\odot$, and $L_X > 10^{42}$ erg s^{-1}. The blue lines show the ULIRG number count and the green lines show the LIRG ($L_{IR} > 10^{11}$ L$_\odot$) number count. The black lines show the 24 μm number count of all mergers. The solid lines show the number counts for major mergers and the dashed lines show the number counts for the merger-triggered AGN only. Data points show the number count of X-ray selected AGN in the GOODS field (Treister et al., 2006).

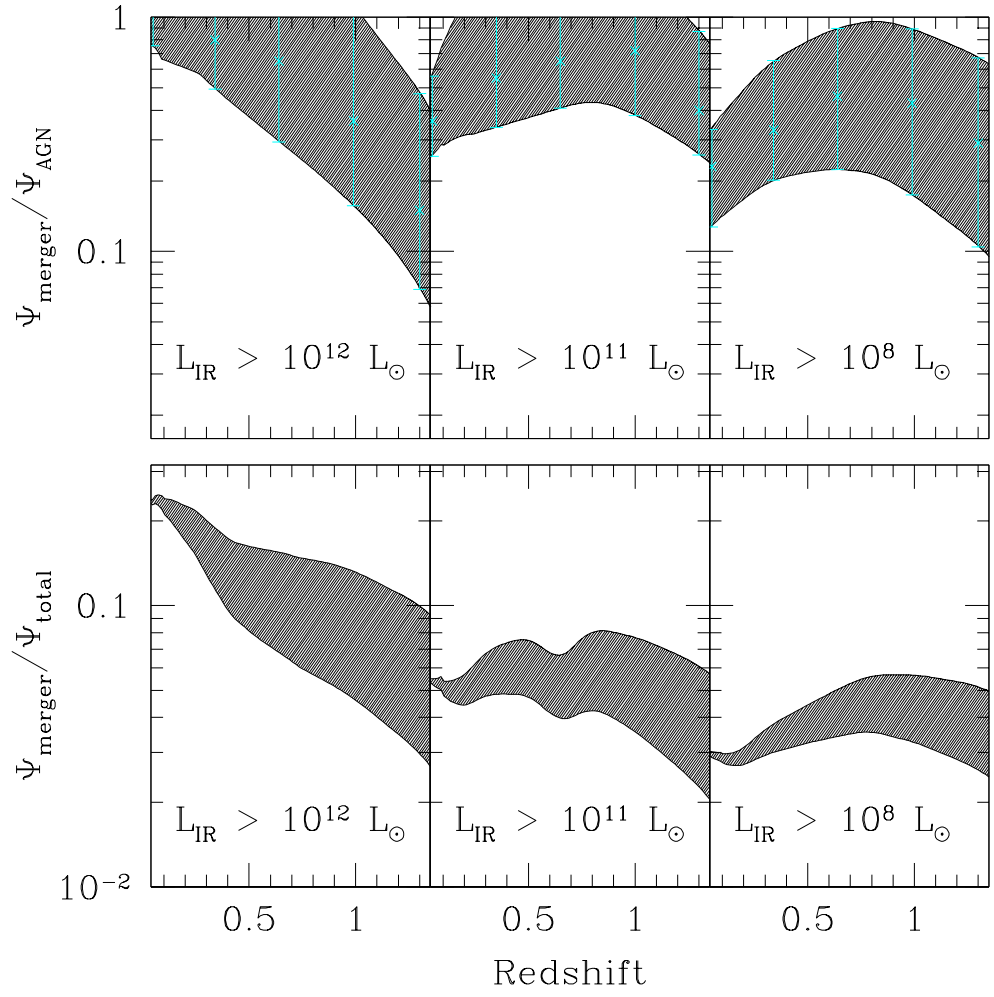

Figure 7.3: Fraction of Ψ_{AGN} and Ψ_{total} contributed by major mergers with $\Delta t = 100$ Myr and $M_{sb} = 10^{10}$ $M_\odot$. The top row shows the fraction Ψ_{AGN} that can be accounted for by mergers for ULIRGs, LIRGs, and sources with $L_{IR} > 10^8$ $L_\odot$. The observed Ψ_{AGN} is determined by fitting the data points from Goto et al. (2010, 2011), which are shown as the cyan points. The bottom row shows the fraction of Ψ_{total}, as reported by Le Floc'h et al. (2005), that can be accounted for by major mergers for ULIRGs, LIRGs, and sources with $L_{IR} > 10^8$ $L_\odot$.

assume a distribution of $M_{sb}(M_*)$ defined by $M_{sb}(M_*) = 0.1M_*$, with the distribution of M_* described by the Pérez-González et al. (2008) stellar mass function, the AGN number count and the local ULIRG Ψ_{total} are over-predicted by at least a factor of 2. However, if $f = 0.05$, the model predictions are in agreement with the AGN number count and the local ULIRG $\Psi_{merger}/\Psi_{total} = 0.28$, only 0.02 higher than the simple calculation with a single M_{sb}. If $f = 0.05$, $\langle M_{sb}(M_*)\rangle = 10^{10.05}$ $M_\odot$. Therefore, for Δt = 0–1 Gyr and $M_{sb} \sim 10^{10}$ $M_\odot$, the local ULIRG $\Psi_{merger}/\Psi_{AGN} \approx 1.0$ and the local ULIRG $\Psi_{merger}/\Psi_{total} \approx 0.20$–$0.28$.

7.4 Discussion

Major mergers can account for at most a quarter of the local ULIRG Ψ_{total}. This suggests that a large fraction of local ULIRGs are triggered by mechanisms other than the coalescence of two massive gas rich galaxies, such as minor mergers, interactions, and secular processes. By $z \sim 1$, the ULIRG $\Psi_{merger}/\Psi_{AGN} < 1$ and by $z \sim 1.25$, the ULIRG $\Psi_{merger}/\Psi_{AGN} \lesssim 0.5$. At $z \sim 1$, the ULIRG $\Psi_{merger}/\Psi_{total} \lesssim 0.12$. Indeed, simulations by Hopkins et al. (2010b) predict that at $z = 1$, the ULIRG $\Psi_{merger}/\Psi_{total} \approx 0.08$, in good agreement with the findings of this study. As major mergers are much more common at $z > 1$ than $z < 1$, this suggests that secular processes are even more important for triggering ULIRGs at high redshift. *Herschel* has provided observational evidence that major mergers are not necessary at $z \gtrsim 1$ to trigger ULIRGs (Sturm et al., 2010); a finding that has been confirmed by simulations (Niemi et al., 2012).

At $z \gtrsim 1$ the majority of ULIRGs appear to be scaled up versions of local normal star forming galaxies. These high redshift ULIRGs tend to have cooler far-infrared dust temperatures (Melbourne et al., 2012) and stronger PAH emission (Elbaz et al., 2011) than local ULIRGs. Furthermore, by comparing the 8 μm flux to the total infrared flux of high redshift ULIRGs, Elbaz et al. (2011) find that most $z \gtrsim 1$ ULIRGs lie on the infrared main sequence and are in a normal star forming mode of evolution. Similarly, Bournaud et al. (2012), Kocevski et al. (2012), and Mullaney et al. (2012) find that at $z \sim 0.7$, $z \sim 2$, and $z \lesssim 3$, AGN tend to be hosted by galaxies on the main sequence of star formation (see Elbaz et al., 2011). Observations and simulations both point out that high redshift galaxies are

more gas rich than local galaxies (e.g., Treister et al., 2010; Di Matteo et al., 2012; Niemi et al., 2012). It is likely that galaxies with large reservoirs of gas and dust are capable of fueling ULIRGs without being triggered by a major merger.

Elbaz et al. (2011) do find that some high redshift ULIRGs are in a starburst mode, possibly triggered by a merger. Moreover, Elbaz et al. (2011) find evidence for a population of very highly obscured AGN embedded in these compact dusty starbursts. Other observational studies also find CT AGN ($N_H > 10^{24}$ cm^{-2}) candidates in high redshift dusty starburst galaxies (e.g., Donley et al., 2010; Melbourne et al., 2012). Fabian (1999) explains that the gas and dust funneled into the central regions of the merger remnant galaxy will fuel a burst of star formation, rapid black hole accretion, and will obscure the resulting AGN. Thus, a significant fraction of CT AGN are expected to be recently triggered, likely by a major merger, and accreting very rapidly (e.g., Draper & Ballantyne, 2010). The results of this study are consistent with the merger-triggered CT AGN scenario, but, as $\Psi_{merger}/\Psi_{total} \lesssim 0.12$ for ULIRGs at $z \sim 1$, the contribution of these merger-triggered CT AGN to the $z \gtrsim 1$ ULIRG population must be fairly small. The fraction of AGN that are CT is hard to observationally constrain due to the severe obscuration that defines CT AGN and AGN population models predict a wide range for the CT fraction (see Ballantyne et al., 2011). Increasing the fraction of AGN that are CT in this model by a factor of 1.5 increases the $z \sim 1$ ULIRG $\Psi_{merger}/\Psi_{total}$ by $\sim$0.01.

Local ULIRG SEDs are often divided into two groups, warm and cool, where warm ULIRG SEDs are characterized by $f_{25\mu m}/f_{60\mu m} > 0.2$ (e.g., Alonso-Herrero et al., 2006), where $f_{25\mu m}$ is the 25 μm flux and $f_{60\mu m}$ is the 60 μm flux. According to Alonso-Herrero et al. (2006), warm ULIRGs are 15–30% of the Bright Galaxy Survey sources (Sanders et al., 1988b). The merger model used here does produce warm ULIRG SEDs with $f_{25\mu m}/f_{60\mu m} \gtrsim 0.5$ at all redshifts; thus mergers can account for the local population of warm ULIRGs. Elbaz et al. (2011) found that galaxies on the main sequence of normal star formation, including galaxies hosting AGN, tend to have cooler dust temperatures than star-bursting galaxies. Because starbursts triggered by major mergers are expected to be more compact than secular star formation, merger-triggered starbursts will be characterized by higher

dust temperatures than normal star formation (e.g., Elbaz et al., 2011; Melbourne et al., 2012). Indeed, observations of local ULIRGs show that compact ULIRGs are more likely to host an AGN than less compact ULIRGs (Nardini et al., 2010). Analyzing simulations of major mergers, Younger et al. (2009) find that warm ULIRGs are likely to be galaxies evolving from the star formation dominated merger phase to the AGN-starburst post-merger phase. Thus, by combining *Herschel* and *Spitzer* or *Wide-field Infrared Survey Explorer* (WISE) observations to select warm ULIRGs, the population of ULIRGs hosting merger-triggered AGN can be identified. As discussed above, the population of ULIRGs hosting AGN triggered by major mergers is likely to include a significant fraction of CT AGN. Thus seeking out high redshift ULIRGs with warm SEDs will also lead to the identification of high redshift CT AGN.

By combining the evolving luminosity function of AGN triggered by major mergers calculated by Draper & Ballantyne (2012) with the merger-triggered starburst model of Hopkins et al. (2010b), we computed an upper limit for the major merger contribution to the ULIRG population. Locally, major mergers can account for the observed population of ULIRGs hosting AGN and ULIRGs with warm SEDs, but the local ULIRG $\Psi_{merger}/\Psi_{total} \lesssim 0.26$. By $z \sim 1$, major merger-triggered ULIRGs hosting AGN can no longer account for the population of ULIRGs observed to have AGN signatures. Indeed, the ULIRG $\Psi_{merger}/\Psi_{AGN} \lesssim 0.50$ by $z \sim 1.25$. Furthermore, at $z \sim 1$, the ULIRG $\Psi_{merger}/\Psi_{total} \lesssim 0.12$. Combining observations by *Herschel* and *Spitzer* or WISE to identify high redshift ULIRGs with warm SEDs is a good tool for identifying the population of ULIRGs hosting merger-triggered AGN, a large fraction of which are expected to be CT.

7.5 References

Alonso-Herrero, A., Pérez-González, P.G., Alexander, D.M., et al. 2006, ApJ, 640, 167

Armus, L., Charmandaris, V., Bernard-Salas, J., et al. 2007, ApJ, 656, 148

Ballantyne, D.R., Draper, A.R., Madsen, K.K., Rigby, J.R., Treister, E. 2011, ApJ, 736, 56

Bournaud, F., Juneau, S., Le Floc'h, E., et al. 2012, ApJ, in press (arXiv:1111.0987)

Brand, K., Dey, A., Weedman, D., et al. 2006, ApJ, 644, 143

Daddi, E., Dannerbauer, H., Elbaz, D., et al. 2008, ApJ, 673, L21

Davies, R.I., Müller Sánchez, F., Genzel, R., et al. 2007, 671, 1388

Di Matteo, T., Khandai, N., Feng, Y., et al. 2012, ApJ, 745, L29

Donley, J., Rieke, G.H., Alexander, D.M., Egami, E., & Pérez-González, P.G. 2010, 719, 1393

Draper, A.R. & Ballantyne D.R. 2010, ApJ, 715, L99

Draper, A.R. & Ballantyne D.R. 2011, ApJ, 729, 109

Draper, A.R. & Ballantyne D.R. 2012, ApJ, 751, 72

Elbaz, D., Dickinson, M., Hwang, H.S., et al. 2011, A&A, 533, 119

Fabian, A.C. 1999, MNRAS, 308, L39

Ferland, G.J., Korista, K.T., Verner, D.A., et al. 1998, PASP, 110, 761

Goto, T., Arnouts, S., Inami, H., et al. 2011, MNRAS, 410, 573

Goto, T., Takagi, T., Matsuhara, H., et al. 2010, A&A, 514, A6

Gruppioni, C., Pozzi, F., Lari, C., et al. 2005, ApJ, 618, L9

Hopkins, P.F. 2012, MNRAS, 420, L8

Hopkins, P.F. & Hernquist, L. 2009, ApJ, 698, 1550

Hopkins, P.F., Hernquist, L., Cox, T.J., et al. 2006a, ApJS, 163, 1

Hopkins, P.F., Bundy, K., Croton, D., et al. 2010a, ApJ, 715, 202

Hopkins, P.F., Younger, J.D., Hayward, C.C., Narayanan, D., & Hernquist, L. 2010b, MNRAS, 402, 1693

Houck, J.R., Soifer, B.T., Neugebauer, G., et al. 1984, ApJ, 278, L63

Houck, J.R., Schneider, D.P., Danielson, G.E., et al. 1985, ApJ, 290, L5

Kartaltepe, J.S., Sanders, D.B., Le Floc'h, E., et al. 2010, ApJ, 721, 98

Kennicutt, R.C. 1998, ARA&A, 36, 189

Kocevski, D.D., Faber, S.M., Mozena, M., et al. 2012, ApJ, 744, 148

Le Floc'h, E., Papovich, C., Dole, H., et al. 2005, ApJ632, 169

Melbourne, J., Soifer, B.T., Desai, V., et al. 2012, AJ, 143, 125

Mullaney, J., Pannella, M., Daddi, E., et al. 2012, MNRAS, 419, 95

Nardini, E., Risaliti, G., Watabe, Y., Salvati, M., & Sani, E. 2010, MNRAS, 405, 2505

Narayanan, D., Dey, A., Hayward, C.C., et al. 2010, MNRAS, 407, 1701

Niemi, S.-M., Somerville, R.S., Ferguson, H.C., et al. 2012, MNRAS, 421, 1593

Pearson, C. 2005, MNRAS, 358, 1417

Pérez-González, P.G., Rieke, G.H., Villar, V., et al. 2008, ApJ, 675, 234

Rieke, G.H., Alonso-Herrero, A., Weiner, B.J., et al. 2009, ApJ, 692, 556

Rodighiero, G., Daddi, E., Baronchelli, I., et al. 2011, ApJ, 739, L40

Rodríguez Zaurín, J., Tadhunter, C.N., & González Delgado, R.M. 2010, MNRAS, 403, 1317

Sanders, D.B., Soifer, B.T., Elias, J.H., et al. 1988a, ApJ, 325, 74

Sanders, D.B., Soifer, B.T., Elias, J.H., Neugebauer, G., & Matthews, K. 1988b, ApJ, 328, L35

Schawinski, K., Thomas, D., Sarzi, M., et al. 2007, MNRAS, 382, 1415

Schawinski, K., Virani, S., Simmons, B., et al. 2009, ApJ, 692, L19

Schmidt, M. & Green, R.F. 1983, ApJ, 269, 352

Soifer, B.T., Rowan-Robinson, M., Houck, J.R., et al. 1984, ApJ, 278, L71

Soifer, B.T., Neugebauer, G., Helou, G., et al. 1984b, ApJ, 283, L1

Sturm, E., Verma, A., Graciá-Carpio, J., et al. 2010, A&A, 518, L36

Treister, E., Urry, C.M., Van Duyne, J., et al. 2006, ApJ, 640, 603

Treister, E., Natarajan, P., Sanders, D.B., et al. 2010, Science, 328, 600

Veilleux, S., Kim, D.-C., & Sanders, D.B. 2002, ApJS, 143, 315

Wild, V., Heckman, T., & Charlot, S. 2010, MNRAS, 405, 933

Younger, J.D., Hayward, C.C., Narayanan, D., et al. 2009, MNRAS, 396, L66

Zavala, J., Avila-Reese, V., Firmani, C., & Boylan-Kolchin, M. 2012, MNRAS, submitted (arXiv:1204.0516)

CHAPTER VIII

CONCLUSION

By combining knowledge of active galactic nuclei (AGN) gained from deep X-ray surveys with theoretical AGN spectral energy distributions (SEDs), I have shown that multi-wavelength population synthesis modeling is an important tool for studying the average properties of AGN and their host galaxy stellar populations and star formation histories. In Chapter 2, I quantified the contribution of blazars to the cosmic X-ray background (XRB), thus constraining the contribution of Compton thick AGN to the XRB. I found that blazars contribute ∼9% of the XRB in the 15–55 keV band, which includes the peak of the XRB at ∼30 keV. Thus, Compton thick AGN account for ∼20% of the XRB in the 15-55 keV band.

In Chapter 3, I calculated the first XRB population synthesis model which classifies AGN based on their physical characteristics of Eddington ratio and black hole mass. Using this model I found that it is likely that a significant fraction of Compton thick AGN are rapidly accreting objects which may have been triggered recently. The remaining Compton thick AGN are likely to be accreting at very low Eddington ratio and are likely obscured by a dense molecular cloud in the inner regions of their host galaxy rather than the canonical dusty torus of the unified model. Thus, it appears that Compton thick AGN do not evolve like less obscured Type 2 AGN and do not seem to follow the unified model.

In Chapter 4, I demonstrated that analysis of far infrared differential number counts of AGN and their hosts, is an important tool in determining the star formation history of AGN host galaxies. The differential number counts from *Herschel* surveys in the 350 μm band should be especially useful for constraining the star formation history of AGN host galaxies. Furthermore, in Chapter 5, I showed that as a natural consequence of the orientation based unified model, the host galaxies of type 1 and type 2 AGN should, on average, be the same. By comparing model stellar populations to observations of AGN and

their host galaxies, I showed that at $z < 1$ type 1 and type 2 AGN appear to have the same average host galaxies. However, at $z > 1$ the unified model appears to not hold; at high redshift type 2 AGN host galaxies are dustier than type 1 AGN host galaxies.

In order to understand why the unified model appears to hold at low redshift but not at high redshift, in Chapter 6 I explored the triggering mechanisms of AGN. I found that at $z \gtrsim 1.5$, major mergers are capable of triggering the majority of AGN. However, by $z \sim 1$, secular processes are the dominant AGN triggering mechanism. Interestingly, major merger triggered AGN-starburst galaxies can account for all local ultra-luminous infrared galaxies (ULIRGs) which host AGN and ∼25% of the total local ULIRG luminosity density, as shown in Chapter 7. By $z \sim 1$, merger triggered AGN-starburst galaxies can no longer account for the space density of ULIRGs hosting AGN and can account for $\lesssim 12\%$ of the total ULIRG luminosity density. Thus, in contrast to the role of major mergers in the AGN population as a whole, major mergers are less important for triggering ULIRGs at high redshift than they are locally.

I have shown that the dominant AGN triggering mechanism appears to change at $z \gtrsim 1$. Thus, during the peak epoch of quasar activity, at $z \sim 2$, major mergers are likely to play an important role in galaxy evolution and triggering AGN. However, at $z \sim 2$, the majority of galaxies with star formation rates which lead to infrared luminosities, $L_{IR} > 10^{12}$ $L_{\odot}$, are undergoing secular evolution fueled by large reservoirs of cold gas. In contrast, at $z \lesssim 1$, secular processes are responsible for triggering the majority of AGN activity; yet, major mergers dominate the population of galaxies with $L_{IR} > 10^{12}$ $L_{\odot}$. These results are interpreted as a natural consequence of cosmic downsizing and illustrate global trends in galaxy evolution.

In order to further understanding of the connection between type 1 and type 2 AGN, work must be done to determine the fraction of AGN which are type 2, f_2, and how f_2 evolves with luminosity and redshift. Currently it is assumed that f_2 does not evolve beyond $z = 1$. However, the results of this dissertation suggest that the AGN population experiences a shift in the relationship between type 1 and type 2 AGN at $z \sim 1$. Constraining f_2 at $z \gtrsim 1$ will be an important step in understanding how the AGN population evolves to high

redshift. The very hard X-ray surveys which will be conducted by the Nuclear Spectroscopic Telescope Array (NuSTAR), launched in 2012, will help to provide a catalog of AGN which extends to redshift $z \gtrsim 2$ and is unbiased against even heavily obscured AGN. This AGN sample will be useful in determining the evolution of f_2 in the redshift range $z = 1$–2. Constraining f_2 and its evolution with luminosity and redshift will also spread light on the nature and geometry of the obscuring material responsible for AGN obscuration and the reflection spectra observed in the spectra of both obscured and unobscured AGN.

An important and daunting task for future researchers will be to develop a substantial sample of AGN securely identified as Compton thick at $z > 0$. To complete this task results from *Herschel*, WISE, and NuSTAR surveys will need be analyzed in concert. This sample will allow the nature and evolution of Compton thick AGN to be more carefully considered. As a significant fraction of Compton thick AGN may be in a special evolutionary stage, gaining better understanding of this class of AGN is important for determining the role of AGN in galaxy evolution.

Future studies should also work to build deep multi-wavelength catalogs of AGN and their host galaxies. This work has shown that multi-wavelength population synthesis modeling is an important tool for constraining the average properties of AGN host galaxies. However, meaningful constraints on the AGN host galaxy population can only be determined if a variety of observational constraints are available for comparing against model predictions. Developing an AGN catalog which includes X-ray, optical, and near-, mid-, and far infrared observations is necessary to enable studies of the stellar populations and the star formation history of AGN host galaxies.

APPENDIX A

CALCULATING THE BLAZAR SED

The synchrotron and IC contributions to the SED are both parametrized in $log(\nu) - log(L)$ space by a linear curve which transitions to a parabolic curve, parametrized by the 151 MHz luminosity, L_{151MHz} (Fossati et al., 1997, 1998; Donato et al., 2001). For $x = \log \nu$, $x_R = \log(151\ \text{MHz})$, $x_X = \log(1\ \text{keV}/h_p)$, where h_p is Planck's constant, $\psi(x) = \log L(\log \nu)$, $\psi_R = \log L_{151MHz}$, and $\psi_X = \log L_{1keV}$, $L(\nu)$ can be found by

$$\psi(x) = \log(10^{\psi_S} + 10^{\psi_{IC}}) \tag{A.1}$$

where

$$\psi_S = \begin{cases} (1-\alpha_s)(x - x_R) + \psi_R & x \leq x_{trs} \\ -[(x - x_s)/\sigma]^2 + \psi_{sp} & x > x_{trs} \end{cases} \tag{A.2}$$

and

$$\psi_{IC} = \begin{cases} (1-\alpha_c)(x - x_X) + \psi_X & x \leq x_{trc} \\ -[(x - x_c)/\sigma]^2 + \psi_{cp} & x > x_{trc} \end{cases} . \tag{A.3}$$

Fossati et al. (1997) gives the synchrotron slope $\alpha_s = 0.2$, the synchrotron transitional frequency $\nu_{trs} = 5 \times 10^{10}$ Hz, and the width parameter

$$\sigma = \left[-\frac{x_{trs} - x_s}{1 - \alpha_s} \right]^{1/2}, \tag{A.4}$$

while Donato et al. (2001) gives the inverse Compton peak slope $\alpha_c = 0.6$.

To ensure continuity of ψ_S at x_{trs}, the parameter ψ_{sp} is defined

$$\psi_{sp} \equiv (1-\alpha_s)(x_{trs} - x_R) + \left[\frac{x_{trs} - x_s}{\sigma} \right]^2 + \psi_R. \tag{A.5}$$

For ψ_{IC} to be continuous and differentiable at x_{trc}, ψ_X must be defined as

$$\psi_X \equiv -\left[\frac{x_{trc} - x_c}{\sigma} \right]^2 - (1-\alpha_c)(x_{trc} - x_X) + \psi_{cp} \tag{A.6}$$

and the transition frequency between the linear and parabolic portion of ψ_{IC}, ν_{trc}, must be defined such that

$$x_{trc} \equiv x_c - \sigma^2(1-\alpha_c)/2. \tag{A.7}$$

In §2.2.1.3 the synchrotron peak frequency $\nu_S = 10^{x_S}$, the ratio between the inverse Compton and synchrotron peak frequencies $\nu_{IC}/\nu_S = x_c - x_s$, and the ratio between the inverse Compton and synchrotron peak luminosities $L_{IC}/L_S = \psi_{cp} - \psi_{sp}$ are set according to observational data and individual blazar SED models.

A.1 References

Donato, D., Ghisellini, G., Tagliaferri, G., Fossati, G. 2001, A&A, 375, 739

Fossati, G., Celotti, A., Ghisellini, G., & Maraschi, L. 1997, MNRAS, 289, 136

Fossati, G., Maraschi, L., Celotti, A., Comastri, A., & Ghisellini, G. 1998, MNRAS, 299, 433

VITA

Aden R. Draper

Aden R. Draper was born in Vermont and raised in southwestern New Hampshire as Denise A. Draper. Denise particularly loved playing sports and wanted to be either a professional basketball or field hockey player. As neither of those options worked out, Denise's love of science became the guiding force of her life. Upon graduation from high school, Denise moved to Decatur, Georgia to study physics and mathematics at Agnes Scott College. While at Agnes Scott, Denise came out as transgender and starting going by Aden. Aden graduated from Agnes Scott *Summa Cum Laude*, with a B.A. in physics and mathematics. Aden then began his graduate studies at the Georgia Institute of Technology. He spends most of his free time enjoying the company of friends and family in the great outdoors, playing guitar, and brewing beer. Although he is sad to be leaving research, Aden looks forward to starting his career as a patent agent in the law offices of Alston + Bird, LLP upon his graduation from Georgia Tech.